ALMA MATER STUDIORUM – Università di Bologna

FACOLTÀ DI CHIMICA INDUSTRIALE

Dipartimento di Chimica Industriale e dei Materiali

H_2 PRODUCTION FROM STEAM ETHANOL REFORMING (ESR)

Tesi di dottorato di ricerca in

CHIMICA INDUSTRIALE (Settore CHIM/04)

Presentata da

Dr. **Irene BERSANI**

Relatore

Dr. **Francesco BASILE**

Coordinatore

Prof. **Fabrizio CAVANI**

Correlatori

Prof. **Giuseppe FORNASARI**

Prof. **Angelo VACCARI**

ciclo XXIII

Anno 2011

ethanol

reforming

hydrotalcite

rhodium

pressure

Contents

1 Introduction

The global energy landscape is constantly and rapidly evolving in response to advancing technologies, energy and environmental policies, and in recent years also to an economic crisis that emphasized widely different growth dynamics among different areas of the world. In the past decade, the prices of the key energy sources have also shown a high level of instability, often not justified by the dynamics of demand and supply fundamentals, but rather related to the speculative behaviour of financial markets (*1*). To meet the challenges of energy security and climate change as well as the growing energy needs of the developing world, a global energy technology revolution is essential.

Renewable energy has already been recognized as playing a key role for a global energy future, with a diversity of renewable energy sources which would vary geographically. In addition energy sources as sunlight, wind and falling water are generally considered renewable and therefore sustainable over the relatively long term. Wastes and biomass fuels are also usually viewed as sustainable energy. Biomass, wind and geothermal energy are commercially competitive and are making relatively fast progress (*2*).

The potential role of hydrogen in the world's future energy system has been analysed in many assessments (*3*) and remains a topic of vigorous, ongoing debate (*4*). Hydrogen is a "building block" product of remarkable industrial interest and it is indicated as energy carrier of increasing relevance (*5*). Today, "hydrogen economy" is high on the political agenda and on the priorities of agencies funding research. Hydrogen is claimed to replace hydrocarbons and to provide a clean fuel with no carbon emissions for use in stationary and mobile applications as well. Fuel cells will play a key role for both applications.

Although hydrogen can be produced from a large variety of sources by using different methods, up to now the most extensively used process is the steam reforming of hydrocarbons. Biomass can be also used to produce H_2 by thermochemical or biological processes. Metabolic processing appears as an interesting alternative for the treatment of wastes while generating H_2 as product. Some other approaches for hydrogen production from water or other hydrogen-containing materials such as photodecomposition or thermochemical processes are also in development. Solar photodecomposition of water still has many technical hurdles remaining that suggest it is decades away from large scale, cost-effective implementation (*6*).

The conversion of hydrocarbons to hydrogen and syngas will play an important role in the 21st century ranging from large gas to liquid plants and hydrogen plants for

refineries to small units providing hydrogen for fuel cells. The choice of technology for manufacture of syngas depends on the scale of operation (*7*).

Among the liquid H_2 sources, C_2H_5OH is a good candidate for several reasons: (i) ethanol is renewable and is becoming increasingly available; (ii) it is easy to transport, biodegradable, and low in toxicity; (iii) it could be easily decomposed in the presence of water to generate a hydrogen-rich mixture; and (iv) it is free from catalyst poisons such as sulfur. Haryanto et al. observed that the ethanol conversion and H2 production varies greatly with the reaction conditions, the type of catalyst and the method of catalyst preparation (*8*). The challenge is, therefore, to develop catalysts exhibiting high stability and activity for ethanol steam reforming with high yields of hydrogen and resistance to coke formation at relatively low temperature.

2 Literature review

2.1 Global view of renewable energy

2.1.1 Global energetic scenario

It is not an exaggeration to say that the future of human prosperity hinges on finding a way of supplying the world's growing energy needs in a way that does not irreparably harm the environment. Until recently, it looked as if we had plenty of time to meet that challenge. No longer. Surging oil and gas prices have drawn attention to the physical and political constraints on raising production - and the vital importance of affordable supplies to the world economy. And the latest scientific evidence suggests that the pace of climate change resulting from man-made emissions of greenhouse gases - the bulk of which come from burning fossil fuels - is faster than predicted. The urgent need for a veritable energy revolution, involving a wholesale global shift to low-carbon technologies, is now widely recognised (*9*).

Climate change, coupled with concerns about high oil and energy prices, is driving a global trend towards the increased use of renewable energy. Unlike fossil fuels which are rapidly being depleted, renewable energy sources such as sunlight and wind are naturally replenished and therefore sustainable. Indeed, it is the perceived notion of sustainability that is driving governments around the world to introduce legislation promoting the use of renewable energy (*10*).

Currently, only about 18% of the world's energy demand is supplied from renewable energy sources (*9*). However, there is great potential to increase this contribution. Indeed, it has been estimated that the technical potential of renewable energy is more than 18 times that of current global primary energy demand (*11*). This estimate, however, does not allow for economic and environmental constraints and is therefore somewhat misleading. Owing to constraints, such as economic competitiveness, the potential that is likely to be realized in practice will be only a fraction of this value.

Despite this estimate, the International Energy Agency (IEA), the U.S. Energy Information Administration (EIA) and British Petroleum (BP) previsions show that in the future the world will see an ever-increasing role of fossil energy sources (*9*) (*12*) (*13*). In its World Energy Outlook 2008, the IEA describes a reference scenario for global energy demand and supply for fossil, nuclear and renewable primary energy sources (*9*). The comparison of IEA data with them of EIA show very similar trends: crude oil continue to be the most important energy source , followed by coal and

natural gas. Nuclear and renewable energies will grow slightly, but the dominance of fossil fuels remains unchanged (Fig. 2.1).

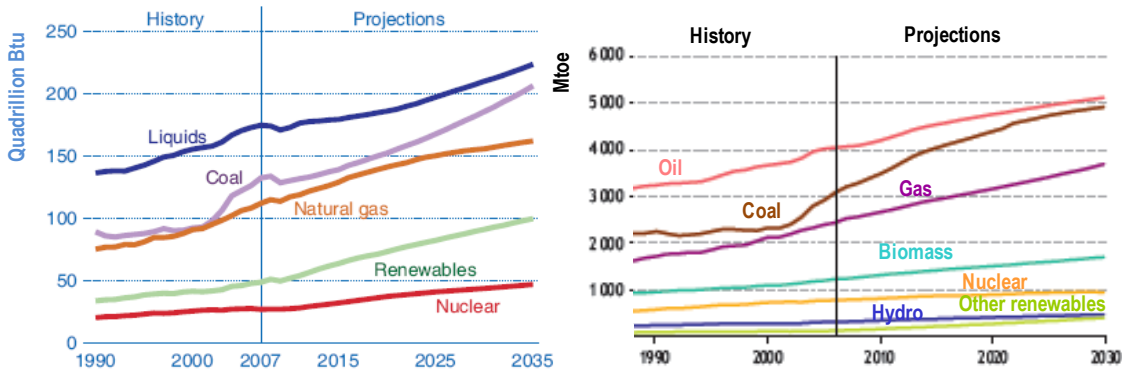

Fig. 2.1 World primary energy demand by fuel a)EIA, b)IEA (*9*) (*12*).

At the same time, although the developed world has accounted for the majority of world energy use, the U.S. Energy Information Administration predicts that demand for energy will increase by 70% from 2007 to 2035 in the world due to substantial economic development with the concomitant increases in energy demand in terms of electricity and fuels (Fig. 2.2 and Fig. 2.3)(*12*) (*13*)(*14*). The most rapid growth in energy demand from 2007 to 2035 occurs in nations outside the Organization for Economic Cooperation and Development (non OECD nations). Current OECD member countries (as of March 2010) are the United States, Canada, Mexico, Austria, Belgium, Czech Republic, Denmark, Finland, France, Germany, Greece, Hungary, Iceland, Ireland, Italy, Luxembourg, the Netherlands, Norway, Poland, Portugal, Slovakia, Spain, Sweden, Switzerland, Turkey, the United Kingdom, Japan, South Korea, Australia, and New Zealand.

This increasing trend in demand of energy of non OECD countries it is due to the necessity to improve standards of living but also to the increase of population, in fact in non OECD nations population continues to increase (Fig. 2.3). At the global level, the most fundamental relationship in energy economics remains robust: more people with more income means that the production and consumption of energy will rise.

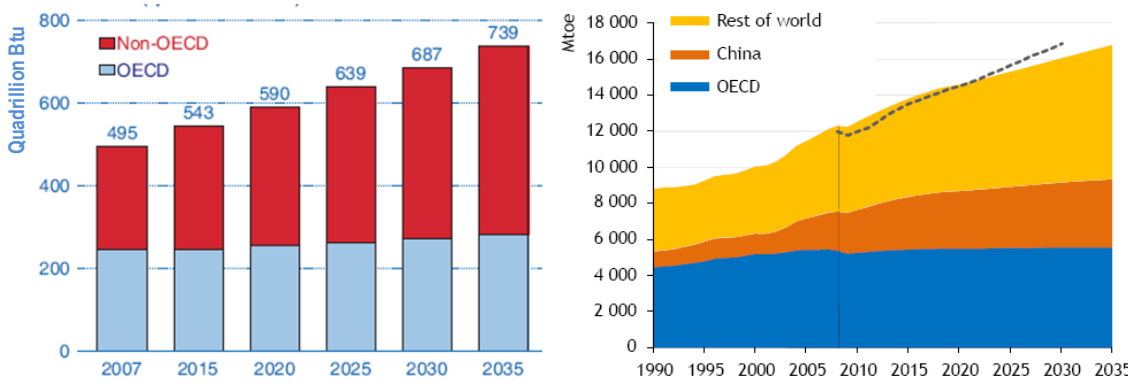

Fig. 2.2 World primary energy demand by region a)EIA, b)IEA (*12*) (*14*).

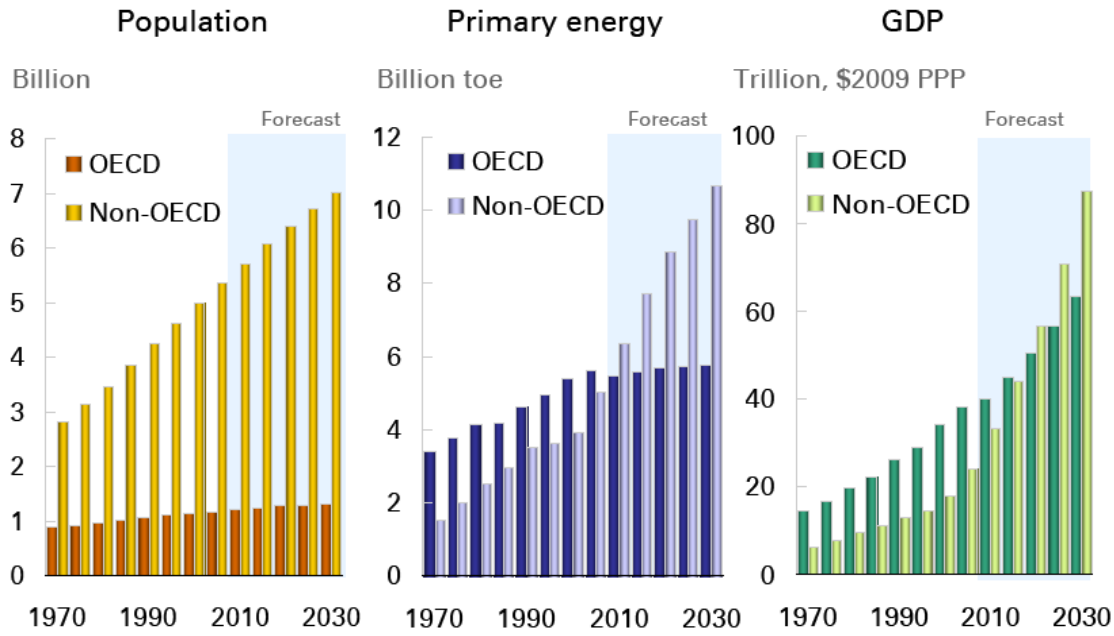

Fig. 2.3 World incremental trends: population, energy and gross domestic products (GDP) (*13*).

Last World Energy Outlook 2010 predicts that differently from non OECD countries, OECD nations show a decline in the demand of oil and coal and an increase of investments in renewables sources. The use of renewable energy triples between 2008 and 2035, driven by the power sector where their share in electricity supply rises from 19% in 2008 to 32% in 2035 (Fig. 2.4 and Fig. 2.5). Renewables are entering the mainstream, but long-term support is needed to boost their competitiveness(*14*).

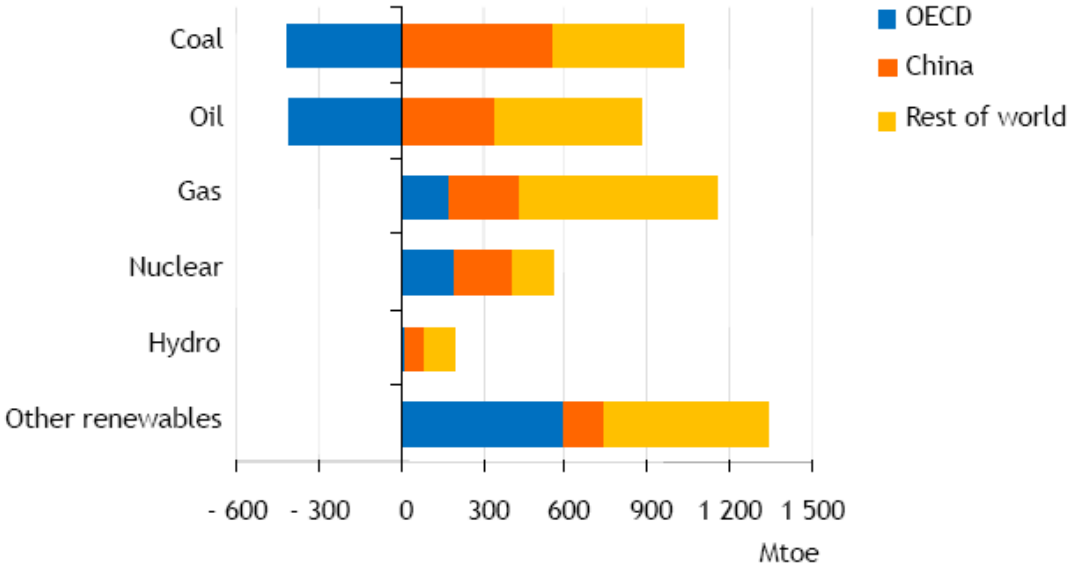

Fig. 2.4 Incremental primary energy demand, 2008-2035 (*14*).

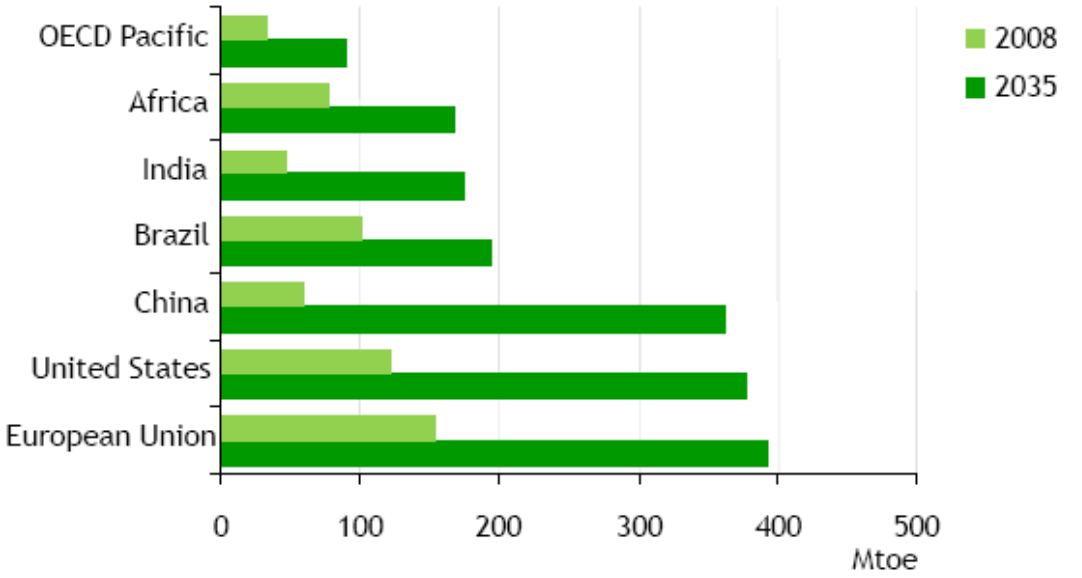

Fig. 2.5 Renewable primary energy demand (14).

About 98% of carbon emissions result from fossil fuel combustion. Reducing use of fossil fuels would considerably reduce the amount of carbon dioxide produced, as well as reducing the levels of the pollutants. Indeed, much of the variation in cost estimates to control carbon emissions revolves around the availability and cost of carbon-free technologies and carbon-reducing technologies, such as energy efficiency and energy conservation equipment. This can be achieved by either using less energy altogether, or using alternative energy resources. Much of the current effort to control such emissions focuses on advancing technologies that emit less carbon or no carbon such as nuclear, hydrogen, solar, wind, geothermal or on using energy more efficiently, and on developing innovative technologies and strategies to capture and dispose of carbon dioxide emitted during fossil fuel combustion.

2.1.2 Renewable Energy Sources (RES)

Renewable energy has already been recognized as playing a key role for a global energy future, with a diversity of renewable energy sources which would vary geographically. In addition energy sources as sunlight, wind and falling water are generally considered renewable and therefore sustainable over the relatively long term. Wastes and biomass fuels are also usually viewed as sustainable energy. Biomass, wind and geothermal energy are commercially competitive and are making relatively fast progress (2).

Main renewable energy sources and their usage forms are given in Fig. 2.6.

Energy source	Energy conversion and usage options
Hydropower	Power generation
Modern biomass	Heat and power generation, pyrolysis, gasification, digestion
Geothermal	Urban heating, power generation, hydrothermal, hot dry rock
Solar	Solar home system, solar dryers, solar cookers
Direct solar	Photovoltaic, thermal power generation, water heaters
Wind	Power generation, wind generators, windmills, water pumps
Wave	Numerous designs
Tidal	Barrage, tidal stream

Fig. 2.6 Main renewable energy sources and their usage form (2).

Hydropower, geothermal, solar and wind can be a useful substitute for power and heating generation, while biomass and biofuels, derived from biomass, appear to be an attractive option respect fossil fuels, in particular if it is considered that oil reserve will be finish in a brief period.

Biomass is an interesting alternative for three main reasons. First, it is a renewable resource that could be sustainably developed in the future. Second, it appears to have formidably positive environmental properties resulting in no net releases of carbon dioxide (CO_2) and very low sulfur content. Third, it appears to have significant economic potential provided that fossil fuel prices increase in the future (*15*).

Mainly advantages of bio-fuels are the following: (a) bio-fuels are easily available from common biomass sources; (b) they are represent a CO_2 cycle in combustion; (c) bio-fuels have a considerable environmentally friendly potential; (d) there are many benefits the environment, economy and consumers in using bio-fuels; and (e) they are biodegradable and contribute to sustainability (*16*).

2.1.2.1 Biomass

Biomass resources can be divided into two broad categories: natural and derived materials. Biomass resources include wood and wood wastes, agricultural crops and their waste by-products, municipal solid waste, animal wastes, waste from food processing and aquatic plants and algae. Biomass resource can be subdivided into three categories (*17*) (*18*):

Wastes. Agricultural production wastes, agricultural processing wastes, crop residues, mill wood wastes, urban wood-wastes, urban organic wastes.

Forest products. Wood, logging residues, trees, shrubs and wood residues, sawdust, bark, etc., from forest clearings.

Energy crops. Short rotation woody crops, herbaceous woody crops, grasses, starch crops (corn, wheat and barley), sugar crops (cane and beet), oilseed crops (soya bean, sunflower, safflower).

The components of biomass include cellulose, hemicelluloses, lignin, extractives, lipids, proteins, simple sugars, starches, water, HC, ash, and other compounds. Two larger carbohydrate categories that have significant value are cellulose and hemi-cellulose. The lignin fraction consists of non-sugar type molecules (*19*).Industrial biomass can be grown from numerous types of plants, including miscanthus, switchgrass, hemp, corn, poplar, willow, sorghum, sugarcane, (*20*)and a variety of tree species, ranging from eucalyptus to oil palm.

There are three ways to use biomass. It can be burned to produce heat and electricity, changed to gas-like fuels such as methane, hydrogen and carbon monoxide or changed to a liquid fuel. When biomass is used directly in an energy application without chemical processing then it is combusted. Conversion may be effected by thermochemical, biological or chemical processes. These may be categorized as follows: direct combustion, pyrolysis, gasification, liquefaction, supercritic fluid extraction, anaerobic digestion, fermentation, acid hydrolysis, enzyme hydrolysis, and esterification (*21*).

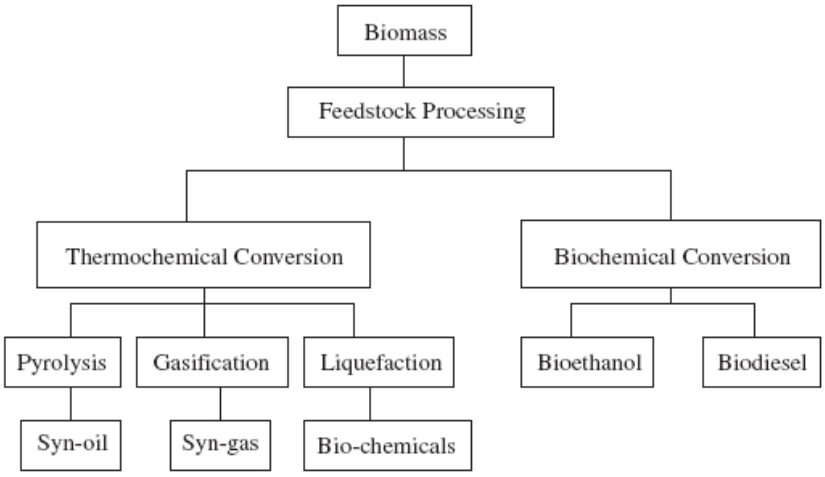

Fig. 2.7 Main biomass conversion processes (*21*).

2.1.2.1.1 Pyrolysis

It is thermo-chemical conversion process and is found to be best suited for conversion of biomass to liquid fuel. Pyrolysis is thermal destruction of biomass in the absence of air/ oxygen. Pyrolysis of biomass starts at 350-550 °C and goes up to 700 °C. This leads to the production of useful liquid oil, gases and solid products. Different condition leads to formation of products in different proportions (*22*). The physical conditions of the pyrolysis of biomass, such as temperature, heating rate and residence time have been shown to have a profound effect on the product yields and composition.

Slow pyrolysis. Biomass is pyrolysed at slow heating rates (5-7 °C/min). This leads to less liquid and gaseous product and more of char production (*22*).

Fast pyrolysis. Initially pyrolysis was done with slow heating rates. This in turn produces more of char. The higher yield of desirable liquid product can be obtained by fast pyrolysis. It involves rapid heating of biomass but not as fast as flash pyrolysis. Heating rate is somewhere about 300 °C/min. Generally, fast pyrolysis is used to obtain high-grade bio oil. Fast pyrolysis is successful with most of fluidized bed reactors as it offers high heating rates, rapid de-volatilization, easy control, easy product collection, etc. (*23*).

Flash pyrolysis. Flash pyrolysis is the process in which the reaction time is of only several seconds or even less. The heating rate is very high. This requires special reactor configuration in which biomass residence times are only of few seconds. Two of appropriate designs are entrained flow reactor and the fluidized bed reactor. Flash pyrolysis of any kind of biomass requires rapid heating and therefore the particle size should be fairly small (*24*).

2.1.2.1.2 Combustion

The biomass is directly burnt in the presence of air to convert chemical energy stored in biomass into heat, mechanical power, or electricity, etc. It is possible to burn any type of biomass but in practice combustion is feasible only for biomass with moisture content of <50%. Combustion process has got many disadvantages. Biomass rarely arises naturally in an acceptable form of burning. In most of the cases it requires some pretreatment like drying, chopping, grinding, etc., which in turn is associated with financial costs and energy expenditure (*25*) (*26*).

2.1.2.1.3 Gasification

Gasification is a form of pyrolysis, carried out at high temperatures (800-900 °C) in order to optimize the gas production. The resulting gas, known as producer gas, is a mixture of carbon monoxide, hydrogen and methane, together with carbon dioxide and nitrogen. The gas is more versatile than the original solid biomass (usually wood or charcoal): it can be burnt to produce process heat and steam, or used in gas turbines to produce electricity (*19*).

2.1.2.2 Biofuels

Biofuel is a renewable energy source produced from natural (biobased) materials, which can be used as a substitute for petroleum fuels. The term biofuel is referred to as solid (bio-char), liquid (ethanol, vegetable oil and biodiesel) or gaseous (biogas, biosyngas and biohydrogen) fuels that are predominantly produced from biomass.

The most common biofuels, such as ethanol from corn, wheat or sugar beet and biodiesel from oil seeds (rape in particular), are produced from classic food crops that require high-quality agricultural land for growth. It is assumed that biodiesel is used as a petroleum diesel replacement and that ethanol is used as a gasoline replacement (*27*).

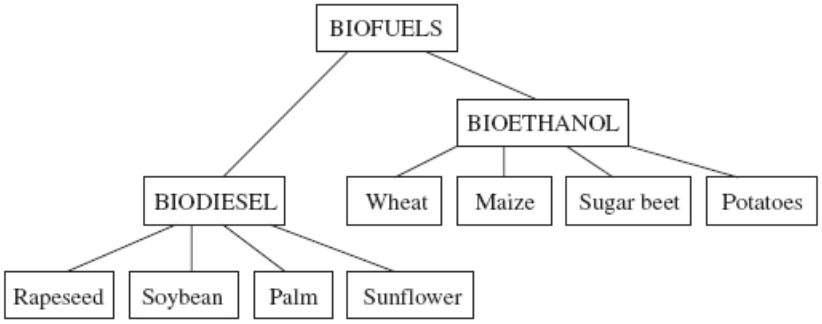

Fig. 2.8 Resources of main liquid biofuels for automotives (*21*).

Ethanol can be used directly in cars designed to run on pure ethanol or blended with gasoline to make "gasohol". Anhydrous ethanol is required for blending with gasoline. No engine modification is typically needed to use the blend. Ethanol can be used as an octane- boosting, pollution-reducing additive in unleaded gasoline.

Most ethanol is currently being produced from sugar cane or corn. Yeast is used to ferment sugars into ethanol. In the case of carbohydrates (such as corn), a pretreatment step of converting carbohydrate into sugars is needed. Currently, the corn ethanol industry uses either a dry-milling or a wet-milling process. Upon fermentation, ethanol content is only about 10%, which requires a significant effort in separation to produce the pure ethanol needed for fuel use. Distillation can concentrate ethanol to just below the azeotropic concentration (95 mol%), after that, specialized separations (molecular sieve, azeotropic distillation, lime drying) are needed.

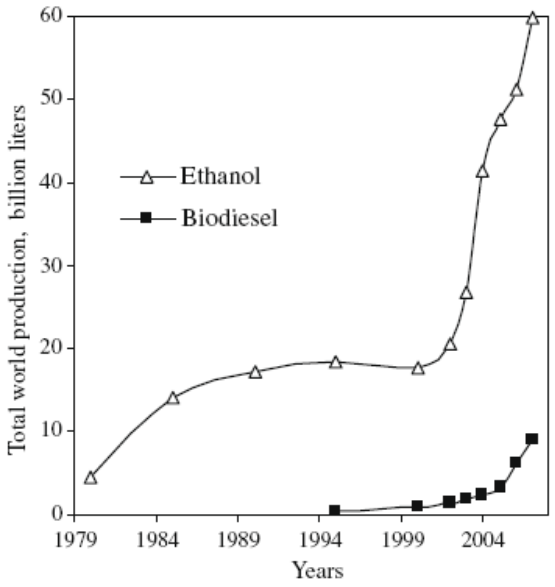

Fig. 2.9 World production of ethanol and biodiesel, 1980–2007 (22).

World production of ethanol from sugar cane, maize and sugar beet increased from less than 20 billion liters in 2000 to over 40 billion liters in 2005. This represents around 3% of global gasoline use. Production is forecasted to almost double again by 2010 (*28*).

Biodiesel is a synthetic diesel-like fuel produced from vegetable oils, animal fats or waste cooking oil. It can be used directly as fuel, which requires some engine modifications, or blended with petroleum diesel and used in diesel engines with few or no modifications. At present, biodiesel accounts for less than 0.2% of the diesel consumed for

transport(*28*). Biodiesel has become more attractive recently because of its environmental benefits.

The cost of biodiesel, however, is the main obstacle to commercialization of the product. With cooking oils used as raw material, the viability of a continuous transesterification process and recovery of high quality glycerol as a biodiesel by-product are primary options to be considered to lower the cost of biodiesel (*29*) (*30*). The oil in the vegetable seeds is converted into biodiesel through oil extraction, oil refining, and transesterification. The cost of biodiesel can be lowered by increasing feedstock yields, developing novel technologies, and increasing economic return on glycerol production by finding other uses for this by-product, which, at the moment, due to oversupply is sold for little or no value.

Biofuels production costs can vary widely by feedstock, conversion process, scale of production and region. On an energy basis, ethanol is currently more expensive to produce than gasoline in all regions considered. Only ethanol produced in Brazil comes close to competing with gasoline. Ethanol produced from corn in the US is considerably more expensive than from sugar cane in Brazil, and ethanol from grain and sugar beet in Europe is even more expensive (Fig. 2.10). These differences reflect many factors, such as scale, process efficiency, feedstock costs, capital and labor costs, co-product accounting, and the nature of the estimates(*31*).

Biofuel	2006	Long-term about 2030
Corresponding pre-tax price of petroleum products	35–60	
Bioethanol from sugar cane	25–50	25–35
Bioethanol from corn	60–80	35–55
Bioethanol from beet	60–80	40–60
Bioethanol from wheat	70–95	45–65
Bioethanol from lignocellulose	80–110	25–65
Biodiesel from animal fats	40–55	40–50
Biodiesel from vegetable oil	70–110	40–75
Fischer–Tropsch synthesis liquids	90–110	70–85

Fig. 2.10 Estimated costs of biofuels compared with the price of oil (biofuels exclusive of taxes),(US cents/liter)(*31*).

For biofuels, the cost of feedstock (crops) is a major component of overall costs. Total biofuel costs should also include a component representing the impact of biofuels production on related markets, such as food. In particular, the cost of producing oil-seed-derived biodiesel is dominated by the cost of the oil and by competition from high-value uses like cooking (Fig. 2.10).

Trying to avoid competition with food a second generation of biofuels was taken in exam for transport field. In general, second generation biofuels are produced from cellulosic materials (lignocellulosic feedstocks). These raw material options may result in the production of more fuel per unit of agricultural land used and require less

chemical and energy input per production and harvesting resulting in a higher yield. Such raw materials may be considered more sustainable and do not compete directly with food. However, there can be competition for land use as well as competition between the potential use of cellulosic materials for liquid biofuels and current use for heat and power generation through combustion as solid biofuels.

At this point biofuels can be classified based on their production technologies: first-generation biofuels; second generation biofuels; third generation biofuels; and fourth generation biofuels. Classification of biofuels based on their generation technologies is shown in Fig. 2.11. The first-generation biofuels appear unsustainable because of the potential stress that their production places on food commodities. Second generation biofuels need to build on the need for sustainable liquid fuels through processing including pyrolysis and hydrothermal liquefaction (*31*).

Generation	Feedstocks	Examples
First-generation biofuels	Sugar, starch, vegetable oils, or animal fats	Bioalcohols, vegetable oil, biodiesel, biosyngas, biogas
Second generation biofuels	Non food crops, wheat straw, corn, wood, solid waste, energy crop	Bioalcohols, bio-oil, bio-DMF, biohydrogen, bio-Fischer–Tropsch diesel
Third generation biofuels	Algae	Vegetable oil, biodiesel
Fourth generation biofuels	Vegetable oil, biodiesel	Biogasoline

Fig. 2.11 Classification of biofuels based on their generation technologies(*31*).

Also for bioethanol, with the current trend in ethanol use (Fig. 2.9), demand is likely to increase significantly in the near future and starch or sugar-based ethanol production has been blamed for the rise in the food prices. To satisfy current and future demands, ethanol production from lignocellulosic biomass fermentation is a viable option that does not compete with the food supply.

2.1.3 H2

The potential role of hydrogen in the world's future energy system has been analysed in many assessments (*3*) and remains a topic of vigorous, ongoing debate (*4*).

Hydrogen is a "building block" product of remarkable industrial interest and it is indicated as energy carrier of increasing relevance (*5*). Hydrogen is found naturally in hydrogen-rich compounds; it cannot be extracted like natural gas or oil, but needs to be released by applying energy. On the one hand, this represents a drawback because the process requires the input of primary energy carriers like coal, natural gas or biomass, of electricity or high temperatures.

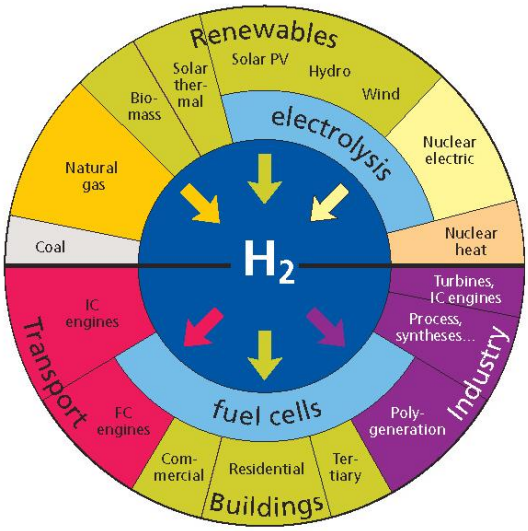

Fig. 2.12 Energy sources for hydrogen production and possible applications (*30*).

The advantage is that a wide range of different feedstocks and energy sources can be used for hydrogen production, in particular from fossil fuels, biofuels by thermochemical way and from water by electrolytic way (*32*).

The interest on hydrogen-based energy systems surged in response to the first oil crisis and the growing concerns about environmental issues. The advantages are the hydrogen nearly zero emissions, its potential role in reducing greenhouse gases (improving air quality), reducing climate changes and the possibility of local production on the basis of a variety of fuels (decreasing dependence on imported oil). In fact, the high end-use efficiency in fuel cells and the possibility to produce hydrogen from non-fossil sources or clean fossil fuels (fossil fuel combustion in combination with coke capture and storage - CCS) could reduce greenhouse gas emissions from the energy system(*33*).

Today, "hydrogen economy" is high on the political agenda and on the priorities of agencies funding research. Hydrogen is claimed to replace hydrocarbons and to provide a clean fuel with no carbon emissions for use in stationary and mobile applications as well. Fuel cells will play a key role for both applications.

2.2 H2 relevance and applications

The development of hydrogen production technologies requires identification of potential markets and the constraints associated with those markets.

For non-carbon-dioxide-emitting hydrogen production technologies (nuclear, renewable, and fossil fuels with carbon dioxide sequestration), restrictions on carbon dioxide emissions to the atmosphere are an important factor in the increasing potential size of a future markets(*34*). Existing and potential hydrogen markets were identified as follows(*34*):

Industrial. The two major industrial markets for hydrogen are fertilizer production as ammonia, steel, methanol and H2 for cracking and hydrodesulphurization. All nitrate fertilizers require hydrogen in their production processes. Some but not all steel production processes require hydrogen. These are large-scale facilities that match large-scale hydrogen production systems.

Vehicle. Transportation requirements can be met with different fuels (methanol, dimethyl ether, Fischer-Tropsch fuels or gasoline, diesel, jet fuel and in the future H2 itself). Each fuel requires different amounts of hydrogen in the production process and has different economics of scale.

Power. Hydrogen is a candidate for power production, particularly as a vector for storage and use for production when necessary.

Commercial. Hydrogen is being considered for commercial applications in buildings with the co-generation of power and heat.

With interest in its practical applications dating back almost 200 years, hydrogen energy use is hardly a novel idea. What is new is the confluence of factors since the mid-1990s that increase the attractiveness of hydrogen energy economy. Those factors include persistent urban air pollution, demand for low or zero-emission vehicles, the need to reduce foreign oil imports, carbon dioxide emissions and global climate change, and the need to store renewable electricity supplies. These considerations are not confined to a single nation or region, and make hydrogen a virtually ideal energy carrier that is abundantly and equitably available to humanity (*35*).

2.2.1 Ammonia synthesis

Ammonia is used in various applications, such as textile processing, water purification, and manufacturing explosives. The main part, however, is used as fertilizer(*36*). Ammonia production consumes about half of the hydrogen produced today and it is the primary chemical industry utilization of hydrogen. Ammonia is currently made where there is inexpensive natural gas that provides economical hydrogen and shipped to the costumer. The low cost of shipping ammonia favors very large ammonia production plants with very large demands for hydrogen (*34*).

At the beginning of the 20th century, the use of nitrogenous fertilizers was already well established. Haber and Bosch developed the direct synthesis of ammonia from hydrogen and nitrogen (*37*).

The synthesis of ammonia from nitrogen and hydrogen is a clean reaction, in that it is not complicated by the formation of byproducts, such as hydrazine, and the thermodynamics are seemingly straightforward.

$$1/2\ N_2 + 3/2\ H_2 \rightarrow NH_3$$

$\Delta H°_{700K}$ = - 52.5 kJ/mol

$\Delta G°_{700K}$ = + 27.4 kJ/mol

$\Delta S°_{700K}$ = + 288 J/molK

The reaction is exothermic and is accompanied by a decrease in volume at constant pressure. The value of the equilibrium constant (Kp) therefore increases as the temperature is lowered, and the equilibrium ammonia concentration increases with increasing pressure.

The formation of ammonia is favoured by operation at high pressure and low temperature. The optimum pressure for economic operation with the available catalysts has been in the range 150 - 350 bar. Normally, the advantages of the higher equilibrium concentration of ammonia at very high pressure are more than offset by the higher costs of both gas compression and additional plant capital.

The temperature at which the synthesis process is operated is determined by the activity characteristics of the catalyst. Thermodynamically, low temperature is advantageous, but for kinetic reasons high temperatures have to be used. The most effective catalyst is clearly the one that will give the highest rate of conversion of ammonia at the lowest temperature.

As the synthesis reaction proceeds, the heat of reaction causes the temperature to rise down the bed, so making the specific rate of reaction faster. Since the equilibrium becomes less favourable at higher temperatures, the rate of the reverse reaction is progressively increased and the overall conversion becomes equilibrium-controlled. Careful control of the temperature profile is therefore necessary for the equilibrium balance to be obtained between the limit set by the thermodynamic equilibria, and by

the kinetics of the catalyzed reactions in both forward (synthesis) and reverse (ammonia decomposition) directions.

The main role of the ammonia catalyst is to dissociate the N_2 bond. Under industrial conditions, this is the rate-determining step (RDS) for NH_3 synthesis on Ru, due to the high bond energy. The dissociation takes place at defects and steps, rendering the NH_3 synthesis extremely structure sensitive(*36*).

All commercial ammonia synthesis catalysts are currently based on metallic iron promoted with alkali (K), and various metal oxides, such as those of aluminium, calcium or magnesium. The principal material used to make these catalysts is usually magnetite (Fe_3O_4), with some of the components in the catalyst originating as impurities in the magnetite. A typical catalyst contains approximately 0,8 % K_2O, 2.0 % CaO, 0.3 % MgO, 2.5 % Al_2O_3 and 0.4 % SiO_2, as well as traces of TiO_2, ZrO_2 and V_2O_5. In developing the process to manufacture catalysts of this sort, it was recognized that these minor components could have a large effect on the performance of the final catalyst, since they may also interact with each other, giving rise to both harmful and beneficial effects. In modern catalysts, these factors have been taken onto account, resulting in optimized performance in terms of high activity and long life.

2.2.2 Methanol synthesis

Methanol is inside the top 10 produced molecules. Methanol has been a common chemical feedstock for several important chemicals such as acetic acid, methyl ter-butyl ether (MTBE), formaldehyde and chloromethane. Moreover, methanol being a clean liquid fuel could provide convenient storage of energy for fuel cell applications, particularly in transportation and mobile devices(*38*). In additions, over the last few decades, methanol-to-hydrocarbons (MTHC) technologies, in particular methanol-to-olefin (MTO) and methanol-to-gasoline (MTG), have been the focus for a large number of researcher dealing with the upgrading of natural resources beneficial both for the petrolchemistry and fuel industries (*39*) (*40*)(*41*).

The process to synthesize methanol from carbon monoxide and hydrogen was introduced by BASF in 1923 and it was the second large-scale application of catalysis (after ammonia synthesis) and high-pressure technology (100-300 bar) to the chemical industry (*37*).

Like the ammonia process, methanol synthesis was dependent on the development of an effective catalyst, but unlike the ammonia synthesis catalyst, the methanol catalyst had to be selective as well as active.

The reactions involved in the methanol synthesis are:

(A) $CO + 2\ H_2 \leftrightarrows CH_3OH$ $\Delta H°_{298K} = -90.6$ kJ/mol

$\Delta G°_{298K}$ = - 25.3 kJ/mol

(B) $CO_2 + 3\ H_2 \leftrightarrows CH_3OH + H_2O$ $\Delta H°_{298K}$ = - 49.5 kJ/mol

$\Delta G°_{298K}$ = + 3.3 kJ/mol

(C) $CO + H_2O \leftrightarrows CO_2 + H_2$ $\Delta H°_{298K}$ = - 41.2 kJ/mol

$\Delta G°_{298K}$ = - 28.6 kJ/mol

Reaction (B) and (C) combined are equivalent to reaction (A), so that either, or both, of the carbon oxides can be the starting point for methanol synthesis.

Reactions (A) - (C) are exothermic; reactions (A) and (B) are accompanied by a decrease in volume. Hence, the value of the equilibrium constant decreases with temperature and increases with pressure ($Kp = p_{CH_3OH} / p_{CO}p^2_{H_2}$). Thus, high conversions to methanol, given a sufficiently active catalyst, will be obtained at high pressures and low temperatures.

In addition to the synthesis of methanol, both carbon monoxide and carbon dioxide can take part in other hydrogenation reactions, producing by-products such as hydrocarbons, ethers and higher alcohols:

(D) $CO + 3\ H_2 \leftrightarrows CH_4 + H_2O$ $\Delta H°_{298K}$ = - 206.2 kJ/mol

$\Delta G°_{298K}$ = - 142.2 kJ/mol

(E) $2\ CO + 4\ H_2 \leftrightarrows CH_3OCH_3 + H_2O$ $\Delta H°_{298K}$ = - 204.8 kJ/mol

$\Delta G°_{298K}$ = - 67.2 kJ/mol

(F) $2\ CO + 4\ H_2 \leftrightarrows C_2H_5OH + H_2O$ $\Delta H°_{298K}$ = - 255.6 kJ/mol

$\Delta G°_{298K}$ = - 122.6 kJ/mol

These reactions are much more exothermic than the methanol synthesis reactions and methanol is thermodynamically less stable and less likely to be formed from carbon monoxide and hydrogen than the other possible products, such as methane. Which of the products is formed is controlled by kinetics factors; that is, by the catalyst being selective in favouring a reaction path leading to the desired product.

The catalytic synthesis of methanol from syngas has been conventionally carried out in two-phase reactors with the syngas and products in the vapour phase and the catalyst as solid phase. The large exothermic heat of reaction in addition to the low heat capacity of the vapour increases the potential for thermal runaway and damage to the catalyst in the vapour phase, thus limiting the maximum operable reaction temperature(*42*).

There are two class of catalysts studied and used for methanol synthesis: high-pressure and low-pressure catalysts (Tab. 2.1). The difference in preparation methods, synthesis conditions, and pre-treatment have a considerable influence on the

structure of the catalysts, which finally leads to disparities in the catalytic performance. It is generally accepted that a large specific Cu surface area leads to an active methanol synthesis catalyst. In addition, the metal-support interaction plays a key role in this catalytic reaction (*43*).

Catalyst composition	Active phase in methanol synthesis	Properties and use
ZnO	ZnO	Original synthesis catalyst, short life
ZnO/Cr_2O_3 (ICI catalyst)	ZnO	Standard high pressure catalyst
$ZnO/MnO/Cr_2O_3$ + alkali	Alkalized ZnO (+MnO)	Standard high pressure catalyst for methanol and higher alcohol mixtures
Cu/ZnO $Cu/ZnO/Cr_2O_3$	Cu	Early low pressure catalysts, short life
$Cu/ZnO/Al_2O_3$ (ICI catalyst)	Cu	Industrial low-pressure catalyst
Pd/SiO_2 Pd/basic oxides	Pd	Active; poorer selectivity than copper catalysts (by-products: hydrocarbons)
Rh/SiO_2 Rh/basic oxides	Rh	Active; poorer selectivity than copper catalysts (by-products: hydrocarbons)
Rh complex	Rh complex	Low activity; poorer selectivity (homogeneous catalyst; co-product: ethylene glycol)

Tab. 2.1 Catalysts proposed or used for industrial methanol synthesis (*37*).

2.2.3 Fischer-Tropsch synthesis

The growing reliance on imported oil gave the synthetic fuels a fresh impetus in the 1980s (*44*)(*45*). The Fischer-Tropsch synthesis (FTS) is the exothermic reaction of carbon monoxide and hydrogen to mainly hydrocarbons together with water and carbon dioxide. It can be represented by the following reaction equation:

$$n\,CO + (2n+1)\,H_2 \rightarrow C_nH_{2n+2} + n\,H_2O$$

Sabatier was the first to react carbon monoxide and hydrogen over a nickel catalyst in 1902. The result was the production of methane and water. Then, in 1923 Franz Fischer and Hans Tropsch of the Kaiser Wilhelm Institute (Germany) developed the Fischer-Tropsch process (i.e. Synthol process), in which a carbon monoxide and hydrogen flow, in the presence of iron, cobalt or nickel catalyst at 180-250 °C and at pressures from atmospheric to 150 bar, produced a mixture of straight hydrocarbons and smaller amounts of oxygenates. The initial objective of this process was gasoline production. Experience at high and medium reactor pressures was disappointing from an unacceptably high oxygenate product content point of view. Hence, it was adopted

an atmospheric reactor pressure. Cobalt became strongly favoured as catalytic element, since iron was less active and deactivated rapidly at atmospheric pressure synthesis operation, while nickel gave high methane selectivity and was affected by its loss due to volatile nickel tetracarbonyls production (*46*) (*47*).

The best catalyst was found to be based on cobalt, supported on Kieselguhr with thoria and magnesium oxide as promoters (100g Co / 5g ThO / 8g MgO / 200g Kieselguhr).

In recent years, we assist to a second renewal of interest in the F-T process for producing liquid hydrocarbons. This new interest centres on making synthetic fuels from natural gas instead of coal.

The process of converting natural gas or coal into marketable liquid hydrocarbons comprises three main elements: 1) synthesis gas production, 2) hydrocarbon synthesis via the F-T conversion process, 3) products work-up.

As far as syngas production is concerned, other feedstocks such as coal, heavy residue or shale oil can be used, but the process becomes less economical.

Sasol is the largest producer of synfuels and chemicals made by coal gasification (Lurgi's technology is employed). Besides coal plants, since 1993 Sasol has also operated natural gas-based plants at Mossgas, South Africa, with a capacity of 44.000 BPD of fuels. The company is by far the most experienced player in the syngas-based chemical business, as far as reactors design, catalytic formulations, process technology are concerned.

Sasol has been opting for iron-based catalyst since 1955. Only in recent years the advantages of cobalt based catalyst for use in slurry phase reactor have been recognized.

For the preparation of Synthol catalyst, Sasol uses iron oxides: the suitable iron oxide is fused together with the required chemical and structural promoters. The fused ingots are milled to a specified particle size range (for optimum fluidization properties). The catalyst is pre-reduced with H2 at about 400 °C and then loaded in the F-T reactors. Because of the simplicity of the preparation and the low cost of the row materials, the cost of Synthol catalyst is a minor part of the overall process (*48*).

Studies performed at Sasol on the commercial spray dried precipitated iron catalyst and Co/Al_2O_3 slurry phase FTS catalyst, resulted in the following conclusions:

1. the cobalt does not show any significant water-gas-shift activity and no water inhibition of the F-T reaction rate,

2. the cobalt catalyst is the preferred option if high per pass conversions are required,

3. desired stabilized intrinsic activity levels can be achieved with cobalt catalyst, implying that extended slurry phase synthesis runs can be realized,

4. cobalt derived hydrocarbon product selectivities show greater sensitivity towards process conditions (i.e. reactor pressure) than that of iron. Iron catalyst, on the other hand, shows marked sensitivity towards chemical promotion. Indeed, the geometric tailoring of pre-shaped support materials can be an optimization tool for effecting increased wax selectivities with cobalt based catalyst, an approach also suggested by others (Exxon, Shell).

The conversion of synthesis gas to hydrocarbons (Fischer-Tropsch synthesis) has been widely studied and extensively described. A number of synthesis reactions can occur and the whole are quite exothermic, ΔH = -170 kJ (C/atom):

Methanation: $CO + 3\ H_2 \leftrightarrows CH_4 + H_2O$

Paraffins: $n\ CO + (2n + 1)\ H_2 \leftrightarrows C_nH_{2n+2} + n\ H_2O$

Olefins: $n\ CO + 2n\ H_2 \leftrightarrows C_nH_{2n} + n\ H_2O$

Alcohols: $n\ CO + 2n\ H_2 \leftrightarrows C_nH_{2n+1}OH + (n-1)\ H_2O$

Some other reactions, such as the water-gas shift or Boudouard reaction also occur:

WGS: $CO + H_2O \leftrightarrows CO_2 + H_2$

Boudouard: $2\ CO \leftrightarrows C(s) + CO_2$

The free energy changes (ΔG°) in the above reactions are such that the hydrocarbon synthesis is normally favoured below about 400 °C. Over the temperature range of 200-400 °C, the formation of methane is favoured. However, since the thermodynamic equilibrium is reached slowly in FT synthesis, it is possible to take advantage of kinetic factors by using suitable catalysts, so that heavier hydrocarbons or alcohols are produced in suitable quantity(*45*).

The production of hydrocarbons using traditional FT catalysts, such as Fe or Co, is governed by chain growth or polymerization kinetics. The so-called "surface carbide" mechanism is a plausible one for the interaction of CO and H_2 with the catalytic surface and the subsequent synthesis of hydrocarbons. Ample evidence shows that this is the prevalent mode of activation of CO at elevated temperatures on the Group VIII metal catalysts Fe, Co, Ni and Ru (*44*)(*45*). The model can be used as a starting point for understanding the formation of various molecular species during FT synthesis and also for examining hydrocarbon chain growth(*45*).

The nature of the product and the product distribution among the carbon numbers will depend upon the catalyst surface, composition (H_2/CO ratio) and the rate of flow feed gas, reaction pressure and the temperature at which FT synthesis is performed. The above parameters will affect the rate of hydrogen and CO dissociation, hydrogenation, degree of polymerization and desorption of the product species(*45*).

At low temperatures, the main primary products are linear 1-alkenes, alkanes, alcohols and aldehydes. The linearity of the product is important for many of their applications. It gives the waxes with high melting point and low viscosity.

The C_9 to C_{15} olefins are ideal for the manufacture of biodegradable detergents. The C_{10} to C_{18} cut is an excellent diesel fuel (with the high cetane number of 75 and zero aromatics). On the other hand, the product linearity is a disadvantage for gasoline production, since a high octane number requires branched alkane and aromatics. Hence, the gasoline requires extensive isomerisation and aromatization.

At higher synthesis temperatures secondary reactions occur, i.e branched hydrocarbons and aromatics are formed. In that way, the diesel cetane number decreases, while the gasoline octane number increases. Olefins in the hydrocarbons reach a maximum at C_3 or C_4 (up to 90 %), to then decrease continuously, the waxes being essentially paraffinic (*47*).

2.2.4 Dimethyl Ether synthesis

Dimethyl ether (DME) is an alternative fuel that could potentially replace petroleum-based fuels(*49*). Dimethyl ether is the simplest ether (CH_3OCH_3). The physical properties of DME are similar to those of liquefied petroleum gases (propane and butane). It burns with a visible blue flame and is non-peroxide forming in the pure state or in aerosol formulations. Unlike methane, DME does not require an odorant because it has a sweet ether-like odour. It is a volatile organic compound, but is non-carcinogenic, non-teratogenic, non-mutagenic and non-toxic(*49*).

Currently, the major usage of DME is as a propellant in the aerosols industry. In addition, it can be used as a clean-burning fuel in diesel engines, as a household fuel (LPG alternative) for heating and cooking, as a fuel for gas and turbines in power generation, as a fuel for fuel cells, and as a chemical feedstock for higher ethers and oxygenates (*42*)(*50*).

Traditionally, DME has been produced in a two steps process where syngas is first converted to methanol, followed by methanol dehydration to dimethyl ether.

$CO + 2\ H_2 \leftrightarrows CH_3OH$	$\Delta H°_{298K} = -\ 90.6$ kJ/mol
$CH3OH \leftrightarrows CH_3OCH_3 + H2O$	$\Delta H°_{298K} = +\ 23.4$ kJ/mol
$H_2O + CO \leftrightarrows H_2 + CO_2$	$\Delta H°_{298K} = -\ 41.2$ kJ/mol

Net reaction:

$$3\,CO + 3\,H_2 \leftrightarrows CH_3OCH_3 + CO_2 \qquad \Delta H°_{298K} = +\,258.6\ kJ/mol$$

Natural gas is not the only resource that can be used to generate syngas, coal and biomass can also be used. Hence, DME production is not limited to one feedstock and the price of DME synthesis process is directly related to the price of the feedstock. New processes are being commercialized to produce DME in a single step via autothermal reactors and slurry phase reactors.

DME can be introduced and exploited with existing technologies, and enable the eventual implementation of advanced technologies, such as fuel cells. Because DME is produced from natural gas, coal or biomass, it can increase the energy security by displacing petroleum derived fuels.

The prominent advantages of DME as a fuel and energy carrier are(*49*):

1. DME, due to its high cetane number(*51*), can be used in the most efficient engine technology currently produced. DME demonstrated lower NO_x and SO_x than conventional diesel, is sootless (*52*).

2. Using exiting engine technology, DME produces the least amount of well-to-wheel greenhouse gas emissions compared to FT diesel, FT naphtha, bio-diesel, bio-naphtha, methanol, methane and ethanol.

3. Excluding natural gas, DME has the highest well-to-wheel efficiency of all non-petroleum based fuels using conventional, hybrid and fuel processor fuel cell vehicle technologies.

4. DME can be used as a residential fuel for heating and cooking.

5. On-board automotive fuel processors using methanol and DME exhibit the lowest start-up energies and the lowest fuel processor volumes - correlating to higher overall efficiencies as compared to ethanol, methane and gasoline fuel processor fuel cell vehicles.

6. The infrastructure of DME is less cost intensive than that for hydrogen because DME can use the existing LPG and natural gas infrastructures for transport and storage.

Synthesis of DME from syngas in a single step is more favourable in thermodynamic and economical (*50*)(*51*).

Single-stage DME synthesis in the vapour phase suffers from low per pass conversions(*44*), due, in part, by the effects of high temperature on the catalysts. Gas-phase DME synthesis processes, in general, suffer from the drawbacks of low hydrogen and CO conversions per pass, along with low yield and selectivity of DME, coupled with a high yield of carbon dioxide. These processes are typically expensive due to high capital costs for reactors and heat exchangers, and high operating costs

due to inefficient CO utilization and high recycle rates. Using an inert liquid as a heat sink for highly exothermic reactions offers a number opportunities in syngas processing. Heat generated by the exothermic reactions is readily accommodated by the inert liquid medium. This enables the reaction to be run isothermally; minimizing catalyst deactivation commonly associated with the more adiabatic gas phase technologies(*42*).

The process is based on dual-catalytic synthesis in a single reactor stage, and based on a combination of an equilibrium limited reaction (methanol synthesis) and an equilibrium unlimited reaction (methanol dehydration). The methanol synthesis and the water gas shift reaction take place over the co-precipitated $Cu/Zn/Al_2O_3$ catalyst and the methanol dehydration takes place over γ- Al_2O_3 or zeolites catalysts (*50*)(*51*)(*52*). Moreover, by varying the mass ratios of methanol synthesis catalyst, it is possible to co-produce DME and methanol in any fixed proportion, from 5 % DME to 95 % DME(*42*).

2.2.5 Direct Reduction of iron ore (DRI)

Direct reduction of iron ore is today's major process for generating metallic iron, necessary in the iron and steel industry. World production of direct reduced iron (DRI) has grown from near zero in 1970 to 45.1 Mt in 2002 (*34*) (*53*).

In the production processes for converting iron ores into iron and steel, carbon, primarily in the form of coke, has been traditionally used to reduce the iron oxides to iron metal. However, in the last several decades, there has been increasing production of iron using the direct reduction iron (DRI) process. In 1998, about 4 % of the primary iron in the world was produced by the DRI process with rapid growth in iron production. In the DRI process, syngas (a mixture of hydrogen and carbon monoxide) made from natural gas is used to reduce iron ores to iron. The major chemical reactions are as follows:

$Fe_3O_4 + CO \rightarrow 3\,FeO + CO_2$

$Fe_3O_4 + H_2 \rightarrow 3\,FeO + H_2O$

$FeO + CO \rightarrow Fe + CO_2$

$FeO + H_2 \rightarrow Fe + H_2O$

The DRI process has lower capital costs than alternative methods used to produce iron, but requires a low-cost source of hydrogen. The primary market for DRI is to provide a purified iron feed for electric arc furnaces (EAFs) that produce various steel products. EAFs have lower capital costs than traditional steel mills and are environmentally cleaner operations than blast furnaces. Over a third of the world's steel production uses this process. It is predicted that by 2010 up to 45 % of the world's steel may be made with EAFs. Historically, scrap metal has been the

traditional feed for EAFs. However, there are two constraints: the availability of scrap metal and the various difficult-to-remove impurities (copper, nickel, chrome, molybdenum, etc.) that are present in the lower-grade scrap metal. Blending clean DRI-process iron with scrap metal dilutes the impurities below the level that affect product quality. Traditional steel-making processes using coke result in iron with a high carbon content and various other impurities from the coke.

Iron production is potentially a significant existing market for hydrogen. If low-cost hydrogen is available, the DRI process would replace other methods of iron production. The economics of DRI relative to other processes (and the potential demand for hydrogen) depend upon three factors.

Technological developments. The continuing improvements in EAF technology in terms of reduced production costs and increased capabilities to produce higher-quality steel have expanded the market share of this technology. That, in turn, creates the demand for more high-purity iron by the DRI process as traditional sources of scrap metal are exhausted.

Environmental protection. Traditional steel processes use coal and generate large quantities of pollutants. Clean air requirements strongly affect the economics of these competing processes.

Hydrogen costs. The process is used where there is low-cost natural gas for hydrogen production near iron deposits.

2.2.6 Hydrodesulfurization

Combustion of sulfur-containing compounds in fossil fuels emits sulfur oxides, which can cause adverse effects on health, environment and economy.

Generally, removal of organic sulfur from fossil fuel is difficult, because sulfur can only be detached from the organic molecule when certain chemical bonds are cleaved. Breakage of such bonds requires high temperature and pressure. One of the current technologies to reduce sulfur in middle distillate/diesel fuels such as gasoline or petrol, jet fuel, kerosene, diesel fuel, and fuel oils, is known as hydrodesulphurization (HDS). In HDS, the sulfur atom in sulfur compounds is reduced to H_2S on $CoMo/Al_2O_3$ or $NiMo/Al_2O_3$ catalyst in the presence of H_2 gas. H_2S is then catalytically air oxidized to elemental sulfur(*54*).

Another important reason for removing sulfur from the naphtha streams within a petroleum refinery is that sulfur, even in extremely low concentrations, poisons the noble metal catalysts (platinum and rhenium) in the catalytic reforming units that are subsequently used to upgrade the octane rating of the naphtha streams(*54*).

In an industrial hydrodesulfurization unit, such as in a refinery, the hydrodesulphurization reaction takes place in a fixed-bed reactor at elevated

temperatures ranging from 300 to 400 °C and elevated pressures ranging from 30 to 130 atmospheres of absolute pressure, typically in the presence of a catalyst consisting of an alumina base impregnated with cobalt and molybdenum (usually called a CoMo catalyst). Occasionally a combination of nickel and molybdenum (called NiMo) is used, in addition to the CoMo catalyst, for specific difficult-to-treat feed stocks such as those containing a high level of chemically bound nitrogen. To reach lower concentration of sulfur (< 15 mg/kg) higher temperature and pressure are required. Among the catalytic desulfurization processes, selective HDS processes like SCANfining® and Prime G+® seem to be very efficient and are already in practice world-wide. Indeed, both of these processes which are based on conventional catalytic fixed-bed technology and need low cost investments, are by far the most attractive for the industry(*55*).

Most metals catalyse HDS, but it is those at the middle of the transition metal series that are most active. Ruthenium disulfide appears to be the single most active catalyst, but binary combinations of cobalt and molybdenum are also highly active(*56*). Aside from the basic cobalt-modified MoS_2 catalyst, nickel and tungsten are also used, depending on the nature of the feed. For example, Ni-W catalysts are more effective for hydrodenitrification (HDN).

Metal sulfides are "supported" on materials with high surface areas. A typical support for HDS catalyst is γ-alumina. The support allows the more expensive catalyst to be more widely distributed, giving rise to a larger fraction of the MoS_2 that is catalytically active. The interaction between the support and the catalyst is an area of intense interest, since the support is often not fully inert but participates in the catalysis.

2.2.7 Hydrodenitrogenation

Hydrodenitrogenation (HDN) occurs simultaneously with hydrodesulfurization (HDS), hydrodeoxygenation (HDO), hydrogenation (HYD) and hydrodemetallization (HDM) during hydroprocessing. Effects of these reactions upon each other are rather complex. The extent of the mutual effects depends on the origin of feed, type of catalyst, and operating conditions. The HDN has been the focus of attention because nitrogen removal is required to attain the level of sulfur (S) required by fuel specifications. If not removed, nitrogen (N)-compounds would inhibit HDS and other reactions because of their preferential adsorption on catalytic sites (*57*). Nitrogen removal is required to maintain NOx emissions below regulatory levels. Also, if present, N-compounds affect the stability of fuels.

The Ni(Co)Mo(W)-based catalysts have been widely used for hydroprocessing of the conventional feeds. However, the quality of crude oils has been changing with the continuous increase in the processed volume of heavy crudes. The anticipated changes in fuel specifications would require modifications of the reactors and

operating conditions, particularly increased hydrogen pressure and longer contact time, unless improvements in the performance of catalysts can be made. In this regard, efforts have been made to increase the catalyst activity and selectivity. Encouraging results have been obtained by combining catalysts with various additives. Replacement of the most often used γ-Al_2O_3 with either more acidic supports such as SiO_2, zeolites, etc., or more neutral supports, such as carbon, resulted in the improved catalyst performance. The efficiency of N removal can be further increased by optimizing operating parameters (e.g., H_2S/H_2 ratio). The research has progressed to the point that tailor-made catalysts, suitable for the HDN of a particular feed can be designed (*57*). The process flow of hydrodenitrogenation is the same as that for an HDS unit.

2.2.8 Fuel cells

The principle of the fuel cell was discovered by German scientist Christian Friedrich Schönbein in 1838 and published in one of the scientific magazines of the time (*58*). Based on this work, the first fuel cell was demonstrated by Welsh scientist and barrister Sir William Robert Grove in the February 1839 edition of the Philosophical Magazine and Journal of Science (*59*).

A fuel cell is defined as an electrochemical device in which the chemical energy stored in a fuel is converted directly into electricity. Fuel cells operate without combusting fuel and with few moving parts, and thus they are very attractive from both energy and environmental standpoints (*60*). A fuel cell can be two or three times more efficient than an internal combustion engine in converting fuel to electricity.

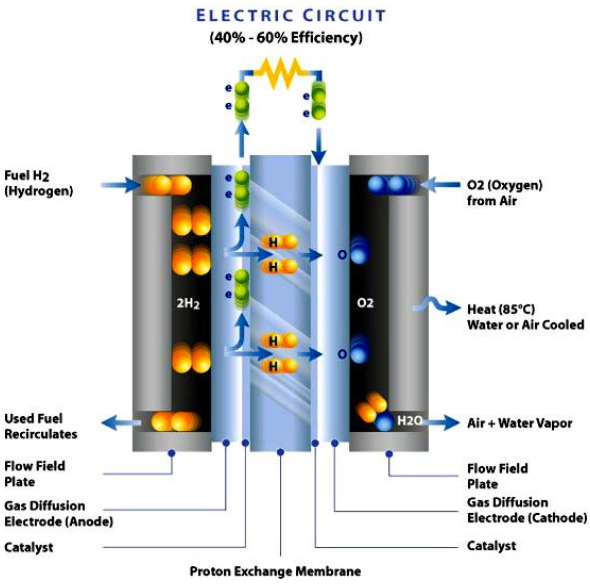

Fig. 2.13 Scheme of fuel cell (*59*).

A fuel cell consists of an electrolyte material, which is sandwiched between two thin electrodes (porous anode and cathode). Specifically a fuel cell consists of an anode - to which a fuel, commonly hydrogen, is supplied - and a cathode - to which an oxidant, commonly oxygen, is supplied. The oxygen needed by a fuel cell is generally supplied by feeding air. The two electrodes of a fuel cell are separated by an ion-conducting electrolyte.

All fuel cells have the same basic operating principle (Fig. 2.13) (*61*). An input fuel is catalytically reacted (electrons removed from the fuel elements) in the

fuel cell to create an electric current. The input fuel passes over the anode (negatively charged electrode) where it catalytically splits into electrons and ions, and oxygen passes over the cathode (positively charged electrode). The electrons go through en external circuit to serve an electric load, while the ions move through the electrolyte toward the oppositely charged electrode. At the electrode, ions combine to create by-products, primarily water and CO_2. Depending on the input fuel and electrolyte, different chemical reactions will occur.

The main product of fuel cell operation is the DC electricity produced from the flow of electrons from the anode to the cathode. The amount of current available to the external circuit depends on the chemical activity and amount of the substances supplied as fuel and the loss of power inside the fuel cell stack. The current producing process continues for as long as there is a supply of reactants because the electrode and electrolyte of a fuel cell are designed to remain unchanged by the chemical reactions.

Most individual fuel cells are small in size and produce between 0.5 and 0.9 V of DC electricity. Combination of several or many individual cells in a "stack" configuration is necessary for producing the higher voltages more commonly found in low and medium voltage distribution systems. The stack is the main component of the power section in a fuel cell power plant. The by-products of fuel cell operation are heat, water in the form of steam or liquid water, and CO_2 in the case of hydrocarbon fuel (*60*).

Because a fuel cell transforms chemical energy directly into electrical energy, its theoretical efficiency is not limited by the Carnot inefficiency problem for heat-to-work conversion, unlike conventional power generation plants and the internal combustion engine (*62*). Therefore, a fuel cell system can exhibit a higher fuel-to-electricity efficiency than almost all the other energy conversion systems.

The operating mode of fuel cells differs dramatically from that of larger fuel cell systems designed for utility power generation, which tend to operate at relatively constant power output with infrequent shutoff and restart. The small systems will operate over a wide load range, with only brief periods at full power, considerable time at 30-50 % of the rated power and relatively frequent shutoff and restart (*62*).

Fuel cells are classified primarily by the kind of electrolyte they employ. This classification determines the kind of chemical reactions that take place in the cell, the kind of catalysts required, the temperature range in which the cell operates, the fuel required, and other factors. These characteristics, in turn, affect the applications for which these cells are most suitable. There are several types of fuel cells currently under development, each with its own advantages, limitations, and potential applications.

Proton-Exchange Membrane Fuel Cell (PEMFC) - PEMFC uses a solid polymer membrane as electrolyte. This membrane is an electronic insulator, but an excellent conductor of protons (hydrogen cations). The ion-exchange membrane used is fluorinated sulfonic acid polymer. The acid molecules are fixed to the polymer and cannot leak out, but the protons on these acid groups are free to migrate through the membrane. The solid electrolyte exhibits excellent resistance to gas crossover. Typically, the anode and cathode catalysts consist of one or more precious metals, particularly platinum supported on carbon. Because of the limitation on the temperature imposed by the polymer and water balance, the operating temperature of PEMFC is less than 120 °C, usually between 70 and 90 °C. The PEMFC technology is primarily suited for residential/commercial (business) and transportation applications. The use of a solid polymer electrolyte eliminates the corrosion and safety concerns associated with liquid electrolyte fuel cells.

In addition to pure hydrogen, the PEMFC can also operate on reformed hydrocarbon fuels without removal of the by-product CO_2. However, the anode catalyst is sensitive to CO, so the traces of carbon monoxide produced during the reforming process must be converted to carbon dioxide by selective oxidation.

Water management is critical: the fuel cell must operate under conditions where the by-product water does not evaporate faster than it is produced because the membrane must be hydrated (*60*).

Phosphoric Acid Fuel Cell (PAFC) - The PAFC uses liquid, concentrated phosphoric acid as the electrolyte. The phosphoric acid is usually contained in a Teflon bonded silicon carbide matrix. The small pore structure of this matrix preferentially keeps the acid in place through capillary action. Some acid may be entrained in the fuel or oxidant streams and addition of acid may be required after many hours of operation.

Platinum supported on porous carbon is used on both anode and cathode sides of the electrolyte. PAFC operates at 180-220 °C, typically around 200 °C, so PAFC plant also produces heat for domestic hot water and space heating (*60*).

Alkaline Fuel Cell (AFC) - The AFC uses aqueous solution of potassium hydroxide (KOH) as electrolyte, which is retained in a solid matrix (usually asbestos), and a wide range of electro-catalysts can be used, including nickel, metal oxides, spinels and noble metals electrode.

The operating range of temperatures can be higher than PAFC: they can work up to 250 °C by using concentrated KOH (85%), or at temperature lower than 120 °C by using less concentrated KOH (35-50%).

The fuel supply is limited to hydrogen, CO is a poison and CO_2 reacts with KOH to form K_2CO_3, thus changing the electrolyte (*60*).

Molten Carbonate Fuel Cell (MCFC) - the MCFC uses a molten carbonates salt mixture as electrolyte. The composition of the electrolyte varies, but usually consist of lithium carbonate and potassium carbonate (Li_2CO_3-K_2CO_3). At the operating temperature of about 650 °C, the salt mixture is liquid and a good ionic conductor. The electrolyte is suspended in a porous, insulating and chemically inert ceramic ($LiAl_2O$) matrix. At the high operating temperature, noble metals are not required for electrodes, nickel or its alloy with chromium or aluminium can be used as anode, and nickel oxide as cathode. The cell performance is sensitive to operating temperature; a change in cell temperature from 650 to 600 °C results in a drop in cell voltage of almost 15 %. The reduction in cell voltage is due to increase ionic and electrical resistance and a reduction in electrode kinetics. The disadvantages of MCFC are that the electrolytes is corrosive and mobile, and a source of CO_2 is requires at the cathode to form the carbonate ion (*60*).

Solid Oxide Fuel Cell (SOFC) - SOFC uses a ceramic, solid phase electrolyte, which reduces corrosion considerations and eliminates the electrolyte management problems associated with the liquid electrolyte fuel cells. To achieve adequate ionic conductivity in such a ceramic, however, the system must operate at high temperatures in the range of 650-1000 °C, typically 800-1000 °C in the current technology. The preferred electrolytes material, dense yttria (Y_2O_3) - stabilized zirconia (ZrO_2), is an excellent conductor of negatively charged oxygen (oxide) ions at high temperatures. The SOFC is a solid-state device and shares certain properties and fabrication techniques with semiconductor devices.

The anode is typically a porous nickel-zirconia (Ni-ZrO_2) cermet (ceramic-metal composite) or cobalt zirconia (Co-ZrO_2) cermet, while the cathode is typically magnesium-doped lanthanum manganate or strontium-doped lanthanum manganate ($LaMnO_3$).

At the operating temperature, internal reforming of most hydrocarbon fuels should be possible, and the waste heat from such a device would be easily utilized by conventional thermal electricity generating plants to yield excellent fuel efficiency. On the other hand, the high operating temperature has its own drawbacks due to the demand and thermal stressing on the materials including the sealants and the longer start up time. Because the electrolyte is solid, the cell can be cast into various shapes such as tubular, planar, or monolithic. Operation up to 1000 °C allows more flexibility in the choice of fuels and can produce better performance in combined-cycle applications (*60*).

Direct Methanol Fuel Cells (DMFC) - Most fuel cells are powered by hydrogen, which can be fed to the fuel cell system directly or can be generated within the fuel cell system by reforming hydrogen-rich fuels such as methanol, ethanol, and hydrocarbon fuels. Direct methanol fuel cells, however, are powered by pure methanol, which is mixed with steam and fed directly to the fuel cell anode.

Direct methanol fuel cells do not have many of the fuel storage problems typical of some fuel cells because methanol has a higher energy density than hydrogen-though less than gasoline or diesel fuel. Methanol is also easier to transport and supply to the public using our current infrastructure because it is a liquid, like gasoline.

Direct methanol fuel cell technology is relatively new compared with that of fuel cells powered by pure hydrogen, and DMFC research and development is roughly 3-4 years behind that for other fuel cell types(*63*).

Direct Ethanol Fuel Cells (DEFC) - The use of ethanol as fuel shows some advantages as 30% higher energy density than methanol, the production from biomass fermentation and the non toxicity. In this type of cell the anode catalysts has been identified in the Pt-Sn-Rh system. Tin increases the activity of ethanol oxidation whereas rhodium promotes the splitting of carbon-carbon bond. One of major problem is the incomplete oxidation of ethanol to CO_2. However the very good performance data make DEFC very promising for applications in the low power range (*4*).

The general advantages of fuel cells are reflected by the following desirable characteristic:

1. High energy conversion efficiency;
2. Extremely low emissions of pollutants;
3. Extremely low noise or acoustical pollutions;
4. Effective reduction of greenhouse gas (CO_2) formation at the source compared to low-efficiency devices;
5. Process simplicity for conversion of chemical energy to electrical energy (*60*).

Depending on the specific types of fuel cells, other advantages may include fuel flexibility and existing infrastructure of hydrocarbon fuel supplies, co-generation capability, modular design for mass production and relatively rapid load response. Therefore, fuel cells have great potential to penetrate into markets for both stationary power plants (for industrial, commercial and residential home applications) and mobile power plants for transportation by cars, buses, trucks, trains and ship, as well as man-portable micro-generators (*60*) (Fig. 2.14) (*64*).

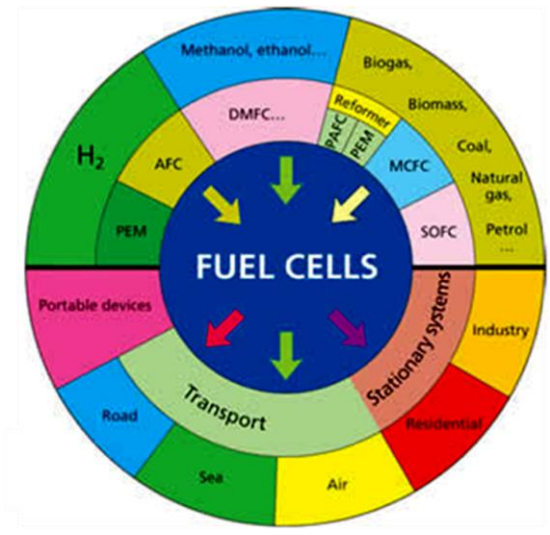

Fig. 2.14 Fuel cells technology (*58*).

Unlike power plants that use combustion technologies, fuel cells plants that generate electricity and usable heat can be built in a wide range of sizes - from 200 kW units suitable for powering commercial buildings, to 100 MW plants that can add base-load

capacity to utility power plants (*6o*).

The disadvantages or challenges to be overcome include the costs of fuel cells and that the hydrogen fuel is not readily available and thus on-site or on-board H2 production via reforming is necessary. There are no readily and affordable ways for on-board or on-site desulphurization of hydrocarbon fuels and this presents a challenge for using hydrocarbon fuels. The efficiency of fuel processing affects the over system efficiency (*6o*).

For a conventional combustion system, a wide range of gaseous, liquid and solid fuels may be used, while hydrogen, reformate (hydrogen rich gas from fuel reforming) and methanol are the primary fuels available for current fuel cells (Fig. 2.15). The sulphur compounds, in hydrocarbon fuels, poison the catalysts in the fuel processor and fuel cells and must be removed. Syngas can be generated from reforming. Reformate can be used as the fuel for high-temperature fuel cells such as SOCF and MCFC, for which the solid or liquid or gaseous fuels need to be reformulated. Hydrogen is the real fuel for low-temperature fuel cells such as PEMFC and PAFC, which can be obtained by fuel reformulation on-site for stationary applications or on-board for automotive applications. When natural gas or other hydrocarbon fuel is used in a PAFC system, the reformate must be processed by water gas shift reaction. A PAFC can tolerate about 1-2 % of CO. When used in a PEMFC, the product gas from WGS must be further processed to reduce CO to < 10 ppm. Synthetic ultra-clean fuels can be made by Fischer-Tropsch synthesis or methanol synthesis using the synthesis gas produced from natural gas or from coal gasification, but the synthetic cleanness is obtained at the expense of extra cost for the extra conversion and processing steps (*6o*).

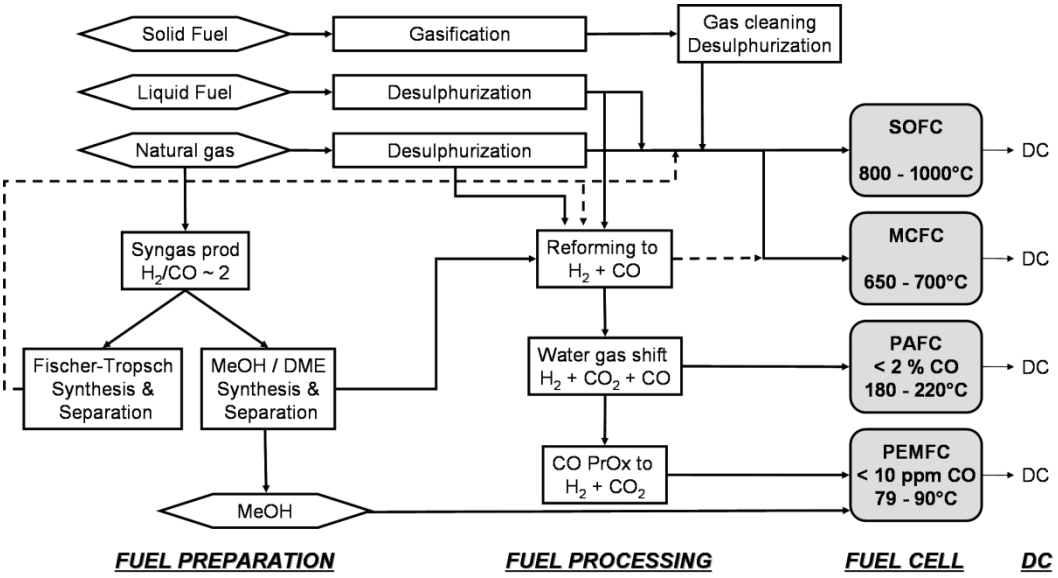

Fig. 2.15 The concept and the steps for fuel processing of gaseous, liquid and solid fuels for high and low temperature fuel cell applications (*6o*).

2.3 H2 production

Although hydrogen can be produced from a large variety of sources by using different methods, up to now the most extensively used process is the steam reforming of hydrocarbons. Biomass can be also used to produce H_2 by thermochemical or biological processes. Metabolic processing appears as an interesting alternative for the treatment of wastes while generating H_2 as product. Some other approaches for hydrogen production from water or other hydrogen-containing materials such as photodecomposition or thermochemical processes are also in development. Solar photodecomposition of water still has many technical hurdles remaining that suggest it is decades away from large scale, cost-effective implementation (*6*).

The conversion of hydrocarbons to hydrogen and syngas will play an important role in the 21st century ranging from large gas to liquid plants and hydrogen plants for refineries to small units providing hydrogen for fuel cells. The choice of technology for manufacture of syngas depends on the scale of operation (*7*).

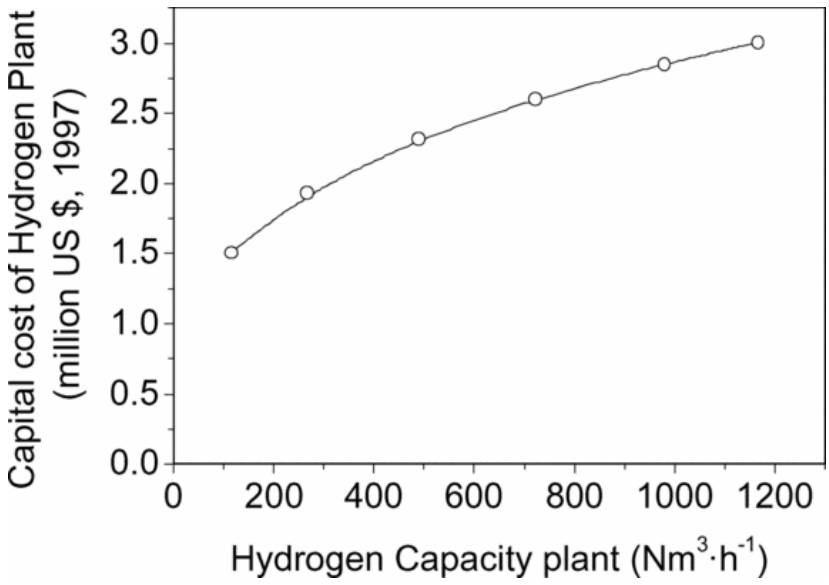

Fig. 2.16 Capital cost of a hydrogen plant as a function of capacity (*6*).

Currently, steam reforming of hydrocarbons (SR) especially steam methane reforming (SMR) is the largest and generally the most economical way to make H_2. Alternative non-catalytic, industrial chemical approaches include partial oxidation (POX) of heavy oil or coal. When electricity is available and relatively inexpensive, electrolysis of water offers an alternative commercial approach (*65*)(*66*).

Industrially, two main reactions are important in the conversion of natural gas to syngas (*67*) : steam reforming (SR) and non-catalytic partial oxidation (POX).

While most syngas is produced by steam reforming, two other process may be more attractive, depending on factors such as H2:CO ratio, downstream use, product purity, the presence of CO2, N2, H2O and CH4, plant capacity, feedstock availability, purity

and cost, including O_2. These processes are: autothermal catalytic reforming (ATR) and catalytic partial oxidation (CPO).

The main processes are listed in :

Process	Reactor	Feedstock	Temperature (°C)	Catalyst
Steam Reforming	Heated reactor of many types	Light hydrocarbons	500-900	Ni/ceramic support
Prereforming	Adiabatic reactors	Natural gas, diesel	400-500	Ni/support
Water gas shift	Adiabatic reactors	Syngas	230-500	Fe_3O_4, $Cu/ZnO/Al_2O_3$
Autothermal reforming	Brick-lined reactor with burner and catalyst bed	Light hydrocarbons	-1050	Ni/ceramic support
Catalytic partial oxidation	Monolithic catalyst reactor	Light hydrocarbons, diesel	-950	Rh/ceramic support
Partial oxidation (gasification)	Brick-lined reactor with burner	Heavy hydrocarbons, coal, petcoke, biomass	1300	None

Tab. 2.2 Characteristic of processes from hydrogen fossil fuels (4).

2.3.1 Steam reforming process (SR)

In areas where natural gas is available in large quantities, interest is centred on steam reforming of methane as hydrogen source (37). The process is more economic than that based on coal. The hydrogen content of the hydrocarbon improved the yield of hydrogen per unit of carbon in the feedstock compared with coal, and there were also fewer unwanted by-products. The methane steam technology was pioneered in the first quarter of 20^{th} century by BASF who established the essential configuration of the primary steam reformer.

The steam reforming reaction took place over catalyst in vertical tubes, which were supported in parallel rows in a radiant furnace. The endothermic heat of reaction was supplied by burning fuel in the furnace. The process was considerably improved by ICI, who developed the fundamental engineering data for the design of the furnace,

improved the catalyst formulation and introduced the desulphurization step using zinc oxide. The catalyst tube have a typical diameter of 10 cm and a length of 10 m. They are made of high-alloy steel to withstand the high tube wall temperatures and the high thermal stresses. The reformer tubes are filled with catalyst which must show high mechanical stability because of exposure to high temperatures and steam partial pressures (*68*). In many situations when natural gas is not available , higher hydrocarbons become the preferred feedstocks for the reforming process. Many refineries benefit from flexibility in feedstock, taking advantage of the surplus of various hydrocarbons streams in the refinery. The higher hydrocarbons are more reactive (per carbon atom) than methane, except for aromatic molecules. This means that liquid hydrocarbons in principle can be easily converted by steam reforming , but in practice this is limited by the higher potential for poisoning by sulfur and the higher risk of carbon formation (*4*).

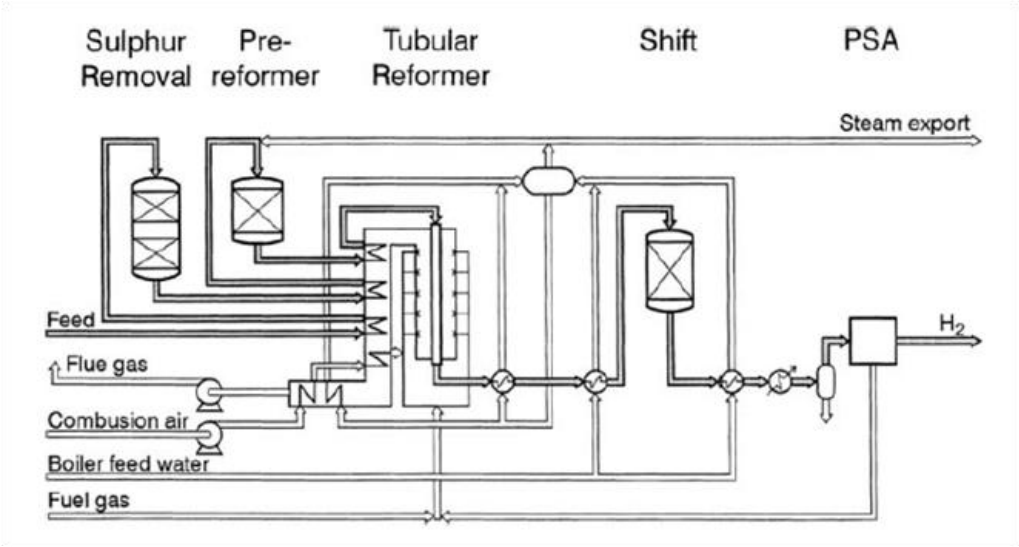

Fig. 2.17 Typical process layout for a hydrogen plant based on advanced tubular steam reforming technology (*6*).

2.3.1.1 Thermodynamic considerations

The objective of the catalytic steam reforming process is to extract the maximum quantity of hydrogen/syngas held in water and in the hydrocarbon feedstock. Thereafter the subsequent manipulation of the gas stream depends on the purpose for which the gas is intended.

The reforming of natural gas utilizes two simple reversible reactions:

(A) reforming: $CH_4 + H_2O \leftrightarrows CO + 3\,H_2O$ $\Delta H^0 = +\,206$ kJ/mol

(B) water gas shift: $CO + H_2O \leftrightarrows CO_2 + H_2$ $\Delta H^0 = -\,41$ kJ/mol

The reforming reaction (A) is strongly endothermic, so the reaction is favoured by high temperature as well as by low pressure, while the shift reaction (B) is exothermic

and is favoured by low temperature but is largely unaffected by changes in pressure. To minimize the overall efficiency (and hence economics) of the conversion of carbon to carbon dioxide and the production of hydrogen, reformers are operated at relative high temperature and pressure. This is followed by the shift process that, by using two different catalysts, permits the shift reaction to be brought to equilibrium at as low temperature as possible. It can be seen that with methane the stoichiometric requirement for steam per carbon atom is 1.0. However, it has been demonstrated that this is not reliable because all catalysts so far developed tend to promote carbon formation under steam reforming conditions. These reactions can be suppressed by using an excess of steam, with the results that the minimum ratio is in the region of 1.7. However, the reforming reaction itself is also promoted by an excess of steam and hence some advantage is derived from this. In practice ratio of 3.0 - 3.5 are commonly used, but in some cases, there can be economic attractions in using lower steams ratios and there is a trend in this direction.

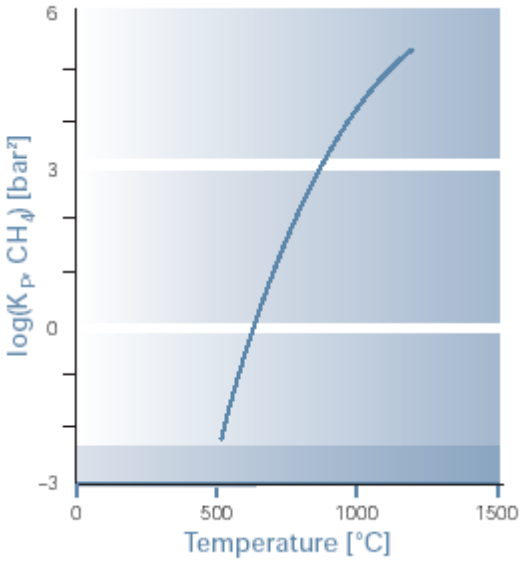

Fig. 2.18 Steam reforming reaction: equilibrium constant.

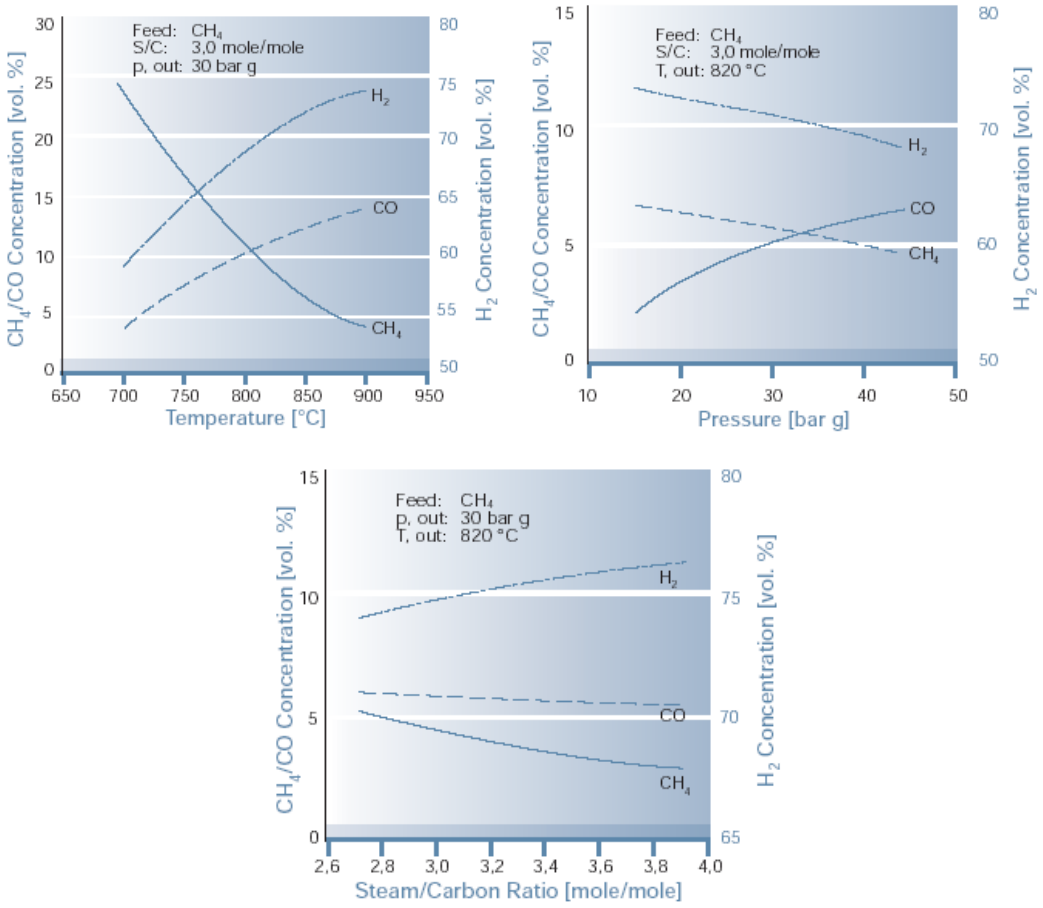

Fig. 2.19 Variation of the reformated gas depending on: (a) outlet temperature; (b) outlet pressure; and (c) inlet S/C ratio.

The reforming of saturated naphthas of general formula C_nH_{2n+2} is based on the following reaction:

(C) $C_nH_{2n+2} + n\ H_2O \leftrightarrows n\ CO + (2n + 1)\ H_2$

(D) $CO + 3\ H_2O \leftrightarrows CH_4 + H_2O$ $\Delta H = -206$ kJ/mol

Reaction (C) is strongly endothermic, absorbing more heat than the following methanation reaction (D) and shift reaction (B) evolve, thus making the overall process normally an endothermic one.

Analogously to methane, the naphtha reforming reaction is favored by high temperature and low pressure, while the shift reaction is inhibited by high temperature but largely unaffected by pressure. The tendency towards carbon formation on catalysts when stoichiometric ratios of carbon and steam are used is greater with naphtha than with methane, and the minimum practical ratio is about 2.2. As with methane, the excess steam favors the reforming reaction, and in practice steam/carbon ratios of 3.5 - 4.5 are common. At low steam/carbon ratio the methanation reaction begins to dominate, and under certain conditions of pressure and temperature can cause the overall reaction to be exothermic.

2.3.1.2 Kinetics and reaction mechanism

The results of a number of studies on the kinetics of the methane steam reforming have been published. There is general agreement that the reaction is first order in methane, but there is less agreement with other kinetic parameters. In part, this is due to the use of different catalysts and experimental conditions, but often it has resulted from a lack of consideration of diffusion and heat transfer limitations. Thus, reported activation energies are spread in a wide range of values due to different degrees of diffusion limitation, and these can also cause misleading total pressure effect. Indeed, with the relatively large catalyst particle sizes used in industrial steam reformers, these effects results in very low effectiveness of the catalyst. Effectiveness factors (η) may, depending on conditions, only be as high as 0.3 at the inlet region, and perhaps as low as 0.01 at the exit. Because of this, apparent activity increases as the particle size is made smaller, but the increased pressure drop, which arises across the reformer, restricts the size of the catalyst that can be used in practice (*37*).

There has been some debate about the first formed products of the steam reforming reactions, and it appears that the relative concentrations of carbon monoxide and carbon dioxide leaving the catalyst surface depend on the efficiency of the catalyst in the water gas shift reaction. With rhodium-based catalysts the CO/CO_2 ratio of the initially formed carbon oxides is relatively high (in keeping with poor shift activity), whereas with nickel catalysts the amount of carbon monoxide is lower (*37*).

A wide variety of rate expressions for the steam reforming of methane have been proposed. These models range in complexity from simple first order dependency on methane, involving two parameters, to complex Langmuir–Hinshelwood models with over ten parameters (*69*). It is generally agreed that the rate of methane reforming has a first order dependency on methane. Furthermore, it is also agreed that the rate-determining step in the reforming process is the formation of adsorbed carbon species: $CH_4 + * - \text{Metal site} \rightarrow C_{ads} - *+2\ H_2$

This mechanism leads to the formulation of rate equations of the following form:

$$r_{CH_4} = - k\, p_{CH_4}\, p_{H_2}{}^{\alpha}$$

In this equation, the value of α is found to depend on temperature, having a value close to -1 at low temperatures (< 700°C) and approaching 0 at high temperatures (> 700°C).

Kinetic rate expressions for the steam reforming of methane found in the literature use the steady state approximation and take the form:

$$r_{CH4} = - k\, p_{CH4} \frac{f\,(p_{H2O},\, p_{H2})}{(1 + f\,(p_{CH4},\, p_{H2O},\, p_{H2},\, p_{CO},\, p_{CO2}))} \times \left(1 - \frac{p_{CO}\, p^3_{H2}}{p_{CH4}\, p_{H2O}\, K_1}\right)$$

2.3.1.3 Catalysts

The catalyst must promote the desired reaction and be as inactive as possible towards unwanted side-reactions, particularly to the formation of carbon. The catalyst should also be as resistant as possible to poisons (*37*).

The catalyst must be able to maintain its activity under the demanding process conditions, necessary to promote the desired reaction (800-1000°C and 20-30 bar). With impregnated catalysts, an important parameter in maintaining activity over prolonged periods is the nature of the support material and its pore structure (*37*).

The catalyst must be strong enough to withstand the handling it receives; from manufacture to charging into the reformer, as well as the stresses generated by the process conditions and the thermal cycles arising from plant start-up and shutdown. The catalyst also must be of a suitable physical shape to provide an appropriate geometric surface area to give an acceptable activity per unit volume of packed bed whilst possessing acceptably low-pressure drop characteristics. The support must not be affected by water condensing on it, nor must it produce an unacceptable quantity of dust and material carryover, which could foul heat exchangers and other catalysts downstream (*37*).

For many years nickel has been recognized as the most suitable metal for steam reforming of hydrocarbons, other metals can be used; for example cobalt platinum, palladium, iridium, ruthenium and rhodium. Although some precious metals are considerably more active per unit weight than nickel, nickel is much cheaper and sufficiently active to enable suitable catalysts to be produce economically.

The reforming reaction takes place on the nickel surface, so the catalyst must be manufactured in a form that produces the maximum stable nickel surface area available to reactants. This is generally done by dispersing the nickel as small crystallites on a refractory support, which must be sufficiently porous to allow access by the gas to the nickel surface.

This is usually achieved by precipitating nickel as insoluble compound, from a soluble salt, in the presence of a refractory support such as mixtures of aluminium oxide, magnesium oxide, calcium oxide and calcium aluminate cement. Alternatively, the nickel can be incorporated by impregnating a preformed catalyst support, such as alumina or an aluminate, with a solution of a nickel salt which is subsequently decomposed by heating to the oxide. Impregnated catalysts are generally stronger than precipitated catalysts, and this is one of the reasons for their widespread use.

The activity of a steam reforming catalyst in service is closely related to the available surface area of the nickel metal and the access the reactants have to it. Most commercial natural gas catalysts are now of the impregnated type and give a relatively high surface area when first reduced, but under normal reforming conditions

the surface area falls as sintering of nickel crystallites occurs. The higher the temperature is, the more rapidly the sintering proceeds.

Activity is a function of the overall nickel content. However, it has been demonstrated that with both impregnated and precipitated catalyst there is an optimum beyond which an increase in nickel content does not produce any further significant increase in activity. Typically, these optima are approximately 20 % for precipitated and up about 15 % for impregnated catalyst, but this depends on the nature and physical properties of the actual support.

2.3.1.4 Main problems for reforming catalysts

2.3.1.4.1 Carbon formation

Coking or the formation of carbonaceous deposits is an important side reaction in many industrial processes. Very often, measures to eliminate or depress coke formation are more decisive for the process layout than, for instance, the activity of the catalyst (*70*).

Deactivation of supported metal catalysts by carbon or coke formation is a problem of serious magnitude in steam reforming. Its causes are generally threefold:

1. fouling of the metal surface,
2. blockage of catalysts pores and voids,
3. actual physical disintegration of the catalyst support.

Carbon may chemisorb strongly, as a monolayer, or physically adsorb in multi-layers and, in either case, block access of reactants to metal surface sites. Furthermore, carbon may totally encapsulate a metal particle, and thereby completely deactivate that particle, and plug micro- and macropores such that access of reactants is denied to many crystallites inside this pores. Finally, in extreme cases, strong carbon filaments may build-up in pores to the extent that they stress and fracture the support material, ultimately causing disintegration of catalyst pellets and plugging of reactor voids (*71*). Carbon accumulation can also cause spalling and pulverization of catalysts, which can also lead to poor heat distribution (*72*).

Carbon is a product of CO disproportionation while coke is produced by decomposition or condensation of hydrocarbon on metals. Nevertheless, coke forms may vary from high molecular weight hydrocarbons such as condensed polyaromatics to carbon such as graphite, depending upon the conditions under which the coke was formed and aged (Fig. 2.20).

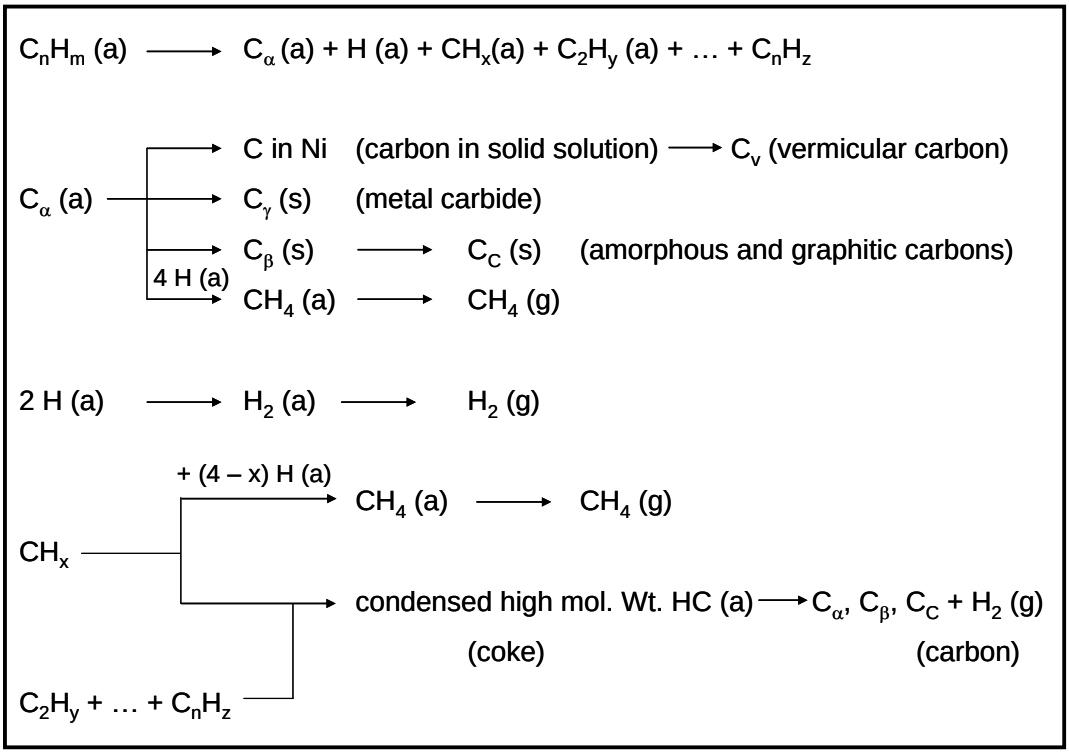

Fig. 2.20 Formation, gasification and transformation of coke and carbons on metal surfaces from hydrocarbons (a = adsorbed, g = gaseous, s = solid).

Three different kinds of carbon or coke species are observed in steam reforming (Tab. 2.3):

1. whiskers like carbon formed at temperature greater than 450°C,
2. encapsulating hydrocarbon films formed by polymerization at less than 500°C,
3. pyrolytic carbon from cracking of hydrocarbon above 600°C.

	Whisker like	Encapsulating film	Pyrolytic carbon
Formation	Diffusion of C through Ni crystal, nucleation and whisker growth with Ni crystal at top	Slow polymeraization of C_nH_m radicals on Ni surface into encapsulating film	Thermal cracking of hydrocarbon. Deposition of C precursors on catalyst
Temperature range	> 450°C	< 500°C	> 600°C
Critical parameters	High temperature. Low H_2O/C_nH_m No enhanced H_2O adsorption Low activity Aromatic feed	Low temperature Low H_2O/C_nH_m Low H_2/C_nH_m Aromatic feed	High temperature High void fraction Low H_2O/C_nH_m High pressure Acidity of catalyst

Tab. 2.3 Carbon species formed in steam reforming of hydrocarbons (*72*).

The rate at which carbon or coke is accumulated in a given reaction under given conditions can vary significantly with catalyst structure, including metal type, metal crystallite size, promoter, and catalyst support. For example, Co, Fe and Ni are active above 350-400°C for filamentous carbon formation from CO and hydrocarbons.

Pt, Ru and Rh catalysts, on the other hand, while equally or more active than Ni, Co, or Fe in steam reforming produce little or no coke or carbon. This is attributed to reduced mobility and/or solubility of carbon in the noble metals, thus retarding the nucleation process. Thus, it is not surprising that addition of noble metals to base metals retards carbon formation; for example, addition of Pt in Ni lowers carbon deposition rate during methanation, while addition of Cu to Ni substantially lowers carbon formation in steam reforming.

Since carbon formation and gasification rates are influenced differently by modifications in metal crystallite surface chemistry, which are in turn a function of catalyst structure, oxide additive or oxide supports may be used to moderate the rate of undesirable carbon or coke accumulation (*71*).

The high temperatures associated with steam reforming favour the formation of carbon (*73*). Four reactions may be involved:

Thermal cracking or decomposition of methane:

$$CH_4 \leftrightarrows C + 2\ H_2 \qquad \Delta H^{o}_{298} = 75\ kJ/mol$$

Thermal cracking or decomposition of hydrocarbons:

$$C_nH_{2n+2} \rightarrow n\ C + (n+1)\ H_2$$

CO disproportionation (Boudouard):

$$2\ CO \leftrightarrows C + CO_2 \qquad \Delta H^{\circ}_{298} = -172\ kJ/mol$$

CO reduction:

$$CO + H_2 \leftrightarrows C + H_2O$$

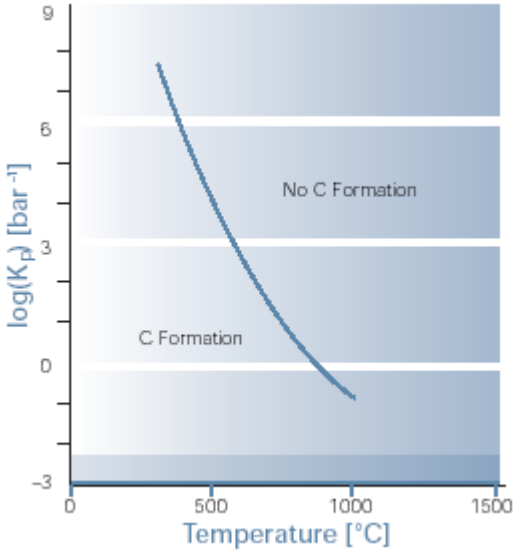

Fig. 2.21 Boudouard reaction: equilibrium constant.

2.3.1.4.2 Sintering

Nickel steam-reforming catalysts are subject to several deactivation mechanisms including coking, poisoning, and sintering. Sintering is the reason for loss of activity for many industrial catalyst systems.

Thermally induced deactivation of catalysts results from (*71*):

1. loss of catalytic surface area due to crystallite growth of the catalytic phase;
2. loss of support area due to support collapse and of catalytic surface area due to pore collapse on crystallites of the active phase,
3. chemical transformations of catalytic phases to non-catalytic phases.

Sintering processes generally take place at high reaction temperatures (> 500°C) and are generally accelerated by water vapour.

Sintering of heterogeneous catalysts is often referred to as the loss of catalytic surface area due to growth of large particles at the expense of smaller particles. Sintering is complex and may be influenced by many parameters such as sintering time, temperature, chemical environment, catalyst composition and structure, and support morphology. A good understanding of the sintering mechanism is necessary, both to predict the extent of deactivation by sintering and to design catalysts that maintain a high activity (*74*).

Particle growth via sintering influences the resistance of the catalyst toward coking and poisoning with sulfur. The coking limits are affected by the nickel particle size and the nickel surface area determines the sulfur capacity of the catalyst. Furthermore, the activity of a steam-reforming catalyst is related to the nickel surface area. To model an industrial reformer with regard to activity and the effect of sulfur poisoning, it is necessary to know the nickel surface area as a function of time, temperature, feed gas composition, chemical composition including promoters, and extent of poisoning.

Several studies of sintering of Ni particles supported on a ceramic carrier are reported in the literature. The most important parameters are the sintering temperature and the composition of the gas over the catalyst. Increasing temperature and the presence of steam accelerates the sintering process. High surface areas of the carrier, on the other hand, increase the stability toward sintering.

Three mechanisms for the metal particle growth have been proposed:

1. particle migration, where entire crystallites migrate over the support followed by coalescence;
2. Ostwald ripening (atom migration), where metal atoms emitted from one crystallite migrate over the support and are captured by another crystallite;
3. vapour transport between particles (at high temperatures).

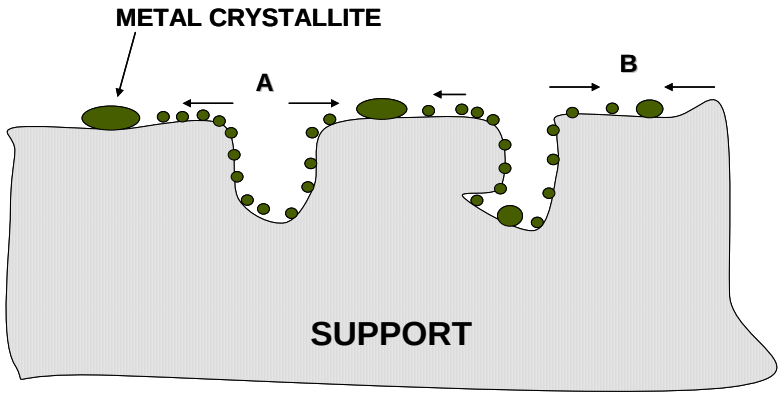

Fig. 2.22 Two conceptual models for crystallite growth due to sintering by (A) atomic migration or (B) crystallite migration (*71*).

Crystallite migration involves the migration of entire crystallites over the support surface followed by collision and coalescence. Atomic migration involves detachment of metal atoms from crystallites, migration of these atoms over the support surface and ultimately, capture by large crystallites (*71*).

Sintering of the support may also occur. Single-phase oxide carriers sinter by one or more of the following processes:

1. surface diffusion,
2. solid-state diffusion,

3. evaporation/condensation of volatile atoms or molecules,
4. grain boundary diffusion,
5. phase transformation.

Additives and impurities affect the thermal properties of carriers by occupying defect sites or forming new phases. Alkali metals, for example, accelerate sintering, while calcium, barium, nickel and lanthanum oxides form thermally stable spinel phases with alumina. Steam accelerates support sintering by forming mobile surface hydroxyl groups that are subsequently volatilized at higher temperatures. Chlorine also promotes sintering and grain growth in magnesia and titania during high temperature calcination.

Dispersed metals, in supported metal catalysts, can also accelerate support sintering, for example, dispersed nickel accelerates the loss of Al_2O_3 surface area in Ni/Al_2O_3 catalysts (*71*).

2.3.2 Water gas shift reaction (WGS)

The water gas shift reaction is moderately exothermic and hence its equilibrium constant decreases with temperature and high conversions are favored by low temperatures. The water gas shift reaction is:

$CO + H_2O \leftrightarrows CO_2 + H_2 \qquad \Delta H = -41.1$ kJ/mol

The position of equilibrium is virtually unaffected by pressure. As expected, additions of greater than stoichiometric quantities of steam improve conversion. Under adiabatic conditions, conversion in a single bed of catalyst is thermodynamically limited – as the reaction proceeds the heat of reaction increases the operating temperature, and so restricts of the conversion are possible. Typical carbon monoxide levels that are achieved at the exit with a single adiabatic bed of chromia-supported iron-based shift catalyst in an ammonia plant are in the range 2-4 %, and because it is necessary to operate these catalysts at high inlet temperatures (typically in the range 370-400°C) they are known as high temperature (HT) shift catalysts (*37*).

The thermodynamic equilibrium limitation on the reaction can be reduced by using two or more beds of HT shift catalyst with inter-bed cooling and, perhaps, removal of carbon dioxide between the stages. In this way, it was possible in the late 1950s to decrease the thermodynamic limitation, and achieve carbon monoxide levels of less than 1 % at the exit. The limitation on conversion was then catalyst activity.

When a single stage or two stages of HT shift were used, the final carbon monoxide removal stage was generally absorption in copper liquor, although some plants used a methanator, because of the simplicity of the process, and accepted the attendant hydrogen loss. At this time, attempts were made to improve the carbon monoxide conversion so that methanation could be used more economically as a means of

removing the remaining traces of carbon oxides. This impetus led to the development and introduction of copper-based shift catalysts in the early 1960s (*37*).

A significant improvement in the conversion of the carbon monoxide could then be obtained with two-bed operation, with the second bed operating at the lowest possible inlet temperature, which in practice was dictated by the dew-point (about 200°C). The conventional iron based catalysts are not sufficiently active for such low temperature operation, but copper based water gas shift catalyst are, and when they are used in the second bed, carbon monoxide exit concentrations as low as 0.1-0.3 % can be achieved, which is an acceptable economic level for subsequent methanation. These copper-based catalysts are known as low temperature (LT) shift catalysts.

In this arrangement, it is necessary to lower the temperature of around 200°C, which is suitable for the inlet of the LT shift catalyst. Inter-bed cooling is usually achieved by heat exchange, which, depending on the steam pressure levels in the plants, may be used to heat boiler feed water or to raise steam. In some cases, the temperature may also be trimmed by injecting either steam or condensate into the process gas. In such plants, the life of the LT shift catalyst may be shortened because of physical damage from entrained water droplets or because of the presence of catalyst poisons in the water itself (*37*).

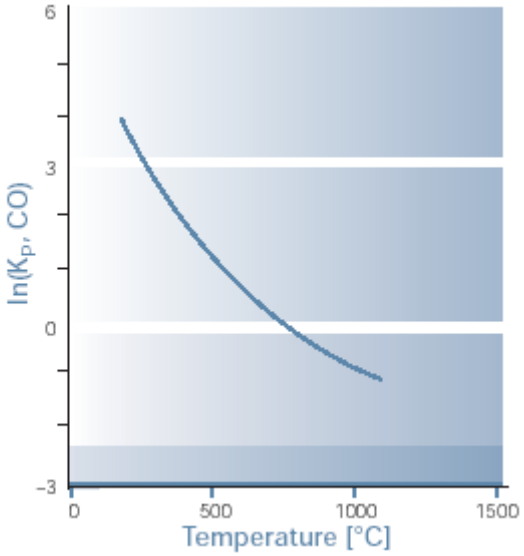

Fig. 2.23 Water gas shift reaction: equilibrium constant.

Numerous studies of the kinetics of the water gas shift reaction over iron oxide/chromia catalysts have been reported and more than 20 different kinetic equations have been proposed. Differences among authors have been especially marked in their opinion of the reaction mechanism, and the effect of pressure on the reaction rate. The reasons for this conflict have been attributed to the presence of impurities in the gases used, to varying degrees of mass transfer limitation and to the fact that kinetic measurements have been mostly obtained with integral rather than

differential reactors, which were often only operating at or near atmospheric pressure(*37*).

The importance of mass transfer effects in the reaction over a commercial catalyst was assessed and the conclusions obtained were:

1. the activation energy in the absence of diffusion effects for the water gas shift reaction over iron oxide / chromia catalyst is 121.8 kJ/mol,
2. the reaction over 5.4 x 3.6 mm pellets is not pore diffusion limited at temperatures below 370°C and at pressure up to 31 bar. Over larger pellets, 8.5 x 10.5 mm, the reaction becomes diffusion limited at temperature above 350°C at 31 bar pressure.

Fewer publication have appeared on the mechanism and kinetics of the water gas shift reaction over copper based catalysts than over high temperature iron based catalysts, but similar types of kinetic expressions have been proposed. Indeed, the pore diffusion limited version of the Langmuir-Hinshelwood equation for copper-based shift catalysts is consistent with plant data and semi-technical scale results. There is little doubt that the copper LT shift catalysts generally operate in a pore-diffusion limited regime, although there is debate over the extent of this limitation on typical industrial catalyst pellets. In addition, they are often self- guarding with respect to poisons (sulphur and chlorine compounds). The pick-up of which is evidently a very rapid process and may itself also be pore-diffusion limited.

The mechanism of the catalyzed shift reaction remains in dispute for copper and iron-based catalysts. Briefly, two types of mechanism have been proposed - adsorptive and regenerative.

In the former mechanism, reactants adsorb on the catalyst surface, where they react to form surface intermediates such as formate, followed decomposition to products and desorption from the surface.

In the regenerative mechanism, the surface undergoes successive oxidation and reduction cycles by water and carbon monoxide, respectively, to form the corresponding hydrogen and carbon dioxide products of the water gas shift reaction.

Dealing first with iron oxide/chromia catalysts, the adsorption mechanism has been supported by tracer studies and apparent stoichiometric number analyses. Unfortunately, however, the kinetics of the water gas shift reaction can equally well be described either by the adsorptive mechanism or by the regenerative mechanism, which was first proposed. Support for the regenerative mechanism is that the rate at which water oxidized the magnetite surface and carbon monoxide reduces it, corresponds to the rate of the water gas shift reaction. In an in situ gravimetric study of oxygen removal from and incorporation into magnetite/chromia catalyst in CO_2/CO

and H_2O/H_2 gas mixtures at about 350°C further supported the regenerative mechanism.

For the copper based LT shift catalysts the regenerative mechanism was rejected on the basis that neither cupric nor cuprous oxide could be formed under reaction conditions from copper metal and steam. An adsorptive mechanism with a surface formate intermediate was proposed. However, an analysis of transient kinetics of the shift reaction over a Cu/ZnO catalyst supports the regenerative mechanism. With both $Cu/ZnO/Al_2O_3$ catalysts and unsupported polycrystalline copper catalysts, it was also produced results consistent with the regenerative mechanism. The occurrence of the four separate steps needed for both forward and reverse reaction shown in the following equations (in which S is a vacant site) has been demonstrated on copper.

$$CO + O_{(a)} \rightarrow CO_2 + S$$

$$H_2O + S \rightarrow H_2 + O_{(a)}$$

For oxygen coverage of half-monolayer or less there is no equilibrium limitation to the second reaction, in contrast with the equivalent reaction forming cuprous oxide, so that objection to regenerative mechanism is invalid for adsorbed oxygen formation. Therefore, it seems likely that the water gas shift reaction proceeds by the same regenerative mechanism on both Fe_3O_4/Cr_2O_3 and $Cu/ZnO/Al_2O_3$ catalysts.

The catalyst used for HT-WGS duty consists of magnetite crystallites stabilized with the addition of a small amount of chromia, although fresh unreduced catalyst contains hematite (Fe_2O_3) 90-95% with 5-10% Cr_2O_3.

Iron based catalysts are not very sensitive to poisoning by sulphur, which is commonly present in feed gas derived from coal or fuel oil, and if the catalyst must be operated under highly sulphiding conditions the deactivated effect can be compensated for by increasing the volume of catalyst used.

Magnetite (Fe_3O_4) has good activity for the reaction at moderately high temperatures and, provided the magnetite crystallites are stabilized by the addition of a refractory oxide component such as chromia (Cr_2O_3), satisfactory long lives are obtained.

The formulation of LT shift catalyst is important in terms of selectivity and resistance to poisoning, as well as activity. Selectivity is important because under LT shift conditions methanation of both carbon monoxide and carbon dioxide is thermodynamically very favourable:

$$CO + 3\,H_2 \leftrightarrows CH_4 + H_2O \qquad \Delta H = -206.2 \text{ kJ/mol}$$

$$CO_2 + 4\,H_2 \leftrightarrows CH_4 + 2\,H_2O \qquad \Delta H = -164.9 \text{ kJ/mol}$$

If these reactions take place to any extent, then valuable hydrogen would be consumed; in addition, since they are very exothermic they could give rise to dramatic and dangerously destructive rises in temperature.

Copper based catalyst have good activity for the water gas shift reaction, and have no methanation activity so they are well suited for use in water gas shift duties.

Alumina together with zinc oxide was a desirable support that could significantly stabilize the copper crystallite against thermally induced sintering, and also enhanced the strength of the catalyst and minimize shrinkage during reduction.

2.3.3 Partial oxidation (POx)

The other major route to hydrogen is non-catalytic partial oxidation of fossil fuels, often referred to as POX (or gasification). One key advantage of this approach is that it accepts all kinds of hydrocarbon feeds. The thermal oxidation is run at 30-100 atm with pure O_2 using a special burner inside a refractory lined vessel at ~ 1300°C. The general reaction is described by:

$C_xH_y + x/2\ O_2 \rightarrow x\ CO + y/2\ H_2$

There are several plants that produce hydrogen by the partial oxidation of hydrocarbons. In the non-catalytic process, a mixture of oxygen and natural gas is pre-heated, mixed and ignited in a burner. In the absence of catalyst, the reactor temperature must be high enough to reach complete CH_4 conversion. Combustion products like CO_2 and H_2O are also formed to a certain extent. Subsequently, endothermic reaction as steam reforming is also involved, which determine the outlet temperature in the order of 1000-1200°C. At this stage, the gas composition is near thermodynamic equilibrium. According to the stoichiometry of reaction the consumption of O_2 should be, in the absence of combustion products, approximately 0.5 O_2/CH_4. However, actual use requires O_2/CH_4 ratio of about 0.7. It appears that if the reactor in principle is simple, the cost of an oxygen plant is considerable. One advantage of this process is that it can work at high pressures, thereby saving costly compressors. Some carbon is formed by the thermal cracking of methane and has to be removed by washing. The outer reactor walls are cold being insulated on the inside. Using this technology, Texaco and Shell commercialize this conversion process (*67*).

In non-catalytic partial oxidation process, steam is not used as a feed, but with higher hydrocarbon feeds there can be a lot of coke as by-product. Since conditions are maintained net reducing, no NO_x or SO_x are produced; however, if the feed contains any sulfur compounds, H_2S and COS are by-product which must be scrubbed. A clear disadvantage is the need to have huge quantities of O_2 available continuously, thus requiring the substantial investment in an adjoining O_2 plant (*67*).

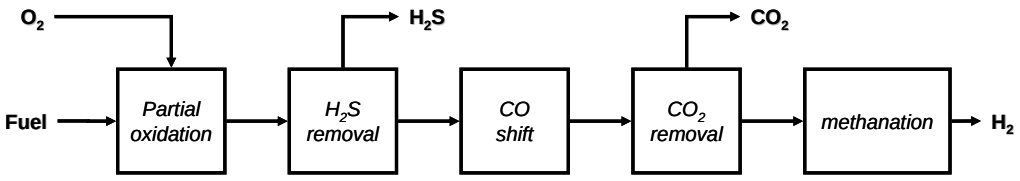

Fig. 2.24 Block diagram of the whole non catalytic partial-oxidation of methane.

Methane is reacted with O_2 in a flame, then after desulphurization, the WGS reaction is used to shift essentially all CO to H_2, and CO_2 is removed. If complete removal of residual CO and CO_2 is required, methanation on a Ni catalyst can reduce carbon oxides to less than 10 ppm (Fig. 2.24) (*67*). Since CO is also a co-product, one has to use high temperature water gas shift to convert CO with steam to H_2. Additional unit operations are required for gas purification (largely to remove H_2S) and to remove soot from the waste water. In addition, the CO_2 can be removed by adsorption, and final traces of CO destroyed by follow-up methanation. Thus POX operations can get quite complex, and in comparison to SMR they are less energy efficient, while eliminating more CO_2 co-product (*65*).

In the Fig. 2.25 it is only shown part of the POX process, steam must also be generated and the product CO/H_2 must also be purified. A strong feature of POX technology versus SMR is that the former is a very attractive process when dealing with the increasing amounts of bottom-of-the-barrel feedstocks. It was estimated that the thermal efficiency of a POX plant feed with heavy hydrocarbons to be ~ 70 % versus 81 % with SMR. Secondary reforming with added O_2 is used in some operations employing SR technologies, especially in connection for the high H_2 demands of ammonia synthesis. In the exothermic, secondary reforming, air is added to the effluent of the primary reformer. The residual methane reacts with the air providing heat for this CO producing reaction, and the unreacted N_2 is used for NH_3 synthesis (*65*).

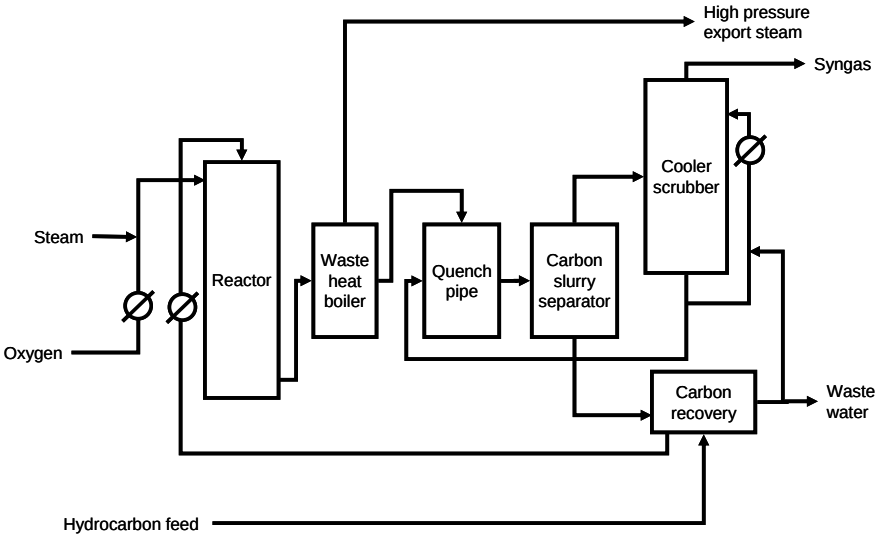

Fig. 2.25 Process flow diagram for POX (*65*).

2.3.4 Autothermal reforming (ATR)

An alternative approach to POX and SMR is autothermal reforming (ATR), which is a combination of both technologies.

This process was developed by Haldor Topsoe in the late 1950s with the aim of performing reforming in a single reactor. In autothermal reforming, the energy for the production of CO and H_2 is produced by partial oxidation of the hydrocarbon feedstock. Like POX, the feeds first react in a large refractory lined vessel with O_2 for non-catalytic combustion at 1200-1250°C. If the product H_2 is intended for NH_3 production, an air feed could be used.

The reformer basically consists of a ceramic lined tube and a fixed catalyst bed for equilibration of the gas. The preheated streams ($CH_4 + H_2O$ and $H_2O + O_2$) are mixed in a burner placed at the top where the POX reactions take place. The final steam reforming and equilibration take place in the catalyst bed below the burner. Typically, the ATR operates at high temperatures ca. 1200-1300°C in the combustion zone and 950-1200°C in the catalytic zone. This results in a lower oxygen consumption (O_2/CH_4 = 0.55-0.60), however, with a certain amount of steam added to the feedstock to eliminate carbon formation. Carbon and soot formation in the combustion zone is an undesired reaction, which leads to carbon deposition on downstream tubes causing equipment damage, pressures losses and heat transfer problems.

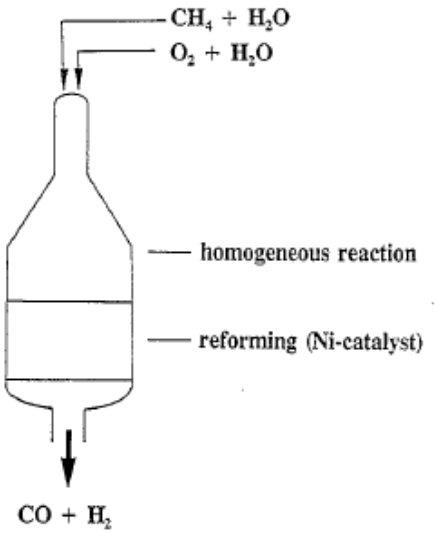

Fig. 2.26 Autothermal reformer.

Although the ATR was originally used to maximize H_2 production in ammonia plants, it can be applied in the production of CO rich gases. In all cases, the H_2/CO ratio at the outlet of the reactor can be precisely adjusted by varying the H_2O/CH_4 and/or O_2/CH_4 molar ratios in the feed.

Since autothermal reforming uses less O_2 than POX, the economics are less sensitive to the price of O_2 when O_2 is cheap. It requires no external fuel while offering some flexibility in feedstock.

2.3.5 Catalytic partial oxidation (CPO)

A new interesting process for conversion of methane into synthesis gas is catalytic partial oxidation. In the 1940s, Prettre et al first reported the formation of synthesis gas by the catalytic partial oxidation of CH_4:

$CH_4 + 1/2\ O_2 \rightarrow CO + 2\ H_2$ $\Delta H^0_{298} = -36$ kJ/mol

They used a Ni-containing catalyst. In contrast to steam reforming of methane, methane partial oxidation is exothermic. However, the partial oxidation requires pure oxygen, which is produced in expensive air separation units that are responsible for up to 40% of the cost of a synthesis gas plant (in contrast, the steam reforming process does not require pure oxygen) (*75*).

In the early 1990s, several papers (*76*) (*77*) (*78*) (*79*) (*80*)reported that one can reach CO and H_2 concentrations in excess of those expected at thermodynamic equilibrium by operating the CH_4 oxidation reaction at exceptionally high space velocities (GHSV = 52,000 ml (g catalyst)$^{-1}$ h^{-1}) in a fixed-bed reactor. The following catalysts were employed: Ni/Yb_2O_3, Co/rare earth oxide, Co/MgO, and Ni/Al_2O_3.

According to the partial oxidation reaction, such a process yields the desired H_2/CO molar ratio of 2 required for methanol or Fischer-Tropsch synthesis. From thermodynamic simulations, it is clear that the reaction is favored at T > 850°C in excess of CH_4, although both CO and H_2 selectivities are modified by the formation of CO_2 and H_2O in combustion reactions which are much more exothermic:

$CH_4 + 1.5\ O_2 \rightarrow CO + 2\ H_2O$ $\Delta H^0_{298} = -519$ kJ/mol

$CH_4 + 2\ O_2 \rightarrow CO_2 + 2\ H_2O$ $\Delta H^0_{298} = -802$ kJ/mol

Since CPO reaction is slightly exothermic, a process based on this reaction would be much more energy efficient than the energy intensive SMR process. In addition the partial oxidation reaction is also much faster than the reforming reactions, suggesting that a single stage process for syngas production would be an attractive alternative to SMR and also results in smaller reactors and higher productivity.

The direct oxidation has not been developed at industrial scale, and it is difficult to study because it involves co-feeding CH_4/O_2 mixtures and reaction close flammable or even explosive conditions.

Local hot spot are usually formed which can irreversible damage the active catalyst. Moreover the gas phase reactions in a high reducing atmosphere can led to carbon and soot deposition over the catalyst surface.

In the 1940s, Prettre et al. reported the formation of synthesis gas via the catalytic partial oxidation of CH_4 catalyzed by a 10 wt % refractory supported nickel, at temperatures between 700 and 900°C. Thermodynamic equilibrium corresponding to the catalyst bed exit temperature was achieved under all conditions investigated. In 1970, it was examined the effect of diffusion on methane partial oxidation catalyzed by a single grain of Ni/mullite catalyst in the temperature range of 760 and 900°C and examined the ignition and extinction characteristics of this catalyst. It was observed that the nickel catalyst deactivated in an oxidative environment but could recover on reduction. In 1984, Gavalas et al (*81*) investigated the effects of the calcination temperature, pre-reduction, and feed ratio on the reaction of CH_4/O_2 mixtures catalyzed by $NiO/\alpha\text{-}Al_2O_3$ at 570–800°C. However, under their experimental conditions, the main products were CO_2 and H_2O. Since 1990, researchers have continued to examine nickel-containing catalysts for the partial oxidation of methane, and they also started to use noble metals as catalysts. In 1992, Hickman and Schmidt (*82*) used platinum monoliths to achieve high selectivities to CO and H_2 in the partial oxidation of methane. During last 10 years, various noble metal catalysts have been examined. Compared with the non-noble metal catalysts, the noble metals exhibit high stability with excellent activities and selectivities. The major drawback of the noble metal catalysts is their high cost, which restricts their potential use in industrial processes.

The major problem encountered with non-noble metal catalysts as nickel and cobalt is their relatively low stability. The main causes of the deactivation of the catalysts are carbon deposition and metal sintering in the catalyst. Nevertheless, numerous effective nickel-containing catalysts have been developed by incorporation in suitable supports, such as La_2O_3, MgO, $SrTiO_3$, and CeO_2; effective promoters, including La_2O_3, Li_2O, and iron oxide; and novel preparation methods, such as a solid phase crystallization method, a sol–gel method, and a citrate method(*75*). However, because the high stabilities reported for these effective nickel-containing catalysts were based on short-term tests (< 100 h), it is unclear how stable these catalysts will be in long term tests (> 1000 h), which is the first step that any candidate catalyst for commercialization must pass.

Mechanistic investigations of the partial oxidation are still challenging, because this exothermic reaction is very fast and causes extremely high catalyst temperature rises, so that the usual methods of investigation are unsuitable.

Two kinds of pathways have been suggested:

1. combustion-reforming pathway, in which CO_2 and H_2O are the primary products, and CO and H_2 are formed by their reactions with CH_4,

2 pyrolysis or dissociative adsorption pathway, in which CO is the primary product formed by the dissociation of methane, $CH_4 \rightarrow CH_x + (2 - 1/2\ x)\ H_2$;

followed by the oxidation of carbon containing species to give CO without the pre-formation of CO_2.

For methane partial oxidation to syngas, the thermodynamic calculation results suggest a high temperature is advantageous for high methane conversion and selectivity to CO and H_2. However, increasing the pressure in the reactor is unfavourable for CH_4 conversion and CO and H_2 selectivity. The prediction of the CH_4 conversion and product selectivity under specific conditions is shown in two-dimensional forms (Fig. 2.27(a) and (b)) (*83*). Apparently, under 1 bar at 800°C, theoretical CH_4 conversion should be up to 90 %, and selectivities to CO and H_2 are 97 %. At 8 bar and 800°C, CH_4 conversion is only 70 %, and CO and H_2 selectivities are around 85 %.

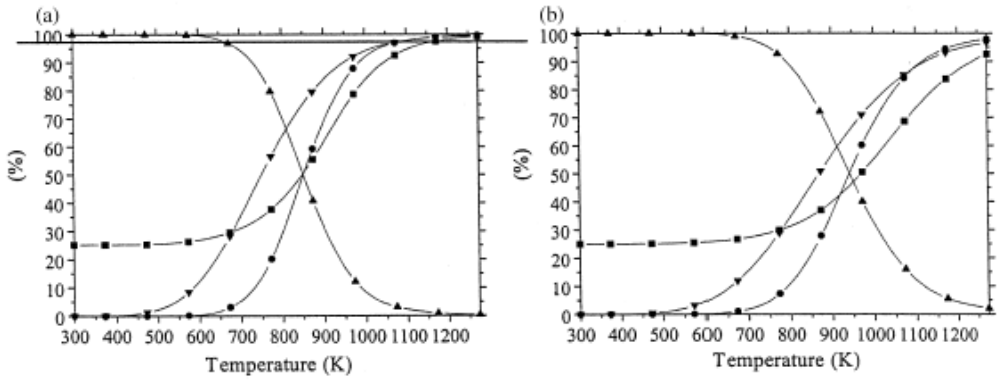

Fig. 2.27 Thermodynamic equilibrium calculations at: (a) atmospheric pressure and (b) at 8 bar); (■) XCH4; (●) S[CO], (▲) S[CO2], (▼) S[H2] (*83*).

This process is likely to become more important in the future of methane conversion due to the thermodynamic advantages this process has over steam reforming:

1. Partial oxidation is mildly exothermic, while steam reforming is highly endothermic. Thus, a partial oxidation reactor would be more economical to heat. In addition, it can be combined with endothermic reactions, such as steam reforming or dry reforming with carbon dioxide to make these processes more energy efficient.

2. The H_2/CO ratio produced in stoichiometric partial oxidation is around 2, and this ratio is ideal for downstream processes, in particular methanol and FT synthesis. This avoids the need to reverse shift hydrogen, which is produced in excess in steam reforming.

3. The product gases from methane partial oxidation can be extremely low in carbon dioxide content, which must often be removed before synthesis gas can be used downstream.

4. Partial oxidation technology avoids the need for large amounts of expensive superheated steam. However, an oxygen separation plant, which is also costly, may

be required in cases where nitrogen (from air) is undesirable in high-pressure downstream processes.

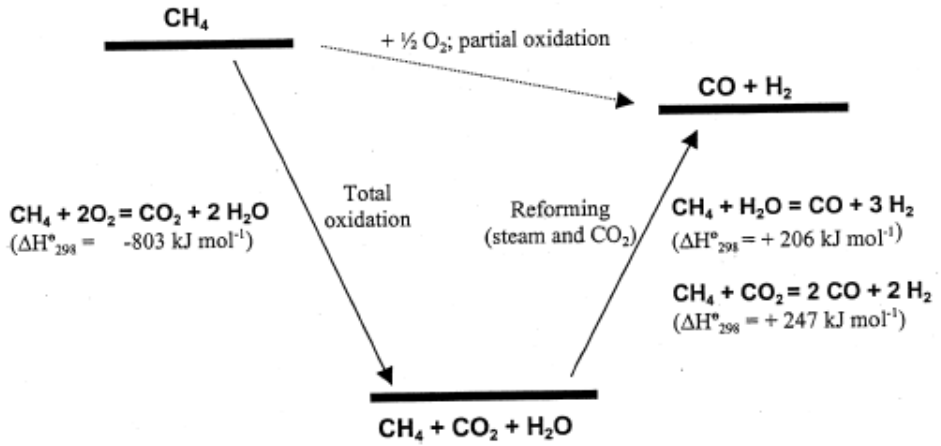

Fig. 2.28 Thermodynamic representation of the partial oxidation of methane(*83*).

2.4 Bioethanol steam reforming

2.4.1 Thermodynamic considerations

The reaction of steam reforming of ethanol is, from a thermodynamic point of view, feasible above 500 K ($\Delta G < 0$). It is strongly endothermic and results in increase in number of moles. Increasing the temperature and lowering the pressure favour ethanol reforming.

Stoichiometrically the basic reaction scheme is:

$C_2H_5OH + 3\ H_2O \leftrightarrows 2\ CO_2 + 6\ H_2$ $\quad \Delta H°_{298} = 174$ kJ/mol (1)

Other by-products such as CO and CH_4 are also usually formed during reaction.

For what concern CO it is formed directly and indirectly by:

$C_2H_5OH + H_2O \leftrightarrows 2\ CO + 4\ H_2$ $\quad \Delta H°_{298} = 256$ kJ/mol (2)

$2\ H_2O + 2\ CO \leftrightarrows 2\ CO_2 + 2\ H_2$ $\quad \Delta H°_{298} = -41$ kJ/mol (3)

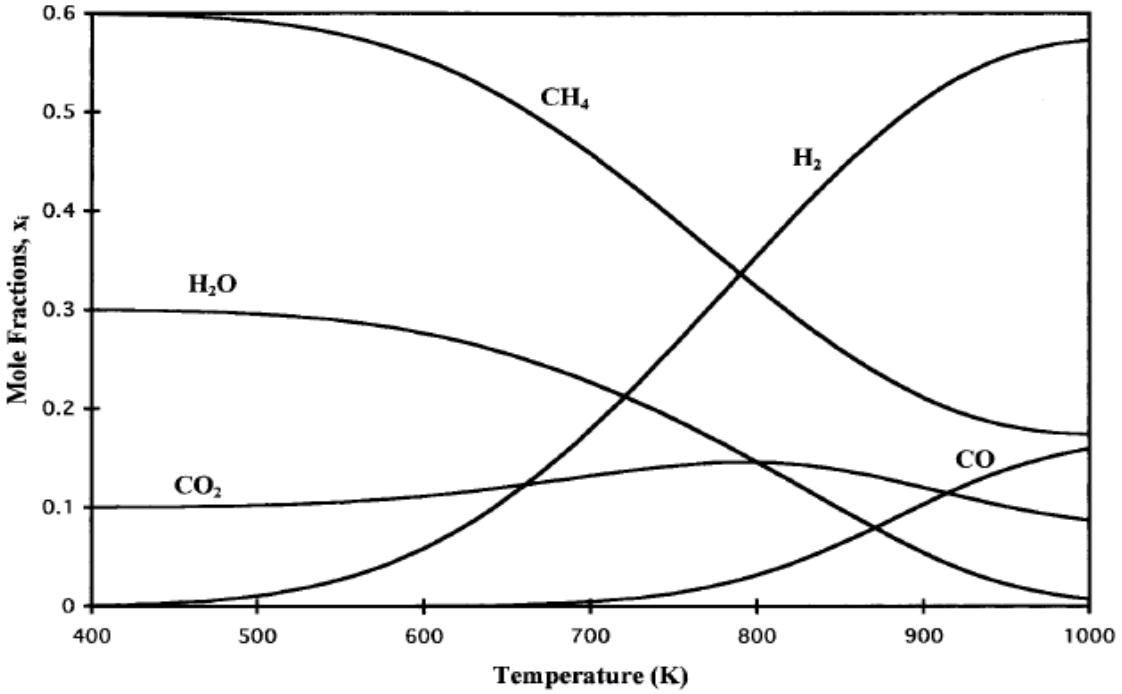

Fig. 2.29 Species distributions as a function of temperature at P= 1 atm, n (C_2H_5OH)=1 mol and n (H_2O)=3 mol obtained from Gibbs free energy minimization (non stoichiometric thermodynamic approach) (*84*).

The difference between the reaction 1 and 2 is the water gas shift reaction; therefore the amount of CO depends on the direction of the water gas shift that is a consequence of reaction temperature and S/C.

The amount of methane is due to both the reaction with hydrogen during the hydrogenolisis of ethanol and the metanation reactions on CO and CO_2 and decomposition of ethanol.

$C_2H_5OH + 2\ H_2 \leftrightarrows 2\ CH_4 + H_2O$ $\Delta H°_{298} = -157$ kJ/mol (4)

$CO + 3\ H_2 \leftrightarrows CH_4 + H_2O$ $\Delta H°_{298} = -206$ kJ/mol (5)

$CO_2 + 4\ H_2 \leftrightarrows CH_4 + 2\ H_2O$ $\Delta H°_{298} = -166$ kJ/mol (6)

$2\ C_2H_5OH \leftrightarrows 3\ CH_4 + CO_2$ $\Delta H°_{298} = -74$ kJ/mol (7)

$C_2H_5OH \leftrightarrows CH_4 + CO + H_2$ $\Delta H°_{298} = 49$ kJ/mol (8)

At low temperatures reactions methane is the favourite product as it observe from Fig. 2.29.

Since the reaction system is very complex, the effect of operational parameters on the equilibrium composition, based on either the stoichiometric or non stoichiometric thermodynamic approach, can be investigated only using numerical methods.

In the non stoichiometric approach, the equilibrium composition of the system is found by the direct minimization of the Gibbs free energy for a given set of species without any specification of the possible reactions which might take place in the system. On the other hand, in the stoichiometric approach, the system is described by a set of stoichiometrically independent reactions (SIRs). The latter, however, are typically chosen completely arbitrarily from a set of possible reactions. As a result, efforts to study the system's response in terms of the arbitrarily chosen chemical reactions can lead to erroneous conclusions.

The arbitrariness in the specification of a set of chemical reactions can, however, be avoided. It appears that the basic equations of chemical thermodynamics can always be transformed so as to be presented as a sum of contributions associated with a special class of reactions, called response reactions (RERs), which have the remarkable property of being unique, independent of the initial choice of the SIRs (*85*).

Fishtik et al. consider a set of reactions to investigate the effects of the process variables on the production of hydrogen. They suppose that at equilibrium the amounts of ethanol and acetaldehyde are negligibly small as compared with the amounts of other species. This means that one may safely neglect the effect of those RERs in which C_2H_5OH and CH_3CHO are concomitantly involved. As a consequence the analysis can be substantially simplified and the ethanol steam reforming can be described by a set of eight RERs (*84*). The relative fractions of the ethanol reactions as a function of temperature and amount of feed water are plotted in Fig. 2.30 and Fig. 2.31.

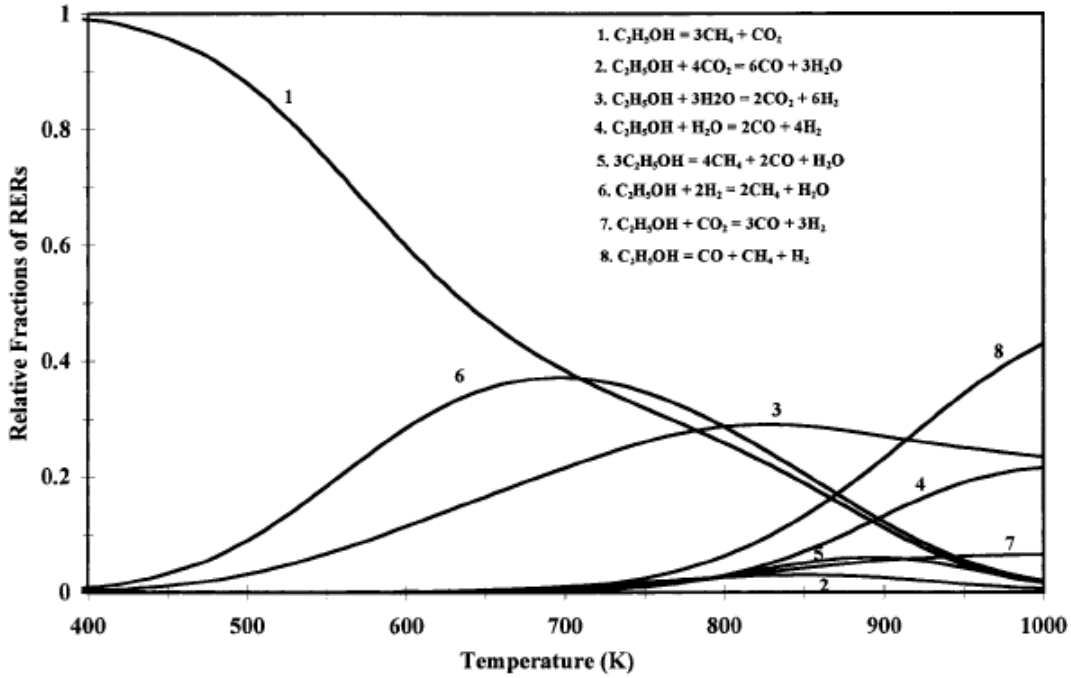

Fig. 2.30 Relative fractions of RERs in which ethanol is involved as a function of temperature at P =1 atm, n (C2H5OH)=1 mol and n (H2O)=3 mol (*84*).

Thanks to this approach it is seen that at small amounts of water, both at low, reaction (7), and high temperatures, reaction (8), the predominant reactions are the decomposition of ethanol.

As the amount of water increases (Fig. 2.31), however, the steam reforming of ethanol becomes the dominant reaction (*84*).

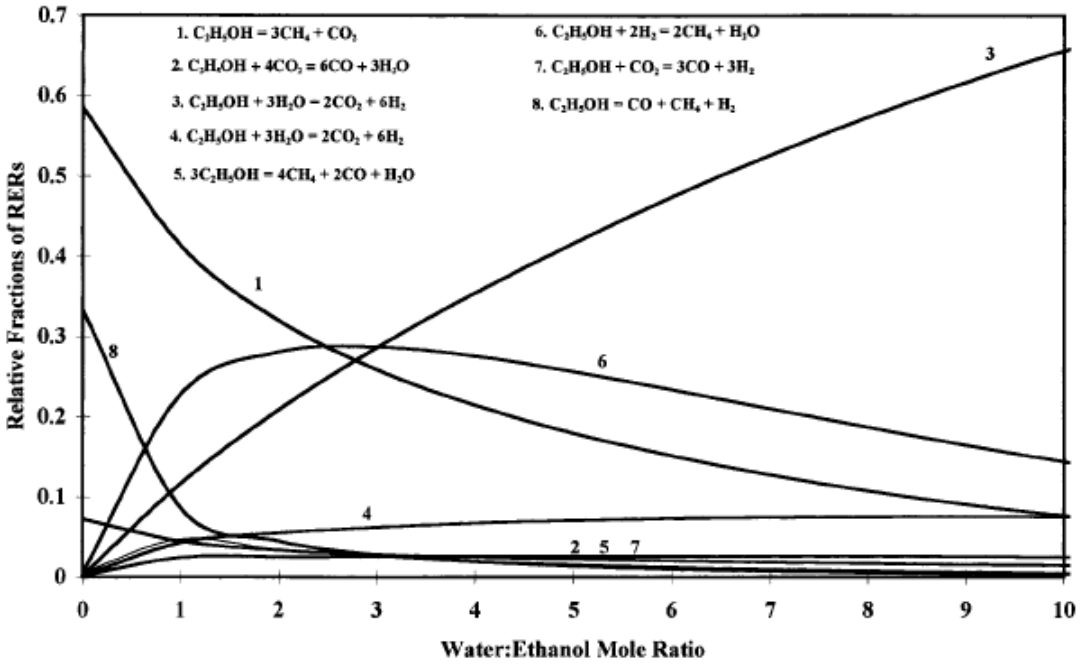

Fig. 2.31 Relative fractions of RERs in which ethanol is involved as a function of the initial amount of water at T =800 K, P= 1 atm, n (C2H5OH) = 1 mol (*84*).

As for the set of reactions in which ethanol is involved, also for the set in which hydrogen is involved it supposes that the contributions coming from those RERs in which ethanol and acetaldehyde are involved are negligibly small. As a result, the hydrogen sensitivity may be very accurately described simply by the set of four RERs.

Then the H_2 yield depends on the temperature and the amount of water as it observes in Fig. 2.32, Fig. 2.33,Fig. 2.34,Fig. 2.35.

At small temperatures and small amounts of water, the contribution of the WGSR is small and an increase in temperature leads to an increase in the amount of H_2. At higher temperatures, the WGSR becomes dominant and the amount of hydrogen decreases with increasing temperature.

Consequently the amount of hydrogen, as a function of temperature, can have a maximum (*84*). After that the hydrogen molar flow decreases.(Fig. 2.33).

Water, CO_2 and methane molar flows decrease with temperature while CO slightly increases.

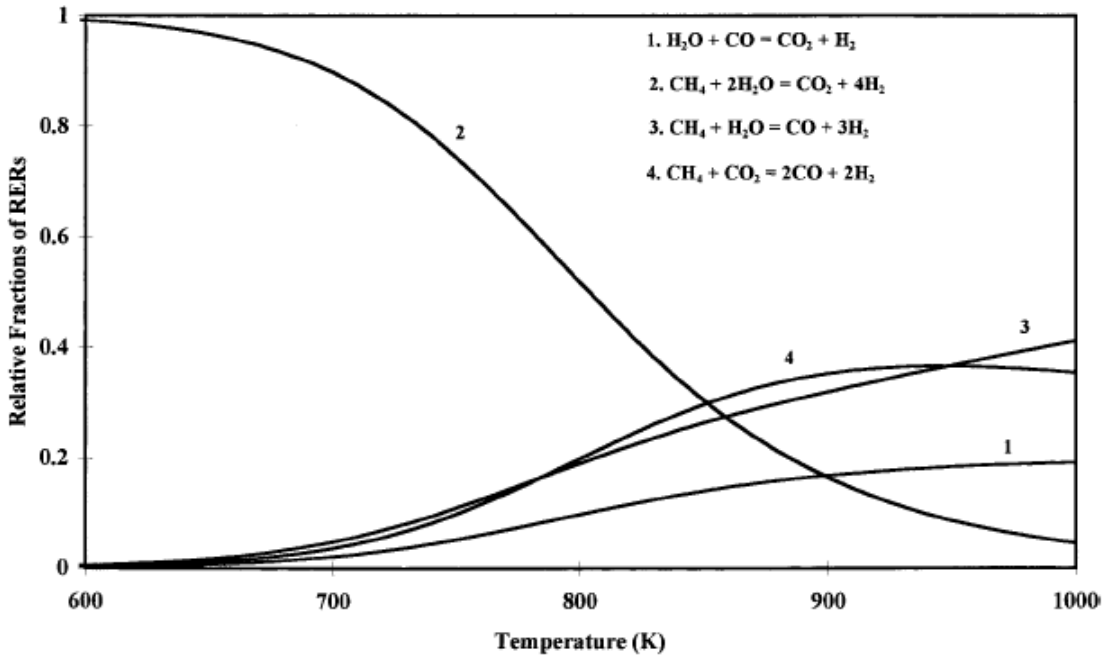

Fig. 2.32 Relative fractions of RERs in which hydrogen is involved as a function of temperature at P= 1 atm, n (C2H5OH)= n (H2O)=1 mol (*84*).

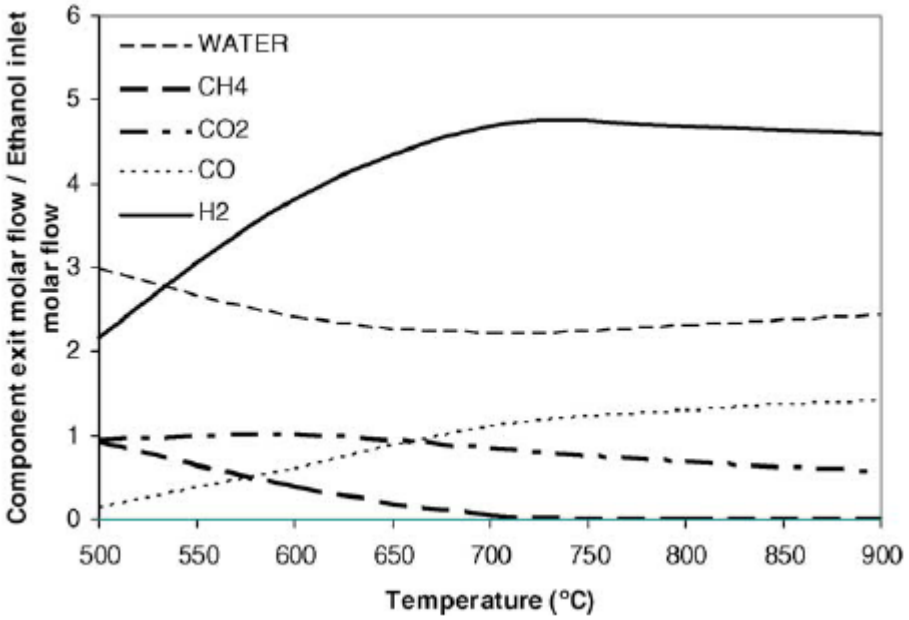

Fig. 2.33 Effect of reactor temperature on equilibrium component molar flows for the steam reforming of ethanol (water/ethanol molar ratio, 4; pressure, 1 atm) (*86*).

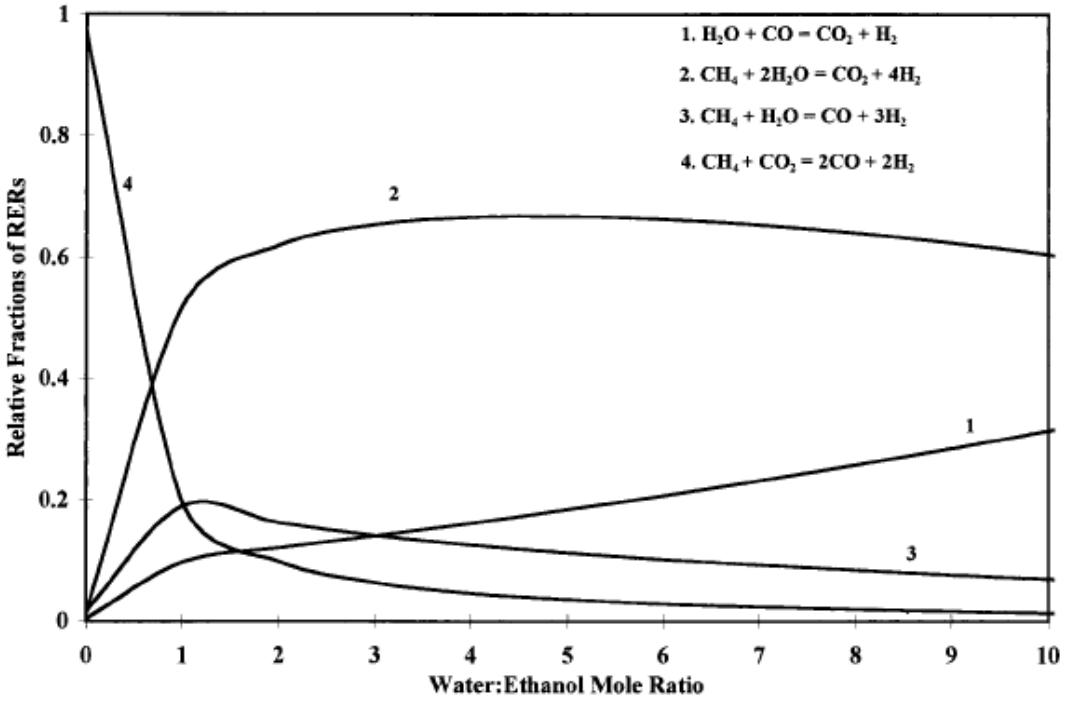

Fig. 2.34 Relative fractions of RERs in which hydrogen is involved as a function of the initial amount of water at T= 800 K, P= 1atm, n (C2H5OH)=1 mol (*84*).

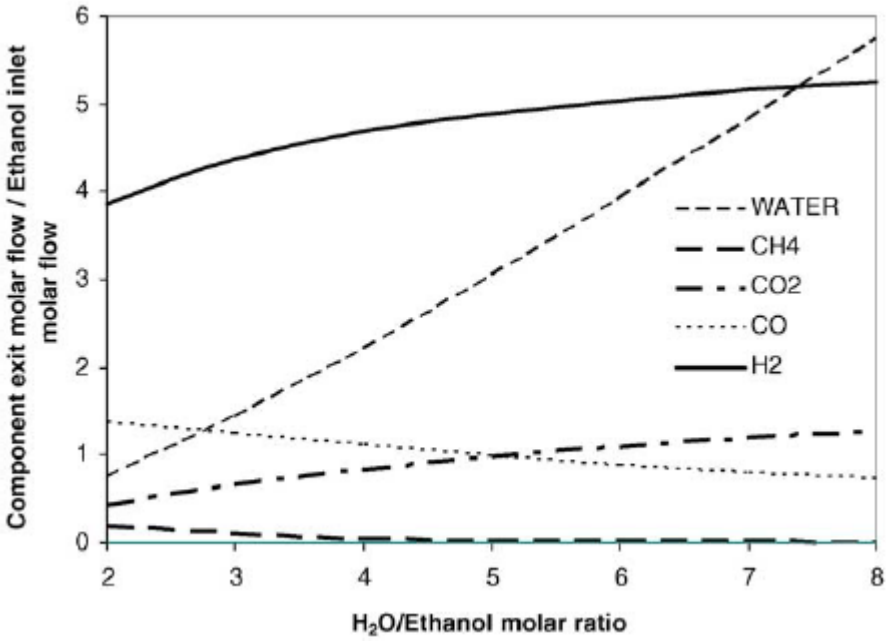

Fig. 2.35 Effect of water/ethanol ratio on the equilibrium component molar flows. Pressure, 1 atm; temperature, 700 °C (*86*).

The addition of water increases the hydrogen production while reducing the methane and CO molar flows. Although high water to ethanol molar ratios are favourable from the thermodynamic point of view, the maximum water to ethanol ratio will be limited by the energy cost of the system and the larger dimension required. A higher ratio will represent a higher energy cost because of the extra steam generated (*86*).

The operating pressures impacts significantly over the equilibrium molar fractions of the system. An increase in pressure can lead to a decrease in the amount of H_2, in fact reactions that give H_2 imply an increase of number of moles (*86*). Going from 1 to 25 bar the [H_2] decrease of a factor > 2.

On the other hand high pressures reduce the CO concentration in the reformer exit, as it see in Fig. 2.36.

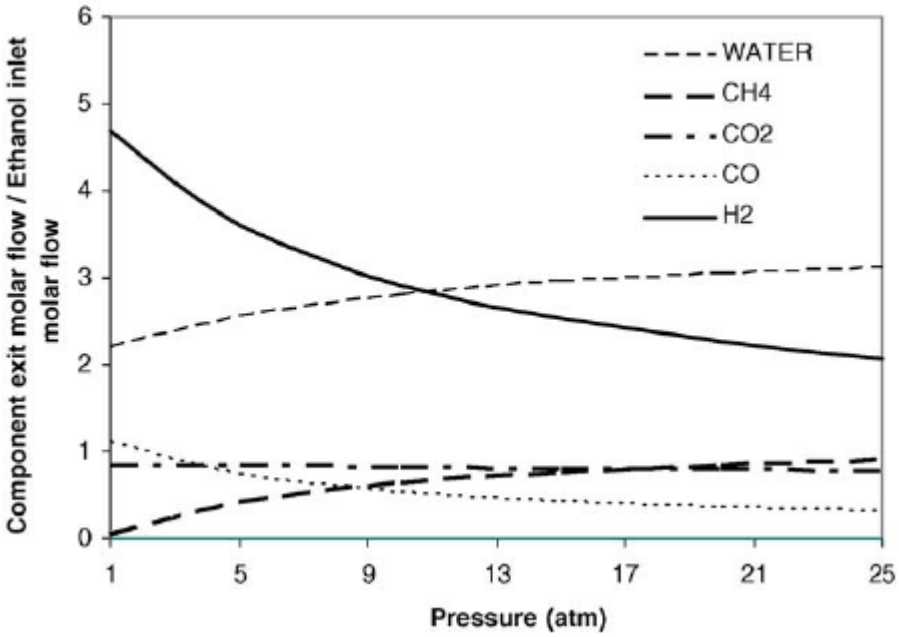

Fig. 2.36 Effect of reactor pressure on equilibrium component molar flows. water/ethanol molar ratio, 4; temperature, 700 °C (*86*).

There are other reactions that could occur in the C_2H_5OH reforming process, depending on the catalyst used and the reaction conditions: ethanol dehydrogenation to acetaldehyde and ethanol dehydration to ethylene.

$$C_2H_5OH \leftrightarrows C_2H_4O + H_2 \qquad \Delta H°_{298} = 68 \text{ kJ/mol} \qquad (9)$$

$$C_2H_5OH \leftrightarrows C_2H_4 + H_2O \qquad \Delta H°_{298} = 45 \text{ kJ/mol} \qquad (10)$$

Acetaldehyde and ethylene are the main products working at very low contact time, in fact these products were not detected while working at moderate and high contact times (*87*).

The equilibrium constant of ethanol dehydrogenation, K_1, and ethanol dehydration, K_2, at different temperatures are shown in Fig. 2.37. Both reactions are endothermic, the equilibrium costant of ethanol dehydration K_2 is larger than the equilibrium costant of ethanol dehydrogenation K_1 in the whole range of temperatures analyzed, although K_1 increases faster than K_2 when temperature is increased.

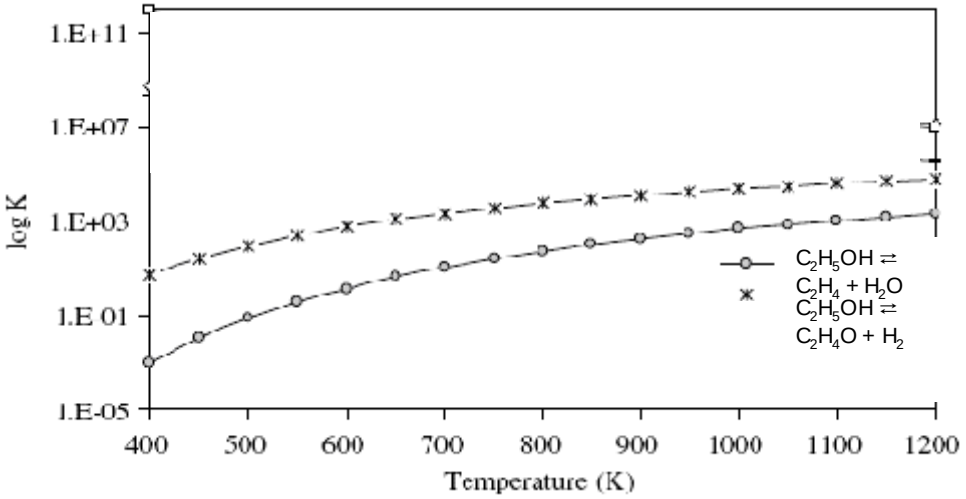

Fig. 2.37 Equilibrium constants at different temperatures (*87*).

Compare the ethanol conversion at different value of temperature and S/C it can be see that the equilibrium conversion of ethanol is 0.96 at 423 K and S/C=0 and at T>500 K conversion is higher than 0.99 at all S/C analyzed. It means that, whatever *r* value is, for T > 500K ethanol is not practically present in the equilibrium mixture (*87*).

The amount of C_2H_4O increases with the temperature, in the whole range. The presence of water works against dehydrogenation and formation of C_2H_4O, because the total mole number increases with S/C and, due to the stoichiometric, the equilibrium is therefore shifted to products (Fig. 2.38) (*87*).

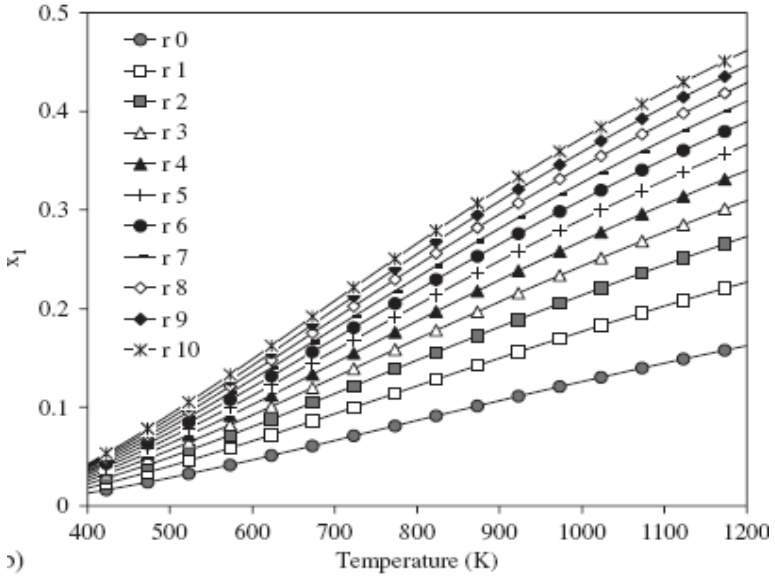

Fig. 2.38 Extent of reaction (9) vs. temperature at different S/C values (S/C = r and x1 = C2H4O) (*87*).

In a different way respect the trend of C_2H_4O, the amount of C_2H_4 as first increases and then decreases with the temperature. This behaviour is a consequence of the

competition between both reactions when the temperature increases. It must be noted that C_2H_4 increases with temperature at low temperatures and when C_2H_4O value is nearly zero. The effect of water on reaction (10) is explained by the stoichiometry of the reaction (Fig. 2.39) (*87*).

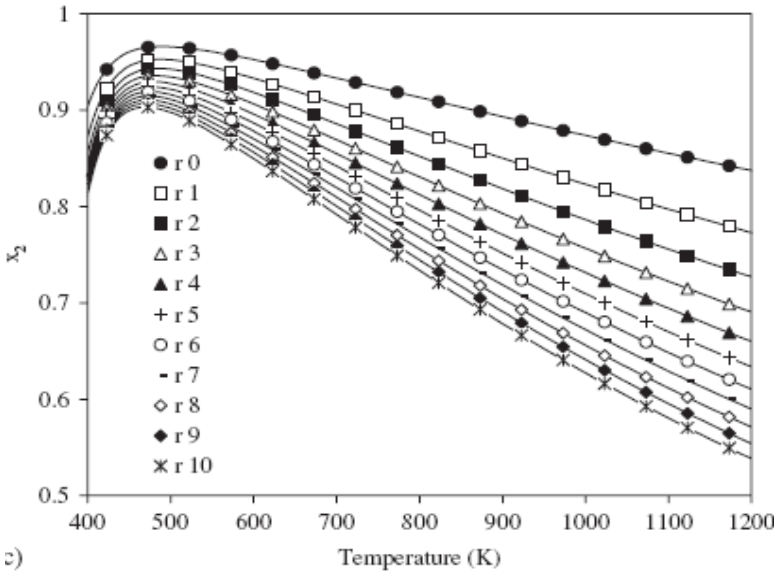

Fig. 2.39 Extent of reaction (10) vs. temperature at different S/C values (S/C = r and x2 = C2H4) (*87*).

Then C_2H_4 is always higher than C_2H_4O, for all T and S/C values analyzed. Furthermore ethanol, from a thermodynamic point of view, is preferentially consumed by the dehydration reaction (10). It must be noted that the free energy of acetaldehyde is lower than the free energy of ethylene in the range of temperature studied. Nevertheless, the stability of water, the other product of reaction 10, explains the preference of ethanol for this reaction. Only for T > 1200K and for high S/C values reaction 9 would be favored (*87*).

Compared with the SR reactions, the ethanol dehydration and dehydrogenation reactions are much faster, and acetaldehyde and ethylene may be considered important intermediates in formation of H_2, in fact they be reformed to:

$C_2H_4O + H_2O \leftrightarrows CH_4 + CO_2 + H_2$ (11)

$C_2H_4 + H_2O \leftrightarrows CH_4 + CO + H_2$ (12)

$C_2H_4 + 2\ H_2O \leftrightarrows CH_4 + CO_2 + 2H_2$ (13)

and acetaldehyde can be decarboxylated to:

$C_2H_4O \leftrightarrows CH_4 + CO$ (14)

At low S/C value the composition are CH4:CO:H2 = 1:1:1 , while at moderate S/C value the composition are CH4:CO2:H2 = 1:1:2. In the first case CO is the primary product, while in the second case CO_2 is the primary product. The ratio CO/CO_2. depends on water gas shift equilibrium represented in Fig. 2.40.

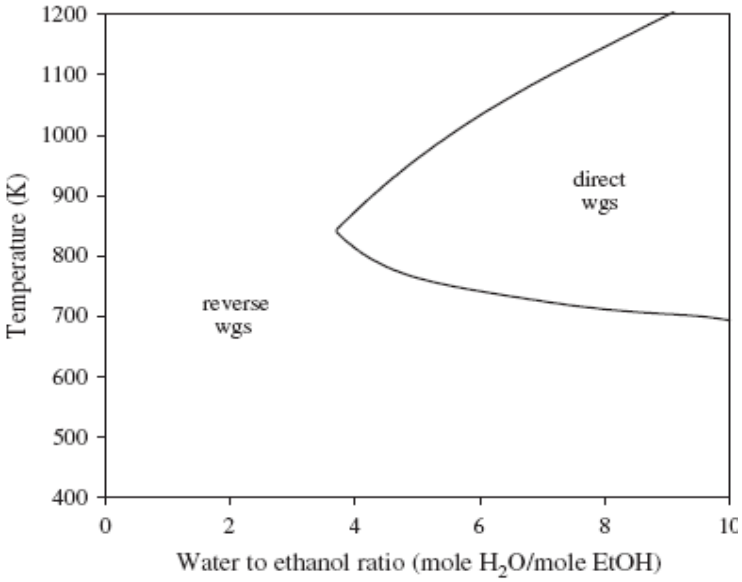

Fig. 2.40 Direct and inverse WGS regions (*87*).

The product distribution is showed in Fig. 2.41, Fig. 2.42 and Fig. 2.43, high temperatures and S/C values favour hydrogen production; the tendency of methane is exactly the opposite of that of hydrogen. In order to minimize CO formation, low temperatures and high S/C are suitable (*87*).

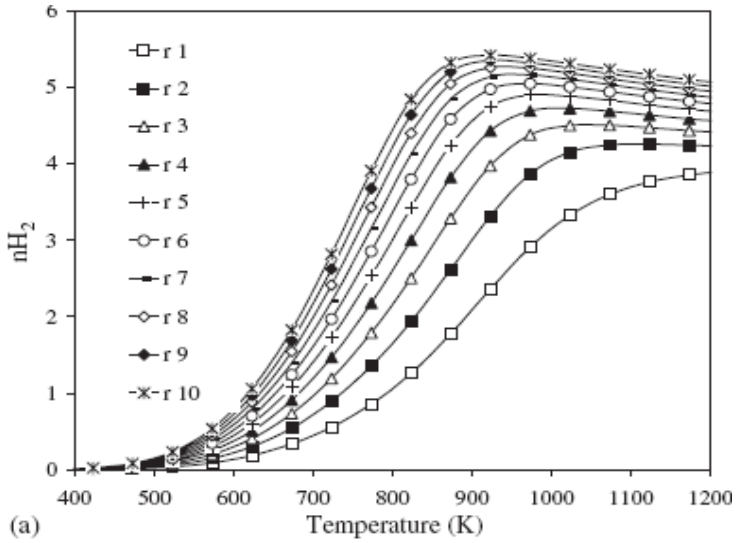

Fig. 2.41 Moles of hydrogen per mole of ethanol fed in the equilibrium at different S/C values (S/C = r) (*87*).

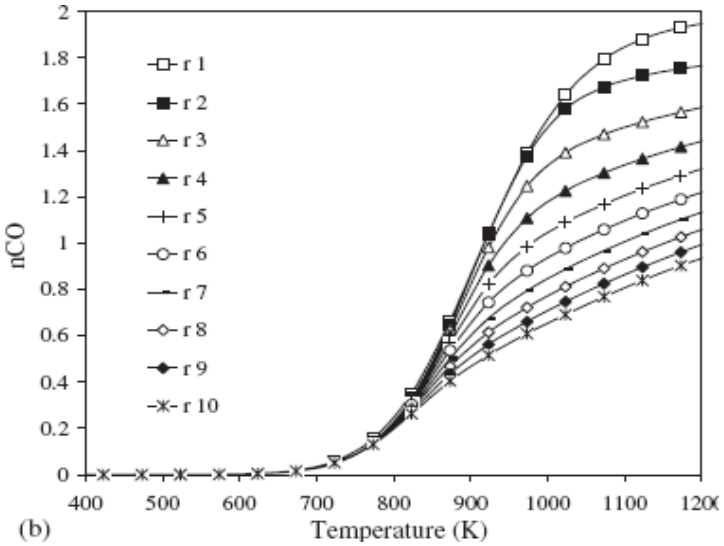

Fig. 2.42 Moles of carbon monoxide per mole of ethanol fed in the equilibrium at different S/C values(S/C = r) (*87*).

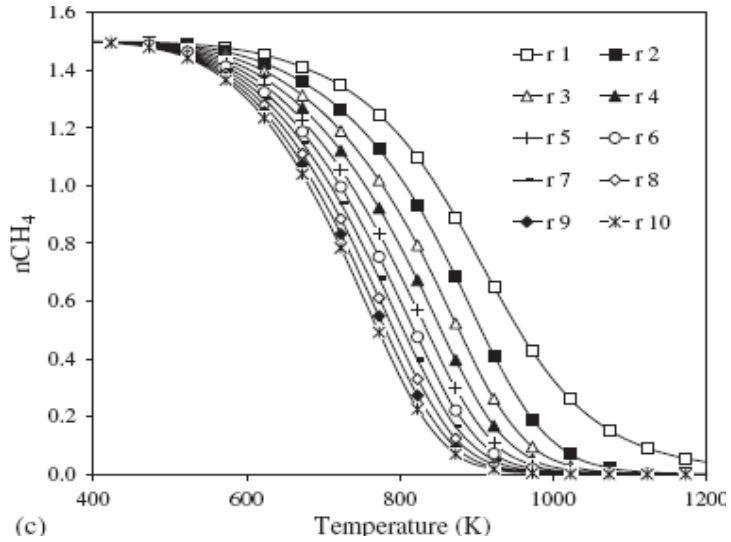

Fig. 2.43 Moles of methane per mole of ethanol fed in the equilibrium at different S/C values (S/C = r) (*87*).

Other possible byproducts are aceton and acetic acid.

$C_2H_5OH + H_2O \leftrightarrows CH_3COOH + 2\ H_2$ (15)

$2\ C_2H_5OH + H_2O \leftrightarrows CH_3COCH_3 + CO_2 + 4\ H_2$ (16)

Acetone is obtained by the decomposition of ethanol, a reaction favoured when the catalyst works at low temperatures (*88*).

The formation of coke on the surface of the catalyst is also not uncommon. Coke formation may occur via the Boudouard reaction:

$2\ CO \leftrightarrows CO_2 + C \qquad \Delta H°_{298} = -171.5$ kJ/mol (17)

Another possible route for the formation of carbon is through ethylene:

C_2H_4 → polymers → coke

Mas et al. have analysed the operation region where coke can be formed, the coke formation is higher if S/C value is lower. If the ethanol steam reforming reactor works in the region where coke formation is thermodynamically feasible, the use of acid catalysts should be avoided (*87*).

Comas et al. have observed that carbon decreases when the water to ethanol ratio and temperature increase, while the pressure effect depends on the operating temperature (*86*).

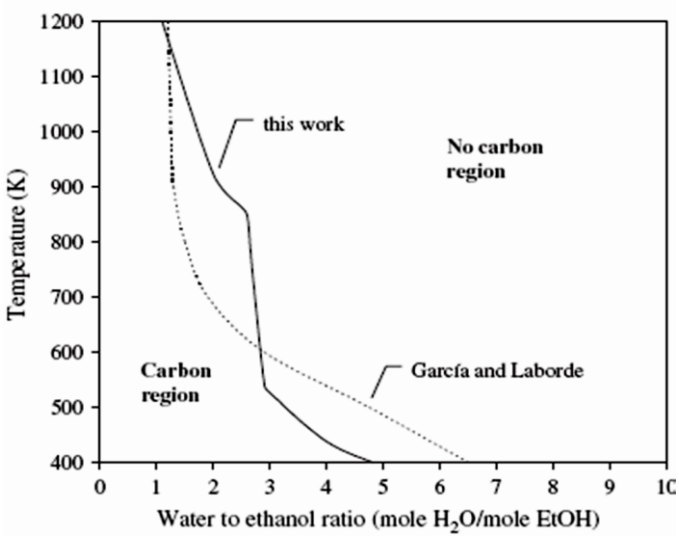

Fig. 2.44 Range of conditions for carbon formation (*87*).

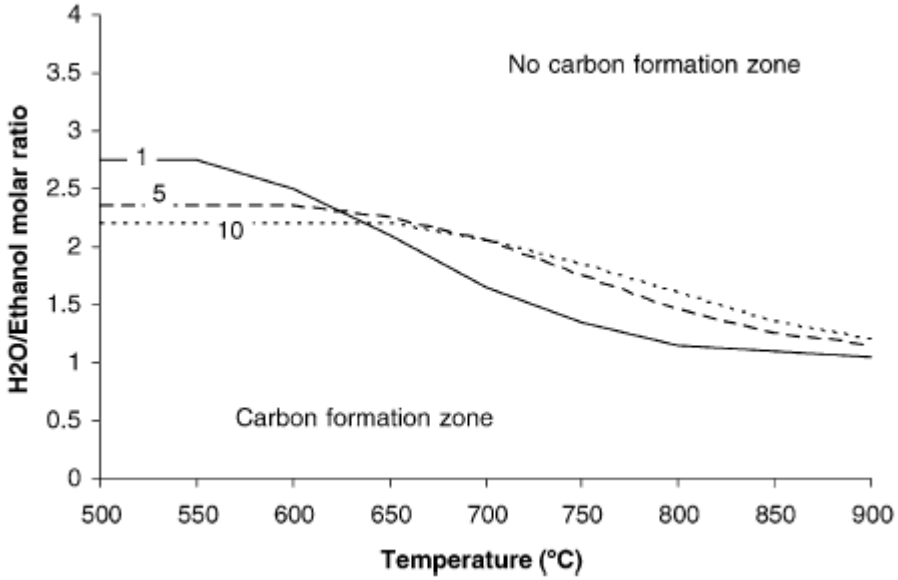

Fig. 2.45 Diagram of C(s) formation with regard to reactor temperature and water/ethanol ratio for different operating pressures (*86*).

2.4.2 Reaction mechanism

Several possible reactions can occur when the ethanol water mixture is in contact with a catalyst at high temperature. The behaviour of each metal can be explained considering its activity towards specific reactions involved in the reaction mechanism.

The knowledge of the reaction mechanism will be very important to design a catalyst resistant to carbon poisoning that can be applied to produce high hydrogen yield and to achieve the requirements demanded in fuel cells.

Then knowledge of the type of ethanol–metal interaction is therefore of prime importance for a thorough understanding of the process.

At low temperatures ethanol could adsorb in two molecular forms on the surfaces of the catalysts: in a form coordinated to the Lewis acid sites of the supports (1) and in a hydrogen bridge bonded form through the OH groups of the supporting oxide (2) (*89*).

1) $CH_3CH_2OH + M^{n+}_{(s)} \rightarrow CH_3CH_2OH$

$\vdots$

$M^{n+}_{(s)}$

2) $CH_3CH_2OH + OH^-_{(s)} \rightarrow CH_3CH_2O^-_{(s)} + H_2O$

Previous workers (*90*) (*91*) (*92*) (*93*) (*94*) (*95*)have examined the decomposition and oxidation of ethanol on well-defined surfaces of transition metals in great detail. At low temperature, ethanol adsorbs molecularly on Pt(lll)], Pd(lll), Cu(llo), Cu(100), Cu(410), Ag(llo), Rh(lll) and Ni(lll).

However, at 300 K on the surfaces of clean nickel, rhodium, platinum and palladium part of the ethanol decomposes to form ethoxy ligand ($-OCH_2CH_3$) (*96*).

$CH_3CH_2OH(a) \rightarrow CH_3CH_2O^-(a) + H(a)$

The general trend of the ethanol decomposition on these surfaces except rhodium reveals that the ethoxy species will sequentially decompose into acetaldehyde:

$CH_3CH_2OH(a) \rightarrow CH_3CH_2O^-(a) + H(a) \rightarrow CH_3CHO(a) + 2H(a)$

upon further heating (about 400-600 K) the C-C bond in the acetaldehyde breaks to produce adsorbed H, CO and CH_x species.

$CH_3CHO(a) \rightarrow CH_x(a) + C(a) + O(a) + (4-x)H$

The adsorbed CH_x group then combines with hydrogen and desorbs as methane or decomposes completely to carbon and hydrogen.

The one exception to this mechanism is on Rh (111) where the ethoxy species dehydrogenates to form a cyclic intermediate ($-OCH_2CH_2-$), which then decomposes into CO and hydrogen (*96*).

In fact a suggest mechanism of steam reforming on Rh metal is:

$CH_3CH_2OH \rightarrow CH_3CH_2O(a) + H(a)$

$CH_3CH_2O(a) \rightarrow (a)CH_2\text{-}CH_2O(a) + H(a)$

$(a)CH_2\text{-}CH_2O(a) \rightarrow CH_4(g) + CO(g)$

$CH_4(g) + H_2O(a) \rightarrow C(a) + 4\,H(a)$

$C(a) + O(a) \rightarrow CO$

$2H(a) \rightarrow H_2(g)$

The adsorbed ethoxide species forms an oxametallacycle intermediate, which favors the C—C bond cleavage effectively. In addition, the reaction also proceeds through the formation of acetaldehyde intermediate which undergoes C-C bond rupture (*97*).

During ethanol reforming it can be form also acetate species from acyl group:

$CH_3CHO(a) + OH(a) \rightarrow CH3COO(a) + H_2$

That is possible only if the catalyst is covered with adsorbed species, so the effect of the support is dominated.

Then acetate species can decompose:

$CH3COO(a) \rightarrow CH3(a) + CO_2$

The CH_3 groups can react with surface OH species:

$CH_3(a) + OH(a) \rightarrow CO + 2H_2$

or in the presence of water:

$2CH3(a) + 2H_2O \rightarrow 2CO + 5H_2$

The acetaldehyde formed can also be decomposed to methane and carbon monoxide:

$CH_3CHO(a) \rightarrow CH_4 + CO(a)$

In the presence of water the steam reforming reaction may also occur:

$CH_4 + H_2O \rightarrow CO + 3H_2$

Erdohelji et al. have studied the interaction ethanol-metal during steam ethanol reforming on various metals like Pt, Pd, Ir, Rh and Ru with two different support (Al_2O_3 and CeO_2). They have found that at 723 K with S/C=3 in all case the hydrogen selectivity decreased but ethylene and acetaldehyde selectivity increased in time (*98*).

The highest changes it was observed on Pt/Al_2O_3 where the hydrogen selectivity was near 100% in the first minutes of the reaction, but after 60 min it was only about 10%.

In contrast with this observation, on alumina supported Ru or Rh the selectivity changes were only about 20%. Ethylene selectivity varied oppositely, on Pt/Al_2O_3 in the first minutes ethylene formed only in traces but after one hour the C_2H_4 selectivity

was more than 80%. Similar features were observed on CeO_2 supported metals, in these cases not only the ethylene but also the acetaldehyde selectivity increased in time.

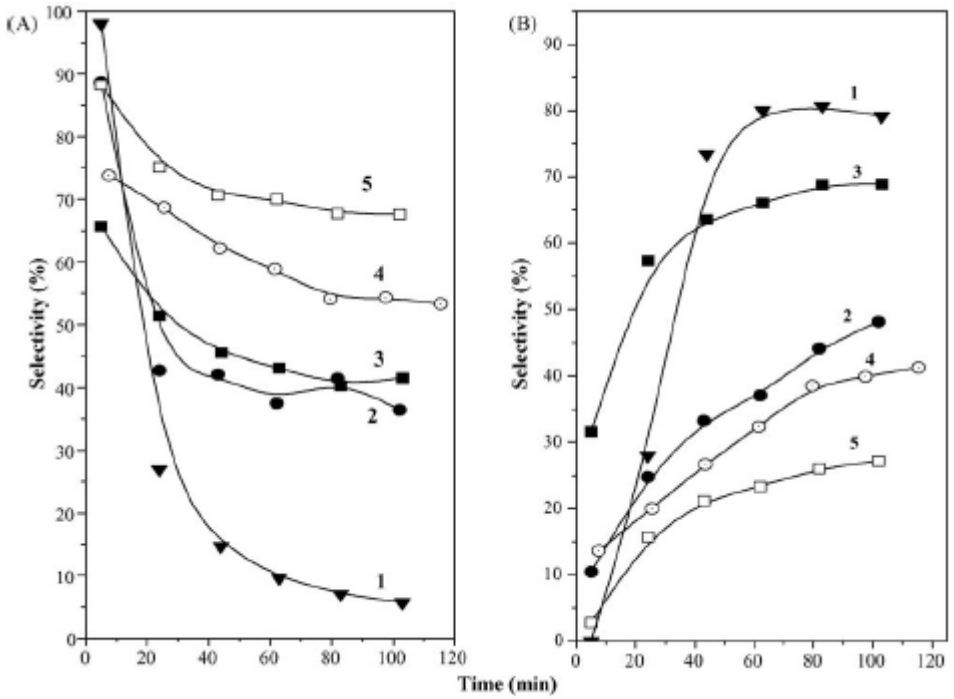

Fig. 2.46 Selectivity of H2 (A) and of ethylene (B) in the reaction of ethanol + water at 723 K on 1: 1% Pt/Al2O3; 2: 1%Pd/Al2O3; 3: 1%Ir/Al2O3; 4: 1%Rh/Al2O3; 5: 1% Ru/Al2O3 (*98*).

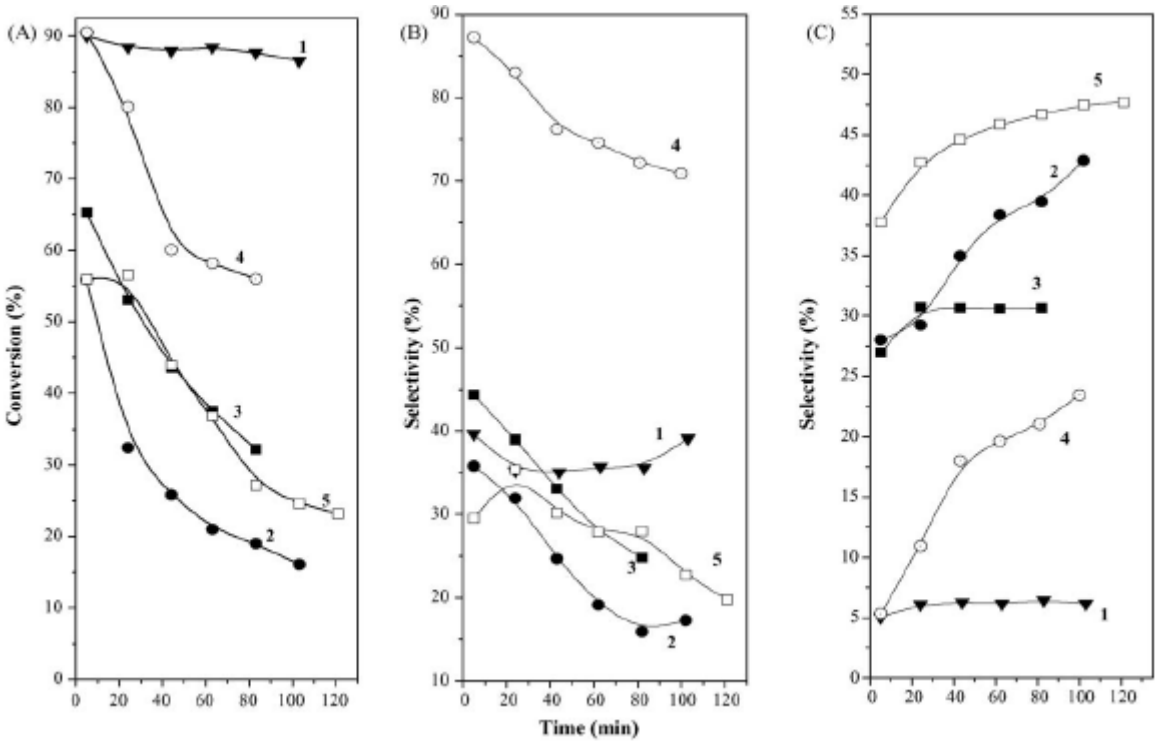

Fig. 2.47 Conversion (A), selectivity of H2 (B) and acetaldehyde (C) in the reaction

of ethanol + water at 723 K on 1: 1% Pt/CeO2; 2: 1%Pd/CeO2; 3: 1% Ir/CeO2; 4: 1% Rh/CeO2; 5: 1% Ru/CeO2 (*98*).

Probably the decrease of H_2 selectivity in the time on stream can be due to poisoning of metal surface (the active surface site for the dehydrogenation of ethanol), consequently the efficiency of the support comes to the forefront.

Besides IR measurements clearly have shown that at the reaction temperature only acetate species are on the surface.

The TPD experiments have revealed that the high temperature desorption stage of adsorbed ethanol depends on the metal. On Rh/Al_2O_3 the acetate species decompose at the lowest temperature and this sample is claimed to have one of the highest hydrogen selectivity.

On Pt/Al_2O_3 the situation is the opposite. They have stated that acetate is located primarily on the support but these groups can poison the reaction. On the basis of these observations they suppose that the acetate groups hindered the migration of ethoxide to the metal, which may cause the decrease of hydrogen formation on the metal sites (*98*).

At higher temperatures (823 and 923 K) the decay of hydrogen was significantly reduced, moreover, at 923 K it could not even be observed.

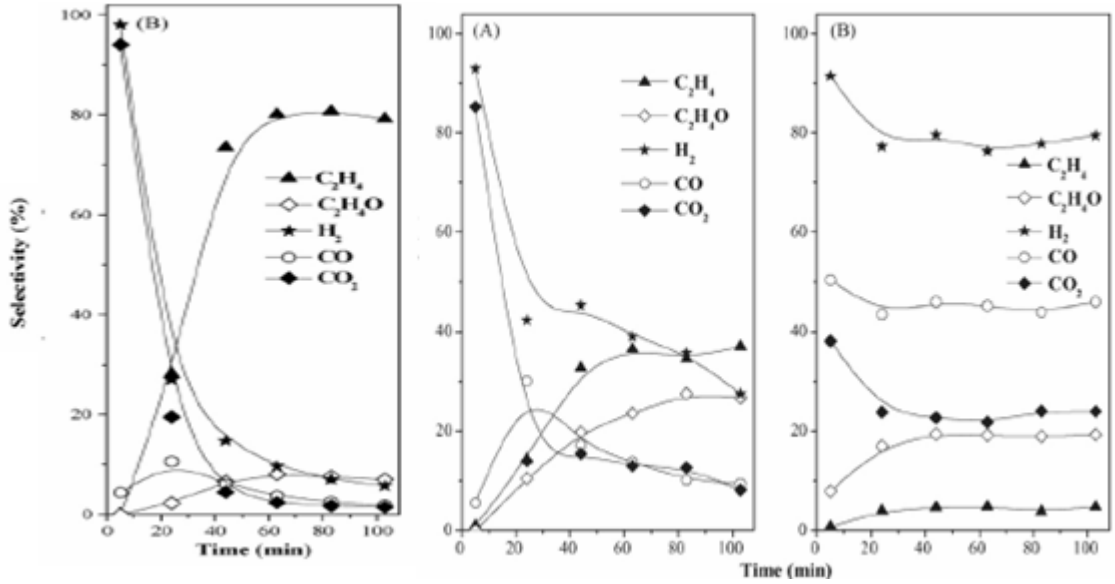

A **B** **C**

Fig. 2.48 The product selectivity of ethanol + water reaction on 1% Pt/Al2O3 at 723 K (A), 823 K (B) and at 923 K (C). The ethanol/water ratio was 1/3 (*96*).

These results clearly show that at lower temperature the surfaces of the catalysts change during the reaction and as a consequence of this process Pt sites are poisoned (*96*).

This trend is similar for Ir, Co and Ni supported on alumina. In fact at higher temperature H_2 selectivity is more stable then at 723 K.

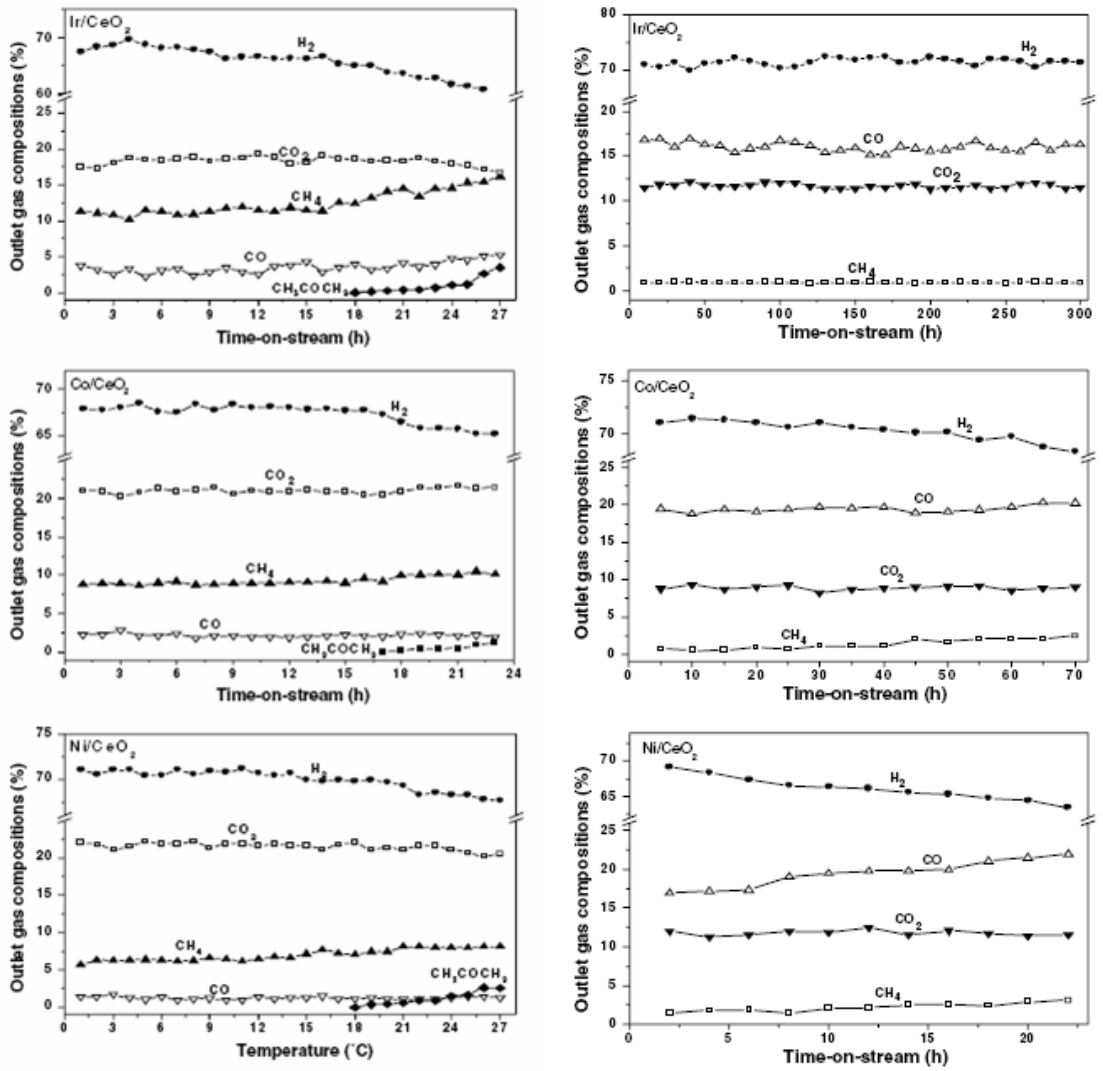

Fig. 2.49 Alteration of the concentrations of H2, CO, CH4 and CO2 with time-on-steam over the M/CeO2 catalysts. Experimental conditions: catalyst: 300 mg (40–60 mesh);H2O:EtOH = 3:1; GHSV = 6000 ml/gh; A) Ir/CeO2 and Ni/CeO2 catalysts at 450 °C, Co/CeO2 catalyst at 500 °C, B) Ir/CeO2 and Ni/CeO2 catalysts at 650 °C, Co/CeO2 catalyst at 700 °C (*99*).

The Ir/CeO_2 catalyst showed rather stable catalytic performance for 300 h time-on-stream without any deactivation. The strong interaction between Ir and CeO_2 effectively prevented the sintering of the highly dispersed Ir particles and also greatly facilitated coke gasification through the high oxygen storage-release capacity of ceria (*99*).

Srinivas et al. have studied ethanol steam reforming on NiO-CeO2-ZrO2 at different composition at 823 K. Sample with Ce/Zr = 1 exhibited a very high catalytic activity over a period of more than 500 h.

Zirconia incorporating in ceria retard the sintering of ceria crystallites because of it facilitates the reduction of Ce^{4+} to Ce^{3+} and preserves the oxygen vacancies which are the source of oxygen storage capacity in ceria based catalyst supports and it explains the major stability.

Also the crystallite size of ceria has a strong influence on the metal dispersion of Ni-Rh catalysts. The catalytic activity for ethanol conversion and H_2 selectivity depends strongly on Rh particle size and dispersion. The smaller the CeO_2 crystallite size, the higher the Rh metal dispersion and consequently the higher the catalytic activity for ethanol conversion and H_2 selectivity.

Adding Ni is claimed to improve the Rh metal dispersion and makes its particle size smaller. These results suggest that Rh is the more active species involved in ethanol reforming and that catalytic activity increases with increasing numbers of active Rh species. Therefore Rh plays a major role in breaking C–C and C–H bonds; compared with Rh, Ni is much less active for EtOH reforming, but the addition of Ni favors the water–gas shift reaction, leading to increased conversion of CO to CO_2 at 723-873 K(*100*).

The presence of a second metal, in addition to Rh, enhances the production of hydrogen from ethanol. Sheng et al. have observed that while Rh is essential for an efficient decomposition of ethanol its presence alone is not sufficient for making hydrogen in reasonable quantities. In the presence of Pt the association reaction of the two H(a) atoms is much faster (*101*).

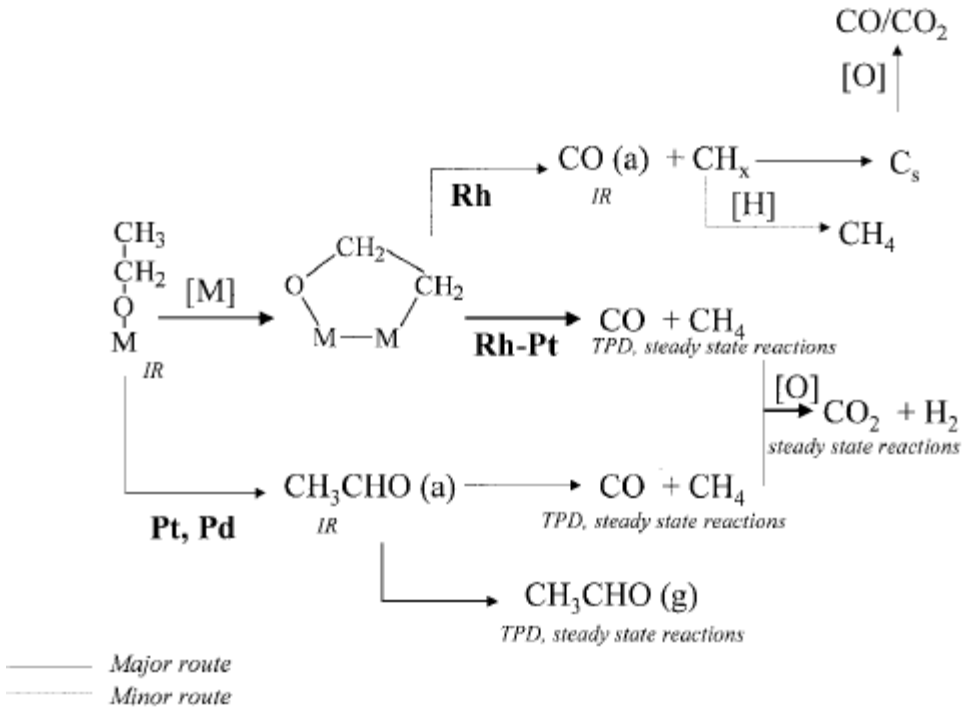

Fig. 2.50 Scheme of ethanol adsorption depends on metal (*101*).

Kugai et al. studied oxidative steam reforming of ethanol over a bimetallic Rh-Ni/CeO_2 catalyst at low temperatures (<723 K) to produce a H_2-rich gas. The presence of O_2 enabled complete conversion of ethanol even at low temperatures (648 K) and reduced the selectivity to CO (*102*). The temperature increases of part of the bed due to combustion reaction has to be taken into account.

Frusteri et al. evaluated catalytic performance of MgO supported Pd, Rh, Ni, and Co for hydrogen production by ethanol steam reforming. Rh/MgO showed the best performance in terms of ethanol conversion and stability, while Ni/MgO exhibited the highest hydrogen selectivity (>95%). Coke formation rate on Rh/MgO was very low as MgO was basic. It was also found that the deactivation was mainly due to metal sintering (*103*).

Depositing Rh on MgAl-based spinel oxide supports exhibited higher basicity, compared with alumina-supported Rh, whereas the surface acidity was strongly reduced, resulting in improved stability (*104*).

The kinetic of coke formation is not depending upon the support nature only, but also from the nature of active metal. In particular, on Pd/MgO higher coke formation rate respect to Ni/MgO were observed, while on Rh/Al_2O_3, in spite of the presence of alumina coke forms with very low rate (*105*).

Fatsikostas and Verykios have studied Ni catalysts supported on Al_2O_3 or La_2O_3 and they find that γ-Al_2O_3 seems to promote primarily the dehydration reaction of

ethanol, probably via ethoxy or acetate species producing ethylene which leads to polymeric carbonate species, at relatively low temperatures.

On the other hand, La_2O_3 seems to promote primarily the dehydrogenation reaction and, to a smaller extent, the dehydration reaction. La_2O_3 in stabilizing the catalyst activity by decorating the Ni particles with a thin film of lanthanum oxycarbonate species, which acts as a cleaner of metallic surface of carbon deposits.

$La_2O_2CO_3 + C \rightarrow La_2O_3 + 2CO$

At 923 K and S/C = 3, Ni/La_2O_3 catalyst resulted to be the most stable and active system but hydrogen selectivity lower than 77% was obtained due to the formation of appreciable amounts of CH_3CHO and CH_4 (*105*).

When both materials (γ-Al_2O_3 and La_2O_3) are used as catalyst carriers in the form of mixed oxide, a combination of catalytic properties is observed. Thus, dehydration and dehydrogenation reactions compete over a large temperature range. It should also be noted that La_2O_3, a basic material, may be adsorbing on the acidic sites of γ-Al_2O_3, thus reducing the dehydration activity of the latter.

Thus, in the La_2O_3-Al_2O_3 carrier, the dehydrogenation reaction competes favourably with the dehydration reaction, although the surface area of Al_2O_3 is significantly higher than that of La_2O_3 .

In the presence of nickel, the catalysts become significantly more active, and there is a shift of conversion to lower temperatures. Pure nickel causes bond breaking of ethanol in the following order: O–H, $–CH_2–$, C–C, and $–CH_3$. Therefore, it should be assumed that the key reaction for catalysts tested at temperatures up to 300 °C is the dehydrogenation of ethanol to surface adsorbed CH_3CHO_{ads}. The following scheme (*106*) seems to describe best the transformations of CH_3CHO_{ads} at this temperature range:

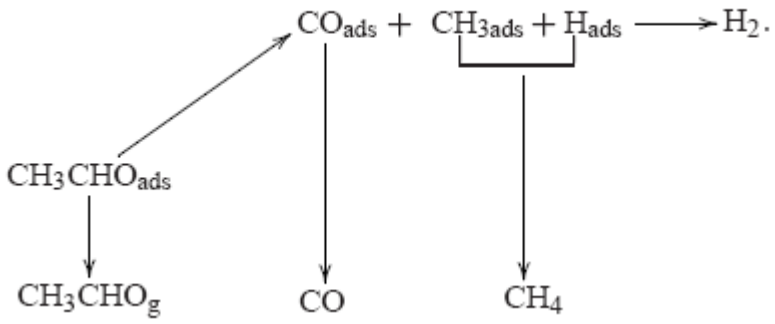

Fig. 2.51 CH_3CHO decomposition pathway (*106*).

The addition of Cu to Ni catalyst improves the activity of the catalyst, in fact Morgenstern and Fornango (*107*)showed that Cu-plated Raney nickel is an active and stable catalyst for low temperature steam reforming of ethanol (523–573 K). and

Luengo et al. reported ethanol reforming over Ni/Cu/Cr/Al_2O_3 catalyst at 573-823K and suggested that the catalytic effect was more pronounced at lower temperatures (*108*)

Fierro et al. found that a Ni–Cu/SiO_2 catalyst is more active and selective towards H_2 production in bio-ethanol oxidative steam reforming than Ni/SiO_2 which rapidly deactivates due to coke formation. In previous studies, these researchers presented optimization of oxidative reforming of ethanol over Ni–Cu/SiO_2 (*109*).

Marino et al. reported that Cu/Ni/K/-Al_2O_3 catalyst exhibited acceptable activity, stability and selectivity to hydrogen at 573 K. A reaction network that accounted for the formation of acetic acid and diethyl ether during reaction was proposed (*110*):

$C_2H_5OH + H_2O \rightarrow C_2H_4O_2 + 2H_2$

$2C_2H_5OH \rightarrow (C_2H_5)_2O + H_2O$

In this system, Cu is the active agent and promotes fast ethanol dehydrogenation to acetaldehyde, Ni promotes C-C bond rupture of acetaldehyde to produce CH_4 and CO and increases hydrogen selectivity while K neutralizes acidic sites of Al_2O_3, avoids formation of products such as ethylene and diethyl ether and improves the general performance of the catalyst.

The benefit of using of K doped catalyst to avoid the formation of carbon filaments with Ni at tip is identified in the electronic enrichment of the active phase which reflects both in depressing the Boudouard reaction and the hydrocarbon decomposition activity which are considered the main responsible in the coke formation during reforming reactions (*111*). As a consequence, the concentration of carbon on metal Ni surface never reach high value and carbon diffusion trough Ni particle is limited.

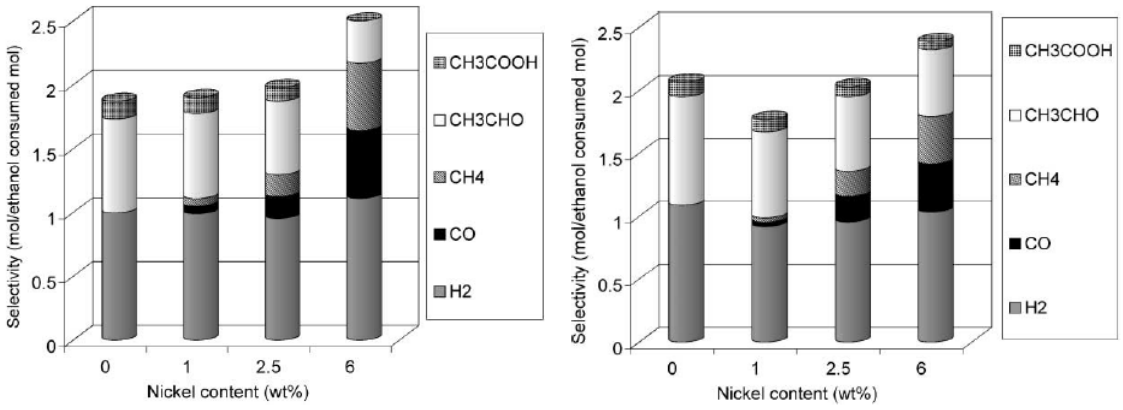

Fig. 2.52 Effect of Ni loading on selectivity for catalyst with A) 3 wt% Cu and B) 6 wt % Cu.

Marino et al. have reported the formation of CuNiAl hydrotalcite type compounds during catalyst preparation. The addition of Ni favored the formation of these compounds thereby suggesting metal-support interaction (*112*).

The increase in the calcination temperature of the precursors produces a strong interaction between nickel and aluminium, decreasing nickel reducibility and the selectivity to C1 compounds. Calcination of Cu-Ni precursors in the range of 673–1073 K produces a CuO segregated phase and/or a phase of copper called "surface spinel". The just reduced bimetallic precursors show the best catalytic performance and an acceptable stability, similar to that of calcined precursors, for the ethanol steam reforming reaction at 573 K (*112*).

A possible mechanism in absence of water over Cu-Ni catalysts is proposed by Marino et al.:

$CH_3CH_2OH + \sigma\,Cu \rightarrow CH_3CH_2OH*$

$CH_3CH_2OH* \rightarrow CH_3CHO + H_2 + \sigma\,Cu$

$CH_3CH_2OH + \sigma\,Ni \rightarrow CH_3CH_2OH**$

$CH_3CH_2OH** \rightarrow CH_3CHO** + H_2$

$CH_3CHO** \rightarrow CH_4 + CO + \sigma\,Ni$

$CH_3CHO** \rightarrow CH_3CHO + \sigma\,Ni$

The behaviour of the CH_3CHO as an intermediary product could be interpreted from this mechanism, but the selectivity changes that they have observed in the presence of water cannot be explained from the stated mechanism.

The dissociative adsorption of water through a redox mechanism has been widely reported for several Cu/Zn/Al catalysts used in the WGS reaction (*113*). Taking into account this background, they have postulated that the presence of water should give an alternative pathway for the ethanol conversion:

$CH_3CH_2OH + \sigma\,Cu \rightarrow CH_3CH_2OH*$

$H_2O + \sigma\,Cu \rightarrow H_2O*$

$H_2O* + \sigma\,Cu \rightarrow HO* + H*$

$HO* + \sigma\,Cu \rightarrow H* + O*$

$H* + H* \rightarrow H_2 + 2\,\sigma\,Cu$

$CH_3CH_2OH* + O* \rightarrow CH_3CHO + H_2O + 2\,\sigma\,Cu$

$CH_3CH_2OH* + O* \rightarrow CH_3COOH + H2 + 2\,\sigma\,Cu$

This additional mechanism should explain the increase of the hydrogen and acetaldehyde selectivity (approximately 20%) observed in presence of water.

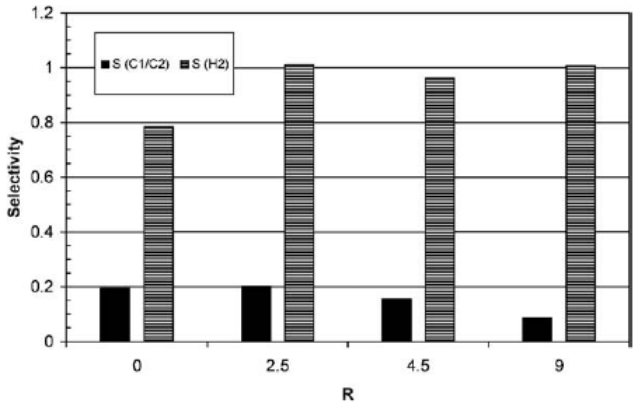

Fig. 2.53 Selectivity as a function of S/C (R=S/C)

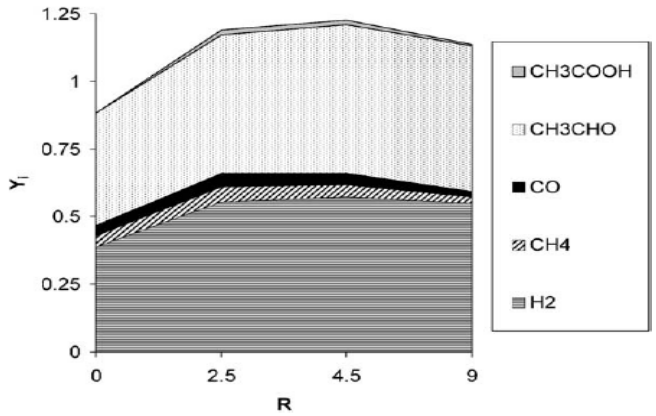

Fig. 2.54 Product distribution as a function of S/C (R=S/C)

Velu et al. have used Cu–Ni–Zn–Al mixed metal oxide catalysts in oxidative steam reforming of bio-ethanol. They found that the dehydrogenation of ethanol to acetaldehyde is favored by Cu-rich catalysts while the introduction of Ni leads to C—C bond rupture producing CO, CO_2 and CH_4 (*114*).

Also Barroso et al. have studied catalysts base on Ni-Zn-Al, they have found that the catalysts were very active and a complete conversion was obtained at 773 and 873 K. The selectivity in H_2 and CO is high (85%) (*115*).

Cavallaro and Freni (*116*) investigated steam reforming of ethanol over $CuO/ZnO/Al_2O_3$ and found that the catalyst exhibited good activity with CO, CO_2 and H_2 as the main products above 630 K. The steam reforming of ethanol over CuO/CeO_2 to produce acetone and hydrogen has also been studied (*117*). The formation of acetone could be described by following reaction:

$2C_2H_5OH + H_2O \rightarrow CH_3COCH_3 + CO_2 + 4H_2$ (25)

Amphlett et al. (*118*)suggested that CuO/ZnO, CuO/SiO_2, CuO/Cr_2O_3 or $CuO/NiO/SiO_2$ might prove promising for reforming of ethanol–water mixtures at 623–723 K. Machado et al. (*119*) studied the performance of Cu/Nb_2O_5 and $Cu/Nb_2O_5/Al_2O_3$

catalysts in ethanol steam reforming. The dispersion of Nb_2O_5 on Al_2O_3 improved catalyst action.

Cobalt is another non noble metal catalyst under extensive investigation as supported Co could break C-C bond. Haga et al. studied the catalytic properties of Co among other metals and found that selectivity to H_2 was in the order Co >Ni >Rh > Pt, Ru, Cu. In another study, they found that the supports vastly influenced the properties of Co catalysts. The formation of H_2 decreased in the order: Co/Al_2O_3 > Co/ZrO_2 > Co/MgO > Co/SiO_2 > Co/C (*120*).

The Co/Al_2O_3 catalyst exhibited a very high selectivity to H_2 (67% at 673 K) by suppressing methanation of CO and decomposition of ethanol. Similarly, Cavallaro et al. found that Co/MgO is more resistant to coke formation than Co/Al_2O_3 at 923 K (*121*).

Co/ZnO showed the best performance, in terms of activity, selectivity to H_2 and stability. Although Al_2O_3 inhibited cobalt reduction, ZnO promoted it. At 723 K the Co/ZnO catalysts was able to convert C_2H_5OH completely with a H_2 selectivity of 80% or even 90% after 50 h time on stream.

Co/ZnO characteristics were influenced by the cobalt precursor and pretreatment. The use of Co(CO)8 as precursor produced a highly stable catalyst that enabled the production of CO-free H_2 at low temperatures (623 K). with a C_2H_5OH conversion of 100% and a H_2 selectivity of 73 %, with no C2 or C3 species produced, and only small amounts of CH_4 (*122*). The catalyst also did not produce any CO. The aforementioned stoichiometry suggests that Co/ZnO catalyst promotes the C_2H_5OH steam reforming reaction via the H_2 and CO_2 pathway.

However, Co/ZnO showed a considerable amount of carbon deposition after the reaction.(*123*) This caused deactivation of the cobalt catalysts. The deactivation rate was dependent on the support used and the temperature (*122*). The addition of 0.98 wt % of sodium to the Co/ZnO catalyst improved the catalytic performance, in terms of the H2 yield and stability, compared to unpromoted catalyst (*124*).

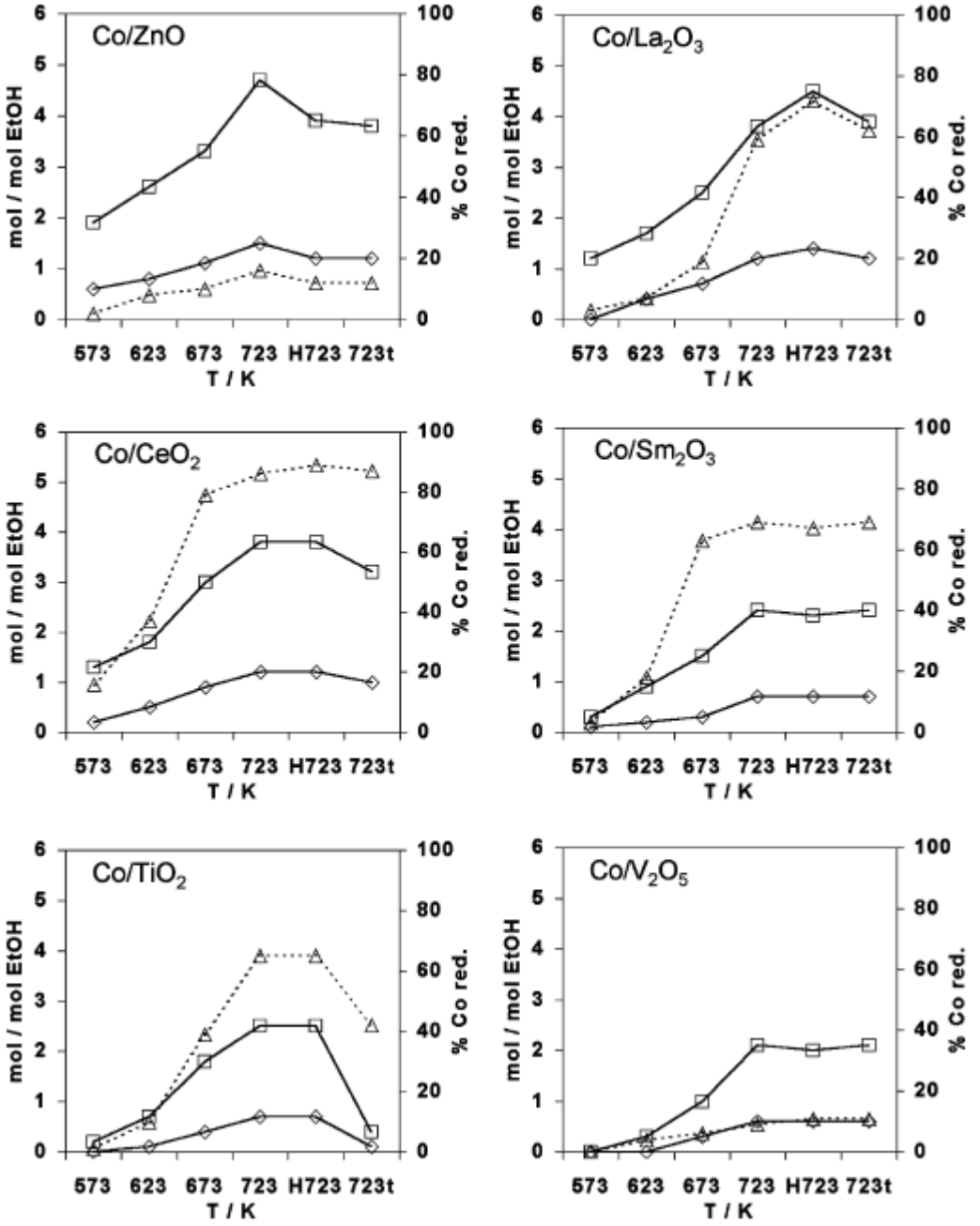

Fig. 2.55 Extent of cobalt reduction (%) () CO2, () H2 produced as a function of ethanol steam reforming temperature . H723 refers to data at 723 after hydrogen treatment at the same temperature. After that, and following 8h on stream, 723t data were obtained.

Kaddouri and Mazzocchia reported high catalytic activity of Co/SiO_2 and Co/Al_2O_3 for steam reforming of ethanol and concluded that the product distribution was dependent on both the nature of the support and the method of catalyst preparation, thereby suggesting metal–support interaction (*125*).

Batista et al. studied ethanol steam reforming over Co/Al_2O_3 and Co/SiO_2. The catalysts showed average conversion higher than 70% at 673 K. The metal loading influenced ethanol conversion and product distribution (*126*).

Different authors have observed significant benefits in performing steam reforming of ethanol in the presence of oxygen, both in terms of activity and catalysts stability (*127*). Oxygen contributes to oxidize carbon residues formed during reaction maintaining free the metal active surface. The behaviour of Ni/MgO and Ni/CeO2 catalysts in reforming of bio-ethanol (Fig. 2.56) in the presence of steam (SR) and oxygen (ATR) have shown the fundamental role exerted by oxygen which, further to contribute to depress coke formation it enhances both catalyst activity and stability.

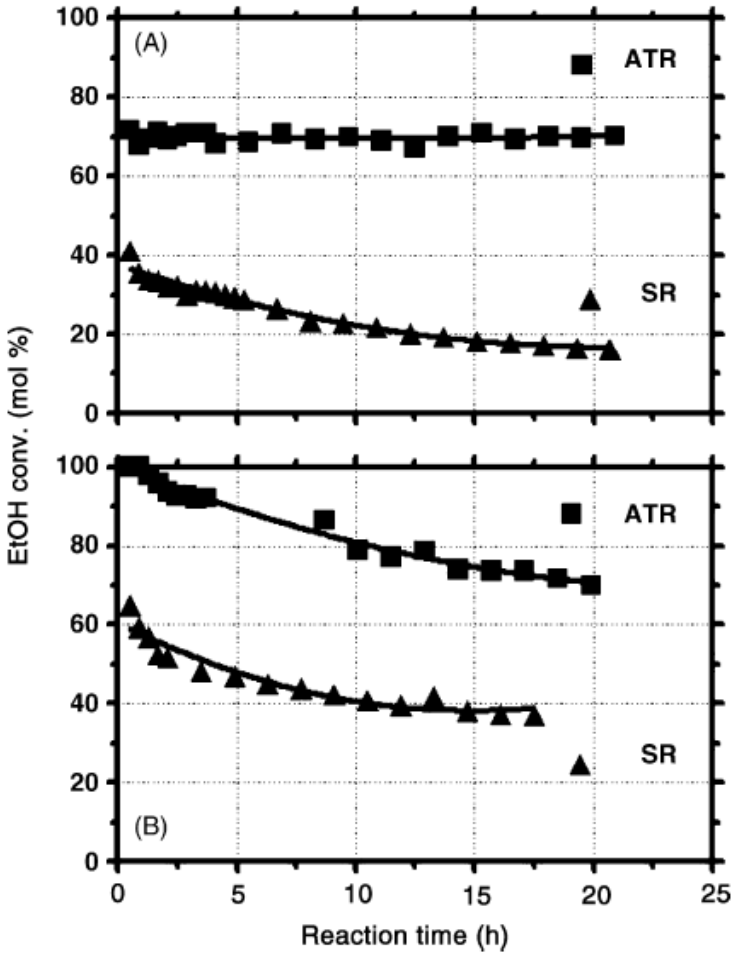

Fig. 2.56 EtOH conversion vs. reaction time on (A) Ni/CeO2 and (B) Ni/MgO catalysts. A comparison between SR and ATR conditions: *T*R = 923K.

In the steam reforming of ethanol at high temperature Rh based catalysts shows the best performance both in terms of specific activity and catalyst stability. However, a perplexity remains concerning the extremely high activity in methanation reaction, which negatively reflects on the hydrogen productivity (CH_4 selectivity higher than 5-10%).

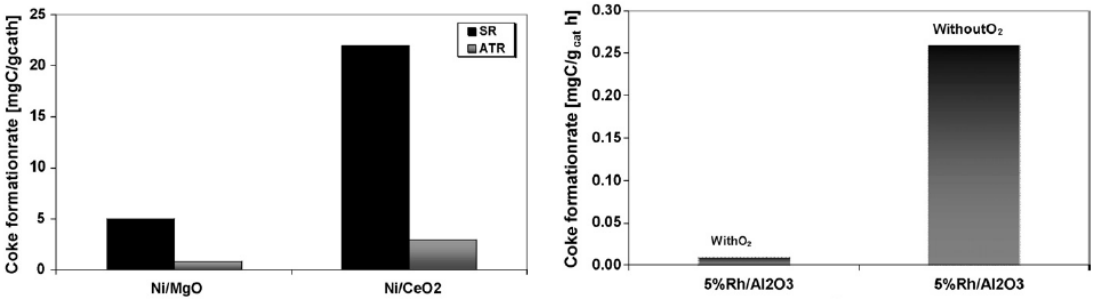

Fig. 2.57. Steam reforming of bio-ethanol over Rh/MgO, Ni/MgO and Ni/CeO2 catalyst: coke formation rate in the absence and in the presence of oxygen in the reaction stream.

Pd resulted to be less active than Rh and in addition is not so active in methane conversion and this negatively affects the hydrogen productivity (*121*).

Ru-containing catalysts supported on cordierite monolith has been recently proposed for the hydrogen production by partial oxidation of ethanol (*121*). Catalyst seems to be enough stable but too high selectivity to CH_4, C_2H_4 and C_2H_6 were found.

2.4.3 Catalysts

The best catalyst for steam reforming of ethanol requires a surface capable of breaking the carbon–carbon bond. There are at least two further requirements for the catalyst: it must be capable of selectively oxidizing both carbon atoms to CO or CO_2 and, in the case of hydrogen production, it must not be active (or must be relatively inactive) for the oxidation of H_2 to H_2O.

Other requirement of the catalyst is the stability in the reaction conditions. In steam reforming reaction, the two factors that largely govern the stability of the catalyst are coke formation and metal sintering(*97*).

Different catalytic system have been studied in this reaction using different metals and various supports(*115*).

Good catalysts for ethanol steam reforming are metals like Co, Ni, Rh, Ru, Pd, Ir and Pt that promote the dehydrogenation to acetaldehyde and prevent the dehydration to ethylene. At certain temperature decompose the organic substrate to C* and H* (dissociative adsorption) getting close to thermodynamic equilibrium.

Rh is significantly more active and selective compared to Pt, Pd, but it has limited water gas shift (WGS) activity (*97*). In comparison, Pt has relatively higher WGS activity. Pt also has good thermal stability (*97*).

Ni is the catalyst of choice in hydrogenation and dehydrogenation reactions due to its high activity and low cost. Ni-based catalysts have high steam reforming activity. Ni has limited WGS activity. Ni possesses hydrogenation activity and hence it may help

in combining adsorbed H atoms on the catalyst surface to form molecular hydrogen, but it forms CH_4 by metanation (*97*).

Cu has limited steam reforming activity, it is a good dehydrogenation catalyst. Cu has high WGS activity (*97*).

Co-based catalysts have exhibited good performance for H_2 production in steam reforming of ethanol. However, supported Co catalysts are adversely affected by metal sintering and surface Co oxidation and hence are not suitable for use at high temperatures (*97*).

Ru is another versatile catalyst having high activity in steam reforming of hydrocarbons.

So the activity order of metals is Rh > Pd > Ni = Pt. When ceria/zirconia was the support ethylene formation was not observed and the order of activity at higher temperature was Pt ≥ Rh > Pd. Aupretre et al. (*128*) studied the effect of both the metal and the support in the steam reforming of bio-ethanol. They found that the hydrogen yield on alumina-supported metal catalysts decreased in the following order at 973 K: 9.7% Ni > 1% Rh > 0.5% Pd > 1% Pt > 9.1% Cu = 9.8% Zn > 0.67% Ru = 8.7% Fe.

They concluded that the high activity of the metals in the ethanol steam reforming and the poor efficiency in the water gas shift reaction (i.e. also for the reverse WGS reaction) would give active and selective catalysts for ethanol reforming.

Liguras et al. also found that among the low-loaded catalysts, Rh was significantly more active and selective towards hydrogen formation than Ru, Pt and Pd. The catalytic performance of Rh and, particularly, Ru was greatly improved by the increase of metal loading. It was shown that the catalytic activity and selectivity of highly loaded Ru catalysts were comparable to those of Rh (*129*).

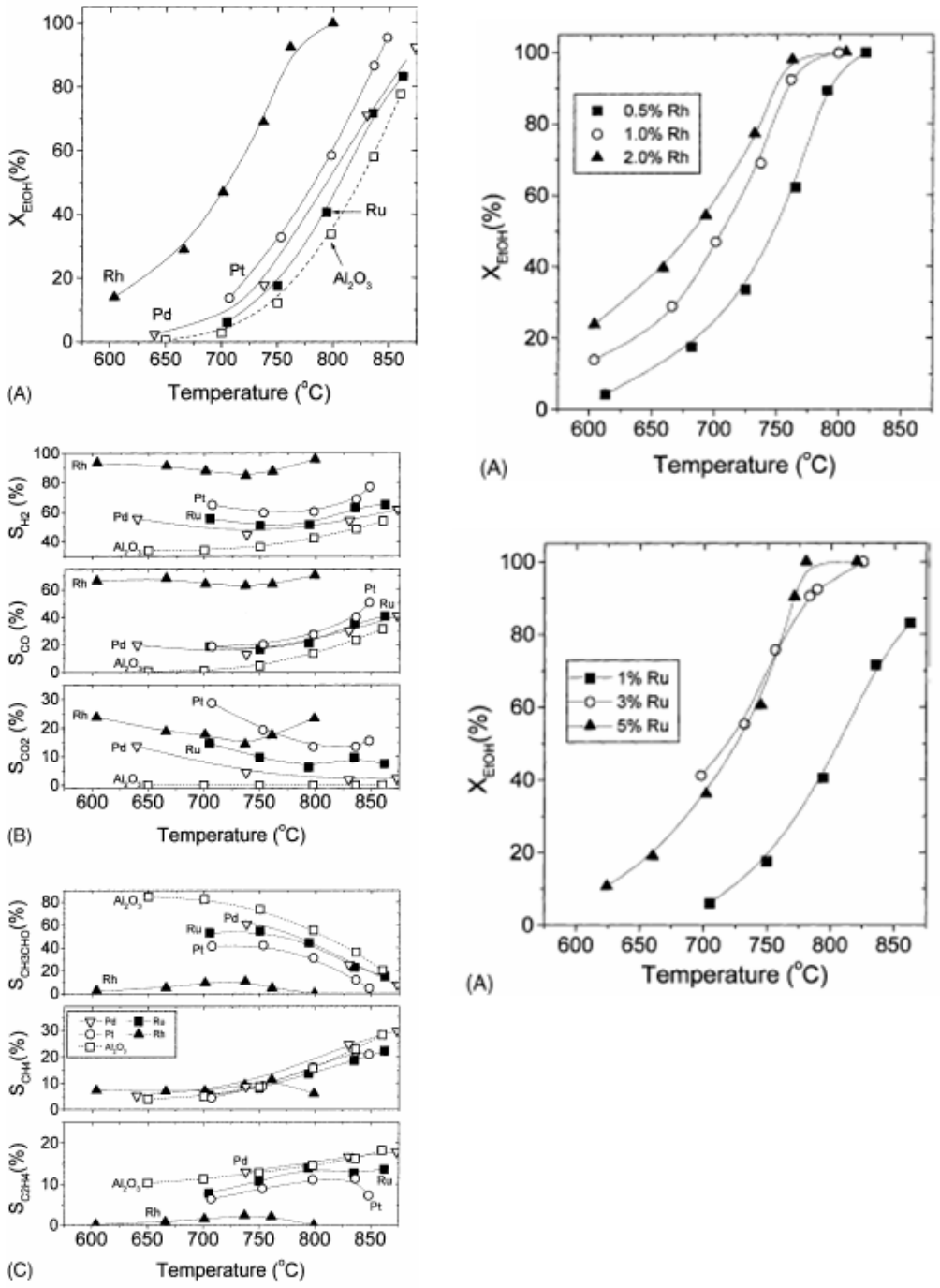

Fig. 2.58 Effect of reaction temperature and metal load on the conversion of ethanol (A), and on the selectivities toward reaction products (B and C) obtained over the 1% Me/Al2O3 catalysts (Me = Pd, Ru, Pt, Rh) and the Al2O3 support.

Rh/MgO showed the best performance in the steam reforming of ethanol at 923 K in terms of activity and stability. It was not so selective, however, towards hydrogen formation (*103*). Kinetic measurements revealed large difference in metal specific activities: Rh sites were 2.3, 3.7, and 5.8 times more active than Pd, Co and Ni sites, respectively (*97*).

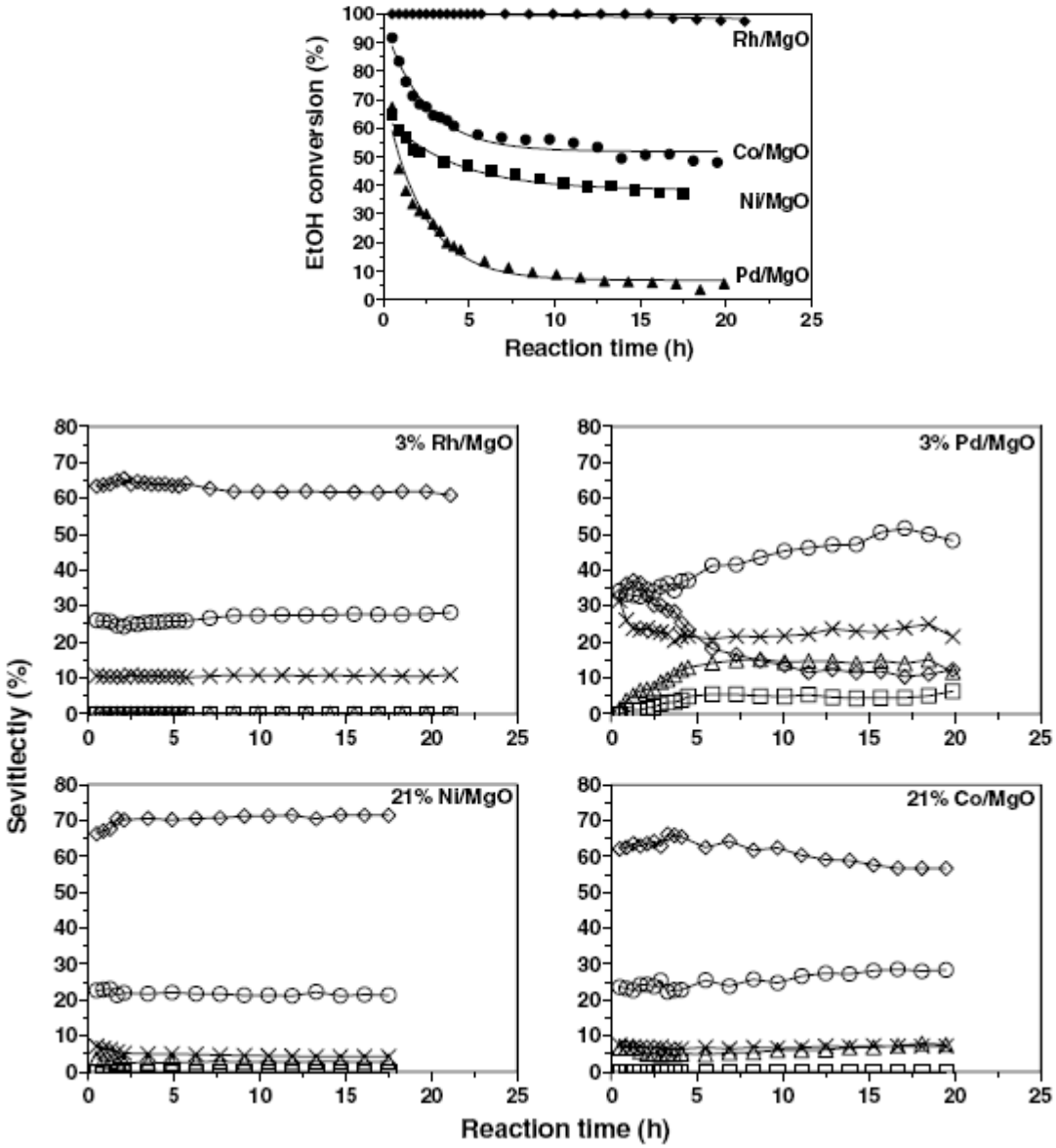

Fig. 2.59 Ethanol conversion and product distribution at 923 K, (◊) CO2, (○) CO, (x) CH_4, (△) CH_3CHO, (□) C_2H_4.

Some studies imply that metals alone do not assist H_2 production significantly. These studies suggest that the performances of metal catalysts could be improved using suitable supporting materials. The nature of the support also plays a key role in determining the selectivity to H_2 (*97*).

Al_2O_3 is commonly used as a support in the steam reforming reaction. However, it is acidic and promotes dehydration of ethanol to ethylene, which in turn polymerizes to form coke on the catalyst surface (*97*).

In contrast, MgO is basic. The highly active Rh catalysts seems no affect from the support (Al_2O_3 or MgO) as far as coke formation is concerned. However, the Co catalyst is more selective and stable when supported on MgO than on Al_2O_3 (*97*).

ZnO also has basic characteristics. In addition, unlike γ-Al_2O_3 and MgO, it also has redox properties. It promotes dehydrogenation to acetaldehyde. The redox properties of ZnO then aid steam reforming . It is extremely selective to the steam reforming of ethanol (*97*).

The catalytic performance and stability of Ni is claimed to be when supported on La_2O_3, compared to Al_2O_3, YSZ and MgO. La_2O_3 does not possess any acidic sites and promotes dehydrogenation to acetaldehyde.

CeO_2 is also basic and has redox properties. It has oxygen storage capacity and hence its presence improves resistance to coke deposition. It also promotes the action of precious metals.CeO_2 is active in the WGS reaction (*97*).

ZrO_2 has both acidic and basic properties and is thermally stable. Addition of ZrO_2 to CeO_2 significantly increases its oxygen storage action, redox properties and thermal resistance.

The addition of alkali like Li, Na and K on Ni/MgO enhanced the catalyst stability mainly by depressing Ni sintering and decreased the amount of coke.

On an acid support the presence of K neutralise acidic sites, therefore alkali avoid the dehydration reactions that lead to products such as ethylene or diethyl ether (*112*).

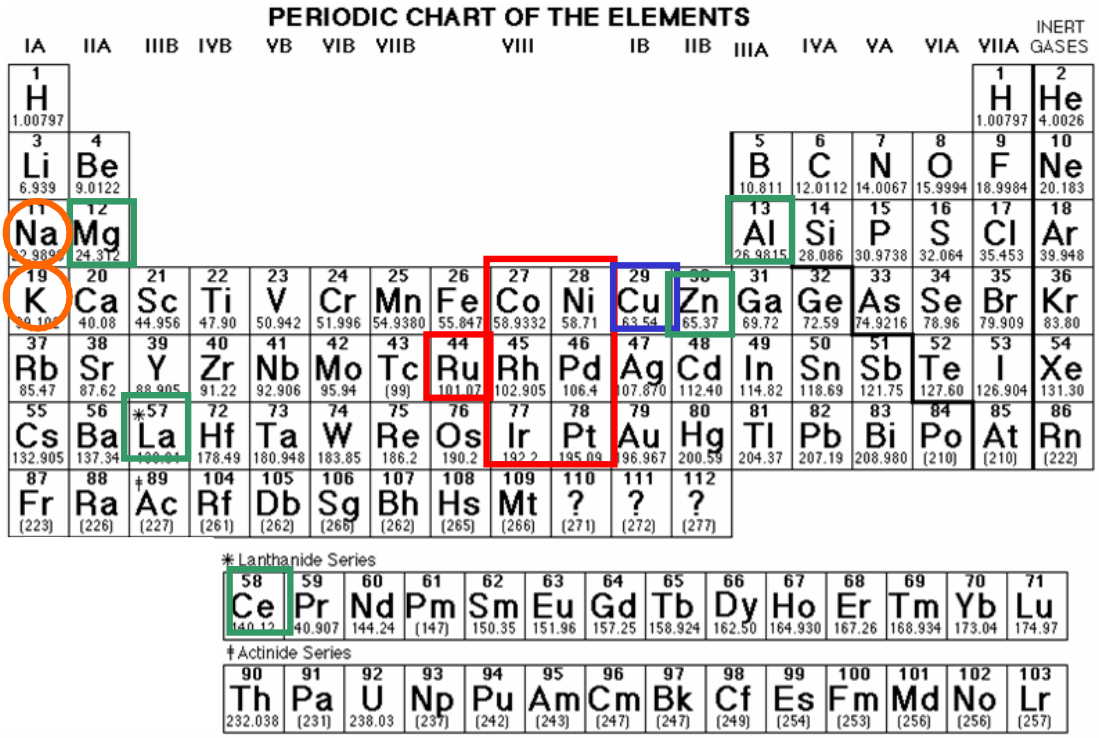

Fig. 2.6o Elemental compounds that are studying as catalyst in ethanol reforming.

2.4.4 Process Considerations

From process engineering point of view: (1) reforming should preferably be carried out at low temperatures and atmospheric pressures to reduce the operating costs; (2) the catalyst should provide high selectivity to H_2 and inhibit CO formation, the formation of by-products such as methane, acetaldehyde and diethyl ether should be minimum; (3) the catalyst must resist coke formation which reduces the number of active sites and hence the reaction rates; (4) the catalyst should not be poisoned by impurities found in the ethanol–water mixtures formed during biomass ethanol source fermentation; (5) the H_2-rich mixture should be purified further to remove CO formed during reaction if the PEMFC should be met.

Catalyst coking strongly depends on the reaction conditions and the properties of the catalyst. Ethylene is a known coke precursor and carbon formation is primarily attributed to its presence in the product stream. However, coke formation can be prevented if ethanol is instead dehydrogenated to acetaldehyde, which has a very low coking activity. Acetaldehyde thus formed can then be subjected to steam reforming. The effectiveness of Cu in dehydrogenation reactions is no novelty. Freni et al. (*130*) studied steam reforming of ethanol over Cu/SiO_2 and found that at temperatures in the range 573-723 K, ethanol conversion was 100% and acetaldehyde and H_2 were the major reaction products. Traces of methane and CO were also detected. Thus, they concluded that at these temperatures, the ethanol dehydrogenation reaction is predominant. At higher temperatures (>773 K), ethylene formation was observed and the selectivity to ethylene increased with increasing temperatures thereby suggesting that the dehydration reaction also takes place at such high temperatures. Nishiguchi et al. (*117*) reported almost selective dehydrogenation of ethanol to acetaldehyde and H_2 over CuO and CuO/SiO_2 in the range of temperatures 473-673 K. Steam reforming of ethanol over CuO/CeO_2 at 533K also led to the formation of acetaldehyde and hydrogen. From the fore goings, it is clear that ethanol can be almost selectively converted to acetaldehyde over Cu-based catalysts at low temperatures. Ni which has high activity in steam reforming will then promote C-C bond rupture in acetaldehyde.

The steam reforming process could therefore be carried out in a two-layer fixed bed catalytic reactor. A schematic diagram of this proposed process is shown in Fig. 2.61. An ethanol–water mixture should be passed at 573-673K over the first layer made of Cu-based catalyst thereby converting ethanol to acetaldehyde.

$C_2H_5OH \leftrightarrows CH_3CHO + H_2$

Ethylene formation can be prevented by working at such low temperatures thereby reducing catalyst coking. Acetaldehyde thus formed may decompose to CH_4 and CO or may undergo steam reforming via the following reactions:

$CH_3CHO \leftrightarrows CH_4 + CO$

$CH_3CHO + H_2O \leftrightarrows 2CO + 3H_2$

$CH_3CHO + H_2O \leftrightarrows CO_2 + CH_4 + H_2$

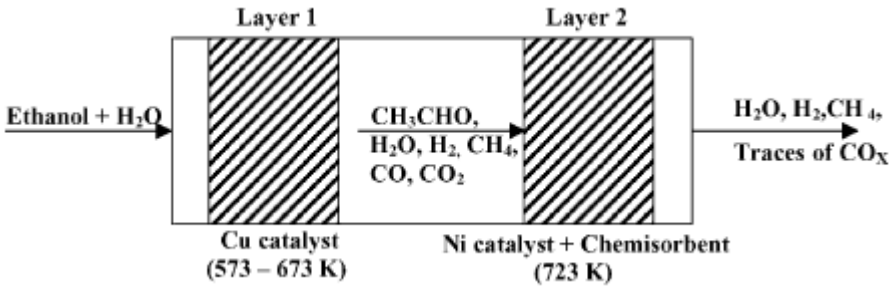

Fig. 2.61 Proposed two-layer fixed bed reactor for ethanol steam reforming.

The following other reactions may also occur:

$C_2H_5OH + 3H_2O \leftrightarrows 2CO_2 + 6H_2$

$C_2H_5OH + H_2O \leftrightarrows 2CO + 4H_2$

However, it is expected that ethanol dehydrogenation reaction will be much faster than the ethanol steam reforming reaction.

Thus, this mixture primarily consisting of acetaldehyde and H_2, excess of water and small amounts of CH_4, CO_2 and CO should then be fed to the second layer made of a mixture of Ni-based catalyst and a chemisorbent. In presence of Ni, the residual acetaldehyde will undergo steam reforming even at low temperatures (around 723 K). The methane steam reforming reaction will however be thermodynamically controlled:

$CH_4 + H_2O \leftrightarrows CO + 3H_2$

The chemisorbent selectively removes CO_2 formed during reaction.

The WGS reaction is reversible and hence the equilibrium shifts to the right and favors the formation of H_2 and CO_2 as products at lower temperatures.

$CO + H_2O \leftrightarrows CO_2 + H_2$

The selective removal of CO_2 from the product stream by chemisorption further enables production of high-purity H_2 at low temperatures along with methane and traces of CO. Further purification by methanation or preferential oxidation should not be necessary. The chemisorbent can then be periodically regenerated by pressure swing adsorption. It should however be noted that the presence of an adsorbent implies a transient operation.

The entire process of ethanol steam reforming coupled with selective CO_2 removal by chemisorption is very promising. In comparison, high temperatures are needed for obtaining high ethanol conversions in conventional steam reforming in a fixed bed reactor packed with the catalyst alone and further purification is necessary.

2.4.5 Alternative solutions

One of the major problem in the steam reforming is the heat transfer boundary layers both on the tube and furnace sides cause heat transfer to be rate limiting in these systems. Possible solutions are autothermal reforming or a catalytic wall reactor.

2.4.5.1 Autothermal reforming of ethanol

Steam reforming is an endothermic process in the absence of oxygen gas and requires energy input to initiate reactions.

Alternatively, hydrogen can be obtained by partial oxidation of ethanol at a temperature of about 773K according to the following reactions.

The addition of different quantities of oxygen (being $\lambda = 1$ the total oxidation stoichiometric amount) can change the enthalpy of the reaction moving it endo to exothermic reaction.

1)$C_2H_5OH + H_2O \leftrightarrows 2CO + 4H_2$	$\Delta H°_{298} = 256$ KJ/mol^{-1}	$\lambda = 02$)
$C_2H_5OH + 1/2O_2 \leftrightarrows 2CO + 3H_2$	$\Delta H°_{298} = 57$ KJ/mol^{-1}	$\lambda = 0.17$
3) $C_2H_5OH + O_2 \leftrightarrows CO_2 + CO + 3H_2$	$\Delta H°_{298} = -226$ KJ/mol^{-1}	$\lambda = 0.33$
4) $C_2H_5OH + 3/2O_2 \leftrightarrows 2CO_2 + 3H_2$	$\Delta H°_{298} = -509$ KJ/mol^{-1}	$\lambda = 0.50$
5) $C_2H_5OH + 3O_2 \leftrightarrows 2CO_2 + 3H_2O$	$\Delta H°_{298} = -1368$ KJ/mol^{-1}	$\lambda = 1$

It is to be noted that the 2:1 = ethanol : oxygen ratio is still endothermic.

However, hydrogen selectivity of ethanol partial oxidation is generally low. In order to enhance hydrogen production, autothermal reforming can be applied. Autothermal reforming, also called oxidative steam reforming, is a combination of ethanol oxidation and steam reforming. The total reaction of autothermal reforming of ethanol can be written as

$C_2H_5OH + 2H_2O + 1/2O_2 \rightarrow 2CO_2 + 5H_2$ $\Delta H°_{298} = -50$ KJ/ mol

This reaction be described by reactions number plus twice WGS is indeed exothermic. This reaction indicates that the autothermal reforming not only attains thermally sustained operation, but also maximizes hydrogen production.

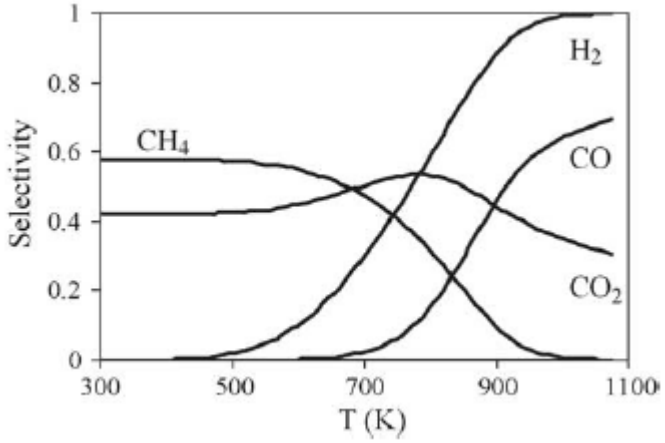

Fig. 2.62 Effect of reactor temperature on equilibrium selectivities to the reaction products for the oxidative steam reforming of ethanol (O2/EtOH = 0.68 and H2O/EtOH = 1.6; pressure= 1 atm).

The ethanol conversion and hydrogen selectivity by autothermal reforming of ethanol vary greatly with the type of catalyst, support and oxygen/ steam/ethanol molar ratios. Autothermal reforming is advantageous as coke formation is greatly inhibited by oxidation. Thus, long-term stable operation can be achieved.

Several studies have reported hydrogen production by autothermal reforming of ethanol over Rh-Ce (*131*), $Cu_{1-x}Ni_x$ ZnAl-mixed metal oxide (*132*), Pt/Al_2O_3 (*133*), Ni-Rh/ CeO_2 (*100*), and Pd/ZnO (*134*) catalysts.

2.4.5.2 Catalytic wall reactors

Other possibility to solve the problem of heat transfer is to eliminate the heat transfer boundary layers by coupling the combustion and reforming reactions catalytically on the opposite sides of a thin wall. The catalytic wall reactor (CWR) increases the heat transfer coefficient by 200 times when compared to a traditional steam reforming reactor (*135*).

Finally, the flat plate CWR allows easy scaling because exothermic and endothermic channels can be alternated to produce a desired amount of hydrogen. A flat plate CWR where methane combustion is coupled to methane steam reforming followed by water–gas shift has been demonstrated in Fig. 2.63.

Those catalytic wall reactors have had problems with material stability that limited maximum temperatures to<800 °C .

Another configuration for a CWR is the concentric tube reactor, which has tested for the homogeneous dehydration of ethane to ethylene (*136*).

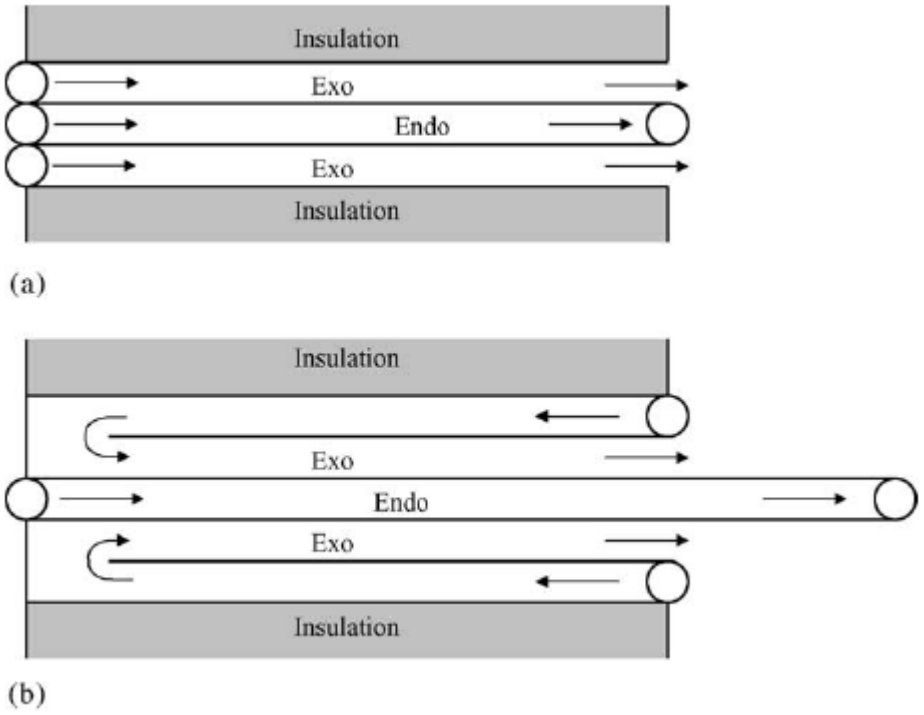

Fig. 2.63 Schematic diagrams of the flat plate configuration CWR (a) and extended CWR (b). The arrows show the direction of flow. The label "Endo" indicates the channel in which the ethanol–water mixture flows. The label "Exo" indicates the channel in which the combustion mixture flows. All channels were 5 cm wide and 8 cm long except for the extended channel in the extended CWR, which was 13 cm long. The channels were nominally 4 mm in height.

2.5 Catalysts obtained from hydrotalcite (HT) type precursor

Anionic clays or layered double hydroxides (LDHs) are lamellar mixed hydroxides with interlayer spaces containing exchangeable anions with general formula:

$$[M^{2+}_{(1-x)}M^{3+}_{x}(OH)_2]^{b+} (A^{n-}_{b/n})\ mH_2O$$

This class of compounds, also called hydrotalcite like compounds (HTlcs), are relatively inexpensive to prepare in the laboratory scale (*137*). The most interesting properties are the homogeneous cation distribution and the ion exchange capacity in the precipitates. In addition, other important properties of the oxides obtained by calcination are (*138*):

(1) high surface area,

(2) basic properties,

(3) formation of homogeneous mixture of oxides with very small crystal size, stable to thermal treatments, which by reduction form small and thermally stable metal crystallites,

(4) "memory effect", which allows the reconstruction, under mild conditions, of the original hydrotalcite structure when contacting the product of the thermal treatment with water solutions containing various anions.

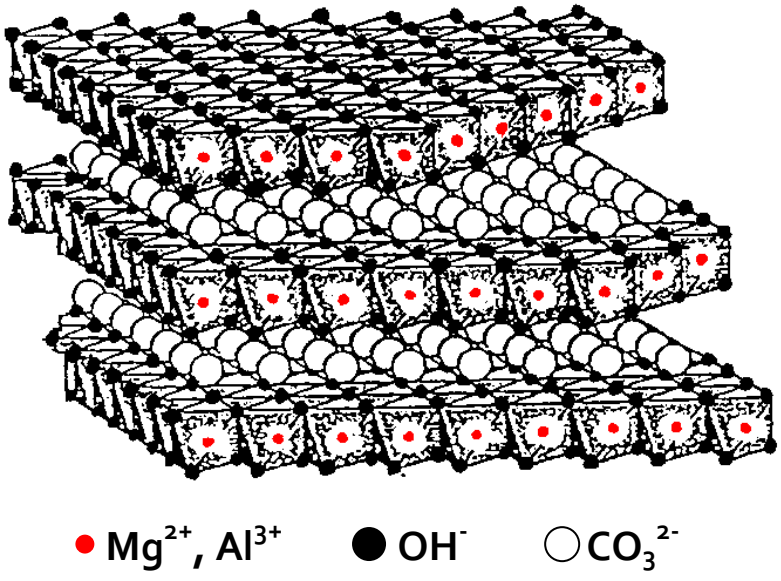

Fig. 2.64 Crystal structure of hydrotalcite-like precursor.

To understand the structure of these compounds, it is necessary to start from the structure of brucite [$Mg(OH)_2$], where octahedra of Mg^{2+} (6-fold coordinated to OH^-) share edges to form infinite sheets. These sheets are stacked on top of each other and

are held together by hydrogen bonding (Fig. 2.65). When Mg^{2+} ions are substituted by a trivalent ion having a suitable ionic radius (such as Al^{3+} for hydrotalcite compounds), a positive charge is generated in the hydroxyl sheet. This net positive charge is compensated by $(CO_3)^{2-}$ anions, which lie in the interlayer region between the two brucite-like sheets, In the free space of this interlayer the water of crystallization also finds a place.

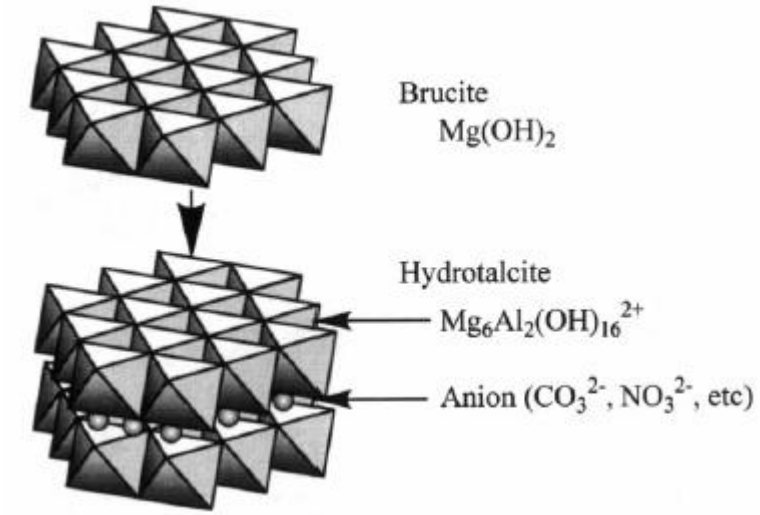

Fig. 2.65 Crystal structure of hydrotalcite-like precursor.

The hydrotalcite-derived catalysts (ex-HT), containing carbonates as interlayer anions, have already been reported as effective catalysts in the production of synthesis gas, using as active phase Ni, Rh and Ni/Rh. The characterization of these catalysts has revealed that the structure is made of MgO type and spinel type phases containing Rh and/or the Ni, which can be extracted to form rather stable metal particles. High activity may be due to the highly dispersed Ni metal particles. Mg-Al hydrotalcite precursor, in which a part of the Mg sites were substituted by Ni, decomposed to Mg(Al)O mixed oxide still containing Ni^{2+} at the Mg^{2+} site. When the mixed oxide was reduced, Ni^{2+} was reduced to Ni^0, migrated to the surface, and crystallized to form fine Ni metal particles on Mg(Al)O mixed oxide as the support (Fig. 2.66). Takehira (*138*) observed that the crystal growths of both Ni metal and $MgAl_2O_4$ spinel after CPO reaction for 560 h, no decline was observed in the activity during the reaction under space velocity of 1.156 $*10^4$ mL h^{-1} g-cat^{-1}. TEM observation of the catalyst after the reaction for 560 h still showed finely dispersed Ni metal particles together with those of large size. The H_2 adsorption measurements still showed a high value of 91.3 μmol g-cat^{-1}, corresponding to a dispersion of 8.5 %. Takehira (*138*) suggests that Ni species was continuously reduced to form fine Ni metal particles during a long term of the reaction. Active metal species is homogeneously distributed from the surface to the bulk of the catalyst particles and therefore a large part of the metal species is still located inside of the particles and cannot work as the active species.

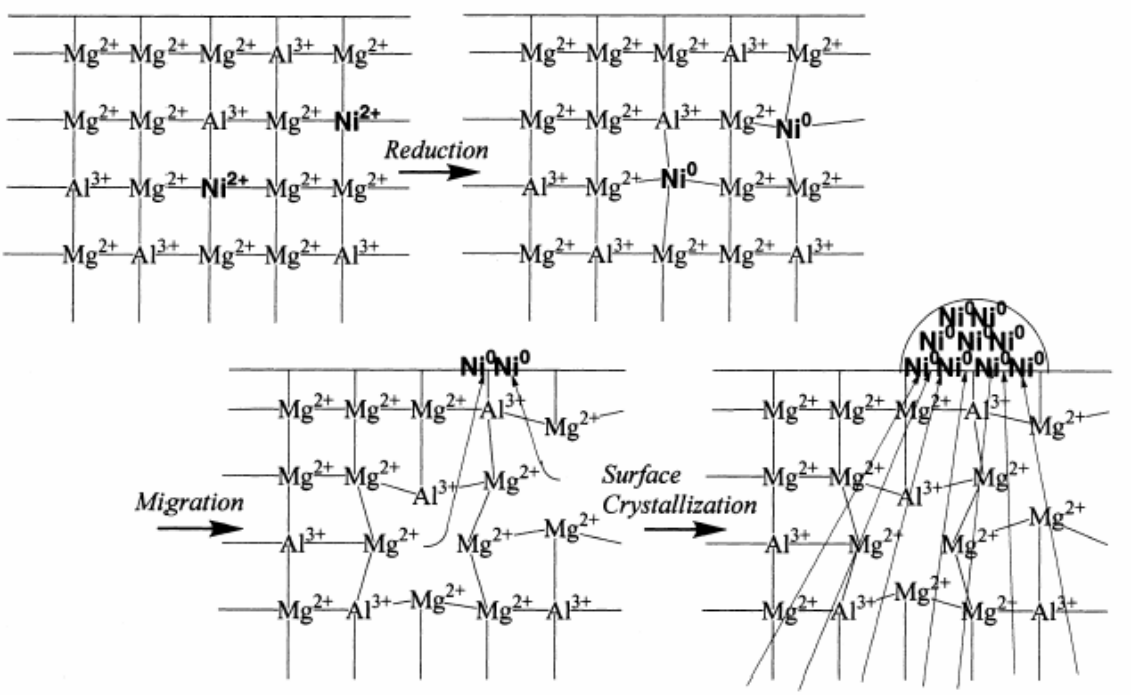

Fig. 2.66 Plausible mechanism of Ni metal crystallization from Mg(Al)O mixed oxide (*138*).

A general property of the ex-HT is that the amount and the nature of M(II) and M(III) modified the ratio between MgO and spinel phases. The reducibility and stability of the Ni catalysts (in which Ni is preferentially present in a solid solution with Mg), are strongly affected by the Mg/Al/Ni ratio due to three main effects (*139*),(*140*):

(1) a low Mg content favors the formation of low active $NiAl_2O_4$,

(2) Ni-rich samples exhibit low Ni^{2+} reduction temperature, and fast deactivation due to the presence of large Ni particles,

(3) a decrease in reducibility of the Ni^{2+} ions is observed for high Mg/Ni ratio, due to the low concentration of Ni in the (Ni/Mg)O solid solution.

These effects limit the activity and stability of Ni containing catalysts that require new formulation. The situation for Rh catalysts is still more complicated, since it is soluted both in the spinel type and in the MgO type phases and the Mg/Al ratio affects the distribution of Rh between the two phases. The presence of other elements can change the correlation between Mg/Al ratio, spinel/MgO phase ratio and the Rh distribution (*141*). In particular, the silicate can form with Mg or Al a specific phase, which can also incorporate Rh and or Ni. Furthermore, the presence of nesosilicate can improve thermal and mechanical resistance at high temperature.

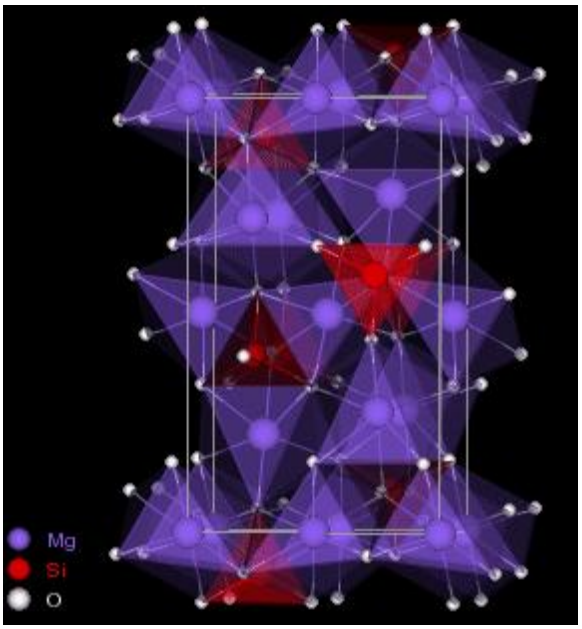

Fig. 2.67 Forsterite-type structure.

The insertion of silicates instead of carbonates as interlayer anion affects the derived structure both before and after calcination (*142*). The silicates remain in the structure forming a new phase characterized by mixed silicate with a forsterite type structure (Fig. 2.67) having formula $Mg_{2-x}M_{2/3x}SiO_4$ (M = Al, Rh), together with a MgO-type structure, other reflections can be attributed to defective spinel type phase. The calcined samples presented high surface area values (100 m^2g^{-1}) also after reaction, confirming the high thermal and mechanical stability of the materials. These catalysts presents higher CH_4 conversion and CO and H_2 selectivity with respect to that with the same formulation, but obtained from an HT containing carbonates, in which the spinel-type phase was present (*143*).

BIBLIOGRAFY

1. Eni. *World gas and oil review;*, 2010.
2. Demirbas, A. Global renewable energy resources. *Energy Sources Part A: Recovery, Utilization and Environmental Effects* **2006,** *28,* 779-792.
3. McDowall, W.; Eames, M. Forecasts, scenarios, visions, backcasts and roadmaps to the hydrogen economy: A review of the hydrogen futures literature. *Energy policy* **2006,** *34,* 1236-1250.
4. Stolten, D., Ed. *Hydrogen and fuel cells.;* Wiley-VCH, 2010.
5. Rostrup-Nielsen, J. R. Fuels and energy for the future: The role of catalysis. *Catalysis Reviews* **2004,** *46,* 247-270.
6. Ferreira-Aparicio, P.; Benito, M. J.; Sanz, J. L. New trends in reforming technologies: From hydrogen industrial plants to multifuel microreformers. *Catalysis Reviews* **2005,** *47,* 491-491.
7. Rustrup-Nielsen, J. R. New aspects of syngas production and use. *Catalysis Today* **2000,** *63,* 159-164.
8. Haryanto, A.; Fernando, S.; Naveen Murali, N.; Adhikari, S. Current status of hydrogen production techniques by steam reforming of ethanol: a review. *Energy & Fuels* **2005,** *19,* 2098-2106.
9. *World Energy Outlook 2008;* International Energy Agency (IEA): Paris, 2008.
10. Martinot, E. *Renewable 2007: global status report.;* REN21 Renewable Energy Policy Network, 2008.
11. Rogner, H. *World energy assessment 2001.;*, 2001.
12. *International Energy Outlook 2010;* US Energy Information Administration, 2010.
13. *Energy Outlook 2030;* British Petroleum: London, 2011.
14. *World Energy Outlook 2010;* International Energy Agency (IEA): London, 2010.
15. Cadenas, A.; Cabezudo, S. Biofuels as sustainable technologies: perspectives for less developed countries. *Technological Forecasting and Social Change* **1998,** *58,* 83-103.
16. Puppan, D. Environmental evaluation of biofuels. *Period Polytech Ser Soc Man Sci* **2002,** *10,* 95-116.

17. Demirbas, A. Biomass resource facilities and biomass conversion processing for fuels and chemicals. *Energy Conversion and Management* **2001,** *42,* 1357–1378.

18. White, L. P.; Plasket, L. G. *Biomass as fuel;* Academic Press: New York, 1981.

19. Demirbas, A. Potential applications of renewable energy sources, biomass combustion problems in boiler power systems and combustion related environmental issues. *Progress in Energy and Combustion Science* **2005,** *31,* 171–192.

20. Volk, T. A.; Abrahamson, L. P.; White, E. H.; Neuhauser, E.; Gray, E.; Demeter, C.; Lindsey, C.; Jarnefeld, J.; Aneshansley, D. J.; Pellerin, R.; Edick, S. Developing a Willow Biomass Crop Enterprise for Bioenergy and Bioproducts in the United States. *Proceedings of Bioenergy 2000* **2000**.

21. Demirbas, A. Progress and recent trends in biofuels. *Progress in Energy and Combustion Science* **2007,** *33,* 1-18.

22. Goyal, H. B.; Seal, D.; Saxena, R. C. Bio-fuels from thermochemical conversion of renewable resources: A review. *Renewable and Sustainable Energy Reviews* **2008,** *12,* 504–517.

23. Luo, Z.; Wang, S.; Liao, Y.; Zhou, J.; Gu, Y.; Cen, K. Research on biomass fast pyrolysis for liquid fuel. *Biomass Bioenergy* **2004,** *26,* 455–462.

24. Gercel, H. F. Production and characterization of pyrolysis liquids from sunflower pressed bagasse. *Bioresource Technology* **2002,** *85,* 113-117.

25. McKendry, P. Energy production from biomass (Part 2): overview of biomass. *Bioresource Technology* **2002,** *83,* 37–46.

26. Bridgwater, A. V.; Peacocke, G. V. C. Fast pyrolysis process for biomass. *Renewable and Sustainable Energy Reviews* **2000,** *1-73,* 4.

27. Demirbas, A. Political, economic and environmental impacts of biofuels: a review. *Applied Energy* **2009,** *86,* S108–S117.

28. United-Nations. The emerging biofuels market: regulatory, trade and development implications. *United Nations conference on trade and development*, New York and Geneva, 2006.

29. Ma, F.; Hanna, M. A. Biodiesel production: a review. *Bioresource Technology* **1999,** *70,* 1-15.

30. Zhang, Y.; Dub, M. A.; McLean, D. D.; Kates, M. Biodiesel production from waste cooking oil: 2. Economic assessment and sensitivity analysis. *Bioresource Technology* **2003,** *90,* 229–240.

31. Demirbas, A. Competitive liquid biofuels from biomass. *Applied Energy* **2011,** *88,* 17–28.

32. HHO-Hydrogen Energy Solutions. http://hho-hydrogen-energy.com/ (accessed Jan 23, 2011).

33. van Ruijven, B.; van Vuuren, D. P.; de Vries, B. The potential role of hydrogen in energy systems with and without climate policy. *International Journal of Hydrogen Energy* **2007,** *32,* 1655-1672.

34. Forsberg, C. W. Future hydrogen markets for large-scale hydrogen production systems. *International Journal of Hydrogen Energy* **2007,** *32,* 431-439.

35. Solomon, B. D.; Banerjee, A. A global survey of hydrogen energy research, development and policy. *Energy Policy* **2006,** *34,* 781-792.

36. Hellman, A.; Honkala, K.; Remediakis, I. N.; Logadóttir, Á.; Carlsson, A.; Dahl, S.; Christensen, C. H.; Nørskov, J. K. Insights into ammonia synthesis from first-principles. *Surface Science* **2006,** *600,* 4264-4268.

37. Twigg, M. V. *Catalyst Handbook,* 2nd ed.; Wolf Publishing Ltd, 1989.

38. Liu, X.; Lu, G. Q.; Yan, Z.; Beltramini, J. Recent Advances in Catalysts for Methanol Synthesis via Hydrogenation of CO and CO2.. *Industrial and Engineering Chemistry Research* **2003,** *42,* 6518-6530.

39. Stöcker, M. Methanol-to-hydrocarbons: Catalytic materials and their behaviour. *Microporous and Mesoporous Materials* **1999,** *29,* 3-48.

40. Keil, F. J. Methanol-to-hydrocarbons: Process technology. *Microporous and Mesoporous Materials* **1999,** *29,* 49-66.

41. Choudary, T. V.; Goodman, D. W. Methane activation on Ni and Ru model catalysts". *Journal of Molecular Catalysis A* **2000,** *163,* 9-18.

42. Lee, S.; Sardesai, A. Liquid phase methanol and dimethyl ether synthesis from syngas. *Topics in Catalysis* **2005,** *32,* 197-207.

43. Guo, Y.; Meyer-Zaika, W.; Muhler, M.; Vukojevic, S.; Epple, M. Cu/Zn/Al xerogels and aerogels prepared by a sol-gel reaction as catalysts for methanol synthesis. *European Journal of Inorganic Chemistry* **2006,** 4774-4781.

44. Mills, G. A. Status and future opportunities for conversion of synthesis gas to liquid fuels. *Fuel* **1994,** *73,* 1243-1279.

45. Rao, V. U. S.; Stiegel, G. J.; Cinquegrane, G. J.; Srivastava, R. D. Iron-based catalysts for slurry-phase Fischer-Tropsch process: Technology review. *Fuel*

Processing Technology **1992,** *30,* 83-107.

46. van de Loosdrecht, J. *Preparation and Properties of Supported Fischer-Tropsch Catalysts;* Ph.D. thesis; Utrecht University: The Netherlands, 1995.

47. Morselli, S. Ph.D. thesis; Scuola Normale superiore di Pisa: Italy, 2001.

48. Dry, M. E. The Fischer-Tropsch Process-Commercial aspects. *Catalysis Today* **1990,** *6,* 183-206.

49. Semelsberger, T. A.; Borup, R. L.; Greene, H. L. Dimethyl ether (DME) as an alternative fuel. *Journal of Power Sources* **2006,** *156,* 497-511.

50. Moradi, G. R.; Nosrati, S.; Yaripor, F. Effect of the hybrid catalysts preparation method upon direct synthesis of dimethyl ether from synthesis gas. *Catalysis Communications* **2007,** *8,* 598-606.

51. Fei, J.; Tang, X.; Huo, Z.; Lou, H.; Zheng, X. Effect of copper content on Cu-Mn-Zn/zeolite-Y catalysts for the synthesis of dimethyl ether from syngas. *Catalysis Communications* **2006,** *7,* 827- 831.

52. Sun, K.; Lu, W.; Qiu, F.; Liu, S.; Xu, X. Direct synthesis of DME over bifunctional catalyst: Surface properties and catalytic performance. *Applied Catalysis A* **2003,** *252,* 243-249.

53. Parisi, D. R.; Laborde, M. A. Modeling of counter current moving bed gas-solid reactor used in direct reduction of iron ore. *Chemical Engineering Journal* **2004,** *104,* 35-43.

54. Soleimania, M.; Bassi, A.; Margaritis, A. Biodesulfurization of refractory organic sulfur compounds in fossil fuels.. *Biotechnology Advances* **2007,** *25,* 570-596.

55. Brunet, S.; Mey, D.; Pérot, G.; Bouchy, C.; Diehl, F. On the hydrodesulfurization of FCC gasoline: a review. *Applied Catalysis A* **2005,** *278,* 143-172.

56. Chianelli, R. R.; Berhault, G.; Raybaud, P.; Kasztelan, S.; Hafner, J.; Toulhoat, H. Periodic trends in hydrodesulfurization: in support of the Sabatier principle.. *Applied Catalysis A* **2002,** *227,* 83-96.

57. Grange, P. Catalytic hydrodesulfurization. *Catalysis Reviews - Science and Engineering* **1980,** *21,* 135-181.

58. Wand, G. Fuel Cells History, part 1. *Johnson Matthey plc* **2008**.

59. Grove, W. R. On Voltaic Series and the Combination of Gases by Platinum. *Philosophical Magazine and Journal of Science* **1839,** *14,* 127-130.

60. Song, C. Fuel processing for low-temperature and high-temperature fuel cells:

Challenges, and opportunities for sustainable development in the 21st century. *Catalysis Today* **2002,** *77,* 17-49.

61. How fuel cells work. http://www.ballard.com/About_Ballard/Resources/How_Fuel_Cells_Work.htm (accessed Feb 4, 2011).

62. Krumpelt, M.; Krause, T. R.; Carter, J. D.; Kopasz, J. P.; Ahmed, S. Fuel processing for fuel cell systems in transportation and portable power applications. *Catalysis Today* **2002,** *77,* 3-16.

63. Fuel cells. http://www1.eere.energy.gov/hydrogenandfuelcells/fuelcells/fc_types.html (accessed Jan 23, 2011).

64. Research and Innovation-Fuel cells. http://ec.europa.eu/research/rtdinfo/42/01/article_1317_en.html.

65. Armor, J. N. The multiple roles for catalysis in the production of H2. *Applied Catalysis A* **1999,** *176,* 159-176.

66. Armor, J. N. Catalysis and the hydrogen economy. *Catalysis letters* **2005,** *101,* 131-135.

67. Peña, M. A.; Gómez, J. P.; Fierro, J. L. G. New catalytic routes for syngas and hydrogen production. *Applied Catalysis A* **1996,** *144,* 7-57.

68. Rostrup-Nielsen, J. R. *Handbook of Heterogeneus catalysys;* Wiley-VCH, 2009; pp 1-24.

69. Jarosch, K.; El Solh, T.; de Lasa, H. I. Modelling the catalytic steam reforming of methane: Discrimination between kinetic expressions using sequentially designed experiments. *Chemical Engineering Science* **2002,** *57,* 3439-3451.

70. Rostrup-Nielsen, J. R. Industrial relevance of coking. *Catalysis Today* **1997,** *37,* 225-232.

71. Bartholomew, C. H. Mechanisms of catalyst deactivation. *Applied Catalysis A* **2001,** *212,* 17-60.

72. Bartholomew, C. H. Carbon decomposition in steam reforming and methanation. *Catalysis Reviews* **1982,** *24,* 67-112.

73. Armor, J. N.; Martenak, D. J. Studying carbon formation at elevated pressure. *Applied Catalysis A* **2001,** *206,* 231-236.

74. Sehested, J.; Gelten, J. A. P.; Remediakis, I. N.; Bengaard, H.; Norskov, J. K.

Sintering of nickel steam-reforming catalysts: Effects of temperature and steam and hydrogen pressures. *Journal of Catalysis* **2004,** *223,* 432-443.

75. Hu, Y. H.; Ruckenstein, E. Catalytic Conversion of Methane to Synthesis Gas by Partial Oxidation and CO2 Reforming. *Advances in Catalysis* **2004,** *48,* 297-345.

76. Choudhary, V. R.; Rajput, A. M.; Prabhakar, B. Low temperature oxidative conversion of methane to syngas over NiO-CaO catalyst. *Catalysis Letters* **1992,** *15,* 363-370.

77. Choudhary, V. R.; Rajput, A. M.; Prabhakar, B. Nonequilibrium Oxidative Conversion of Methane to CO and H2 with High Selectivity and Productivity over Ni/Al2O3 at Low Temperatures. *Journal of Catalysis* **1993,** *139,* 326-328.

78. Choudhary, V. R.; Rajput, A. M.; Rane, V. H. Low temperature oxidative conversion of methane to synthesis gas over Co/rare earth oxide catalysts. *Catalysis Letters* **1992,** *16,* 269-272.

79. Choudhary, V. R.; Rajput, A. M.; Rane, V. H. Low-temperature catalytic selective partial oxidation of methane to CO and H2 over Ni/Yb2O3. *Journal of Physical Chemistry* **1992,** *96,* 8686-8688.

80. Choudhary, V. R.; Sansare, S. D.; Mamman, A. S. Low-temperature selective oxidation of methane to carbon monoxide and hydrogen over cobalt-MgO catalysts. *Applied Catalysis A* **1992,** *90,* L1-L5.

81. Gavalas, G. R.; Phichitcul, C.; Voecks, G. E. Structure and activity of NiO α-Al203 and NiO ZrO2 calcined at high temperatures. II. Activity in the fuel-rich oxidation of methane. *Journal of Catalysis* **1984,** *88,* 65-72.

82. Hickman, D. A.; Schmidt, L. D. Synthesis gas formation by direct oxidation of methane over Pt monoliths. *Journal of Catalysis* **1992,** *138,* 267-282.

83. York, A. P. E.; Xiao, T.; Green, M. L. H. Brief overview of the partial oxidation of methane to synthesis gas. *Topics in Catalysis* **2003,** *22,* 345-358.

84. Fishtik, I.; Alexander, A.; Datta, R.; Geana, D. Thermodynamic analysis of hydrogen production by steam reforming of ethanol via response reactions. *International Journal of Hydrogen Energy* **2000,** *25,* 31-45.

85. Fishtik, I.; Gutman, I.; I., N. Unnoticed identities in chemical thermodynamics. *Journal of the Chemical Society, Faraday Transactions* **1995,** *91,* 1325-1331.

86. Comas, J.; Laborde, M.; Amadeo, N. Thermodynamic analysis of hydrogen production from ethanol using CaO as a CO2 sorbent. *Journal of Power Sources* **2004,** *138,* 61-67.

87. Mas, V.; Kipreos, R.; Amadeo, N.; Laborde, M. Thermodynamic analysis of ethanol/water system with the stoichiometric method. *International Journal of Hydrogen Energy* **2006,** *31,* 21-28.

88. Benito, M.; Sanz, J. L.; Isabel, R.; Padilla, R.; Arjona, R.; Daza, L. Bio-ethanol steam reforming: Insights on the mechanism for hydrogen production. *Journal of Power Sources* **2005,** *151,* 11-17.

89. Rasko, J.; Hancz, A.; Erdohelji, A. Surface species and gas phase products in steam reforming of ethanol on TiO2 and Rh/TiO2. *Applied Catalysis A* **2004,** *269,* 13-25.

90. Sexton, B. A.; Rendulic, K. D.; Hughes, A. Z. Decomposition pathways of C1C4 alcohols adsorbed on platinum (111). *Surface Science* **1982,** *121,* 181-198.

91. Davis, J. L.; Barteau, M. A. Decarbonylation and decomposition pathways of alcohol's on Pd(111). *Surface Science* **1987,** *187,* 388-406.

92. Davis, J. L.; Barteau, M. A. The influence of oxygen on the selectivity of alcohol conversion on the Pd(111) surface. *Surface Science* **1988,** *197,* 123-152.

93. Houtman, C. J.; Barteau, M. A. Divergent pathways of acetaldehyde and ethanol decarbonylation on the Rh(111) surface. *Journal of Catalysis* **1991,** *130,* 528-546.

94. Xu, J.; Zhang, X.; Zerobi, R.; Yoshihobu, J.; Xu, Z.; Yates, J. T. *Surface Science* **1991,** *256,* 288.

95. Gates, S. M.; Russell, J. N.; Yates, J. T. Bond activation sequence observed in the chemisorption and surface reaction of ethanol on Ni(111). *Surface Science* **1986,** *171,* 111-134.

96. Cong, Y.; van Spaendonk, V.; Masel, R. I. Low temperature C-C bond scission during ethanol decomposition on Pt(331). *Surface Science* **1997,** *385,* 246-258.

97. Vaidya, P. D.; Rodrigues, A. E. Insight into steam reforming of ethanol to produce hydrogen for fuel cells. *Chemical Engineering Journal* **2006,** *117,* 39-49.

98. Erdohelyi, A.; Rasko, J.; Kecskes, T.; Totha, M.; Domok, M.; Baan, K. Hydrogen formation in ethanol reforming on supported noble metal catalysts. *Catalysis Today* **2006,** *116,* 367-376.

99. Zhang, B.; Tang, X.; Li, Y.; Cai, W.; Xu, Y.; Shen, W. Steam reforming of bio-ethanol for the production of hydrogen over ceria-supported Co, Ir and Ni catalysts. *Catalysis Communications* **2006,** *233,* 367-372.

100. Kugai, J.; Subramani, V.; Song, C.; Engelhard, M. H.; Chin, Y. H. Effects of nanocrystalline CeO2 supports on the properties and performance of Ni-Rh

bimetallic catalyst for oxidative steam reforming of ethanol. *Journal of Catalysis* **2006,** *238,* 430–440.

101. Sheng, P. Y.; Yee, A.; Bowmaker, G. A.; Idriss, H. H2 production from ethanol over Rh-Pt/CeO2 catalysts: The role of Rh for the efficient dissociation of the carbon-carbon bond. *Journal of Catalysis* **2002,** *208,* 393–403.

102. Kugai, J.; Velu, S.; Song, C. Low-temperature reforming of ethanol over CeO2-supported Ni-Rh bimetallic catalysts for hydrogen production. *Catalysis Letters* **2005,** *101,* 255-264.

103. Frusteri, F.; Freni, S.; Spadaro, L.; Chiodo, V.; Bonura, G.; Donato, S. H2 production for MC fuel cell by steam reforming of ethanol over MgO supported Pd, Rh, Ni and Co catalysts. *Catalysis Communications* **2004,** *5,* 611–615.

104. Aupretre, F.; Descorme, C.; Duprez, D.; Casanave, D.; Uzio, D. Ethanol steam reforming over MgxNi1-xAl 2O3 spinel oxide-supported Rh catalysts. *Journal of Catalysis* **2005,** *233,* 464–477.

105. Frusteri, F.; Freni, S. Bio-ethanol, a suitable fuel to produce hydrogen for a molten carbonate fuel cell. *Journal of Power Sources* **2007,** *173,* 200-209.

106. Fatsikostas, A. N.; Verykios, X. E. Reaction network of steam reforming of ethanol over Ni-based catalysts. *Journal of Catalysis* **2004,** *225,* 439–452.

107. Morgenstern, D. A.; Fornango, J. P. Low-temperature reforming of ethanol over copper-plated raney nickel: A new route to sustainable hydrogen for transportation. *Energy and Fuels* **2005,** *19,* 1708-1716.

108. Luengo, C. A.; Ciampi, G.; Cencig, M. O.; Steckelberg, C.; Laborde, M. A. A novel catalyst system for ethanol gasification. *International Journal of Hydrogen Energy* **1992,** *17,* 677-681.

109. Fierro, V.; Akdim, O.; Mirodatos, C. On-board hydrogen production in a hybrid electric vehicle by bio-ethanol oxidative steam reforming over Ni and noble metal based catalysts. *Green Chemistry* **2003,** *5,* 20-24.

110. Marino, F.; Boveri, M.; Baronetti, G.; Laborde, M. Hydrogen production from steam reforming of bioethanol using Cu/Ni/K/γ-Al2O3 catalysts. Effect of Ni. *International Journal of Hydrogen Energy* **2001,** *26,* 665-668.

111. Frusteri, F.; Freni, S.; Chiodo, V.; Spadaro, L.; Bonura, G.; Cavallaro, S. Potassium improved stability of Ni/MgO in the steam reforming of ethanol for the production of hydrogen for MCFC. *Journal of Power Source* **2004,** *132,* 139–144.

112. Marino, F.; Baronetti, G.; Jobbagy, M.; Laborde, M. Cu-Ni-K/γ-Al2O3 supported

catalysts for ethanol steam reforming: Formation of hydrotalcite-type compounds as a result of metal-support interaction. *Applied Catalysis A* **2002,** *238,* 41-54.

113. Amadeo, N.; Laborde, M. Low temperature water gas shift reaction: catalyst, kinetics and reactor. *Trends in Chemical Engineering* **1996,** *3,* 159–183.

114. Velu, S.; Satoh, N.; Gopinath, C. S.; Suzuki, K. Oxidative reforming of bio-ethanol over CuNiZnAl mixed oxide catalysts for hydrogen production. *Catalysis Letters* **2002,** *82,* 145-152.

115. Barroso, M.; Gomez, M.; Arrua, L.; Abello, M. Hydrogen production by ethanol reforming over NiZnAl catalysts. *Applied Catalysis A* **2006,** *304,* 116-123.

116. Cavallaro, S.; Freni, S. Ethanol steam reforming in a molten carbonate fuel cell. A preliminary kinetic investigation. *International Journal of Hydrogen Energy* **1996,** *21,* 465-469.

117. Nishiguchi, T.; Matsumoto, T.; Kanai, H.; Utani, K.; Matsumura, Y.; Shen, W.-J.; Imamura, S. Catalytic steam reforming of ethanol to produce hydrogen and acetone. *Applied Catalysis A* **2005,** *279,* 273-277.

118. Amphlett, J. C.; Leclerc, S.; Mann, R. F.; Peppley, B. A.; Roberge, P. R. Fuel Cell Hydrogen Production By Catalytic Ethanol-Steam Reforming. *Proc. of the 33rd Intersociety Energy Conversion Engineering Conference*, Colorado Springs, CO., USA, 1998.

119. Machado, N. R. C. F.; Rizzo, R. C. P.; Peguin, R. P. S. Performance of catalysts with Nb2O5 for hydrogen production from ethanol steam reforming. *Maringa* **2002,** *24,* 1637-1642.

120. Haga, F.; Nakajima, T.; Yamashita, K.; Mishima, S. Effect of crystallite size on the catalysis of alumina-supported cobalt catalyst for steam reforming of ethanol. *Reaction Kinetics and Catalysis Letters* **1998,** *63,* 253-259.

121. Cavallaro, S.; Mondello, N.; Freni, S. Hydrogen produced from ethanol for internal reforming molten carbonate fuel cell. *Journal of Power Sources* **2001,** *102,* 198-204.

122. Llorca, J.; Homs, N.; Sales, J.; de la Piscina, P. R. Efficient production of hydrogen over supported cobalt catalysts from ethanol steam reforming. *Journal of Catalysis* **2002,** *209,* 306-317.

123. Llorca, J.; de la Piscina, P. R.; Dalmon, J.-A.; Sales, J.; Homs, N. Co-free hydrogen from steam-reforming of bioethanol over ZnO-supported cobalt catalysts: Effect of the metallic precursor. *Applied Catalysis B* **2003,** *43,* 355-369.

124. Llorca, J.; Homs, N.; Sales, J.; Fierro, J.-L. G.; de la Piscina, P. R. Effect of sodium addition on the performance of Co-ZnO-based catalysts for hydrogen production from bioethanol. *Journal of Catalysis* **2004,** *222,* 470-480.

125. Kaddouri, A.; Mazzocchia, C. A study of the influence of the synthesis conditions upon the catalytic properties of Co/SiO_2 or Co/Al_2O_3 catalysts used for ethanol steam reforming. *Catalysis Communications* **2004,** *5,* 339-345.

126. Batista, M. C.; Santos, R. K. S.; Assaf, E. M.; Assaf, J. M.; Ticianelli, E. A. High efficiency steam reforming of ethanol by cobalt-based catalysts. *Journal of Power Sources* **2004,** *134,* 27-32.

127. Fierro, V.; Klouz, V.; Akdim, O.; Mirodatos, C. Oxidative reforming of biomass derived ethanol for hydrogen production in fuel cell applications. *Catalysis Today* **2002,** *75,* 141–144.

128. Aupretre, F.; Descorme, C.; Duprez, D. The multiple roles for catalysis in the production of H_2. *Catalysis Communications* **2002,** *3,* 263-267.

129. Liguras, D. K.; Kondarides, D. J.; Verykios, X. E. Production of hydrogen for fuel cells by steam reforming of ethanol over supported noble metal catalysts. *Applied Catalysis B* **2003,** *43,* 345-354.

130. Freni, S.; Mondello, N.; Cavallaro, S.; Cacciola, G.; Parmon, V. N.; Sobyanin, V. A. Hydrogen production by steam reforming of ethanol: A two step process. *Reaction Kinetics and Catalysis Letters* **2000,** *71,* 143-152.

131. Deluga, G. A.; Salge, J. R.; Schmidt, L. D.; Verykios, X. E. Renewable Hydrogen from Ethanol by Autothermal Reforming. *Science* **2004,** *303,* 993-997.

132. Velu, S.; Suzuki, K.; Vijayaraj, M.; Barman, S.; Gopinath, C. S. In situ XPS investigations of Cu1-xNixZnAl-mixed metal oxide catalysts used in the oxidative steam reforming of bio-ethanol. *Applied Catalysis B* **2005,** *55,* 287–299.

133. Navarro, R. M.; Alvarez-Galvan, M. C.; Cruz Sanchez-Sanchez, M.; Rosa, F.; Fierro, J. L. G. Production of hydrogen by oxidative reforming of ethanol over Pt catalysts supported on Al_2O_3 modified with Ce and La. *Applied Catalysis B* **2005,** *55,* 229–241.

134. Casanovas, A.; Llorca, J.; Homs, N.; Fierro, J. L.; de la Piscina, P. R. Ethanol reforming processes over ZnO-supported palladium catalysts: Effect of alloy formation. *Journal of Molecular Catalysis A* **2006,** *250,* 44-49.

135. Venkataraman, K. *Short contact time catalytic wall reactors;* Ph.D. Thesis; University of Minnesota: U.S.A., 2003.

136. Wanat, E. C.; Venkataraman, K.; Schmidt, L. D. Steam reforming and water-gas shift of ethanol on Rh and Rh-Ce catalysts in a catalytic wall reactor. *Applied Catalysis A* **2004,** *276,* 155-162.

137. Trifirò, F.; Vaccari, A. In *Comprehensive Supramolecular Chemistry;* Atwood, J. L., Davies, J. E. D., MacNicol, D. D., Vögtle, F., Eds.; Pergamon Press: Oxford, 1996 Chapter 8,; Vol. 7, p 251.

138. Takehira, K. Highly Dispersed and Stable Supported Metal Catalysts Prepared by Solid Phase Crystallization Method. *Catalysis Surveys from Japan* **2002,** *6,* 19-32.

139. Basile, F.; Basini, L.; D'Amore, M.; Fornasari, G.; Guarinoni, A.; Matteuzzi, D.; Del Piero, G.; Trifirò, F.; Vaccari, A. Ni/Mg/Al anionic clay derived catalysts for the catalytic partial oxidation of methane: residence time dependence of the reactivity features. *Journal of Catalysis* **1998,** *173,* 247-256.

140. Basile, F.; Fornasari, G.; Poluzzi, E.; Vaccari, A. Catalytic partial oxidation and CO2-reforming on Rh- and Ni-based catalysts obtained from hydrotalcite-type precursors.. *Applyed Clay Science* **1998,** *13,* 329-345.

141. Basile, F.; Fornasari, G.; Rosetti, V.; Trifirò, F.; Vaccari, A. Effect of the Mg/Al ratio of the hydrotalcite-type precursor on the dispersion and activity of Rh and Ru catalysts for the partial oxidation of methane. *Catalysis Today* **2004,** *91-92,* 293-297.

142. Albertazzi, S.; Arpentinier, P.; Basile, F.; Fornasari, G.; Gary, D.; Vaccari, A. WO03099436 , 2003.

143. Arpentinier, P.; Basile, F.; Del Gallo, P.; Fornasari, G.; Gary, D.; Rosetti, V.; Vaccari, A. Role of the hydrotalcite-type precursor on the properties of CPO catalysts. *Catalysis Today* **2005,** *99,* 99.

3 Experimental

3.1 Catalysts preparation

Catalysts tests were carried out on different type of catalysts. First step was tested bulk catalysts obtained from hydrotalcite type precursors with several amounts of active metal. Then catalytic activity of bulk catalysts prepared in the laboratory of Industrial Chemistry of Bologna were compared with a catalyst prepared by CTTC of Limoges with same active metal but different matrix based on $CeZrO_2$. Best bulk catalyst formulation was chosen to coat on alumina foam prepared by CTTC of Limoges.

3.1.1 Catalysts from hydrotalcite type precursors

The hydrotalcite type precursors (HT) of general formula

$$[M^{2+}_{(1-x)}M^{3+}_{x}(OH)_2]\,(A^{n-}_{x/n}).mH_2O$$

with $M^{2+} = Ni^{2+}$ and Mg^{2+}

$M^{3+} = Rh^{3+}$, Al^{3+} and Fe^{3+}

$A^{n-} = Si_nO_{2n+1}^{2-}$ (silicate) or CO_3^{2-} (carbonate)

were synthesized in the laboratory using the following coprecipitation method:

1) Preparation of aqueous solution (1.5 M) of the nitrate of the metals:

» $Mg(NO_3)_2 \cdot 6H_2O$ (99 %)

» $Al(NO_3)_3 \cdot 9H_2O$ (98 %)

» $Ni(NO_3)_2 \cdot 6H_2O$ (99 %)

» $Rh(NO_3)_3$ (10 % solution)

» $Fe(NO_3)_3 \cdot 9H_2O$ (98 %)

2) Preparation of aqueous silicate or carbonate solution (in excess with respect to the amount required by the stoichiometry)

» SiO_2·NaOH 27%

» Na_2CO_3

3) The cation solution is dropped, under magnetic stirring, into the solution of silicates, at constant temperature (50-60°C). The pH was maintained constant (10.5 ±

0.1) by adding NaOH (3 M). Once the dropping was finished, the obtained dispersion was maintained under magnetic stirring for 45 minutes (at 50-60°C and pH = 10.5).

4) The precipitate has been then separated from the mother liquor by filtration under vacuum, washed with abundant hot water (60°C) and dried overnight at 70°C.

5) The dried precursor samples were grinded to obtain powder. The catalysts (ex-HT) were obtained from the precursors by calcination at 900°C for 12 h (heating rate 10°C/min).

3.1.2 Catalyst from $CeZrO_2$ matrix

The $CeZrO_2$ catalyst was prepared by coprecipitation of nitrates of Rh, Ce and Zr. To obtain the precipitation of all hydroxide species the pH was kept over 6.5 at 20°C by adding drop by drop ammonia. During coprecipitation the slurry was stirring. Then the precipitate was centrifugated and dryed at 70°C. After that the powder was calcined at 700°C for three hours.

3.1.3 Foam catalysts

Alumina foams were processed by impregnation of polymeric sponge-like templates. Slurries of highly pure α-Al_2O_3 modified and stabilized with organic additives, were used to impregnate polyurethane foams. 10, 20 and 30 ppi (pore per inch) foams were employed. Foams were totally impregnated with the slurry, and the slurry excess was then removed to leave the porosity open. Impregnated foams were dried, and the organics (PU foams, additives) were then pyrolysed at low heating rate. Finally the remaining ceramic was sintered at high temperature (*1*).

Before to prepare slurries to coat the ceramic foams the calcined hydrotalcite was milled by attrition with zirconia balls for 4 hours with the addition of dispersing agent to obtain the average diameter of the grains close to 1 μm. After that the solvent and dispersing agent were evaporated.

Catalysts slurries were prepared using a planetary ball-milling equipment. Catalysts powder were dispersed in MEK-CH_3CH_2OH with adequate binders and dispersing agents. A dip-coating process was used to coat the catalyst onto the surface of alumina foams: foams were dipped once in the slurry, without controlling the atmosphere. The catalyst coating thickness was controlled by the catalyst powder loading in the slurry.

3.2 Catalysts characterization

3.2.1 X-Ray diffraction (XRD) analysis

The XRD powder analyses were carried out using a Philips PW1050/81 diffractometer equipped with a graphite monochromator in the diffracted beam and controlled by a PW1710 unit (Cu Kα, λ = 0.15418 nm). A °2θ range from 5° to 80° was investigated at a scanning speed of 70°/h.

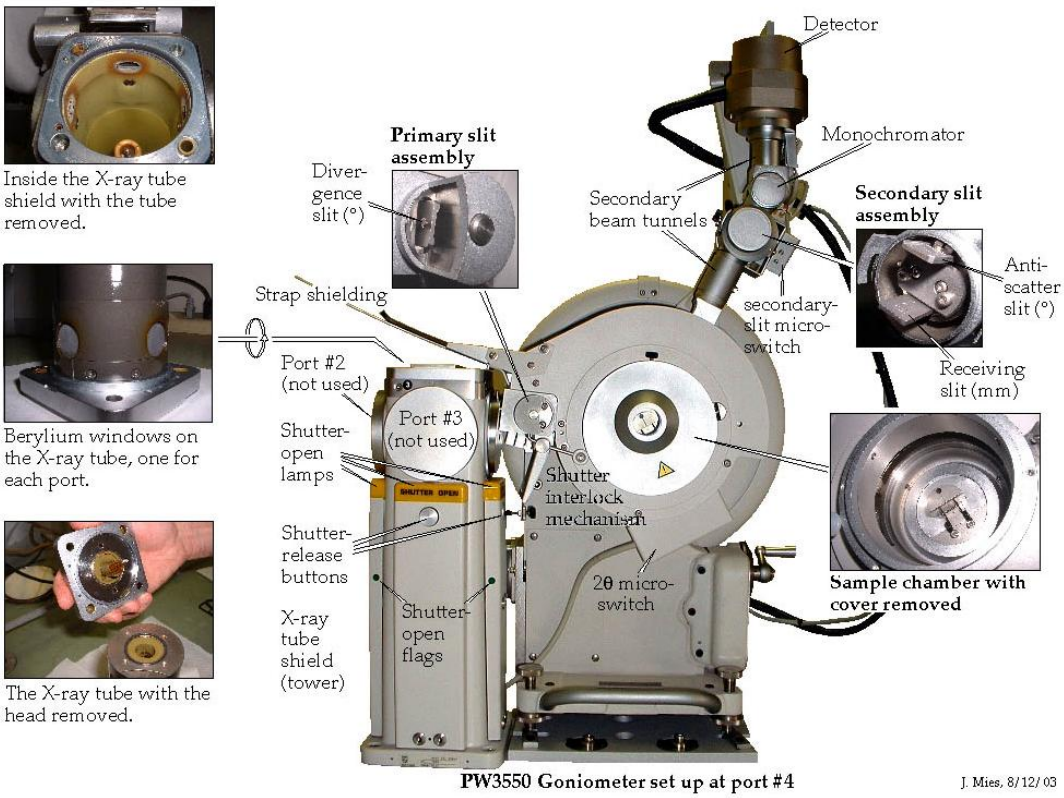

Fig. 3.1 Scheme of the instrument for the X-ray diffraction analysis (2).

The analysis of the phases present in the patterns were analyzed using the Bragg's Law:

$$n\lambda = 2d\,sen\theta$$

in order to calculate the d values to compare with those reported in the literature [Powder Diffraction Files - Inorganic Phase, ICDD (International Centre for *Diffraction Data)*]. In addition, the particle sizes are calculated using the Sherrer's Law:

$$D = \frac{k\lambda}{\cos\theta\sqrt{B^2 - b^2}}$$

3.2.2 Surface area and porosimetry analysis

Fig. 3.2 Scheme of the instrument for the porosimetry analysis (2).

Specific surface area and porosimetry analysis were carried out in a Micromeritics ASAP 2020 instrument (Accelerated Surface Area and Porosimetry System). This instrument measures the adsorption and desorption isothermal curve (at 77 K) by the volume of adsorbed/desorbed N_2, as a function of relative pressure (via-multi-point method).

BET analyses were performed for the precursors of catalysts and for calcined catalysts. The precursors were previously degassed under a vacuum at 120 °C until a pressure of 30 mmHg was reached and maintained for 30 min. Calcined solids were heated up to 150 °C until a pressure of 30 mmHg was reached, then kept 30 min at this temperature and finally heated up to 250 °C and maintained for 30 min.

Each analysis required about 0.3-0.5 g of catalyst sample.

3.2.3 Temperature programmed reduction (TPR) and oxidation (TPO) analysis

The reduction and oxidation profiles have been measured using a ThermoQuest Instrument TPD/R/O 1100 Catalytic Surface Analyzer. The analyses were carried out loading 0.1 g of sample, using the following procedure:

- **Pre-treatment** : the sample was pre-treated under N_2 (20 ml/min) from room temperature to 150°C (temperature rate of 20°C/min) and hold for 30 minutes at 150°C.

- **Reduction** : after cooling until 100°C, the reduction analysis was carried out with 5 % of H_2 in Ar (20 ml/min) from 60 to 950°C (temperature rate of 10°C/min) and hold for 30 minutes at 950°C.

- **Oxidation** : after cooling until 60°C, the oxidation analysis was carried out with 5 % of O_2 in He (20 ml/min) from 60 to 950°C (temperature rate of 10°C/min) and hold for 30 minutes at 950°C.

The oxidation step was carried out after the reduction on fresh samples to evaluate the reoxidation of the active metals, or after the pretreatment (coupled with

quadrupole mass analyzer) on the used samples to evaluate possible carbon deposits on the surface of the catalyst.

3.2.4 Scanning and Transmission Electron Microscopy analysis

A high-resolution scanning electron microscope equipped with a Field-Emission Gun FEG-SEM (JEOL-6700F), equipped with an EDS detector (PGT Spirit, Si(Li) diode detector), was used to observe the microstructure of the surface and of the bulk of alumina foam after coating. Samples were prepared by attaching the foam struts to brass sample carriers with a silver paste.

Transmission Electron Microscopy (TEM, JEOL 2010), combined with Energy Dispersive X-ray Spectrometry (EDS) was used to study rhodium particle size before and after reaction. Before measurement every sample was reduced under H_2.

Two different temperature of reduction were chosen to compare the effect of reduction temperature on particle size and density. First temperature was 750 °C for two hours while the second one was 1000 °C for four hours, for both temperature the amount of H_2 was 3 % in Argon and the flow of mixture was 30 ml/min.

3.2.5 Infrared (IR) spectroscopy analysis

For the IR spectroscopy characterization the powder was pressed in a thin self-supported pellet, placed inside a gold hand-made envelope and located in the IR cell (Fig. 3.3).

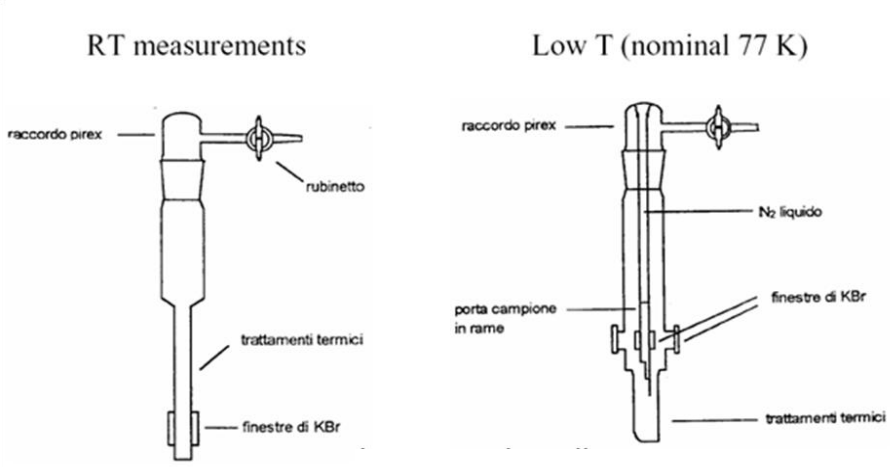

Fig. 3.3 Home made cells for IR measurements.

Before of each measurement the sample was reduced and then a further pre-treatment was carried out. The pre-treatment of the reduced sample in the IR cell was been as follows: heating up to 750 °C, reduction at 750 °C in H_2 for 1 hour, outgassing

at 650 °C for 2 hours, cooling down in inert atmosphere (Ar). The reduction treatment was necessary to observe Rh^0 species. The outgassing step at 650 °C for 2 hours was necessary to avoid the chemisorption of CO.

After reduction treatment the sample was cooled down and IR spectra were collected on a Bruker IFS 55 Equinox instrument equipped with an MCT cryodetector working with 2 cm^{-1} resolution. The dosing of gas/vapours was carried out by connecting the IR cell to a vacuum ramp, equipped with one Pirani vacuum gauge and one manometer. During adsorption measurement, a set of spectra is recorded, where each spectrum refers to a specific gas equilibrium pressure. In order to carry on a comparative semi-quantitative characterization, the spectra are normalized with respect to the sample amount, so that intensities of bands observed for different samples may be used to evaluate the concentration of adsorbed species (and the concentration of adsorbing sites).

3.2.6 Other analysis

The particle size distributions were determined using a laser diffraction granulometer (Malvern Mastersizer 2000). The measurement was carried on a slurry of the powder in water or in organic MEK/CH_3CH_2OH solution.

The powders density was measured by an Helium pycnometer (Micromeritics AccuPyc 1330).

3.3 Laboratory plant

In order to study the bio-ethanol steam reforming reaction, a laboratory plant with a fixed bed reactor was built (Fig. 3.4).

The plant can be divided in four zone: (1) ethanol and water feeds mixing and preheating, (2) microreactor, (3) system of liquid condensation, and (4) system of analysis.

The mix liquid of ethanol and water is fed by a HPLC pump and pre-heated at 200°C before enter in the reactor. During diluted conditions, helium and the vapours of ethanol and water are mixed before the head of reactor. During last test it was used surfin ethanol which is bio-ethanol after a purification treatment.

Due to the hard reaction conditions, such as high temperature (600-800°C), pressure (until 20 bar) and reducing atmosphere, the constituting material of the reactor undergoes to severe restrictions. To avoid the break of the reactor in these conditions, it was built in a special alloy material (Incoloy 800HT) constituted by chromium (20-25%), nickel (30-35 %) and iron (40-45 %).

Inside the reactor (Fig. 3.5), along the axial direction a thermocouple shell is inserted, in this fixed shell it is possible to move the cromel-alumel thermocouple (0.8 mm of diameter) in the axial direction in order to measure the axial thermal profile during reaction. The reactor is placed inside an electric oven.

The gas, going out from the reactor, is kept at 200°C until it is split in two flows: one is kept at 200°C to analyze online all possible condensable products while the other passes through a condenser that separates the condensable products from permanent gas and through a trap containing a dehydrator agent (Drierite, $CaSO_4$, 8 mesh, containing an indicator) in order to remove any residual traces of water or ethanol.

Previously of the split of flows, a back pressure regulator is placed to maintain the feed zone and the microreactor under the operative pressure conditions, while after this control device the pressure is atmospheric, that is useful for the analysis.

All the products are then analyzed online using two gas-chromatograph equipments.

The first gas-chromatograph is a Perkin Elmer Instrument Clarus series equipped with two TCD detectors and it is used both to separate O_2, N_2, CO, CH_4 and CO_2, using a Carbosieve packed column and CO_2, H_2O, CH_3CHO, CH_3CH_2OH, CH_3COCH_3 and CH_3COOH, using a HaySept P packed column [Isotherm at 120°C for 3 min, ramp 10°C/min until 200°C, cooling; carrier gas: He 20 ml/min].

The second gas-chromatograph is a Perkin Elmer Instrument Autosystem series, for the hydrogen analysis using a similar Carbosieve packed column. The analysis was carried out at 45°C using as carrier gas N2, (20 ml/min).

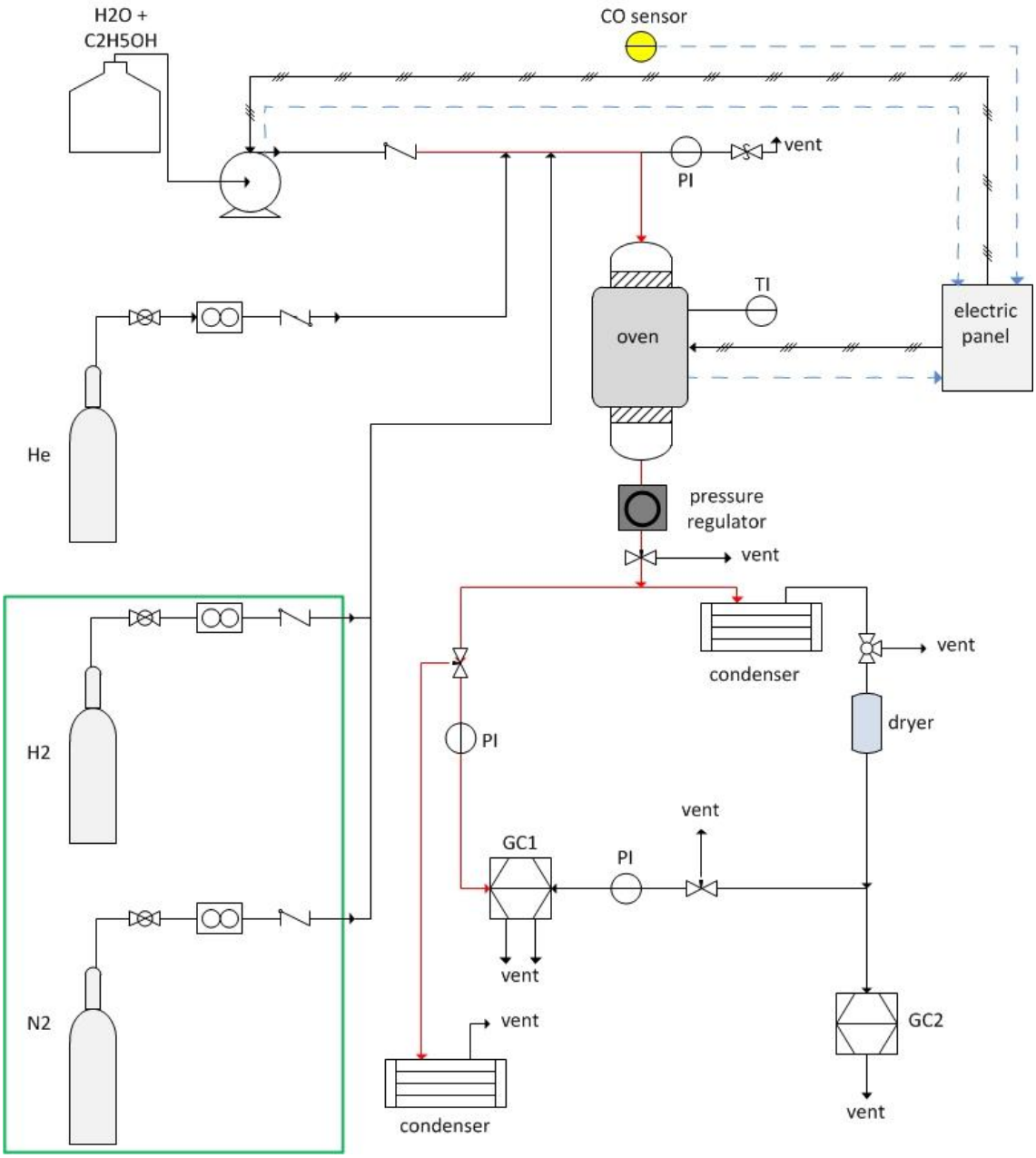

Fig. 3.4 Laboratory plant for bio-ethanol steam reforming

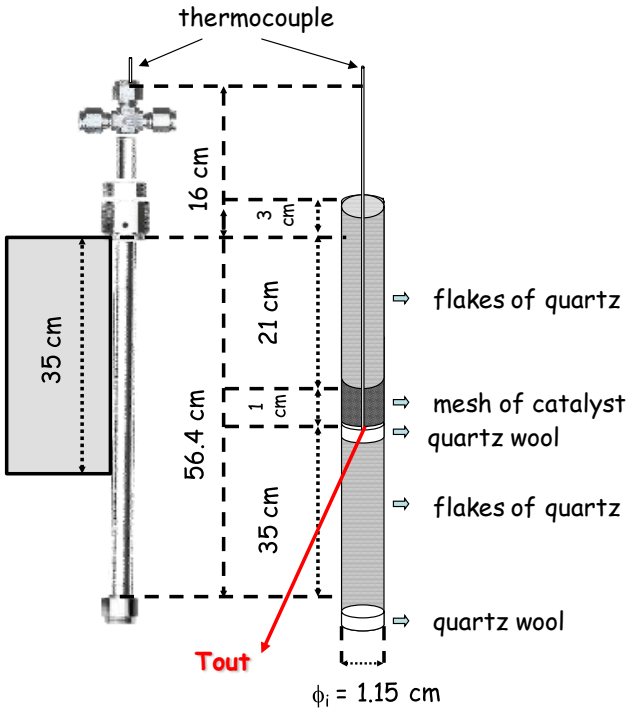

Fig. 3.5 Scheme of filling of reactor.

Before the catalytic reaction, the catalysts were activated by reduction in situ under H2 flow at reduction temperature (800 °C) for 2 h. At the end of tests, the water/ethanol flow was stopped and the catalyst was cooled under helium stream.

The catalytic tests were carried out in different reaction conditions. Here after it is shown only a summary of values for every parameter because each table of conditions will be show with results.

-P = atmospheric and 20 bar

-Toven = 300°C, 450°C, 600°C and 750°C

-S/ CH_3CH_2OH = H_2O / CH_3CH_2OH = 5 ml/mol

-fD = He / (H_2O / CH_3CH_2OH) = 9, 4, 1, 0

-Dp = 1.410 - 0.841 mm (granulometry of 14-20 mesh) and 0.590-0.420 mm (granulometry of 30-40 mesh)

-Vcat = 1, 2, 4 and 6 ml.

Contact time is calculated respect real condition of temperature and pressure and it is related to the volume of the catalyst. In order to compare contact time of foams with pellets, it is considered contact time related to the weight of catalyst.

Ethanol and water conversion and products selectivities were calculated using the following calculations:

$$\textbf{Conv. } CH_3CH_2OH = \frac{100 \times (CH_3CH_2OH \text{ in} - CH_3CH_2OH \text{ out})}{CH_3CH_2OH \text{ in}} = \frac{100 \times (CH_3CH_2OH \text{ conv})}{CH_3CH_2OH \text{ conv} - CH_3CH_2OH \text{ conv}} =$$

$$= \frac{100 \times (^1/_2 \times (\%CH_4 + \%CO_2 + \%CO) + \%CH_3CHO + \%C_2H_4 + \%CH_3COOH + {}^3/_2 \times \%CH_3COCH_3)}{(^1/_2 \times (\%CH_4 + \%CO_2 + \%CO) + \%CH_3CHO + \%C_2H_4 + \%CH_3COOH + {}^3/_2 \times \%CH_3COCH_3) + \%CH_3CH_2OH \text{ out}}$$

$$\textbf{Conv. } H_2O = \frac{100 \times (H_2O \text{ conv} - CH_3CH_2OH \text{ conv})}{(H_2O \text{ conv} - CH_3CH_2OH \text{ conv}) + H_2O \text{ out}}$$

$$= \frac{100 \times [(\%CO + \%CH_3CHO + \%CH_3COCH_3 + 2 \times (\%CO_2 + \%CH_3CH_2OH)] - (^1/_2 \times (\%CH_4 + \%CO_2 + \%CO) + \%CH_3CHO + \%C_2H_4 + \%CH_3COOH + {}^3/_2 \times \%CH_3COCH_3)}{100 \times [(\%CO + \%CH_3CHO + \%CH_3COCH_3 + 2 \times (\%CO_2 + \%CH_3CH_2OH)] - (^1/_2 \times (\%CH_4 + \%CO_2 + \%CO) + \%CH_3CHO + \%C_2H_4 + \%CH_3COOH + {}^3/_2 \times \%CH_3COCH_3) + \%H_2O \text{ out}}$$

$$\textbf{H}_2 \textbf{ sel.} = \frac{100 \times (H_2 \text{ out})}{3 \times (CH_3CH_2OH \text{ in} - CH_3CH_2OH \text{ out}) + (H_2O \text{ in} - H_2O \text{ out})}$$

$$= \frac{100 \times (\%H_2)}{\%H_2 + 2 \times (\%CH_4 + \%CH_3CHO + \%C_2H_4 + \%CH_3COOH) + 3 \times (\%CH_3COCH_3)}$$

$$\textbf{CH4 sel.} = \frac{100 \times (CH4 \text{ out})}{2 \times (CH_3CH_2OH \text{ in} - CH_3CH_2OH \text{ out})}$$

$$= \frac{100 \times \%\,CH_4}{\%\,CH_4 + \%\,CO + \%\,CO_2 + 2 \times (\%\,CH_3CHO + \%\,C_2H_4 + \%\,CH_3COOH) + 3 \times \%\,CH_3COCH_3}$$

$$\textbf{\textit{CO sel.}} = \frac{100 \times (CO\ out)}{2 \times (CH_3CH_2OH\ in - CH_3CH_2OH\ out)}$$

$$= \frac{100 \times \%\,CO}{\%\,CH_4 + \%\,CO + \%\,CO_2 + 2 \times (\%\,CH_3CHO + \%\,C_2H_4 + \%\,CH_3COOH) + 3 \times \%\,CH_3COCH_3}$$

$$\textbf{\textit{CO}}_2\textbf{\textit{ sel.}} = \frac{100 \times (\%\,CO_2\,out)}{2 \times (CH_3CH_2OH\ in - CH_3CH_2OH\ out)}$$

$$= \frac{100 \times CO_2}{\%\,CH_4 + \%\,CO + \%\,CO_2 + 2 \times (\%\,CH_3CHO + \%\,C_2H_4 + \%\,CH_3COOH) + 3 \times \%\,CH_3COCH_3}$$

$$\textbf{\textit{CH}}_3\textbf{\textit{CHO sel.}} = \frac{100 \times (CH_3CHO out)}{CH_3CH_2OH\ in - CH_3CH_2OH\ out}$$

$$= \frac{100 \times \%\,CH_3CHO}{{}^1/_2 \times (\%\,CH_4 + \%\,CO + \%\,CO_2) + (\%\,CH_3CHO + \%\,C_2H_4 + \%\,CH_3COOH) + {}^3/_2 \times \%\,CH_3COCH_3}$$

$$\textbf{\textit{CH}}_2\textbf{\textit{CH}}_2\textbf{\textit{ sel.}} = \frac{100 \times (\%\,CH_2CH_2\ out)}{CH_3CH_2OH\ in - CH_3CH_2OH\ out}$$

$$= \frac{100 \times \%\,CH_3CH_2}{{}^1/_2 \times (\%\,CH_4 + \%\,CO + \%\,CO_2) + (\%\,CH_3CHO + \%\,C_2H_4 + \%\,CH_3COOH) + {}^3/_2 \times \%\,CH_3COCH_3}$$

$$\boldsymbol{CH_3COCH_3\ sel.} = \frac{100 \times (\%\,CH_3COCH_3\,out)}{CH_3CH_2OH\,in - CH_3CH_2OH\,out}$$

$$= \frac{100 \times \%\,CH_3COCH_3}{{}^1/_3 \times (\%\,CH_4 + \%\,CO + \%\,CO_2) + {}^2/_3 \times (\%\,CH_3CHO + \%\,C_2H_4 + \%\,CH_3COOH) + \%\,CH_3COCH_3}$$

$$\boldsymbol{CH_3COOH\ sel.} = \frac{100 \times (\%\,CH_3COOH\,out)}{CH_3CH_2OH\,in - CH_3CH_2OH\,out}$$

$$= \frac{100 \times \%\,CH_3COOH}{{}^1/_2 \times (\%\,CH_4 + \%\,CO + \%\,CO_2) + (\%\,CH_3CHO + \%\,C_2H_4 + \%\,CH_3COOH) + {}^3/_2 \times \%\,CH_3COCH_3}$$

3.4 Preliminary/Blank tests

Before catalytic tests, the laboratory plant was subjected to preliminary activity tests filling the reactor with three different "inert" materials, to chose what material show less activity and it can be chose as inert filling. These blank tests were carried out at different temperatures (250, 400, 550 and 700°C) and S/CH_3CH_2OH ratio (5 and 4 mol/mol).

At low temperature all materials show CH_3CH_2OH conversion less than 5 % but increasing temperature alumina shows higher conversion and therefore worse results.

Quartz is the best choice as inert because, in particular at high temperatures, ethanol conversion of quartz is lower than ethanol conversion of corundum and alumina (Fig. 3.6).

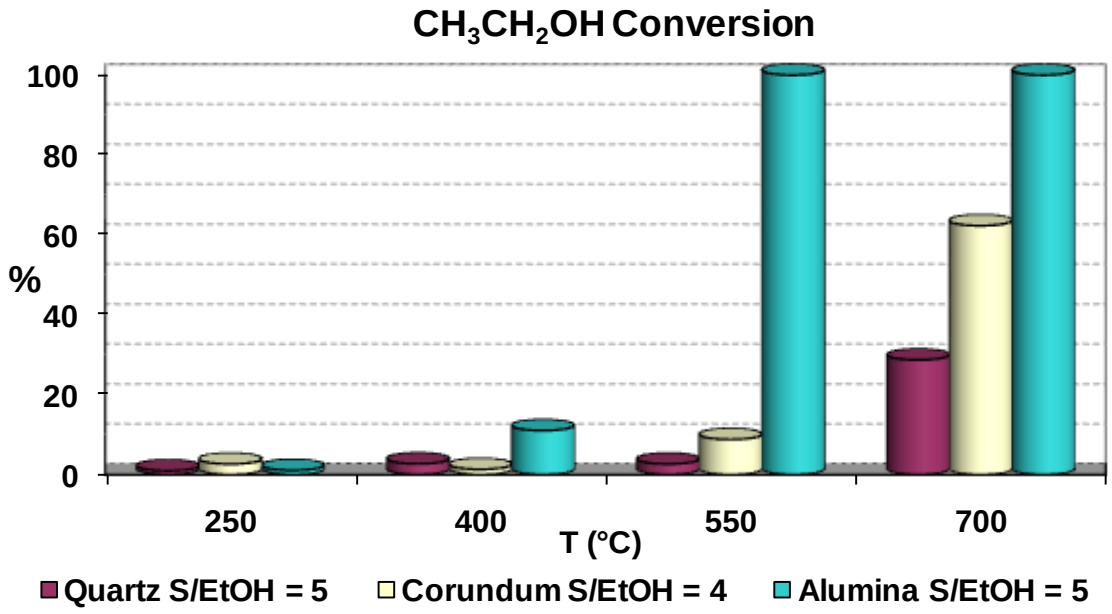

Fig. 3.6 CH_3CH_2OH conversion of three different filling.

An isothermal zone of 10 cm, was found at 20 cm from the oven entry (Fig. 3.7). The catalytic bed was located in the isothermal zone.

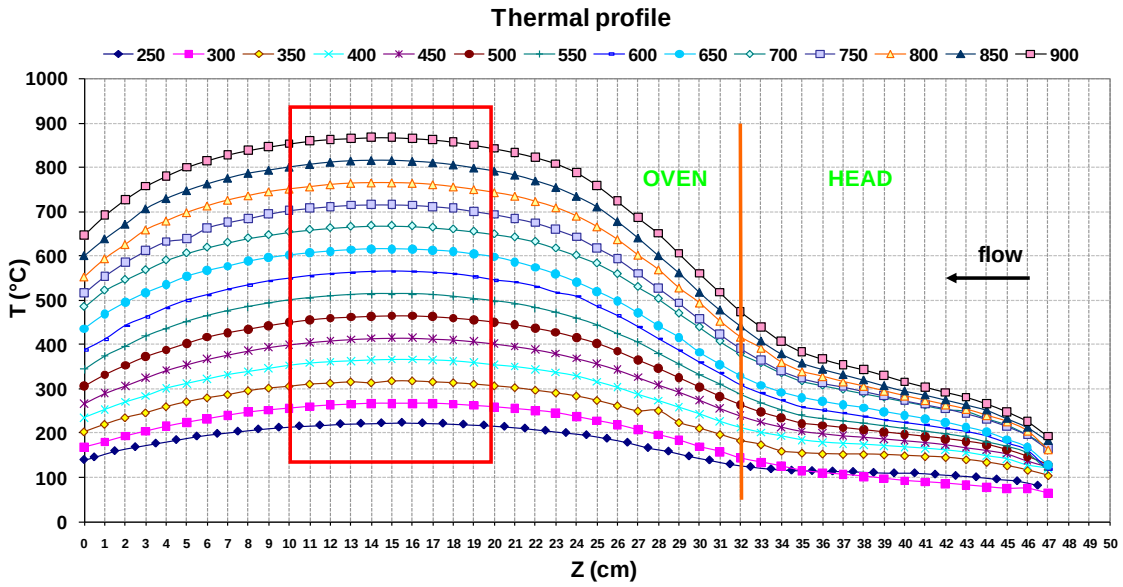

Fig. 3.7 Thermal profile of the reactor inside(OVEN) and outside(HEAD) the oven.

BIBLIOGRAFY

1. Faure, R.; Basile, F.; Bersani, I.; Chartier, T.; Cuni, A.; Cornillac, M.; Del Gallo, P.; Gary, D.; Rossignol, F.; Vaccari, A. Elaboration of ceramic foam-supported catalysts for Ethanol Steam Reforming. *International Workshop on Advanced Ceramics*, Limoges, 2008.

2. Geology-XRD Lab. http://www.utc.edu/Faculty/Jonathan-Mies/xrd/xrd.html (accessed Feb 2, 2011).

3. Micromeritics - ASAP 2020, Surface Area & Porosimetry System. http://www.globalspec.com/FeaturedProducts/Detail/Micromeritics/ASAP_2020_Surface_Area_Porosimetry_System/16063/0 (accessed Feb 10, 2011).

4 Results and discussion

4.1 Aim of work

Aim of this work is the study of new process for hydrogen production using bioethanol instead of methane in the steam reforming reaction.

Thermodynamic data indicate high temperature, over 700°C, and atmospheric pressure as conditions to maximize hydrogen production with no methane presence. On the other hand the feasibility of the process is influenced also from industrial conditions that require pressure of 20 bar to operate in optimal economical conditions and integration with the downstream processes. This compromise entails a deep study on reaction conditions and on catalysts which have to show very high activity and selectivity towards hydrogen at atmospheric pressure and very high stability during tests at 20 bar for long time (one week).

The study on catalysts is focus on mixed oxide obtained after calcination of hydrotalcites like compounds. This type of materials presents both redox and acid-basic properties which could play a determinant role in the selectivities of products. Moreover they show high surface area and very small crystal size of the mixed oxide structure produced after calcination, after reduction it is possible to obtain small and thermally stable metal crystallites.

Another important part of work, always about catalysts, is focus on the optimization of coating of selected active phase between hydrotalcite on alumina foams. It was decided to study foam coating because they show advantages respect pellets as less pressure drops and higher geometrical area.

First part of study is dedicated to ethanol decomposition study to understand the relevance of gas phase reactions and the effect of reactor wall versus quartz as reactor material and the use of quartz as inert used to fill the reactor.

Afterward different tests were carried out with a reference catalyst which had shown very good performances in methane steam reforming (*1*), always obtained from an hydrotalcite, to study the effect of various parameters as temperature, steam to ethanol ratio and contact time and choose conditions for catalysts discriminations.

Comparisons of different active phases are studied by decreasing contact times to study deeply reaction mechanism, intermediates and by-products. These tests were carried out only at temperature above 500 °C to maximize hydrogen selectivity and therefore some elements which show interesting results in literature as cobalt (*2*)(*3*)(*4*)(*5*)(*6*) are not taken in exam.

Since in the ethanol steam reforming high relevance on selectivities is due to acid-basic properties of the catalyst (7), also the effects of different type of matrix are studied. Catalysts which exhibited best performances were selected to prepare the slurry to coat on ceramic foams trying to obtain homogeneous and thin coating without cracks.

Last part of the work is dedicated to select under pressure conditions that can enhance lifetime of catalysts by minimize coke formation. Tests were carried out both with pure and surfin ethanol. Activity, selectivity and stability of pellets and foams catalysts were compared.

4.2 Thermal decomposition of ethanol

Thermal decomposition of ethanol can occurs in different zone of reactor:

1. empty space,
2. wall INCOLOY 800HT reactor,
3. "inert" material as quartz.

Each of these contributions was evaluated by means of specific tests and calculations.

4.2.1 Reactivity with INCOLOY 800HT reactor

Since from previous tests (experimental part) ethanol conversion results very low at temperature lower than 500 °C, for the study on ethanol decomposition only tests at high temperature were considered.

In particular two type of tests were carried out: tests with empty reactor and one test with reactor filled of quartz. It is chosen quartz because it is the inert which shows the lowest conversion of ethanol at high temperature and therefore the lowest contribution to ethanol decomposition.

	INCOLOY REACTOR		
Filling	**Empty**	**Empty**	**Quartz**
P (bar)	1	1	1
S/EtOH (mol/mol)	4	4	5
f D (mol/mol)	9	9	4,7
V empty (mL)	60	60	20
Toven (°C)	750	750	750
Tout (°C)	688	691	702
Conv. CH_3CH_2OH (%)	89,99	73,61	29,64
Conv. H_2O (%)	-0,05	-1,20	-0,78
Sel H_2 (%)	45,39	42,84	47,70
Sel. CO (%)	21,24	19,38	0,00
Sel. CO_2 (%)	1,32	0,69	1,25
Sel. CH_4 (%)	8,80	8,41	0,00
Sel. CH_2CH_2 (%)	14,88	15,91	19,46
Sel. CH_3CH_3 (%)	1,98	2,82	0,00
Sel. CH_3CHO (%)	51,81	52,80	79,30

Tab. 4.1 Reactivity of ethanol.

These data show that decreasing empty space in the reactor, a diminution of ethanol conversion is observed with a CH_3CHO/CH_2CH_2 ratio equal to 4. The contribution of

gas phase is determinant, therefore as first approach it is possible to describe the process considering a gas phase reaction which depending on concentration. The rate law equations for a plug flow reactor in steady state are of first order is:

$$k\tau_{mix} = -(1+\varepsilon_{EtOH}\chi_{EtOH})\ln(1-\chi_{EtOH}) - \varepsilon_{EtOH}\chi_{EtOH} \qquad \textbf{I order}$$

In this way it is hypothesized that the most important contribution is due to empty space. In fact the τ_{mix} depends on only empty volume of the reactor, in the formula of calculation of τ_{mix} is not considered the volume of quartz. In addition also the costant K for order zero is considered as a further confirmation that reaction occurs mainly in gas phase.

To compare the contribution of empty space in the tests it is measured the fraction of void when the reactor is filled of inert material. The total volume of the reactor is 60 mL, while the volume of quartz is 40 mL, therefore it is considered 20 mL empty space with quartz tests. The volume of quartz in the reactor was measured in a cylinder. A little amount of water was added in the cylinder, then the quartz loaded in the reactor was put in the cylinder and the increase of volume of water was noted. The difference of water volume is considered as the volume of the quartz.

Then it is calculated the contact time of mix and it is replaced τ_{mix}, C_{EtOH0} and χ_{EtOH} with the right values inside the equation to calculate the costant K and to evaluate which order describe better the system (K more similar).

Filling	**Empty**	**Empty**	**Quartz**
Empty volume (mL)	60	60	20
EtOH $_{std}$ (mL/min)	7,2	14,4	19,1
H_2O $_{std}$ (mL/min)	28,8	57,6	95,7
He $_{std}$ (mL/min)	324,0	648,0	539,7
EtOH $_{r}$ (mL/min)	15,5	25,9	42,3
H_2O $_{r}$ (mL/min)	61,9	103,5	211,5
He $_{r}$ (mL/min)	696,6	1164,6	1193,1
χ_{EtOH}	0,90	0,74	0,30
τ_{mix} **(s)**	**4,651**	**2,782**	**0,829**
x_{EtOH}	0,02	0,02	0,03
C_{EtOH0}	0,000376	0,000451	0,000550

Tab. 4.2 Calculations of τ_{mix}.

With:

EtOH $_{std}$: stream of ethanol in standard conditions

H_2O $_{std}$: stream of water in standard conditions

He_{std} : stream of helium in standard conditions

$EtOH_r$: stream of ethanol in reaction conditions

H_2O_r : stream of water in reaction conditions

He_r : stream of helium in reaction conditions

$\tau_{mix} = V_{empty\ reactor} / (EtOH_r + H_2O_r + He_r)$, calculated in reaction condition

x_{EtOH} : molar fraction of ethanol

$C_{EtOHo} = P_r * x_{EtOH} / (R * T_r)$

P_r : pressure of the reaction

T_r : temperature of the reaction

		Empty (4.65 s)	Empty (2.78 s)	Quartz (0.829 s)
$k = (- (1+\varepsilon_{EtOH}\chi_{EtOH}) \ln (1-\chi_{EtOH}) - \varepsilon_{EtOH} \chi_{EtOH}) / \tau_{mix}$	**I order**	0,5086	0,4918	0,4378

Tab. 4.3 Calculations of K constant for different reaction order.

The K costant for the first order reaction is very similar for each tests, while is different for the reaction order zero. Therefore the rate equation which describe better the system is a reaction order one because the same equation, that of order one, solves three different conditions with different data. Also Morgenstern et al.(*8*), Akande et al. (*9*) and Vaidya et al. (*10*) found this order of reaction while Mas et al. found a reaction order 0.75-0.8 (*11*).

These data allow to know the ethanol decomposition and conversion at different contact time. In addition, the previous assumption that the contribution of quartz is unimportant is confirmed. In fact in the formula of the rate equation it makes equal the $\mathbf{k\tau_{mix}}$ as a $\mathbf{f (\chi_{EtOH}) .}$ If this equation is verified for the three different conditions then all ethanol converted is due to fraction of void because in τ_{mix} only empty space is considered.

4.2.2 Reactivity with quartz reactor

To study the contribution of the reactor some tests were carried out using a quartz reactor filling of quartz. When ethanol conversion is around 70 - 80% CH_3CHO is close to 50 % and in lower amounts than CH_3CHO also CO and CH_4 are observed due to CH_3CHO decomposition By decreasing contact time CO and CH_4 decreases whereas CH_3CHO and CH_2CH_2 increases showing the typical trends of intermediates. As observed previously when the amount of CO and CH_4 is low the ratio between

CH_3CHO and CH_2CH_2 is close to 4. Therefore, considering a similar conversion, quartz reactor shows similar intermediates selectivities to incoloy reactor.

	QUARTZ REACTOR	
Filling	**Quartz**	**Quartz**
τ_{mix} (s)	**2.46**	**0.513**
P (bar)	1	1
S/CH_3CH_2OH (mol/mol)	5	5
f D (mol/mol)	4	4
V empty (mL)	20	20
Toven (°C)	750	750
Toven (°C)	695	695
Conv. CH_3CH_2OH (%)	74.46	20.66
Conv. H_2O (%)	-3.59	-0.92
Sel H_2 (%)	26.66	23.85
Sel. CO (%)	13.01	3.68
Sel. CO_2 (%)	0.26	0.00
Sel. CH_4 (%)	10.85	3.02
Sel. CH_2CH_2 (%)	18.48	17.00
Sel. CH_3CH_3 (%)	1.19	0.49
Sel. CH_3CHO (%)	56.22	75.81

Tab. 4.4 Reactivity of ethanol.

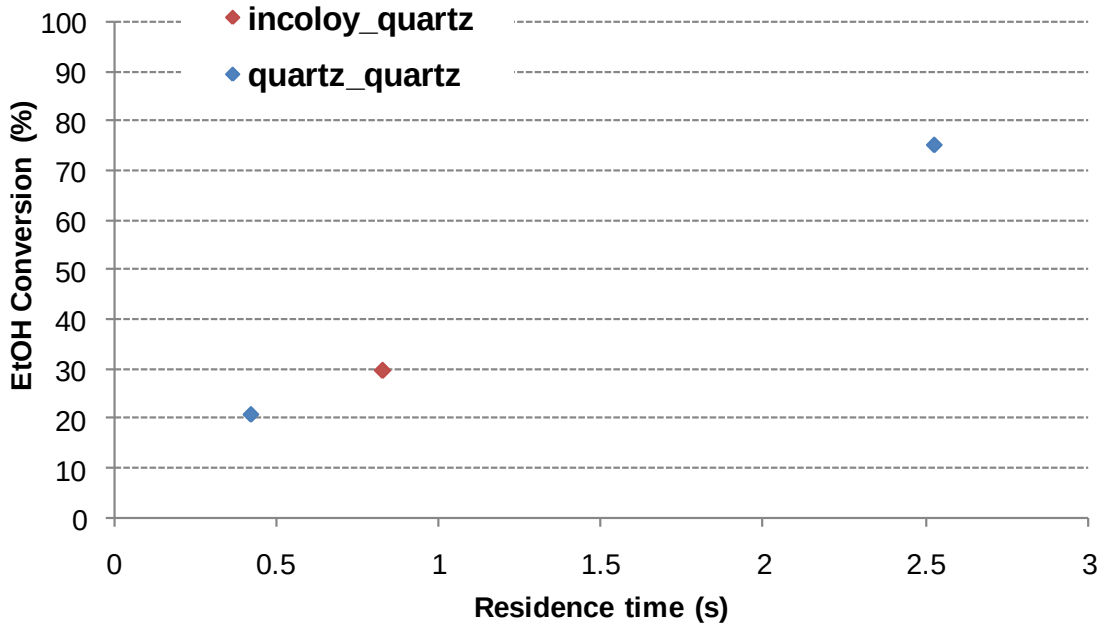

Fig. 4.1 Comparison of ethanol conversion versus residence time for two type of reactors and same filling.

Also data with reactor in quartz show a k constant very similar to previous one calculated for incoloy tests. Therefore it seems that the decomposition occurs mainly in the gas phase and it is not affected by reactor wall or quartz filling.

$k = (- (1+\varepsilon_{EtOH}\chi_{EtOH}) \ln (1-\chi_{EtOH}) - \varepsilon_{EtOH} \chi_{EtOH}) / \tau_{mix}$	**I order**

	INCOLOY REACTOR			QUARTZ REACTOR	
	Empty (4.65 s)	**Empty (2.78 s)**	**Quartz (0.829 s)**	**Quartz (2.46 s)**	**Quartz (0.513 s)**
I order	0.5086	0.4918	0.4378	0.5487	0.5598

Tab. 4.5 Calculations of K constant for different reaction order and different conditions.

4.3 Choice of formulation

4.3.1 Rh-Ni catalyst: study of operative parameters

4.3.1.1 Characterization of fresh sample

First tests, with the aim to study the operative conditions, were carried out on a calcined hydrotalcite based on rhodium and nickel (atomic ratio: $Rh_{0.15}Ni_8Mg_{60}Al_{31.85}$) which had shown very good performances in methane steam reforming (*1*).

Calcined hydrotalcite with silicate as interlayer anions shows mainly the reflections of the forsterite type phase (Mg_2SiO_4) and the MgO type phase, beside those phases a defective spinel type phase (such as $MgAl_2O_4$) is also present (Fig. 4.2). Literature indicates that Rh is soluted in the $MgAl_2O_4$ and MgO while Ni is preferentially present in the MgO type phase (*12*) (*13*).

For what concern the textural properties of the catalyst obtained from hydrotalcite precursor, the catalyst maintains high surface area (96.5 m^2/g) also after calcination at 900°C for 12 h. The sample presents good pore volume and a monomodal distribution of the pore width around 150 Å.

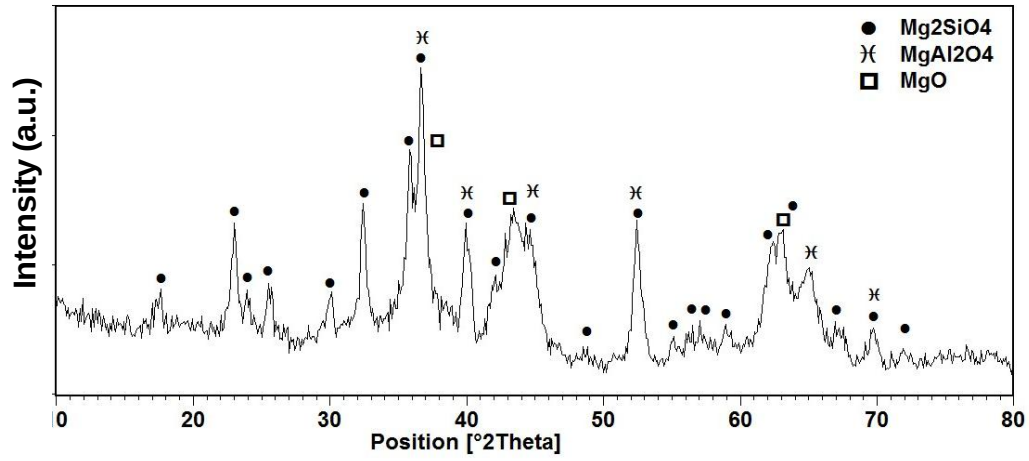

Fig. 4.2 XRD of fresh RNMA.

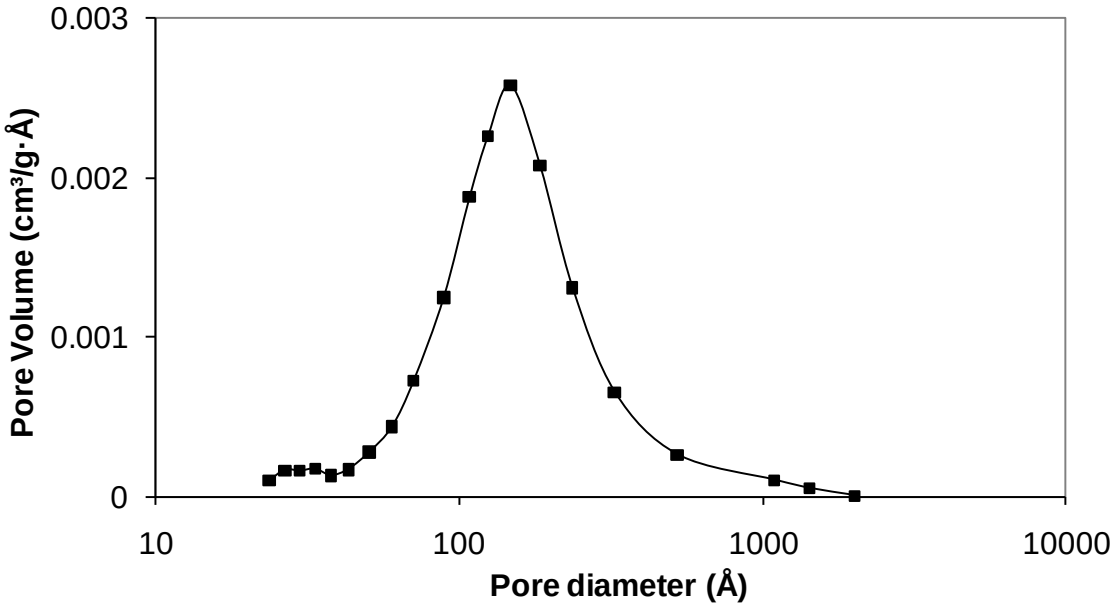

Fig. 4.3 BJH pore size distribution of fresh RNMA.

The fresh sample was analysed by TPR to study the reduction properties and evaluate the suitable temperature for the in situ activation before the catalytic tests (Fig. 4.4).

The nickel is reduced in one single step at 830°C, the high temperature is clear indication of the presence of Ni in a solid solution, while the presence of free NiO and supported Ni can be excluded. The solid solution, as previously described, is mainly constituted by (Mg/Ni)O with probably a minor contribution of Ni in the spinel phase (*12*). Most likely the low rhodium content (0.26 wt %) cannot be detected or may be overlapped by the main peak.

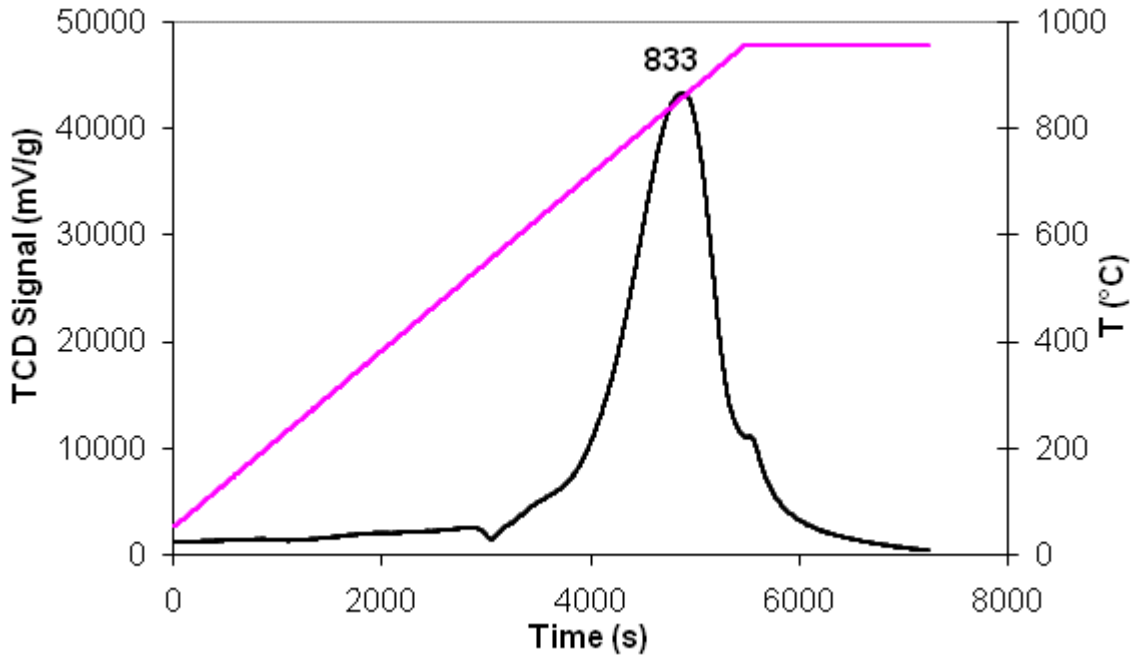

Fig. 4.4 TPR of fresh RNMA.

4.3.1.2 Activity

The tests were carried out changing the following reaction parameters:

P = 1 bar;
Toven = 300, 450, 600 and 750 °C;
S/CH_3CH_2OH = 5 and 4 mol/mol;
fD = He/(H_2O+CH_3CH_2OH) = 9 mol/mol;
CT (calculated in standard conditions) = 1 and 0.5 s;
V = 6 mL;
Pellets size = 14-20 mesh.

As general trend it can be stated that the real temperature inside the reactor is about 50 °C less than that of the oven and it changes with residence time and therefore this temperature is chosen as reference during description and discussion of results while, Tout is specified and discussed to identify the specific temperature of the catalytic tests because of it can change with residence time and conditions. Tests were carried out starting from 250 °C and increasing temperature, for each temperature, except 250 °C, two contact times were tested and the same S/CH_3CH_2OH ratio was maintained equal to 5. After that the catalyst was unloaded and a fresh sample was loaded again to repeat tests with S/CH_3CH_2OH ratio equal to 4.

The evolution of the ethanol and water conversions and products selectivities is presented in Fig. 4.5 as a function of temperature.

The high amount of catalyst influences positively ethanol conversion which is complete also at 250 °C and water to ethanol 5 while water conversion is very low. The

complete conversion of ethanol affects positively the presence of intermediates: no CH_3CHO and only some traces of CH_2CH_2 are observed with total ethanol conversion.

CO selectivity is similar to H_2 selectivity because at 250 °C main reaction is ethanol decomposition into CO, CH_4 and H_2 as it is showed by products distribution.

$$CH_3CH_2OH \rightarrow CH_3CHO + H_2 \rightarrow CH_4 + CO + H_2$$

$$CH_3CH_2OH \rightarrow CH_2CH_2 + H_2O \rightarrow CH_4 + CO + H_2$$

In principle CO and H_2 can react to give CH_4 and water but in this case this would generate a higher methane selectivity.

$$CO + H_2 \leftrightarrows CH_4 + H_2O$$

As clear showed in the Fig. 4.5 this is not the case and even if a slight methanation can be present and it explains the slightly higher CH_4 selectivity respect CO and H_2, it can concludes that at 250°C the activity in methanation is very poor. Beside the methanation similar consideration can be drawn also taking into account the low CO_2 concentration, which can be attributed to low presence of water gas shift reaction.

$$CO + H_2O \leftrightarrows CO_2 + H_2$$

This is confirmed looking at the results at higher temperature (400°C) where, due to the water gas shift equilibrium, the amount of CO_2 is higher while CO is very low. At this temperature the methanation reaction is more evident and the results are not far from the equilibrium. Following the CO_2 selectivity variation with temperature it can be observed a maximum at 550°C as thermodynamic predicts.

The amount of CO and CH_4 depends on the temperature and related equilibrium. At 400 °C the amount of CH_4 is high because at low temperatures the methanation of CO is favored. However, increasing the temperature (550-700 °C) the equilibrium is shifted towards the methane reforming with a total conversion of methane in CO and H_2. In particular the hydrogen selectivity is already close to 95% at 550°C and it is very close to 100% at 700°C. Furthermore the increasing amount of CO at 700 °C respect 550 °C may be due to water gas shift equilibrium, that at high temperature is shifted to CO production.

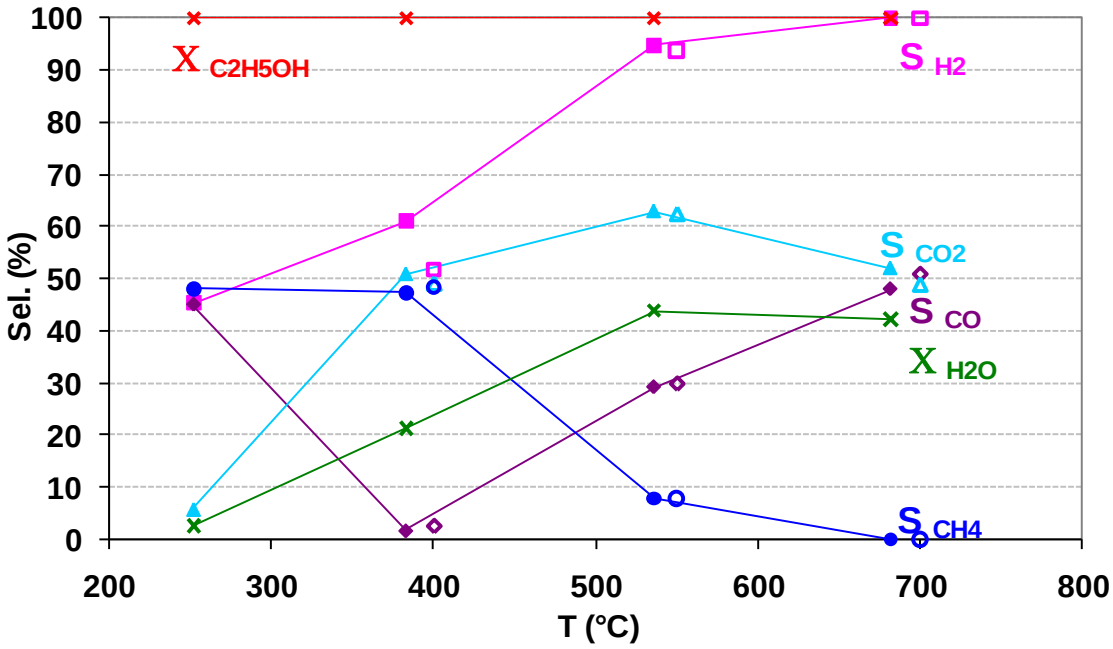

Fig. 4.5 Effect of T at CT = 1 s and S/CH_3CH_2OH = 5 mol/mol.

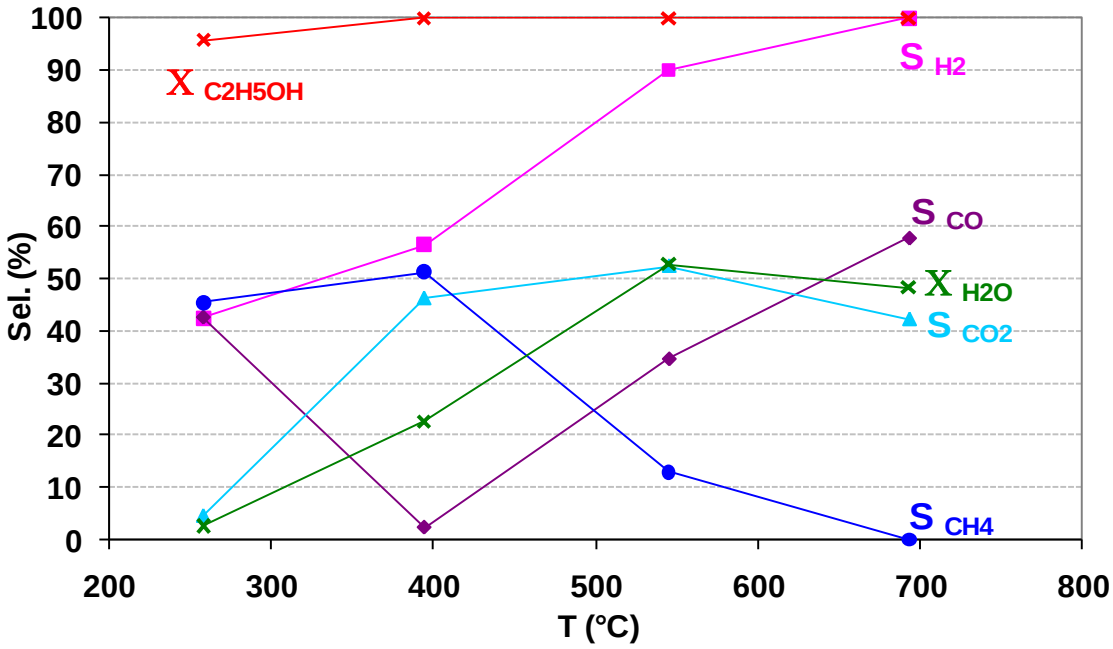

Fig. 4.6 Effect of T at CT = 1 s and S/CH_3CH_2OH = 4 mol/mol.

The effect of contact time and water to ethanol ratio are showed in Fig. 4.7 and Fig. 4.8.

The halving of contact time (0.5 s respect to 1 s) doesn't influence products distribution which presents very similar results, therefore it is possible to confirm and conclude that even at 400 °C the system is close to thermodynamic equilibrium.

The comparison of the tests at different water/ethanol ratio is affected by the equilibrium trends with an increase of hydrogen production by increasing of water to ethanol ratio, while the CO and CH_4 selectivities decrease. Results confirm these trends: at 400 and 550°C higher H_2 selectivity is obtained with water to ethanol equal to 5 with respect to the tests at a ratio H_2O/CH_3CH_2OH of 4. At high ratio, water gas shift reaction and reforming are more favourite while methanation is less favourite and therefore its contribution is lower than with water to ethanol equal to 4. At 700 °C no differences are observed in H_2 selectivity because it was calculated not considering hydrogen linked in water as by-product, although considering the dry gas composition it is evident that higher H_2 amount is obtained with water to ethanol 5 (Tab. 4.6). A further confirmation of this is the higher CO_2 selectivity by increasing the ratio.

CT (s)	0.50	0.50	0.50	0.50	0.50	0.50
S/CH_3CH_2OH (mol/mol)	**5**	**5**	**5**	**4**	**4**	**4**
Toven (°C)	450	600	750	450	600	750
H_2 (%)	60.85	73.71	73.63	56.88	72.24	72.10
CO (%)	0.82	7.39	13.71	1.03	9.61	17.76
CO_2 (%)	19.43	17.22	12.66	17.55	14.05	10.14
CH_4 (%)	18.90	1.68	0.00	24.55	4.10	0.00

Tab. 4.6 Dry gas composition at two different steam to ethanol ratio.

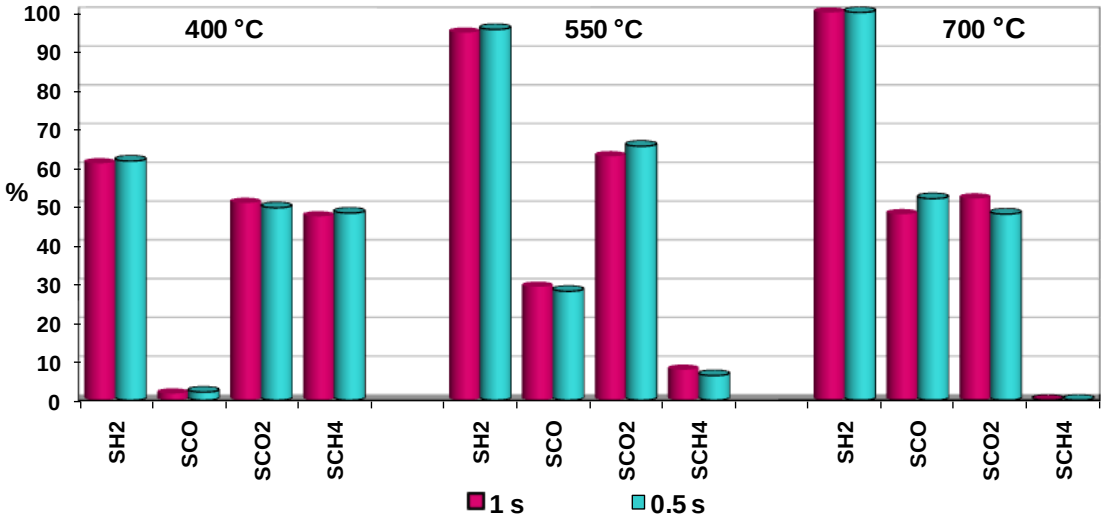

Fig. 4.7 Effect of CT at S/CH_3CH_2OH = 5 mol/mol.

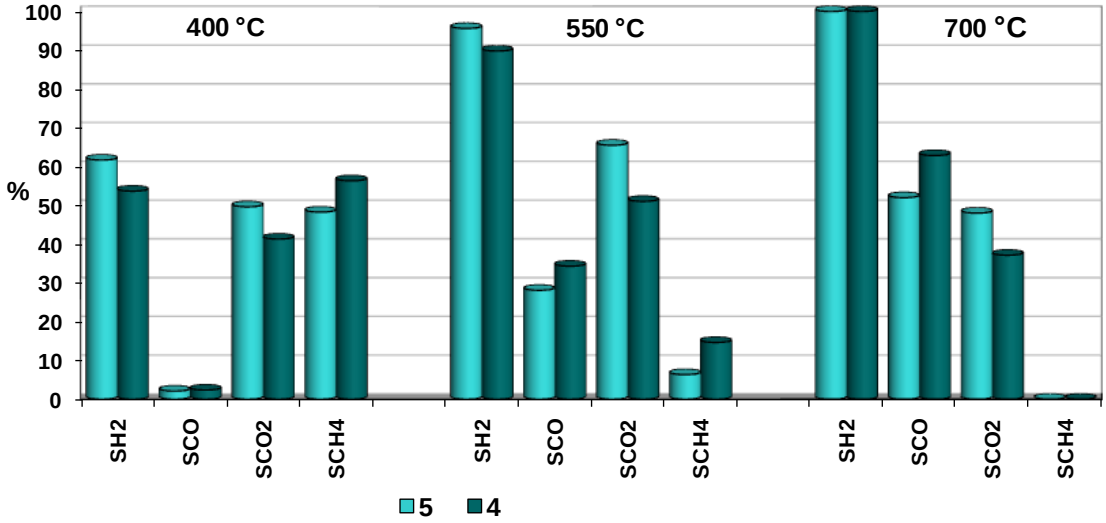

Fig. 4.8 Effect of S/CH_3CH_2OH at CT = 0.5 s.

4.3.1.3 Characterization of spent sample

Two spent catalysts are named as:

RNMAs5 for the spent catalyst with steam to ethanol equal to 5 and
RNMAs4 for that one with steam to ethanol equal to 4.

Both catalysts show similar XRD pattern, with same phases Mg_2SiO_4, MgO and $MgAl_2O_4$ furthermore Ni° phase is observed. Mg_2SiO_4 and $MgAl_2O_4$ phases appear more defined but it is not possible the calculation of the particles dimension because the reflections are not well resolved.

The steam to ethanol ratio influences coke presence: only RNMAs4 presents a broad peak at 25 2θ which is probably due to amorphous coke as it was reported by Hardiman et al.(14) (Fig. 4.9).

The values of specific surface area, pore volume and desorption pore widths of the fresh and spent catalysts are reported in Tab. 4.7, while the pore size distributions are showed in Fig. 4.10.

After the catalytic tests the surface area and pore volume are slightly lower respect to the fresh sample and a shift of the maximum pore width is observed. This same trends can be due to a slightly sintering of the catalysts.

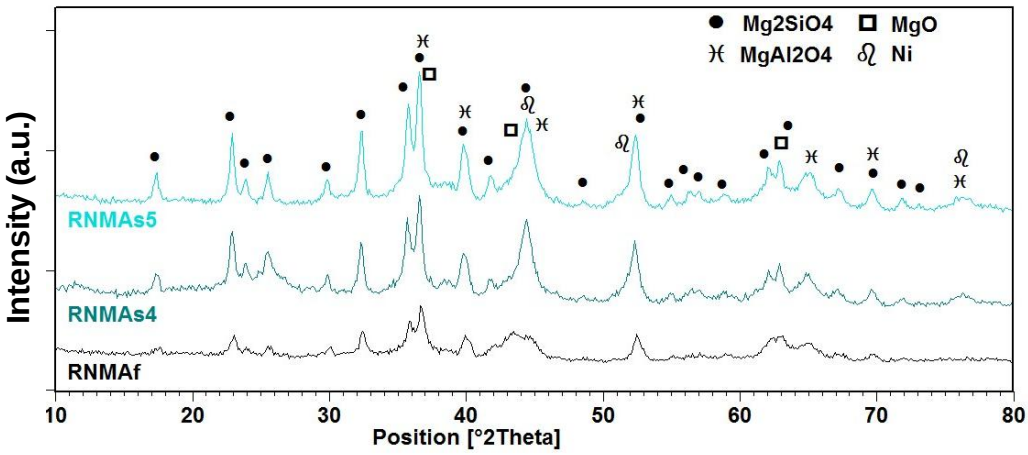

Fig. 4.9 XRD of fresh and spent RNMA.

		RNMAf	RNMAs5	RNMAs4
BET surface area	m^2g^{-1}	96.54	94.95	93.96
t-plot micropore area	m^2g^{-1}	11.59	13.61	14.79
BJH desorption cumulative volume of pores	cm^3g^{-1}	0.680	0.646	0.631
BJH desorption maximums pore widths	Å	148	27,35,165	35,169

Tab. 4.7 Surface area and pores volume and width of fresh and spent RNMA.

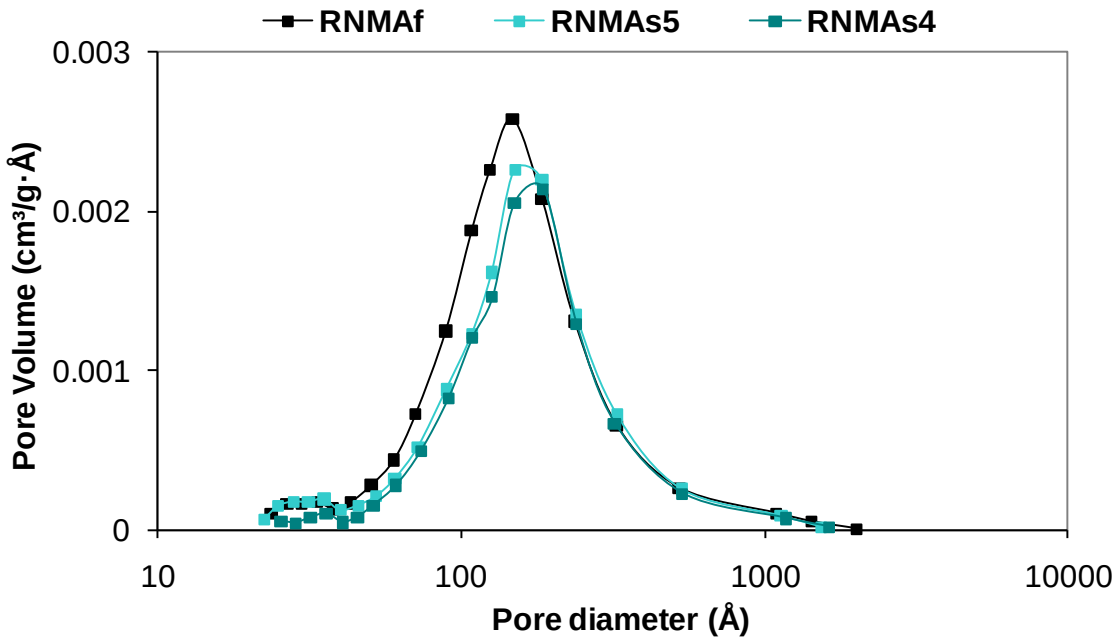

Fig. 4.10 BJH pore size distribution of fresh and spent RNMA.

The oxidation profile of both spent RNMA show a peak at 310°C (Fig. 4.11), which is assigned to free Ni. For both spent samples the value of the temperature of the oxidation of free Ni is slightly higher than the fresh sample. As porosimetry data suggest, a slightly sintering of the catalyst was occurred.

During this analyses the CO2 formation was monitored (Fig. 4.12). The CO_2 formed at about 200-300 °C may be due to carbonaceous deposits mainly in the form of amorphous carbon, while the CO_2 formed at about 550 °C may be due to oxidation of filamentous form of carbon.

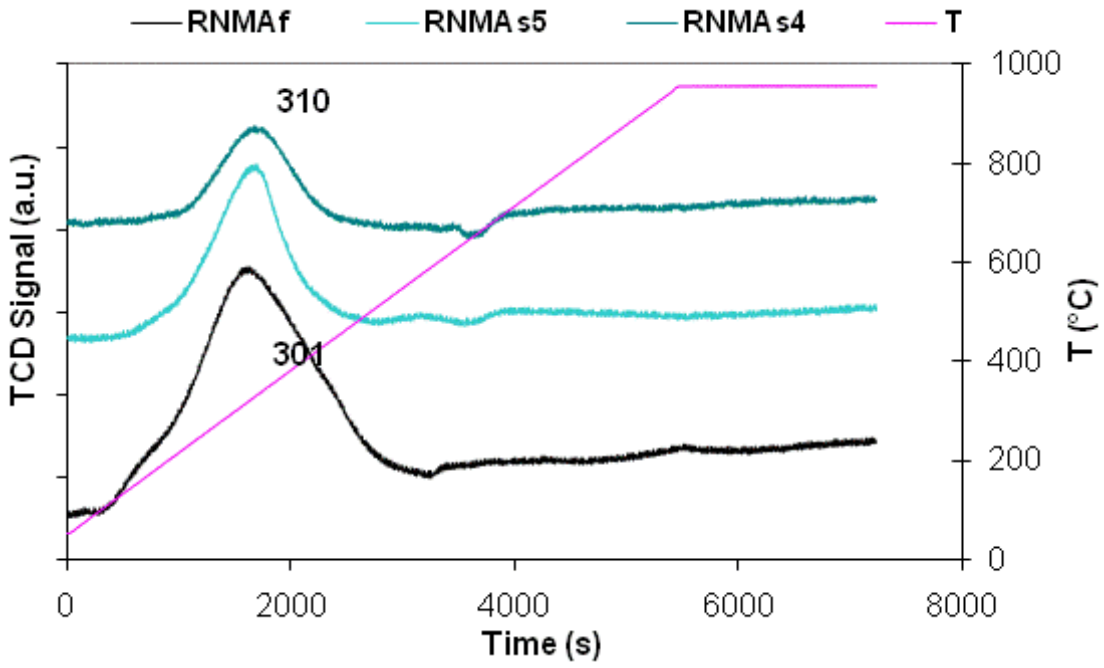

Fig. 4.11 TPO of fresh and spent RNMA.

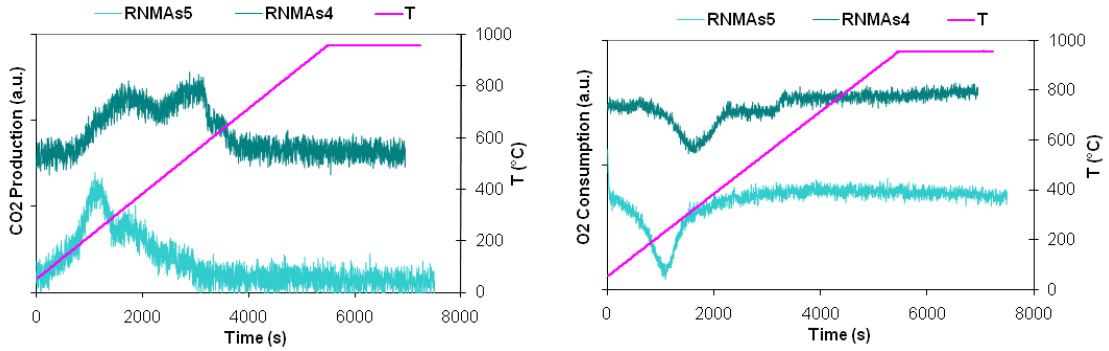

Fig. 4.12 CO_2 production and O_2 consumption during TPO analyse.

4.3.2 Rh catalysts: effect of a second metal

After preliminary tests in which it was studied some trends as effect of temperature and steam to ethanol ratio of a reference catalyst, it was chosen new reaction conditions to study the effect of a second metal and at the mean time to maximize H_2 selectivity. Furthermore, in consideration of the high activity shown by the RNMA which are close to the thermodynamic equilibrium, the contact time of the new tests was decreased in the attempt to discriminate the catalysts activity and selectivities. The used catalysts formulation (as atomic ratio percentage) is summarized in the following table:

	RNMA	R0075N4MA	RMA	R05MA	RFMA
Mg	60	64	68	68	68
Al	31.85	31.925	31.85	31.45	15.85
Rh	0.15	0.075	0.15	0.55	0.15
Ni	8	4	/	/	/
Fe	/	/	/	/	16
anions	silicates	silicates	silicates	silicates	silicates

Tab. 4.8 Compositions of catalysts.

4.3.2.1 Characterization of fresh catalysts

The RNMA catalyst described in the previous paragraph was compared with two similar catalysts containing only Rh and Rh-Fe maintaining the same M^{2+}/M^{3+} ratio, i.e. replacing in the HT precursor preparation the Ni^{2+} with Mg^{2+} or the Al with Fe^{3+}.

The comparison of rhodium hydrotalcite (RMAf) with that one with also nickel shows more crystalline forsterite type phase (Mg_2SiO_4), preferentially combined with silicate in the forsterite type phase with respect to the Ni^{2+} preferentially present as Ni/MgO phase. Beside that rhodium hydrotalcite shows MgO type phase and spinel type phase. The MgO type phase is also clearly visible in the Rh calcined hydrotalcite while spinel type phase is overlapped to the mixed oxide and forsterite type phase. Differently in the hydrotalcite in which part of aluminium was substituted by iron, XRD patterns show broad reflections of mixed oxide and spinel type phase widely overlapped, while as a side phase also forsterite is present. The high intensity of the spinel type phase is due to the higher tendency of Fe to form spinel and to the higher lattice factor (due to the high atomic number) of Fe whit respect to Al also present in the spinel type phase. The broad peak are due to the possibility to have several type of

spinel ($MgFe_2O_4$, $MgAlFeO_4$) which are overlapped with the forsterite and the mixed oxide phase (*15*).

It is not excluded that part of iron could be present as Fe^{2+} (*16*) (Fig. 4.13).

Also textural properties of calcined hydrotalcite are influenced by nickel presence: catalysts RNMAf and R0075N4MAf show different volume of pore distributions, while rhodium hydrotalcite both RMAf and R05MAf show two superimposable curves of pore distributions. RMAf, R05MAf and R0075N4MAf show bimodal curve with huge porosity at maximum of 98 Å for Rh-Ni sample and 120-130 Å for Rh sample and minor porosity for all three samples at 36 Å (Fig. 4.14).

The insertion of iron changes type of curve: it shows a broad and an inhomogeneous pore size distribution with two maxima at about 65 and 143 Å (Fig. 4.14).

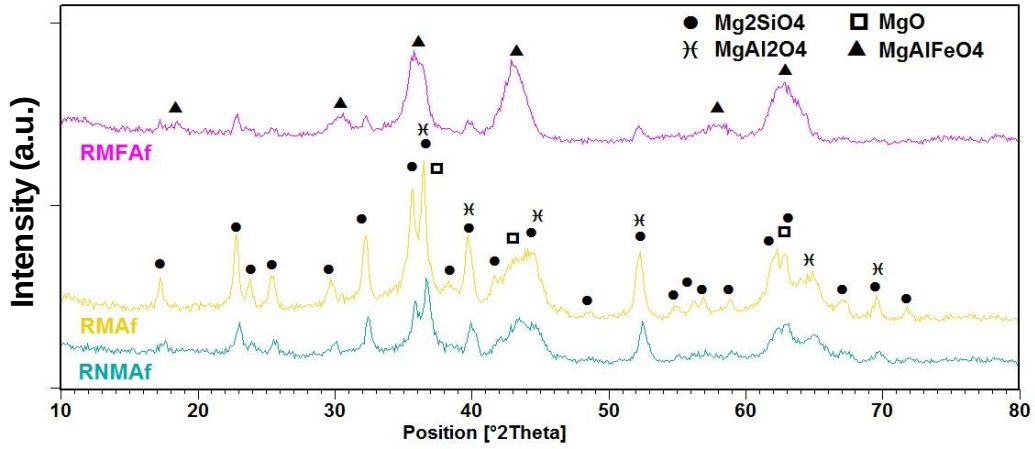

Fig. 4.13 XRD of fresh catalysts.

	BET surface area (m^2g^{-1})	t-plot micropore area (m^2g^{-1})	BJH desorption cumulative volume of pores (cm^3g^{-1})	BJH desorption maximums pore widths (Å)
RNMAf	96.54	11.59	0.680	148
R0075N4MAf	138.73	16.15	0.708	36, 98
RMAf	113.61	19.42	0.562	36, 129
R05MAf	114.79	20.03	0.556	36, 122
RFMAf	108.24	15.78	0.512	65, 143

Tab. 4.9 Surface area and pores volume and width of fresh catalysts.

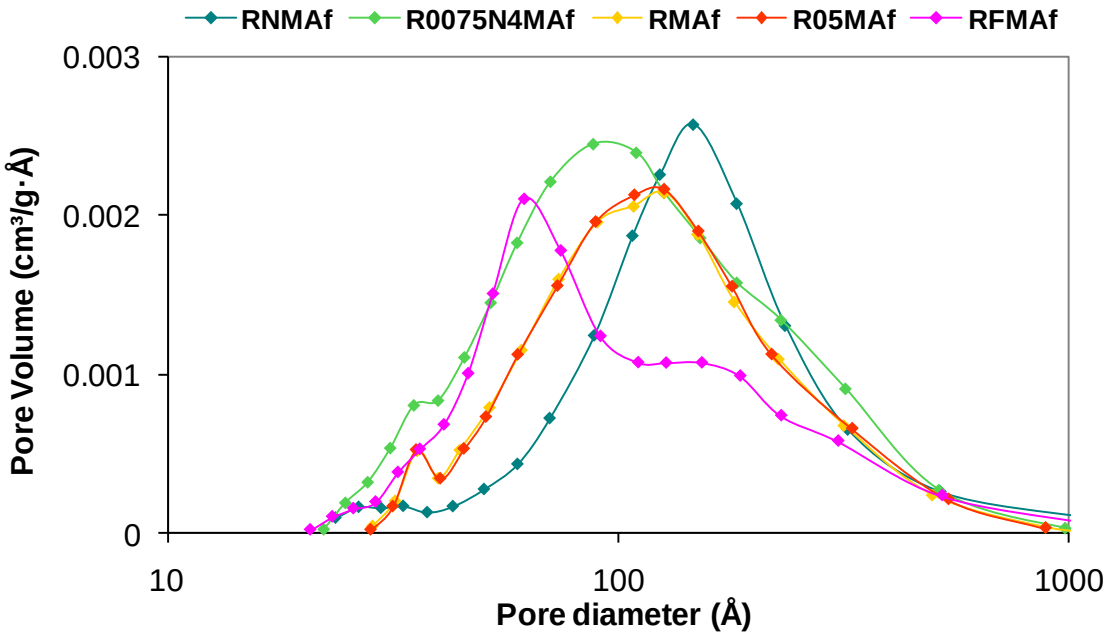

Fig. 4.14 BJH pore size distribution of fresh catalysts.

The TPR analysis of R0075N4MAf is reported in Fig. 4.15. As for RNMAf nickel is reduced in one single step at high temperature and also for this sample Ni is inserted in the structure forming a solid solution. The temperature of reduction is slightly higher than RNMAf (860°C vs 830 °C), higher amount of nickel is responsible of sintering phenomena. The second TPR after oxidation confirms the profile of temperature reduction.

The TPR analysis of RMAf and R05MAf are reported in Fig. 4.16. The TPR profiles show an H_2 consumption peak at 450 °C, together with smaller peaks at higher temperatures. These reduction trends are characteristic of highly stabilized Rh^{3+} species inserted in the structure of mixed oxide phases (*13*).

The TPR analysis of RFMAf is reported in Fig. 4.15. The TPR of fresh catalyst shows not well defined peaks, anyway three peaks are observed at 299, 559 and about 950 °C. The first peak at low temperature suggests a reduction of Rh in the spinel phase assisted by the presence of a reducible cation such as Fe which decreases the reduction temperature of Rh(III) to Rh° of 50°C. The broad peak with a maximum at 559°C are due to a combination of reduction peaks: the Fe is reduced from Fe(III)/Fe(II) in the spinel structure with displacement of Fe in the B position of the AB_2O_4 phase and/or the Fe reduction inserted in the spinel $MgFeAlO_4$ into $Mg_{1-x}Fe_xO$.The peak at 950 °C corresponds to the reduction of $Mg_{1-x}Fe_xO$ to metallic Fe^0(*15*).

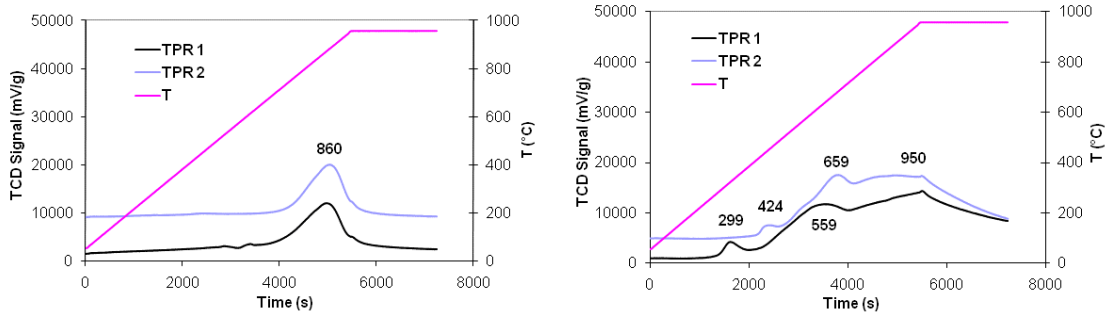

Fig. 4.15 TPR of Ro075N4MAf (left) and RFMAf (right).

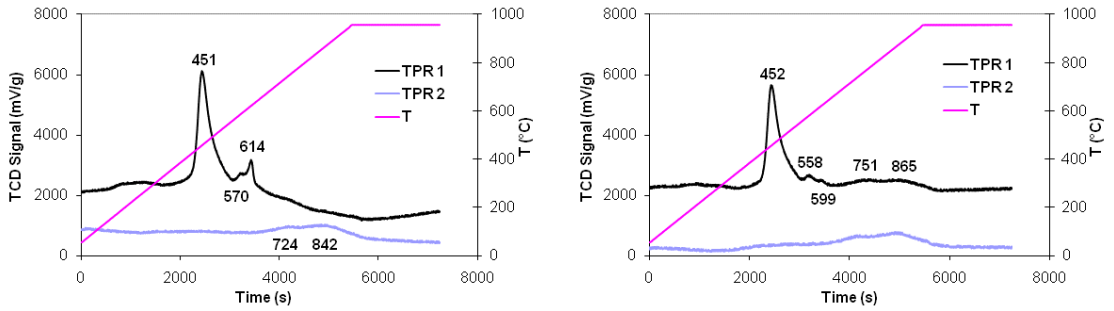

Fig. 4.16 TPR of RMAf (left) and Ro5MAf (right).

4.3.2.2 Activity

The new reaction conditions can be summarized in:

P = 1 bar;
Toven = 600 and 750 °C;
S/CH_3CH_2OH = 5 mol/mol;
fD = He/(H_2O+CH_3CH_2OH) = 4 mol/mol;
V = 1 mL;
Pellets size = 14-20 mesh

Conditions	x	2x	4x	6x
CT (standard) (s)	0.333	0.167	0.083	0.056
CT (700°C) (s)	0.102	0.051	0.025	0.017
CT (550°C) (s)	0.121	0.060	0.030	0.020

Tab. 4.10 Contact time, calculated in standard conditions, at 750 and 600°C.

Rh-Ni catalysts were reduced at 800 °C, while Rh sample are reduced at 500 °C, for all samples reduction time is 2 hours.

For each catalysts tests were started at 700 °C and high contact time, then it was continued by decreasing contact time. Afterwards temperature was decreased to 550

°C and same contact times were repeated at this temperature. In the figures equilibrium values are inserted as empty symbols.

The RNMA performances are reported in Fig. 4.17. At 700 °C initial ethanol conversion is total with H_2 selectivity close to 100 % and no intermediates are observed. During last condition, the presence of some traces of CH_3CHO is observed with the slightly decrease of ethanol conversion. This relationship is more evident at 550 °C when the decrease of ethanol conversion is significant and the presence of CH_3CHO is more marked. Always at 700 °C, CH_4 selectivity is close to zero as predicted by the equilibrium data, by decreasing the contact time the CH_4 selectivity increases both due to kinetic and to thermodynamic reason since at low residence time the temperature decreases due to the endotermicity of the reaction. The effect of the thermodynamic is also visible on the water gas shift equilibrium for which lower residence time leading to lower temperature, decrease of CO selectivity and increase of CO_2 selectivities. At high residence time tests carried out at 550 °C show values close to thermodynamic equilibrium, with a CH_4 selectivity close to 20%; also in this case the decrease of contact time and the consequent decrease of temperature determines an increase of CH_4. Furthermore the presence of C2 intermediates can be observed at low residence time and their increasing trend with residence time affects also C1 products that decreases proportionally.

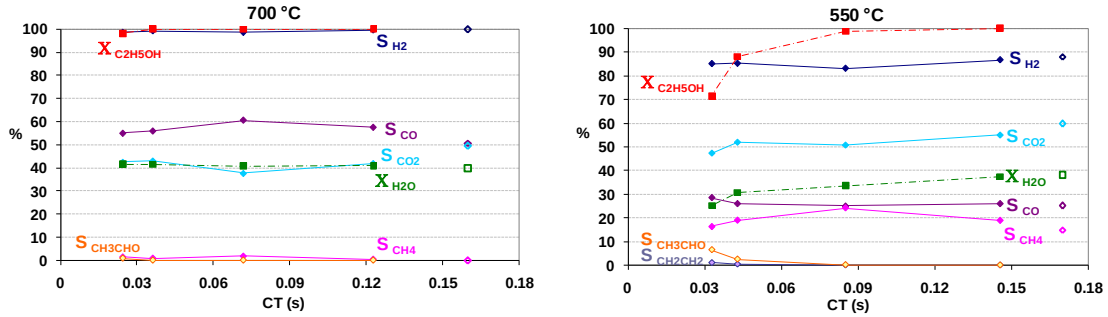

Fig. 4.17 Activity and selectivities of RNMA.

In the sample R0075N4MA the amount of active phase was halved but it is high enough to obtain, at 700 °C, total ethanol conversion and H_2 selectivity close to 100 %. In both conditions at 700 and 550 °C, ethanol conversion is less active than previous one and, in particular at 550 °C, a drop of ethanol conversion is observed. As it was said before ethanol conversion affects gas phase distribution and therefore the presence of intermediates as CH_3CHO and CH_2CH_2 is observed when ethanol conversion is not complete and only traces when it is complete.

At 700 °C, during high residence time tests, products distribution is quite close to thermodynamic equilibrium, but the decreasing of contact time determines the decrease of ethanol conversion, the presence of CH_3CHO, the increase of CH_4 due to less reforming and decrease of CO_2 selectivity due to less water gas shift. At 550 °C

ethanol and water conversions significantly decreases with contact time. As consequence an increase of intermediates and a drop in CO_2 selectivity are observed.

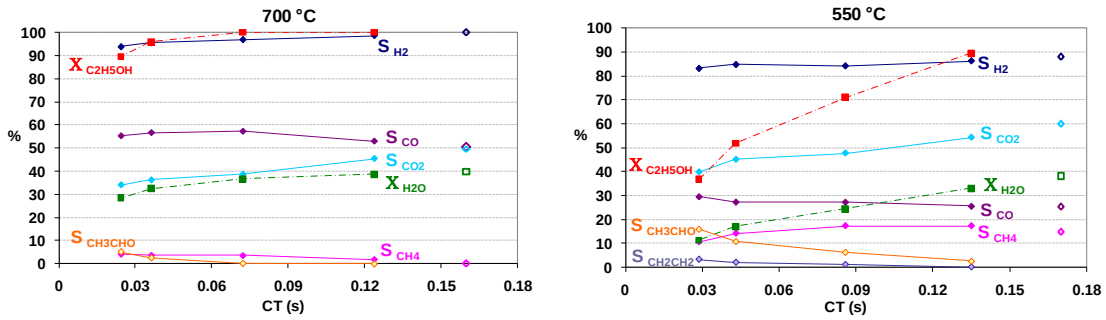

Fig. 4.18 Activity and selectivities of R0075N4MA.

Catalyst with low amount of Rh (RMA) shows initially complete ethanol conversion, but, differently from Rh-Ni series, gas phase distribution is far from thermodynamic predictions. In detail, at 700 °C CO_2 selectivity is lower than equilibrium, while CH_4 selectivity is higher, therefore the decrease of active phase and the absence of Ni affect negatively water gas shift and reforming reactions. At 550 °C ethanol conversion is under 60 % and drops until 20 % in last condition, while water conversion is negative (not present in figure) for all conditions. C1 selectivities are lower than 10 % while significant amounts of CH_3CHO and CH_2CH_2 are observed. In particular CH_2CH_2 selectivity close to 40 % is accompanied by formation of same amount of water due to dehydration reaction which explains negative water conversion due to water formation instead of water consumption.

$CH_3CH_2OH \rightarrow CH_2CH_2 + H_2O$

Furthermore, always at 550 °C, CH_3COCH_3 is observed during first tests. This by-product can be due to aldolic condensation of two molecules of CH_3CHO, the decrease of contact time determines the decrease of CH_3COCH_3 and the increase of CH_3CHO confirming this mechanism.

$2CH_3CHO \rightarrow CH_3COCH_2CHO + O(s) \rightarrow CH_3COCH_2COO(s) + H(s) \rightarrow CH_3COCH_3 + CO_2$

Increasing the amount of Rh (R05MA) CO, CO_2 and CH_4 selectivities are close to thermodynamic equilibrium with gas phase trends similar to Rh-Ni series. During tests 550 °C ethanol conversion drastically drops. Higher C1 selectivities than RMA is obtained but also CH_3COCH_3 is detected.

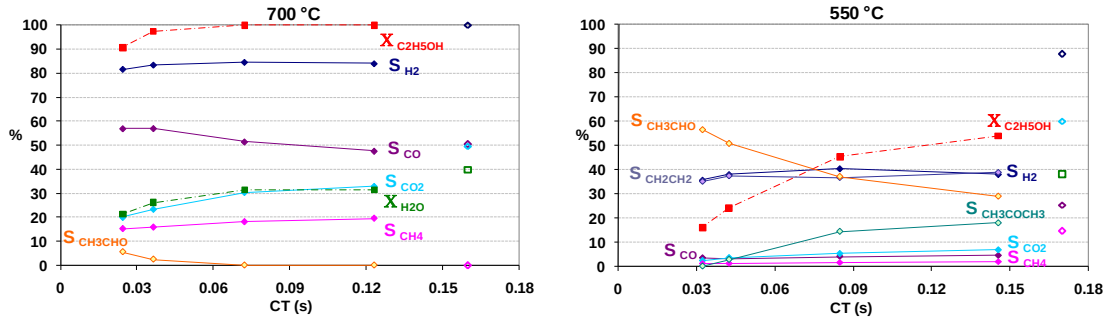

Fig. 4.19 Activity and selectivities of RMA.

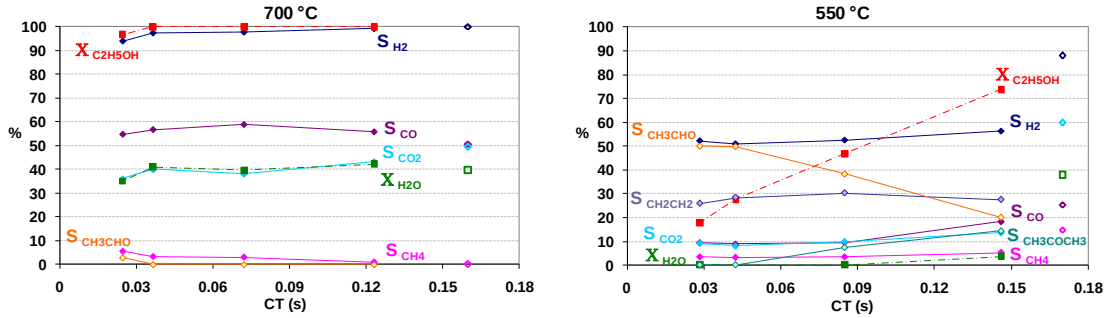

Fig. 4.20 Activity and selectivities of R05MA.

RFMA is the most active catalyst in ethanol conversion since, even at 700 °C and low contact time , shows total ethanol conversion. Despite that gas phase distribution doesn't reach thermodynamic predictions and H_2 selectivity is close to 75 % rather than 100 %. CH_4 selectivity above and CO under equilibrium suggest that the catalyst is less active in the CH_4 reforming. Some traces of CH_2CH_2 are detected. At 550 °C ethanol conversion is complete during first tests, even if it decreases by decreasing contact time. As for all previous catalysts the decrease of ethanol conversion is accompanied by increase of CH_3CHO, CH_2CH_2 and CH_3COCH_3 selectivities.

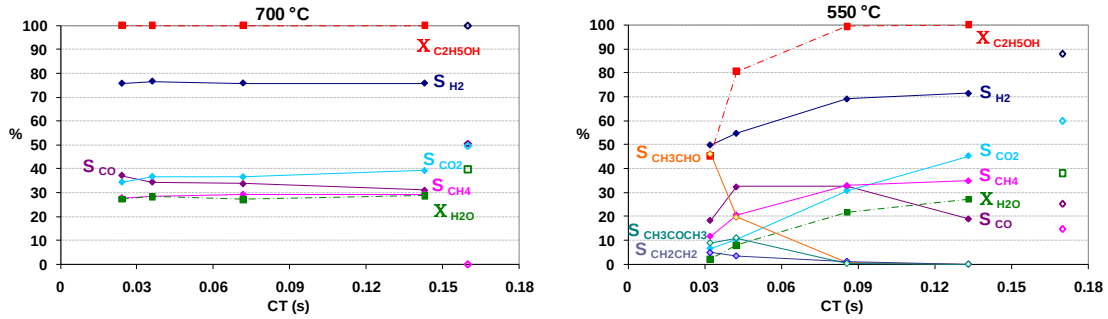

Fig. 4.21 Activity and selectivities of RFMA.

4.3.2.3 Characterization of spent samples

Rh-Ni spent samples don't show significant differences with fresh ones, except the presence of coke (Fig. 4.22). Both spent samples present a large peak at 20-30° 2θ which is probably due to amorphous coke as it was observed for the sample RNMAs4

(14). Furthermore the sample RNMAs shows a peak at 27° 2θ that could be assigned to graphite.

As Rh-Ni, Rh samples show same phases that fresh ones and only for RMAs a low and broad peak at 20-30° 2θ is observed. Also in this case it could be assigned to amorphous coke while graphitic carbon is not present after reaction (Fig. 4.23).

The RFMAs sample shows the same phases than the fresh one, which are fosterite type phase, MgO type phase and spinel type phase, the peaks of the present phases appear more defined in the used one (Fig. 4.24).

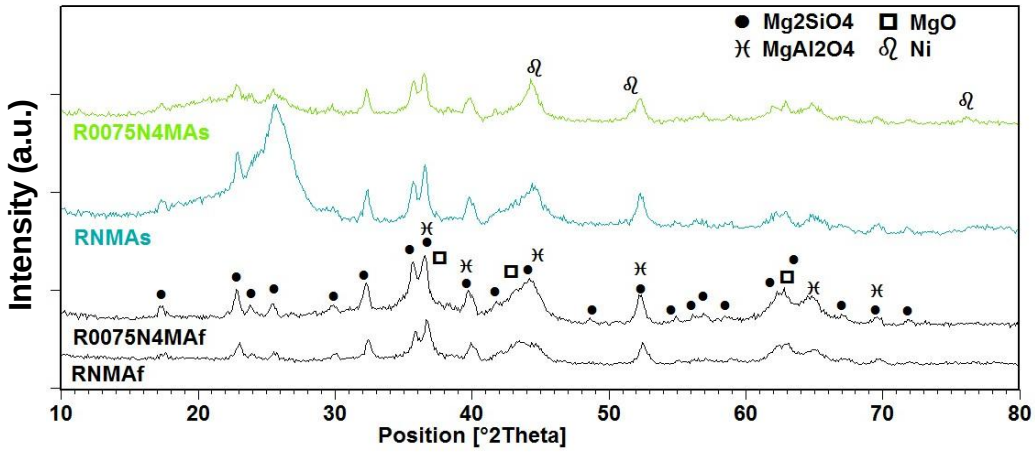

Fig. 4.22 XRD of fresh and spent RNMA and R0075N4MA.

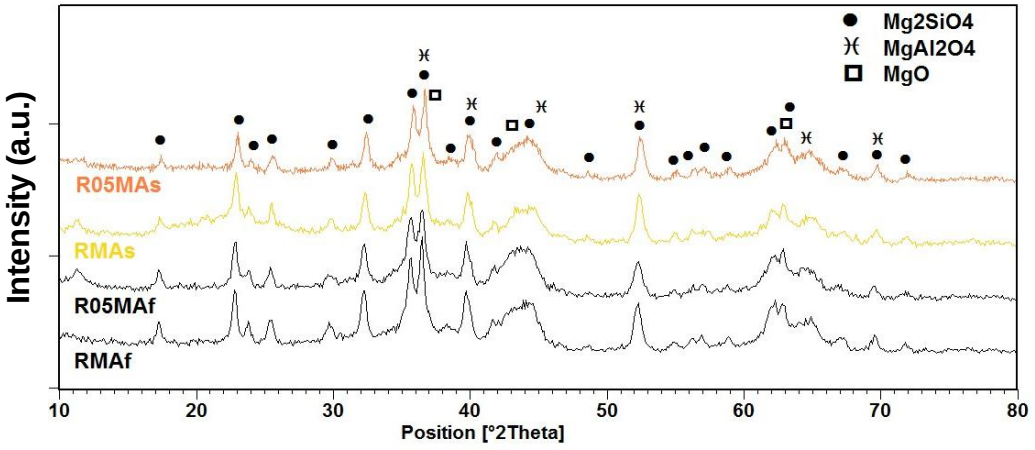

Fig. 4.23 XRD of fresh and spent RMA and R05MA.

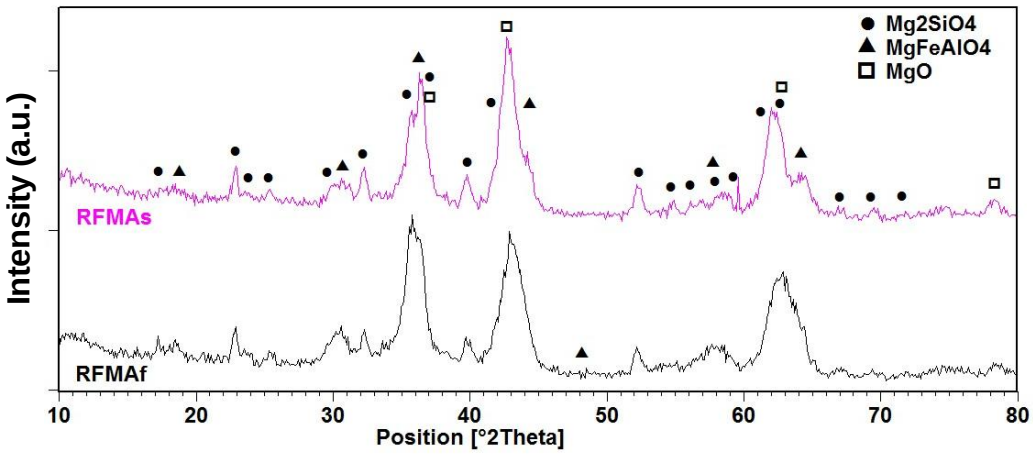

Fig. 4.24 XRD of fresh and spent RFMA.

After catalytic tests the specific surface area and the micropore area of RNMAs are higher than fresh one, instead of R0075N4MAs which shows a drop of both surface area. For both samples pores volume is significantly lower than the fresh one (Tab. 4.11). These different trends could be due to a drastic decrease of mesoporosity in both samples, as BJH pore size distributions show (Fig. 4.25), but in the RNMAs the high surface area is correlated to microporosity while R0075N4MAs show low microporosity and therefore low surface area. The increase of surface area and microporosity confirm XRD data related to coke and graphite formation on the catalyst.

Also RMAs shows a decrease of surface area and pores volume, but it is not so pronounced as for Rh-Ni series, while R05MAs shows higher stability for what concern textural property because surface area and pores volume are very similar to fresh sample. The pore size distribution plots of Rh catalysts are quite similar to fresh ones, two regions of porosity are observed in both fresh and used samples. For what concern the maximum pores width for both spent samples a similar trend is observed: the width of small pores remains constant while the width of large pores slightly increases (Fig. 4.26).

After catalytic tests the specific surface area and pores volume of RFMAs are significantly lower than those of fresh one. The pore size distribution plot of RFMAs is quite different from fresh sample: fresh sample shows two region of porosity from 42 to 101 Å and from 101 to 402 Å, while the spent sample shows the first region at lower width than that of the fresh one (32-40 Å) and the second large region between 40 and 400 Å (Fig. 4.27). The decrease of surface area and pores volume could be due to a sintering of the catalyst.

The comparison of all pore size distribution plots shows that Rh catalysts are the most stable while RNMAs shows the highest coke formation (Fig. 4.28).

	BET surface area (m^2g^{-1})	t-plot micropore area (m^2g^{-1})	BJH desorption cumulative volume of pores (cm^3g^{-1})	BJH desorption maximums pore widths (Å)
RNMAf	96.54	11.59	0.680	148
RNMAs	158.19	33.72	0.196	39
Ro075N4MAf	138.73	16.15	0.708	36, 98
Ro075N4MAs	43.41	5.83	0.185	36,152
RMAf	113.61	19.42	0.562	36, 129
RMAs	85.65	4.70	0.452	36, 155
Ro5MAf	114.79	20.03	0.556	36, 122
Ro5MAs	113.15	3.39	0.553	36, 142
RFMAf	108.24	15.78	0.512	65, 143
RFMAs	77.44	0.00	0.393	36, 72, 142

Tab. 4.11 Surface area and pores volume and width of fresh and spent catalysts.

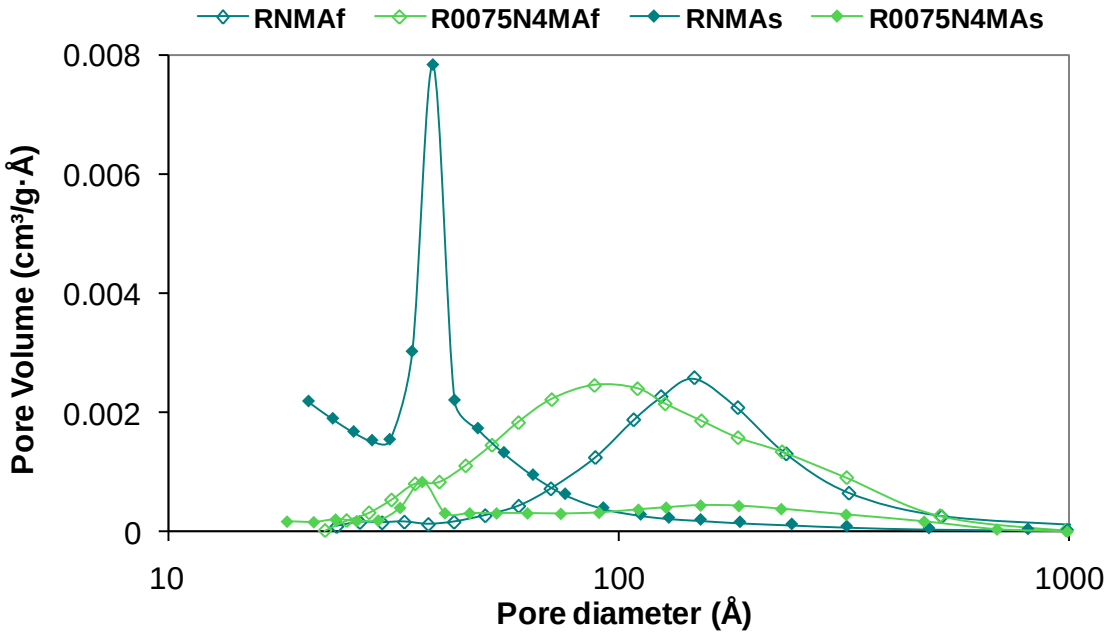

Fig. 4.25 BJH pore size distribution of fresh and spent RNMA and Ro075N4MA.

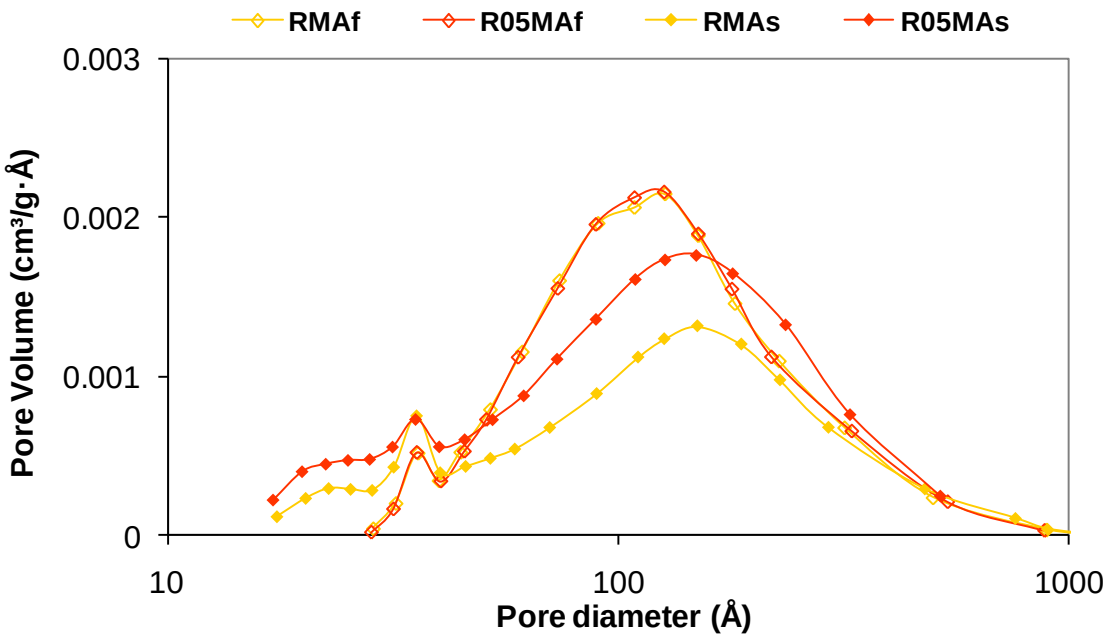

Fig. 4.26 BJH pore size distribution of fresh and spent RMA and R05MA.

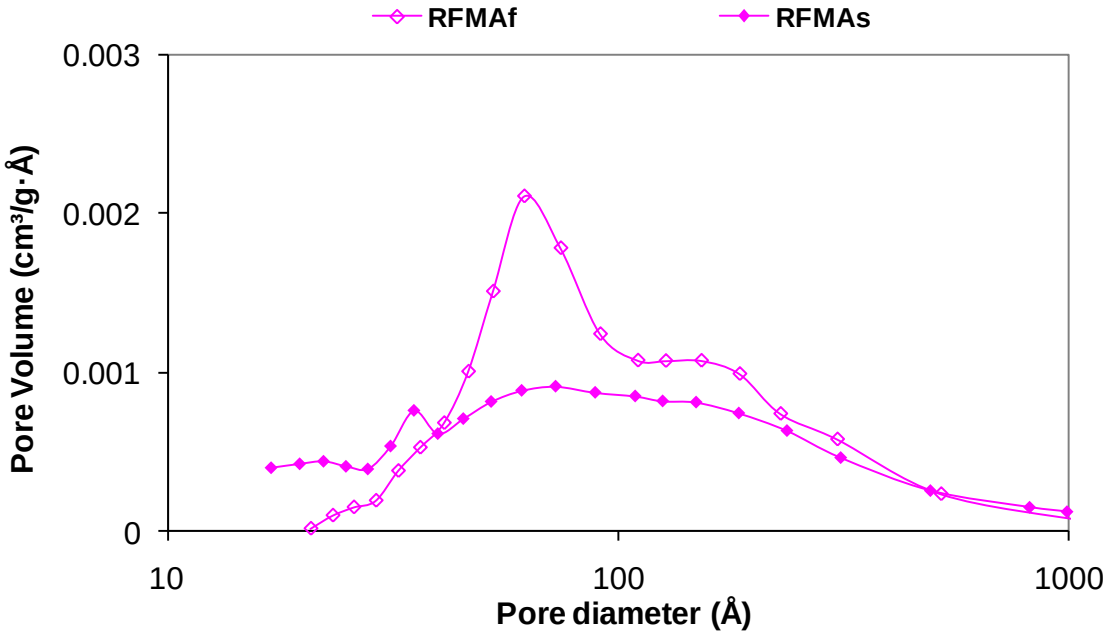

Fig. 4.27 BJH pore size distribution of fresh and spent RFMA.

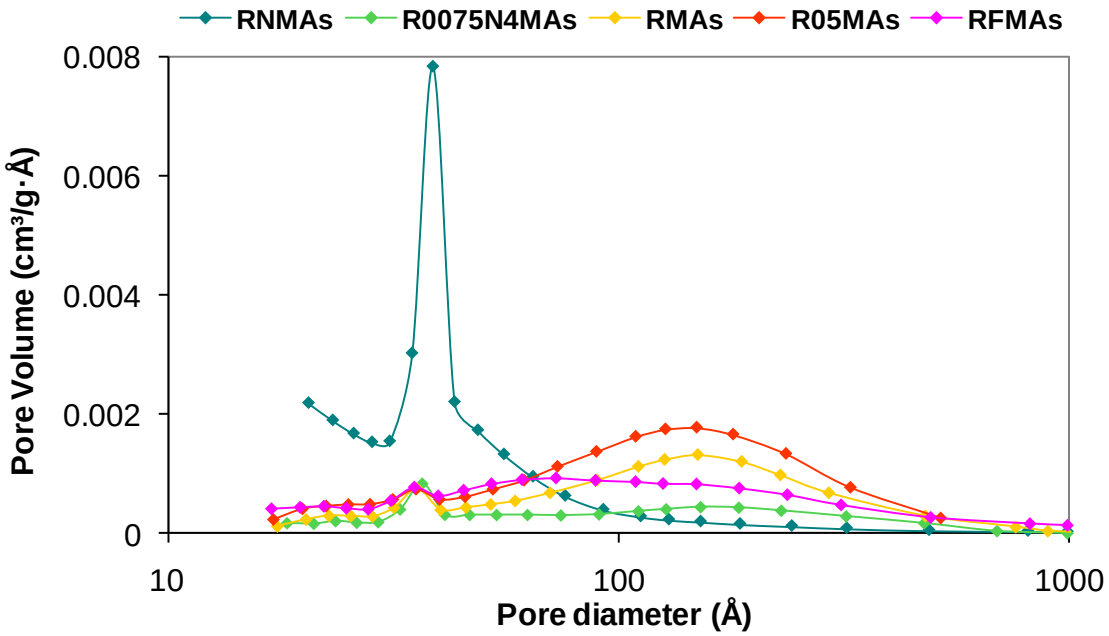

Fig. 4.28 BJH pore size distribution of spent catalysts.

The oxidation profile of RNMAs shows many overlapped peaks in the range of 388 - 681 °C. All these negative peaks can be due to coke because MS analysis presents the same trend of CO_2 production in this range of temperature (Fig. 4.29). The high temperature of oxidation suggests that coke formed during reaction is filamentous coke. Peaks assigned to oxidation of nickel is not observed probably because it is covered by the carbon oxidation peak.

TPO analyses after TPR of R0075N4MAf shows only one peak at 300 °C due to oxidation of reduced nickel while the spent sample shows also two negative peaks at higher temperature that are attributed to filamentous coke as CO_2 trend of mass analyses confirms.

Rh catalysts don't show any peak of oxidation after reduction since the low amount of rhodium inside the samples is difficult to be observed. Anyway spent samples show similar TPO profile: two weak negative peaks, the first and higher in intensity at 489°C with a corresponding CO_2 MS peak that can be attributed to amorphous coke oxidation while the second very weak TPO peak at 620 °C without a corresponding CO_2 peak.

TPO analysis after TPR of RFMAf shows two large overlapping peaks at low temperature due to oxidation of iron because rhodium doesn't exhibit oxidation peaks. Spent sample shows very low intensity peaks due to amorphous carbon oxidation at temperature of 460 °C, while at 620 °C only a very weak TPO peaks is present.

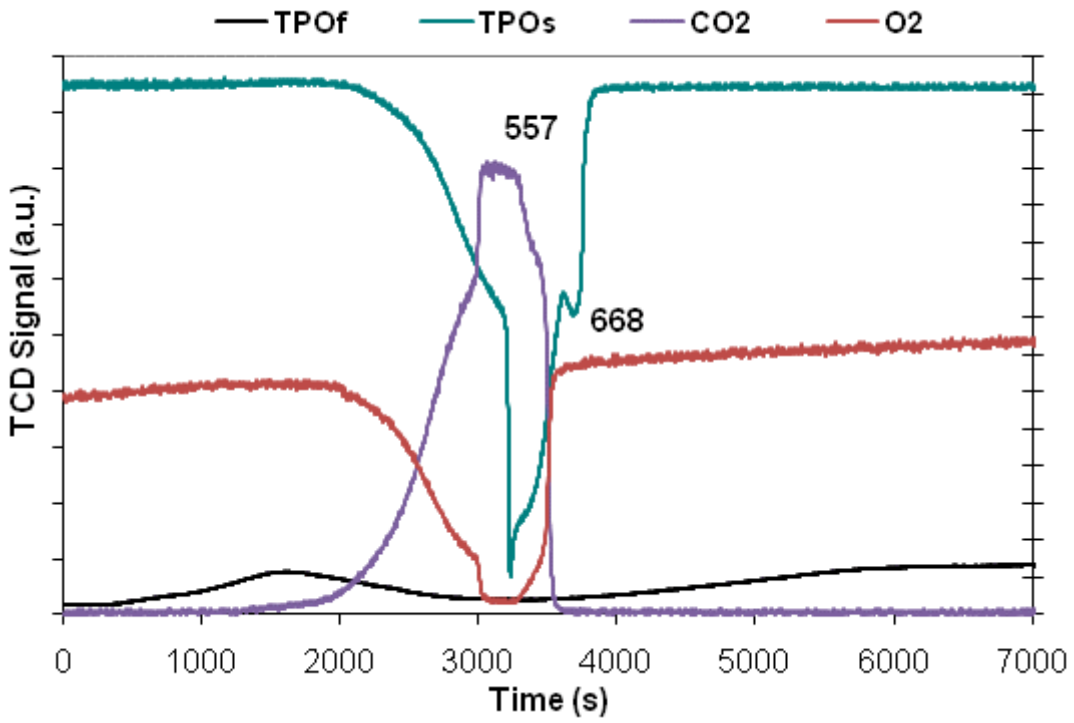

Fig. 4.29 TPO of fresh and TPO, CO_2 and O_2 of spent RNMA.

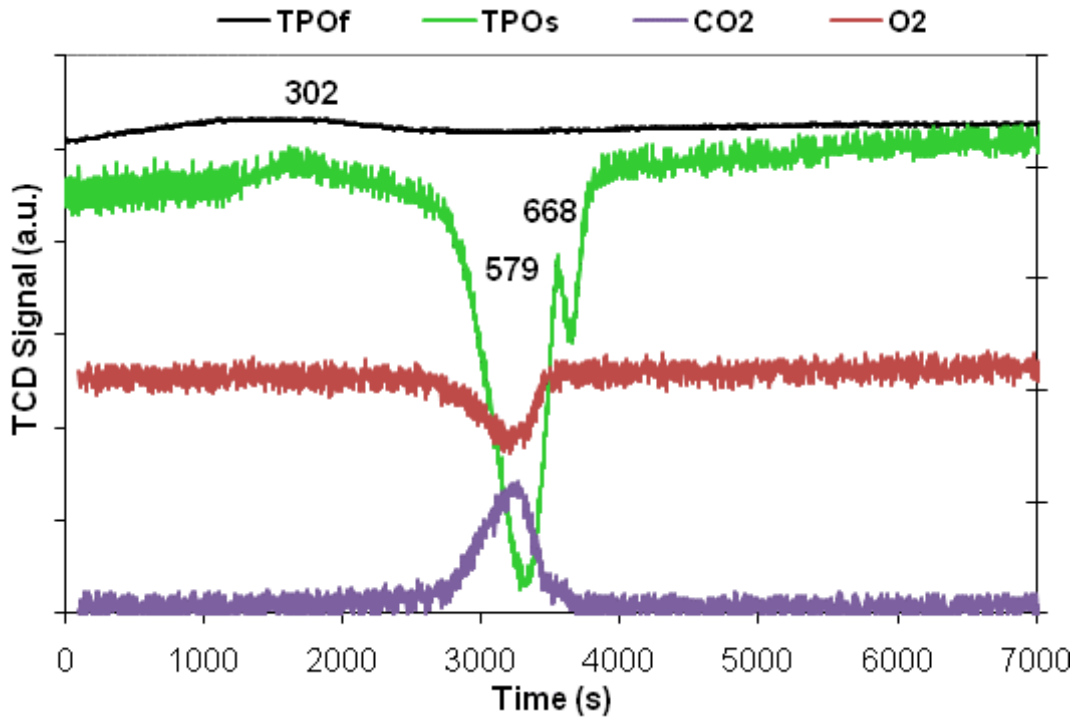

Fig. 4.30 TPO of fresh and TPO, CO_2 and O_2 of spent R0075N4MA.

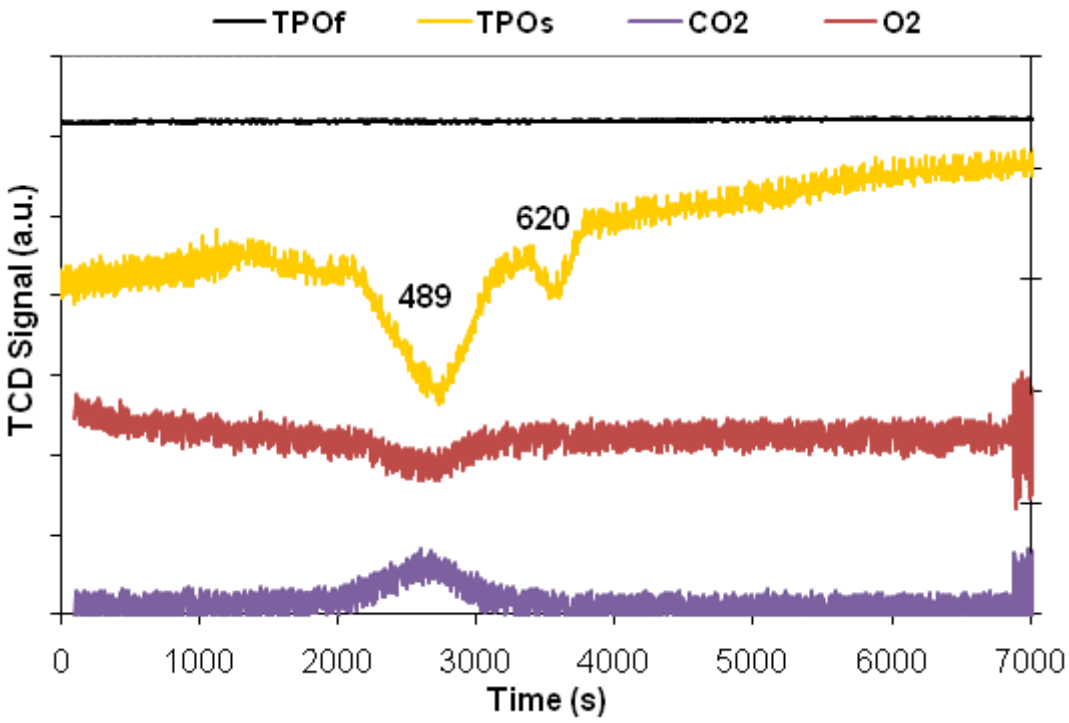

Fig. 4.31 TPO of fresh and TPO, CO_2 and O_2 of spent RMA.

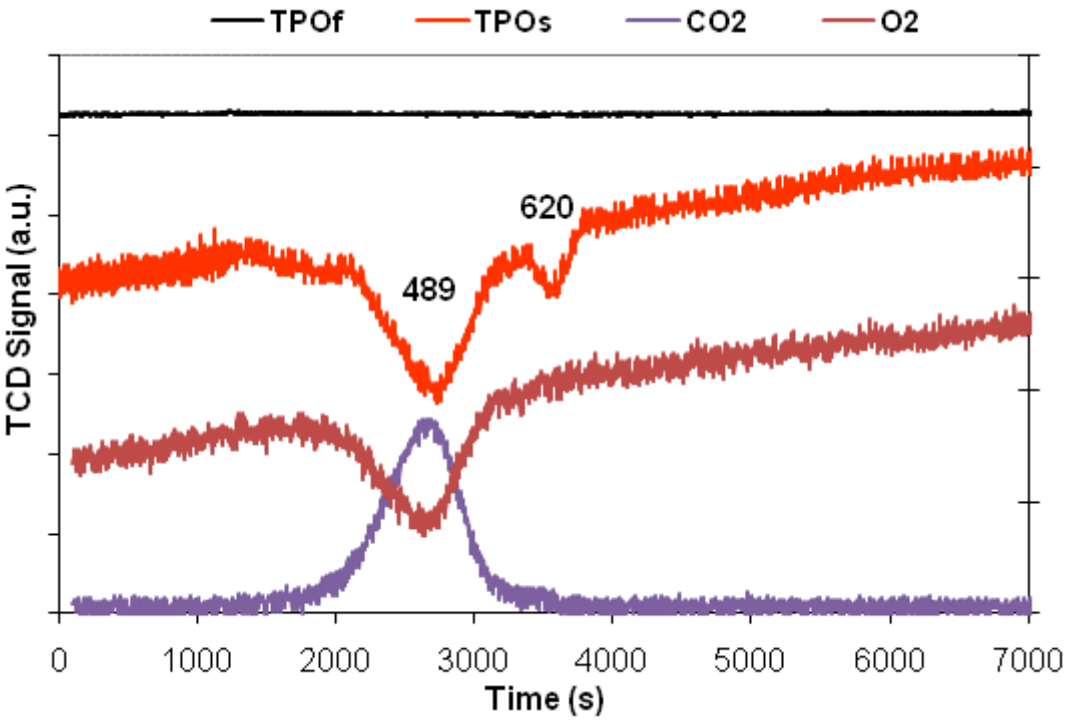

Fig. 4.32 TPO of fresh and TPO, CO_2 and O_2 of spent Ro5MA.

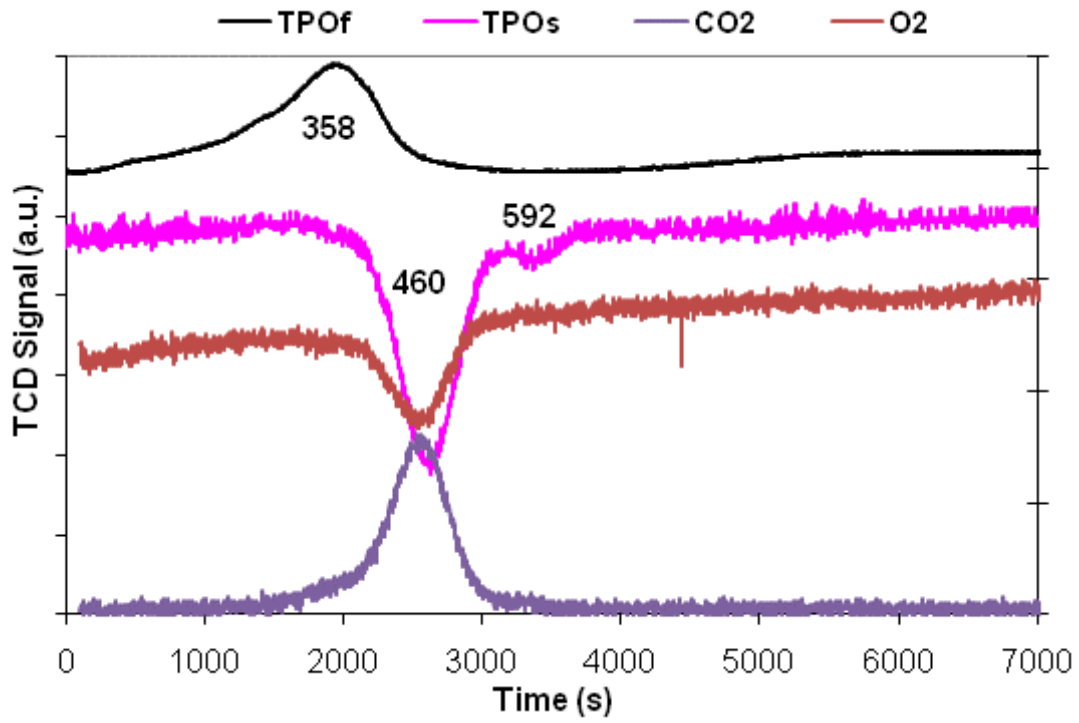

Fig. 4.33 TPO of fresh and TPO, CO_2 and O_2 of spent RFMA.

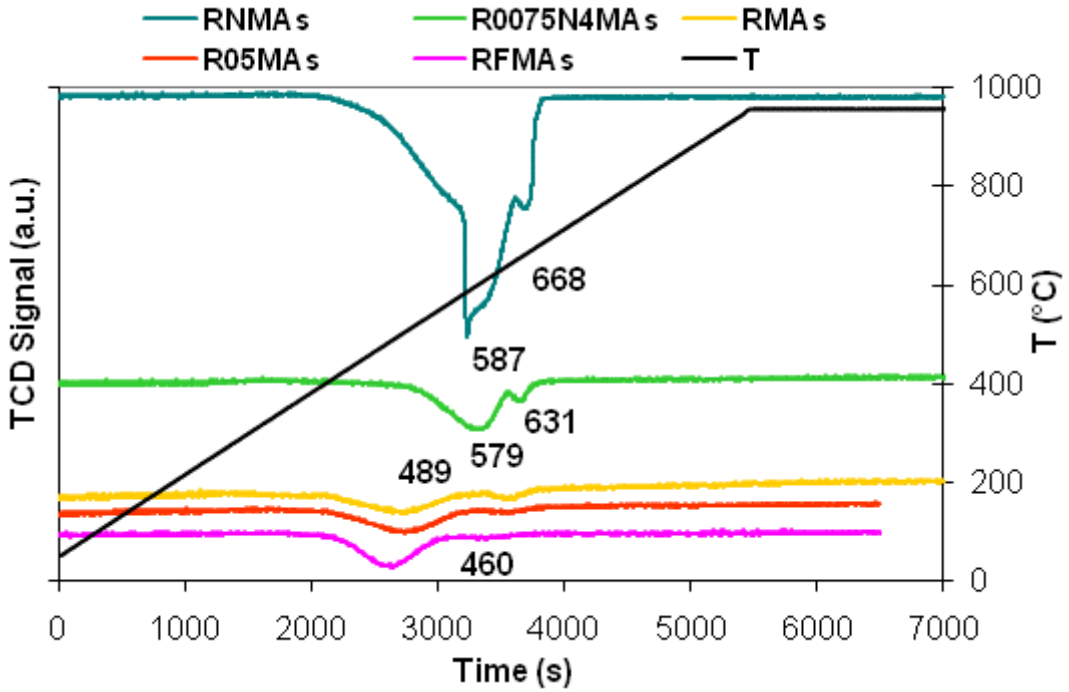

Fig. 4.34 TPO of spent catalysts.

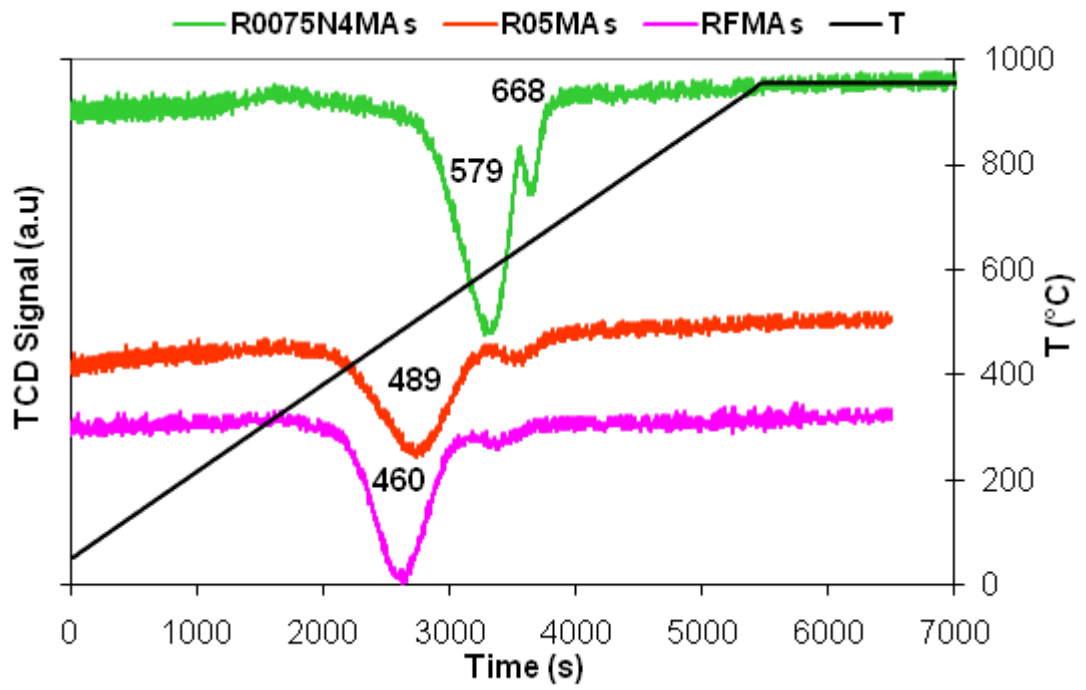

Fig. 4.35 TPO of spent catalysts (detail).

4.3.2.4 Comparisons and conclusions

Three different catalysts were tested at different contact times and temperatures (700 and 550 °C).

At 700 °C all catalysts show very high ethanol conversion (Fig. 4.36), while at lower temperature best conversion is obtained with RNMA catalyst. In all conditions the highest H_2 selectivity is observed with the catalysts containing Rh-Ni (Fig. 4.37), these samples favour the break of C-C bond more than others (Fig. 4.40). By decreasing the amount of active phase Rh-Ni series show coherent trends of selectivities: the decrease of CO and CO_2 is proportionally to decrease of ethanol conversion, while for Rh series the decrease of active phase show a complete different trend giving indication of a different active species or a structure sensitive reaction. Rh-Fe catalyst shows higher amount of CH_4 then all other catalysts both at 700 and 550 °C and therefore this catalyst doesn't favour methane reforming.

Unfortunately highest and more crystalline amount of coke is observed with RNMA catalyst, while it is low with Rh and Rh-Fe samples. Also the drastic decrease of surface area and the increase of microporosity are closely linked to a loss of mesoporosity that is probably due to coke formation.

Considering high amount of coke of Rh-Ni samples and high amount of CH_4 with Rh-Fe sample it was chosen R05MA to continue the study and enhance the performances of this catalyst.

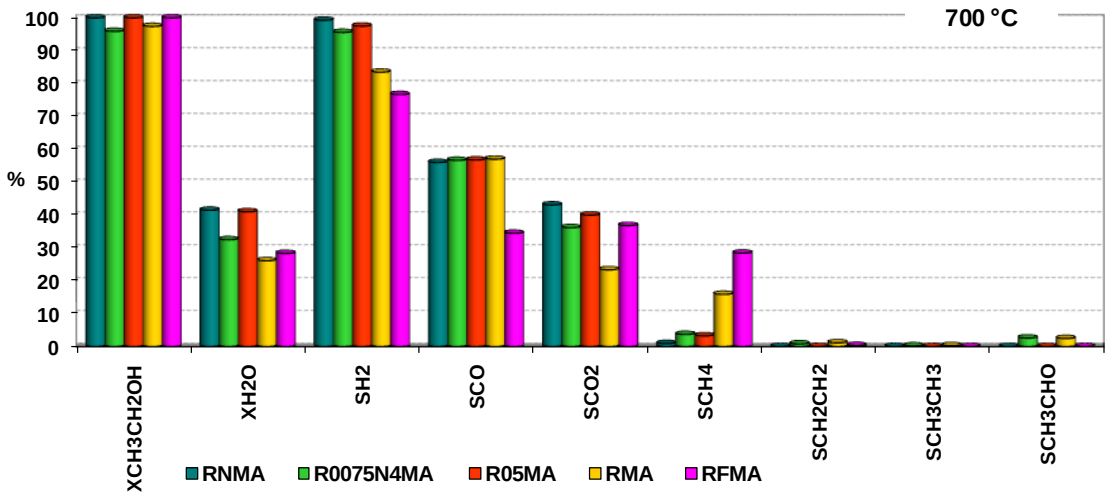

Fig. 4.36 Comparisons of gas phase distribution at 700 °C during 4x condition.

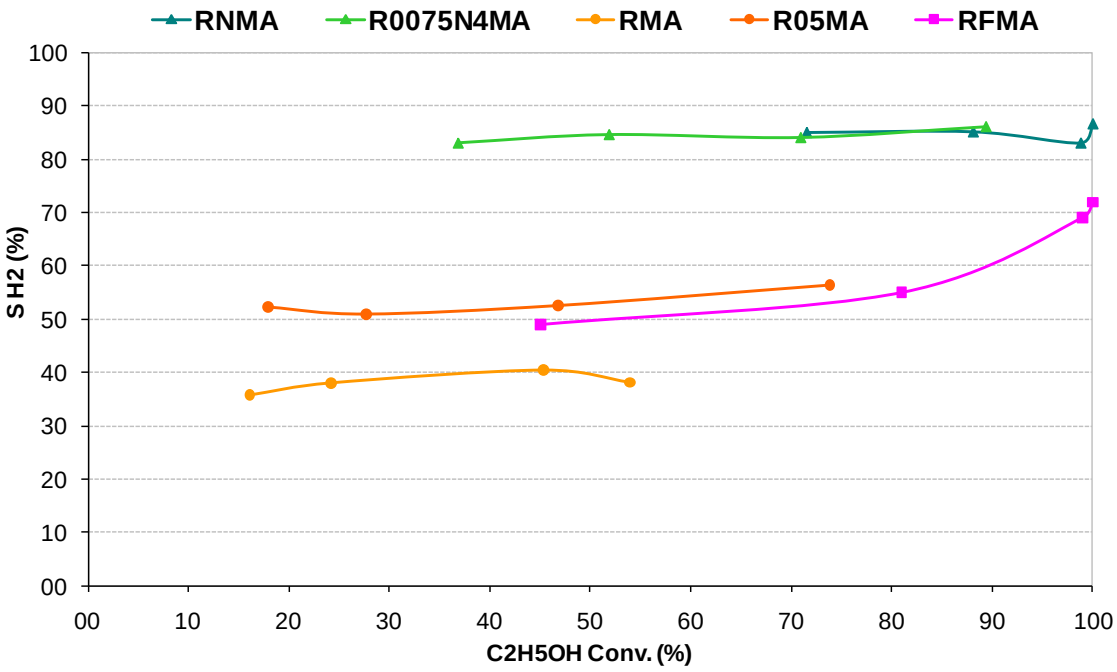

Fig. 4.37 Comparison of H_2 selectivities at 550 °C.

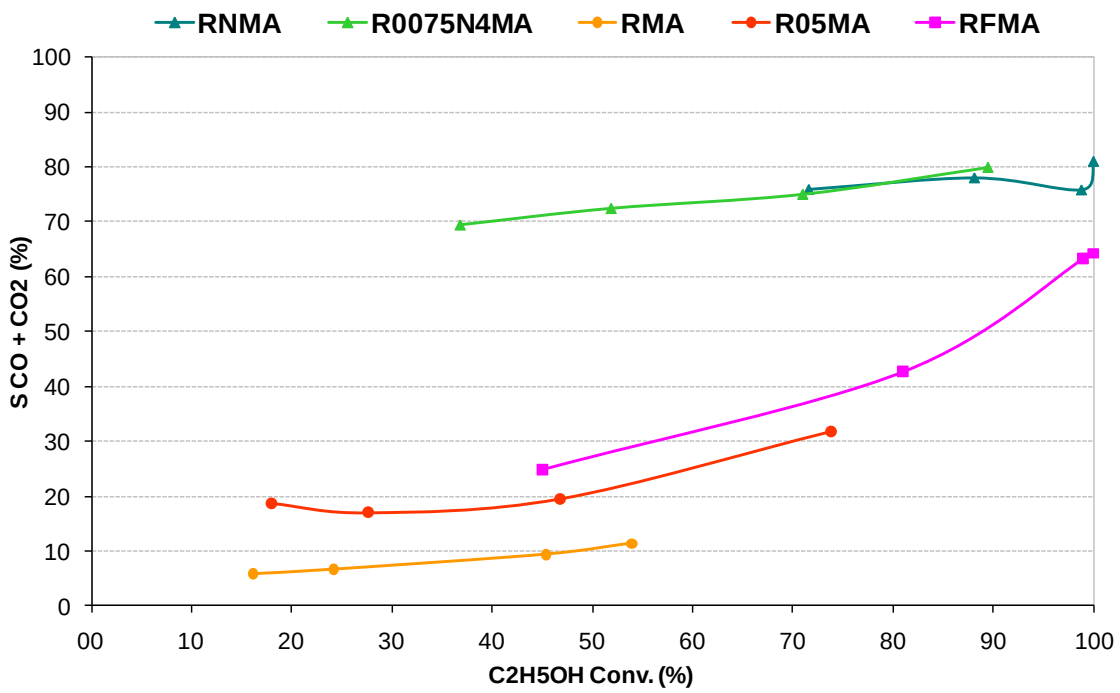

Fig. 4.38 Comparison of $CO+CO_2$ selectivities at 550 °C.

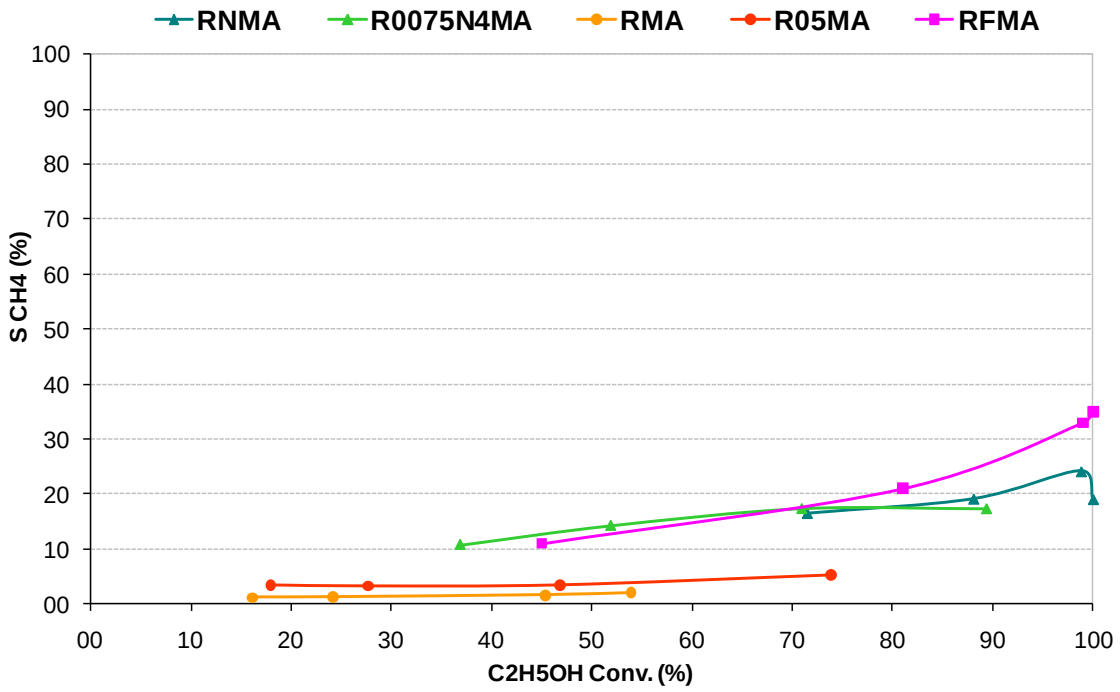

Fig. 4.39 Comparison of CH_4 selectivities at 550 °C.

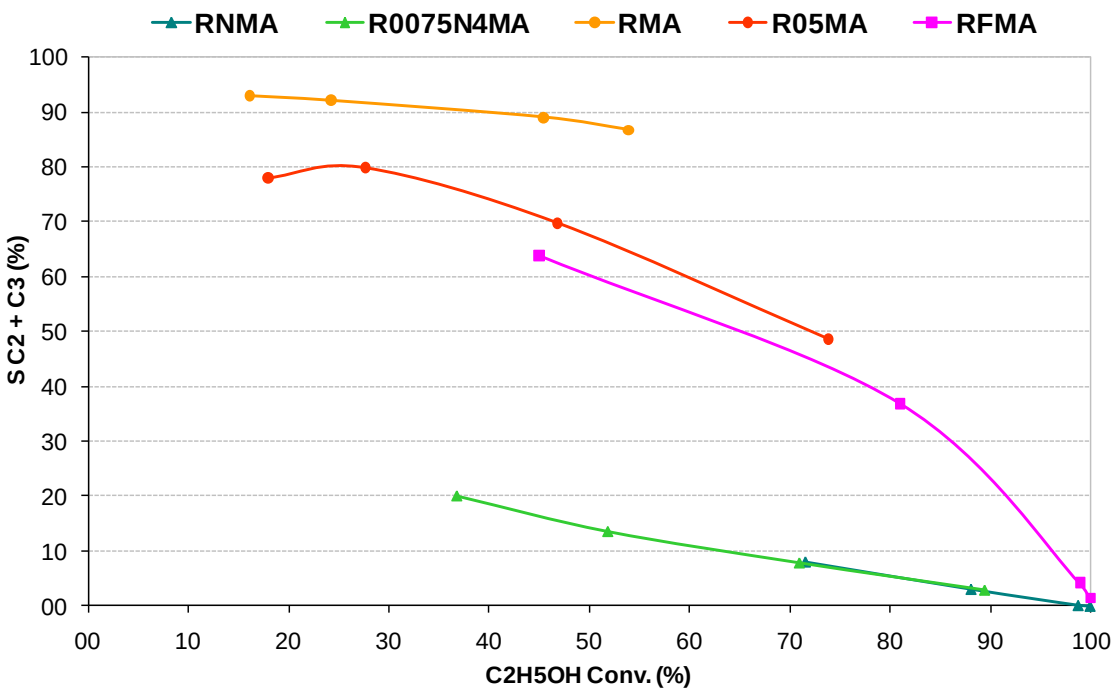

Fig. 4.40 Comparison of C2 selectivities at 550 °C.

4.3.3 Rh catalysts: effect of the matrix

After the study of the active phase selection and in consideration that the Ni containing catalysts show carbon formation, the interest was focused in improving the Rh catalysts. The work started with the study of the matrix by changing the ratio Mg/Al and the anion between layers in the preparation of hydrotalcites. Then a catalyst prepared with $RhCeZrO_2$, with Ce/Zr ratio equal to 75/25, was taken in exam to compare its results with catalysts obtained by hydrotalcites. All catalysts contain 1 % wt of rhodium as noble metal to avoid problems related with the possibility to have Rh trapped in the matrix even after reduction when using low Rh loading.

The composition of hydrotalcites is summarized in Tab. 4.12.

	R055MAs	R05M80As	R043MAc	R043M80Ac
Mg	68	80	68	80
Al	31.45	19.45	31.57	19.57
Rh	0.55	0. 5	0.43	0.43
anions	silicates	silicates	carbonates	carbonates

Tab. 4.12 Compositions of catalysts.

Since in previous conditions at 700 °C almost all catalysts show high ethanol conversion, it was decided to decrease further the contact time to study catalytic

performances in more drastic conditions far from the thermodynamic equilibrium. Furthermore the pellets diameter was decreased to avoid inter and intradiffusional problems.

4.3.3.1 Characterization of fresh catalysts

4.3.3.1.1 X-Ray diffraction (XRD) analysis

The PXRD patterns of the carbonate and silicate containing compounds are shown in Fig. 4.41. The pattern of the HT carbonate sample (R043MAc) shows the characteristic diffraction pattern of hydrotalcite-like compounds with sharp and intense diffraction lines due to basal reflection lines and broad and less intense peaks related with non-basal planes; the basal spacing is 7.6 Å (*17*).

The insertion of silicates (R055MAs), rather than carbonates, in the interlayer leads to a solid with a lower crystalline structure and with a rather similar interlayer spacing. Decreased crystallinity is observed not only perpendicular to the plane direction but also within layers, as can be seen by the considerable reduction in the intensity of the first reflection line and the poor resolution of the doublet (recorded in the 60–65° 2θ range) due to the ((110) and (113)) diffraction planes (*18*).

Increasing the amount of magnesium, a shift of basal planes ((003), (006) and (009)) towards lower 2θ is observed both for carbonate and silicate sample (Fig. 4.41). The lower amount of Al causes lower electronic charge of the layers and as consequence the distance between the layers is higher. For Bragg law higher distance causes lower 2θ to obtain the same result (*18*).

After calcination at 900 °C, a spinel-type phase and a rock-salt phase are obtained for the HT carbonate sample (Fig. 4.43). In this catalyst, rhodium cations are well dispersed into the MgO and spinel phases (*13*). On the other hand, by calcining the HT silicate sample a more complex pattern is obtained. New diffraction peaks assigned to a forsterite-like phase (Mg_2SiO_4) are indexed; conversely, no well-defined phase containing Al ($MgAl_2O_4$) was detected, while the MgO phase is still present (Fig. 4.44).

Some reflection lines due to a spinel-type phase are observed in the diffraction patterns; however, they are weak and broad and the first two reflections at 19 and 32° 2θ ascribed to (111) and (220) are not observed, thus suggesting the formation of a defective spinel phase. It would appear that the presence of silicates which react with MgO to form the forsterite phase affects and possibly delays the formation of the spinel phase.

The diffraction patterns of the calcined catalysts (Fig. 4.43 and Fig. 4.44) show that by increasing the Mg/Al, together with the expected increase in the intensity of the MgO phase diffraction lines, the amount of spinel phase decreases. Moreover, the amount and the crystallinity of the forsterite phase for the 80/20 is lower. It is worth noting that by reducing the amount of trivalent cations, the charge excess of the hydroxyl

layers decreases, as does the silicate content in the structure in order to balance it (Fig. 4.42).

RCZO catalyst shows $CeZrO_2$ phase and no reflections attributed Rh phase because of the amount of metal is too low.

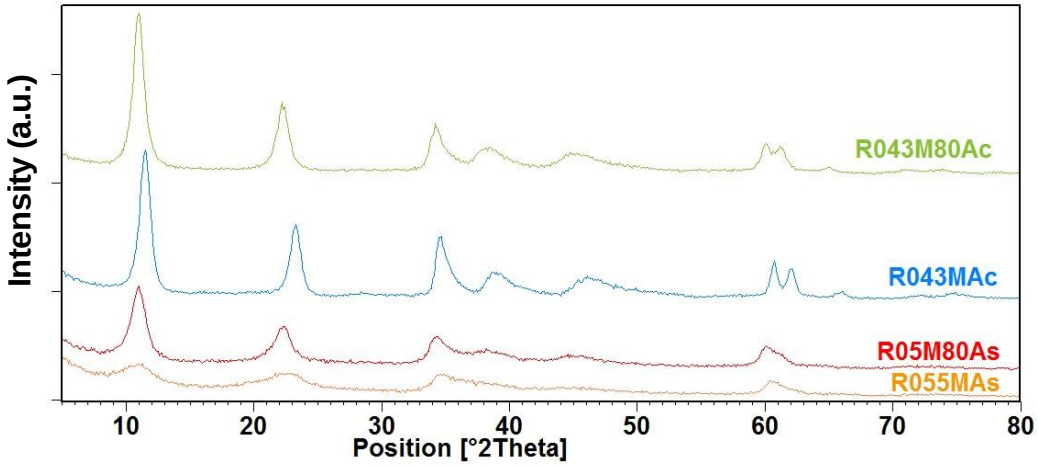

Fig. 4.41 XRD of HT samples.

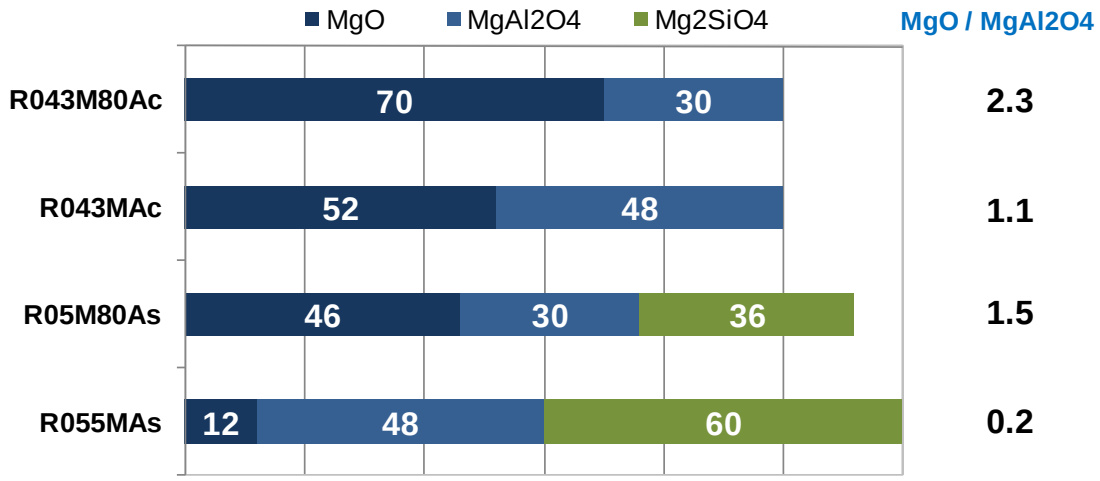

Fig. 4.42 Amounts of different phases HT samples after calcination (Ex-HT).

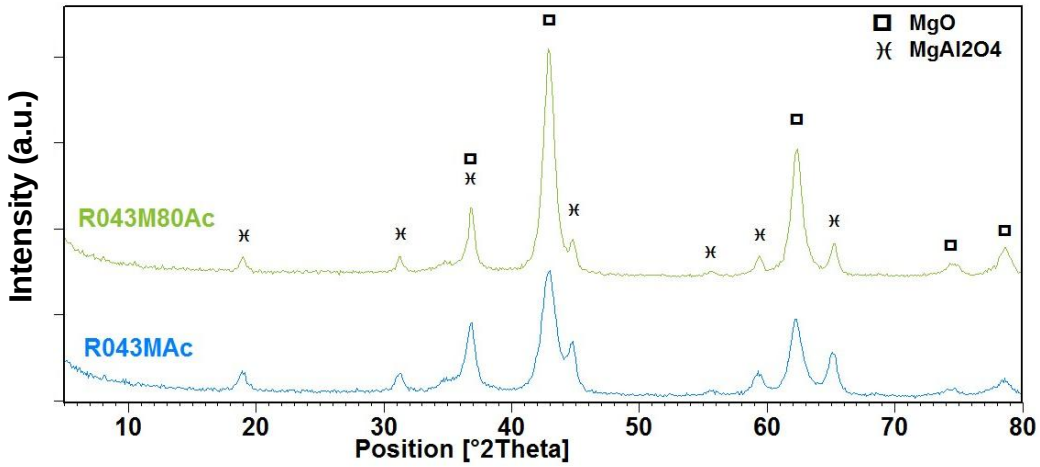

Fig. 4.43 XRD of carbonates Ex-HTs: effect of Mg/Al ratio.

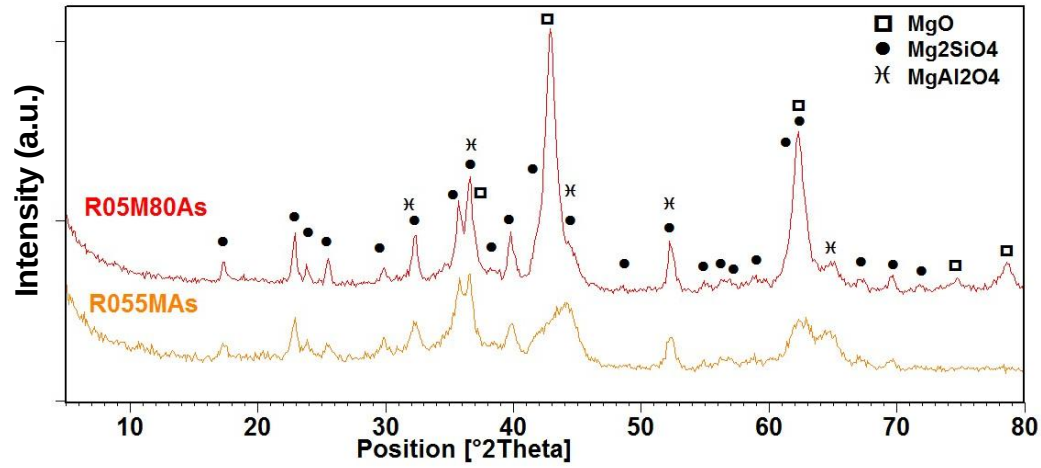

Fig. 4.44 XRD of silicates Ex-HTs: effect of Mg/Al ratio.

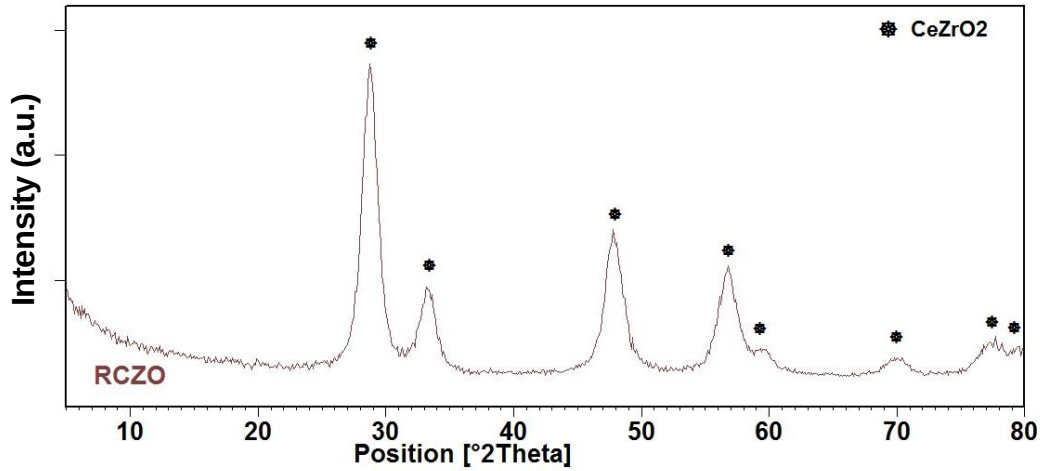

Fig. 4.45 XRD of fresh RCZO.

4.3.3.1.2 Surface area and porosimetry analysis

The values of specific surface area pores volume and desorption pore widths of the fresh catalysts are reported in Tab. 4.9, while the pore size distributions are shown in Fig. 4.46 and Fig. 4.47.

The change from carbonate to silicate improves the values of surface area: silicates samples show higher (about two times) surface area then carbonates.

By comparison with calcinated products, the surface area of hydrotalcites with silicate is almost two times respect calcinated products, while in the carbonates, values of hydrotalcites and calcinated are more similar even if the surface area of hydrotalcite samples are slightly lower than calcined. The different trend between carbonates and silicates can be due to different answer of the anions interlayers to thermal treatment. For carbonates samples the increase of surface area is due to "cratering" mechanism which occurs through the removal of CO_2 and H_2O and it is favourite at medium temperature (400-600 °C) (*19*). Since these materials are stable against sinterization, calcination at high temperature (900 °C) doesn't decrease the surface area. On the other hand, for silicate samples, first of all, since the anions located in the interlayer are mainly polysilicates, the "cratering" mechanism would lead to a lesser increase of the surface area (*18*).

The carbonate sample with large excess of magnesium (R043M80Ac) shows lower value of surface area then common values reported in literature for carbonate hydrotalcites. The large amount of magnesium can make hydrotalcite formation difficult because the ratio Mg/Al 80/20 is the limit for stoichiometric hydrotalcites (*18*).

The RCZO catalyst shows both surface area and pores volume very lower than hydrotalcites and hydrotalcites after calcination. This data are explained by the low widths of pore close to 43 Å.

	BET surface area (m^2g^{-1})	t-plot micropore area (m^2g^{-1})	BJH desorption cumulative volume of pores (cm^3g^{-1})	BJH desorption maximums pore widths (Å)
HT R043MAc	102.75			
R043MAc	121.16	17.47	0.631	122
HT R043M80Ac	14.72			
R043M80Ac	105.16	19.97	0.250	37 , 60 , 125
R05MAs	114.79	20.03	0.558	36 , 127
HT R055MAs	263.43			
R055MAs	113.20	10.08	1.129	36 , 235
HT R05M80A	154.74			
R05M80As	107.13	16.52	0.452	34 , 126
RCZO	53.08	3.19	0.122	43

Tab. 4.13 Surface area, pores volume and width of fresh catalysts.

Pore size distributions figures are referred only to Ex-HT samples.

The pore size distribution of carbonate samples (R043MAc, R043M80Ac and MAc) show some differences, the sample R043MAc shows mainly monomodal and quite broad pore distribution curve, while that one of R043M80A shows three different pore regions in the ranges [33 – 41], [41 – 106] and [106 – 151] Å.

Differently of carbonate samples, silicate samples show more stable porosimetry profiles: very large pore distribution curve with two regions of pores. The largest distribution is in the range [43 – 545] Å while the second lower region is in the range [33 – 43] Å.

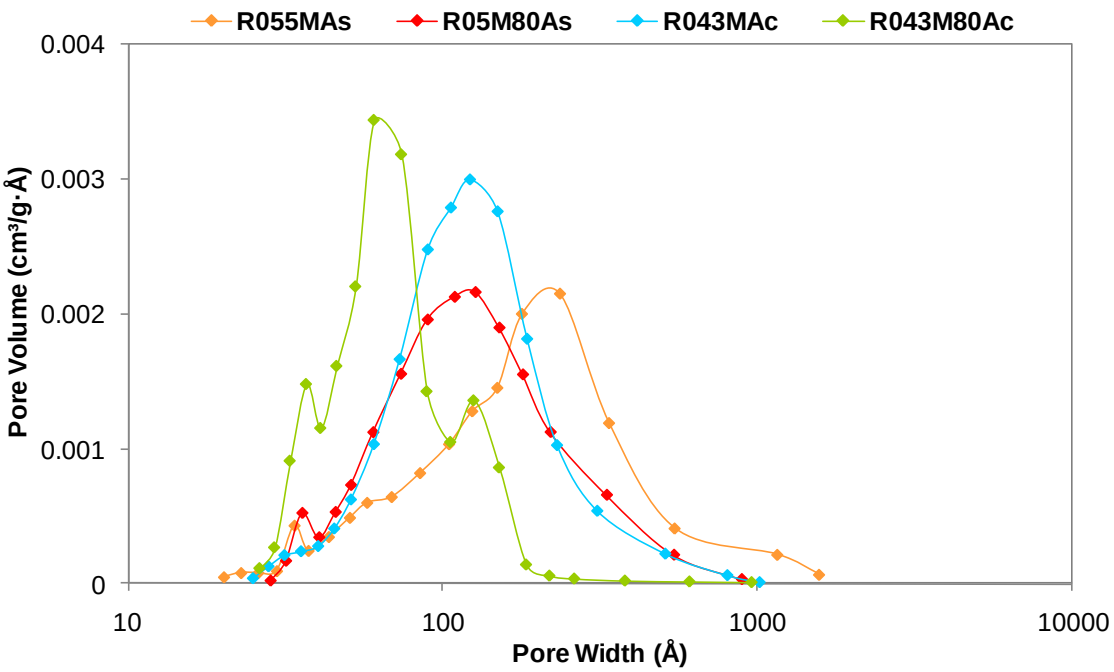

Fig. 4.46 BJH pore size distribution of fresh Ex-HTs.

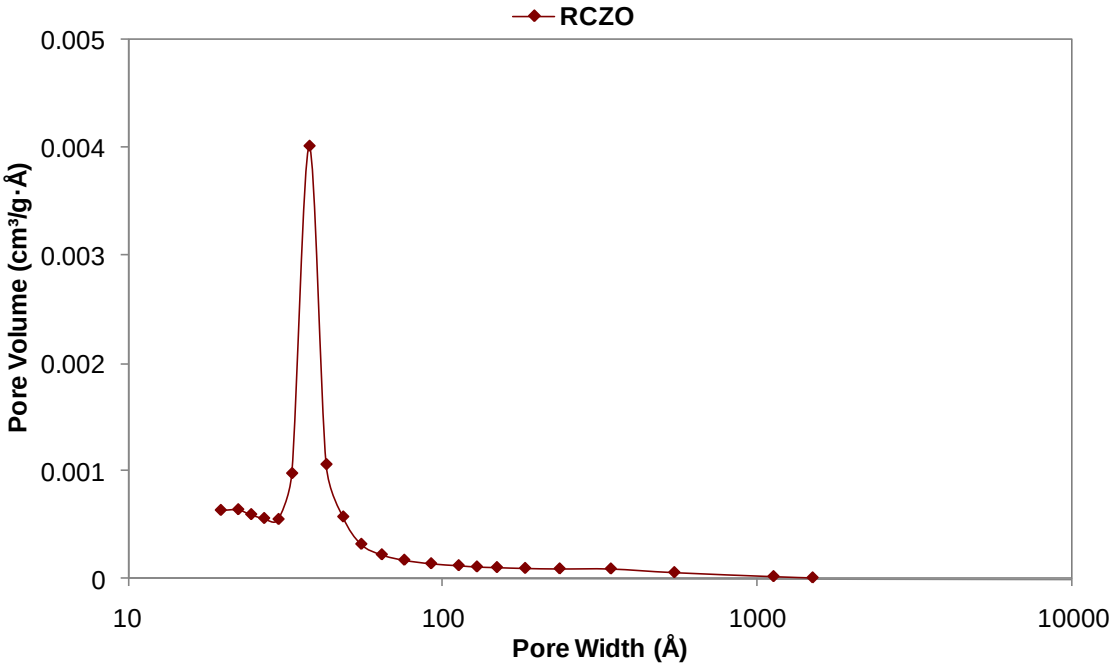

Fig. 4.47 BJH pore size distribution of fresh RCZO.

4.3.3.1.3 Temperature programmed reduction (TPR) and oxidation (TPO) analysis

The TPR profiles for all catalysts show a H_2 consumption peak at ca. 400 °C, together with smaller peak at higher temperature (ca 850 °C). These reduction temperatures are characteristic of highly stabilized Rh^{3+} species, which are inserted into the mixed oxide phases.

A TPO-TPR cycle was performed to study the stability of the metal particles under oxidizing conditions. No relevant consumption of O_2 is observed during TPO analyses (flat line), while H_2 consumption is observed in the second TPR run, but differently from first TPR, it is observed only at high temperature.

By comparison of TPR analyses, the reduction of the silicate containing samples occurs at lower temperature (394-414 °C) than the ones with carbonate (422 °C) as interlayer anions. The comparison of the intensity shows that the R043MAc has the area of the first peak lower than other samples while the second reduction peak exhibits similar height and it is extended above 900 °C (maximum temperature of the TPR) making difficult to calculate the area. Therefore, considering that all the samples contain the same amount of rhodium, the degree of R043MAc reduced at low temperature is less than other samples.

The TPR profile of RCZO shows 3 peaks of H_2 consumption at ca. 160, 370 and 850 °C. The low temperature of first peak is associated to rhodium free on the surface of catalyst and it can attributed mainly to Rh_2O_3, while the others a higher temperature are due to $CeZrO_2$.TPR profile of $CeZrO_2$ without rhodium shows two peaks at 600 and 850 °C which are associated with the reduction of the surface and the bulk. The presence of rhodium determines a significant promotion in the reduction due to the spillover of H_2 onto the support, i.e. the reduction peaks at 600 °C shift to lower temperatures at 350 °C. The oxidation profile of RCZO shows only one peak at 131 °C which is attributed to $CeZrO_2$ because it is present also in the TPO of $CeZrO_2$ without rhodium.

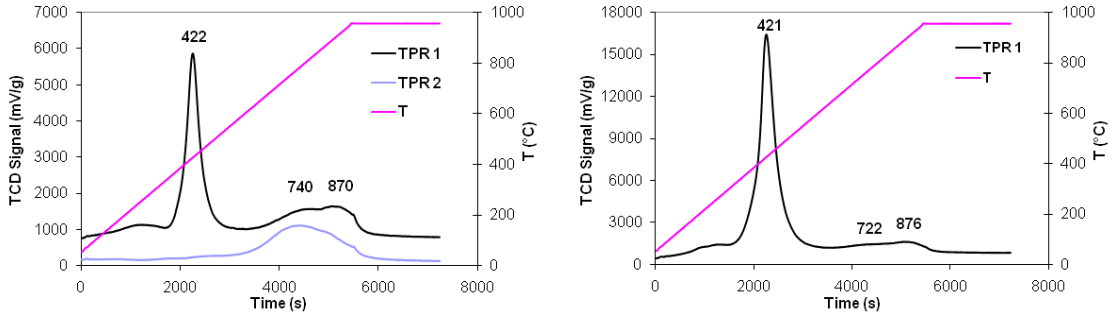

Fig. 4.48 TPR of R043MAc (left) and R043M80Ac (right).

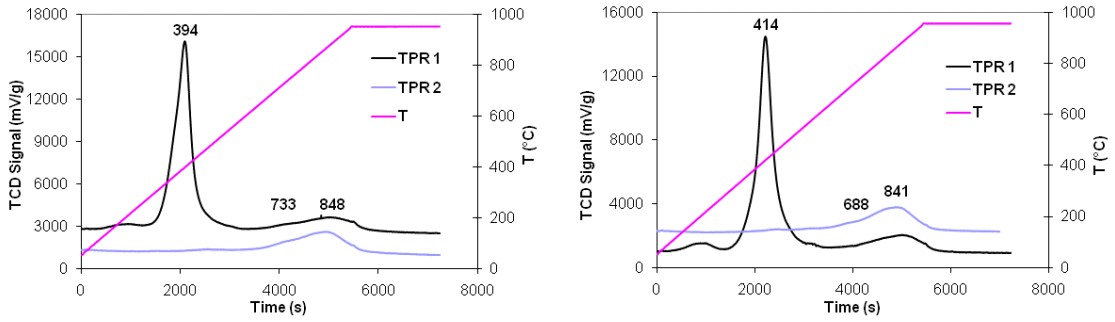

Fig. 4.49 TPR of R055MAs (left) and R05M80As (right).

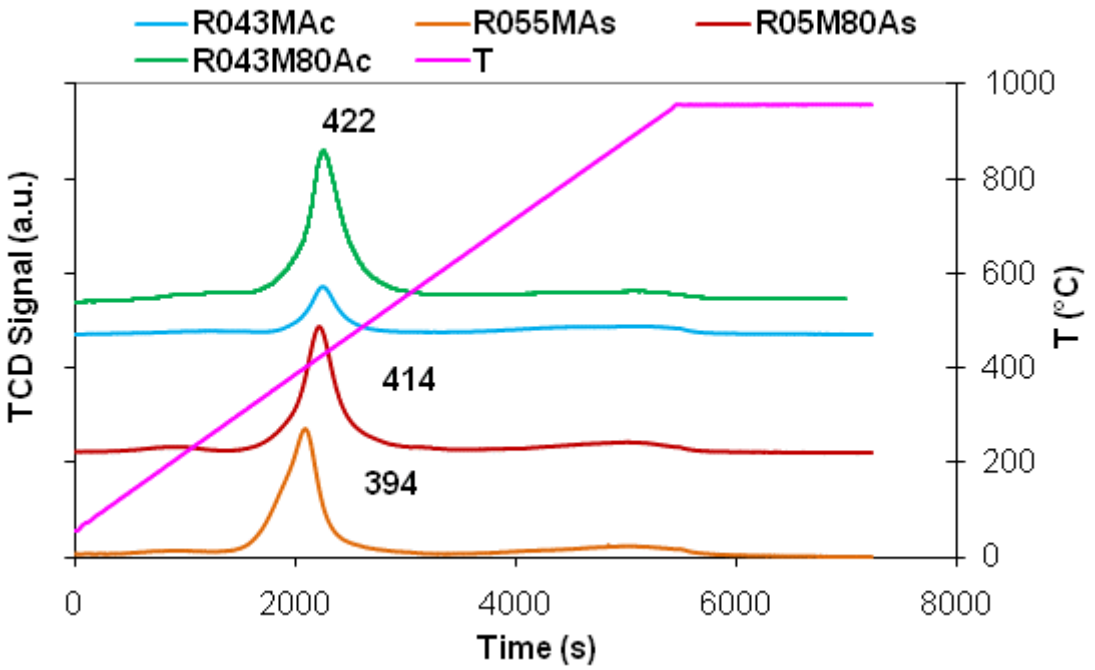

Fig. 4.50 TPR of fresh Ex-HTs.

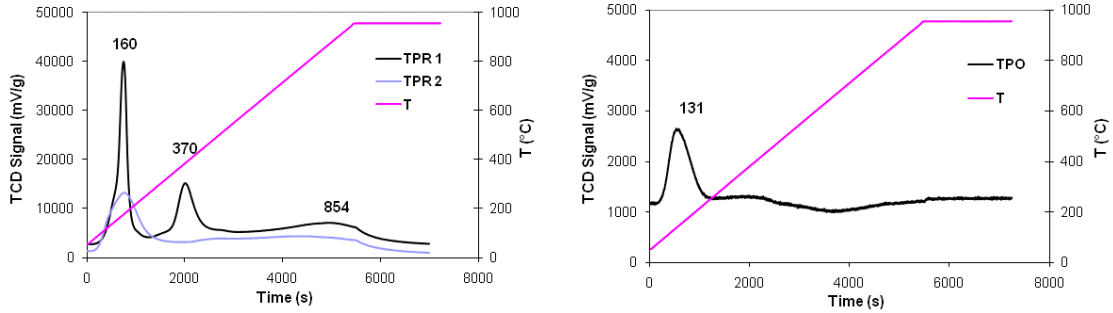

Fig. 4.51 TPR of RCZO.

4.3.3.1.4 Scanning and Transmission Electron Microscopy analysis

All three samples (R043MAc, R055MAs and R05M80As) show the typical lamellar hexagonal structure of hydrotalcite compounds, except the sample R043M80Ac which doesn't show lamellar structure, but big particles with no defined shape and as a consequence without porosity. These images explain the low surface area of this sample, probably the ratio Mg/Al is too high to obtain a stable material and after XRD could be occur a partial change of phase.

For samples with lamellar structure, particles size are about 100-200 nm. After calcination the catalysts keep a porosity structure, but the structure is less defined probably because photos are less clear.

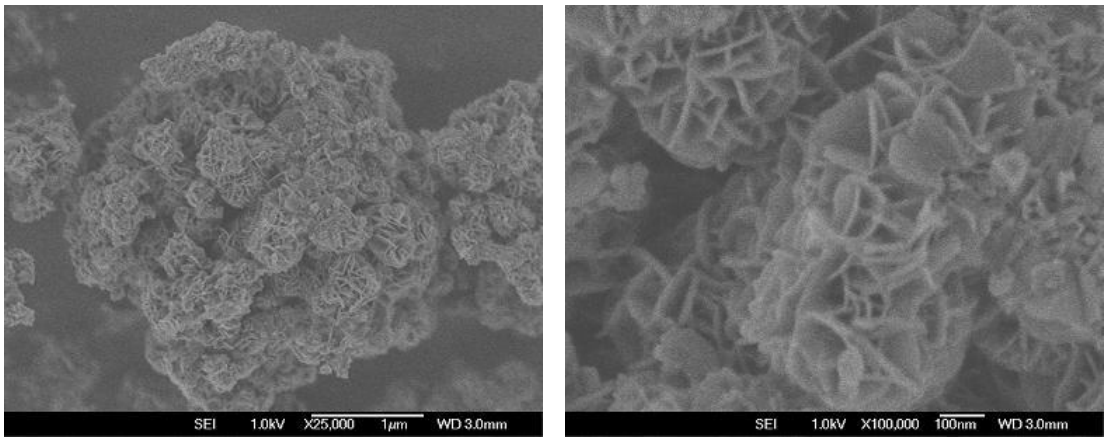

Fig. 4.52 HT R043MAc.

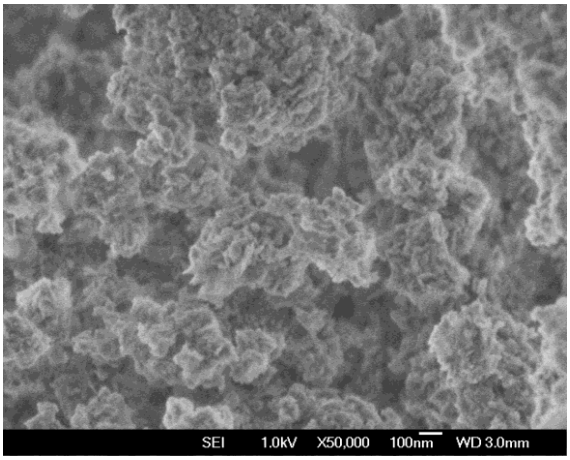

Fig. 4.53 Ex-HT R043MAc.

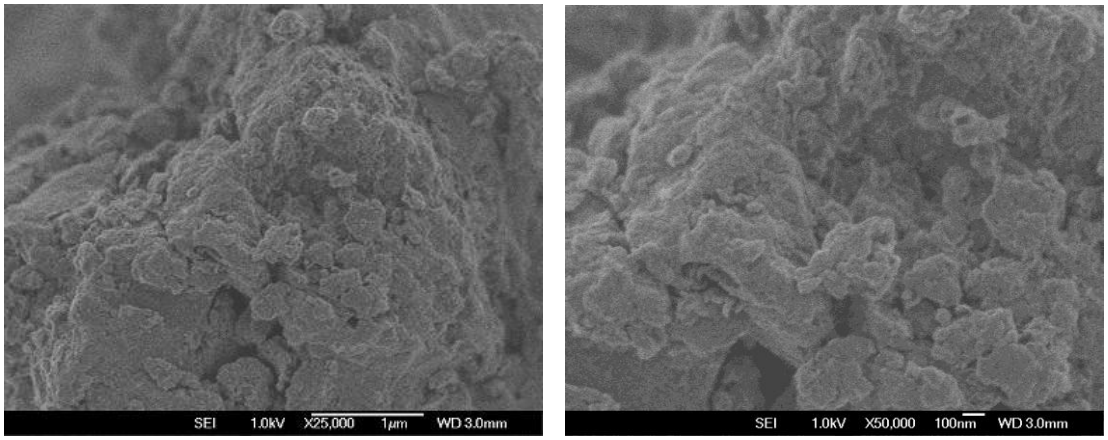

Fig. 4.54 HT R043M80Ac.

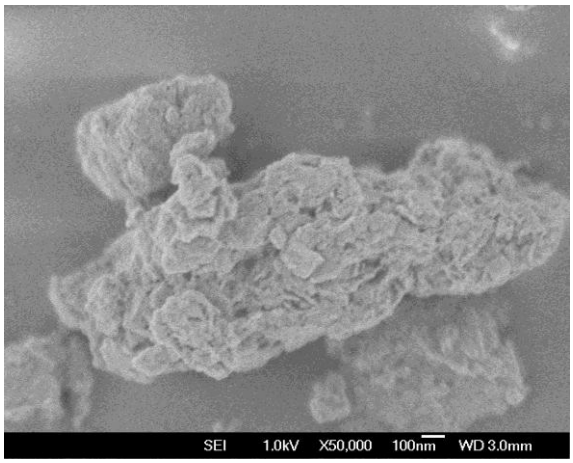

Fig. 4.55 Ex-HT R043M80Ac.

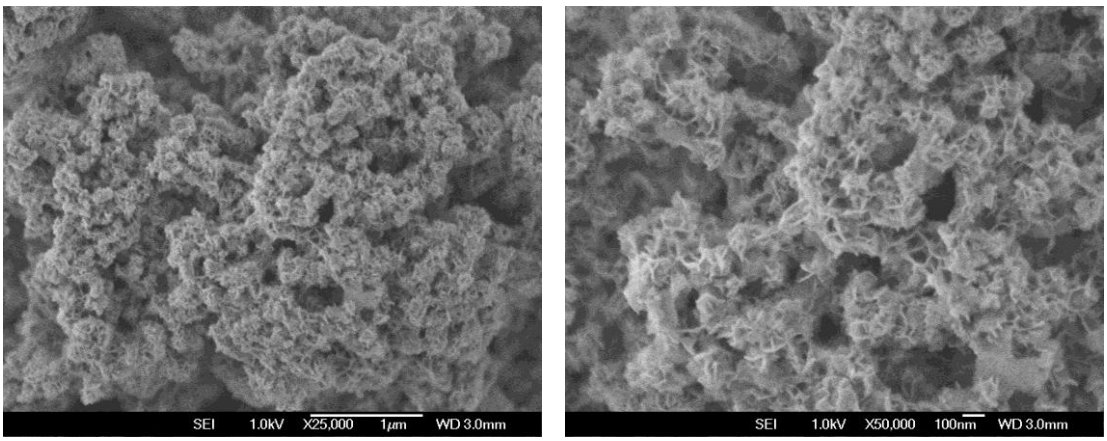

Fig. 4.56 HT R055MAs.

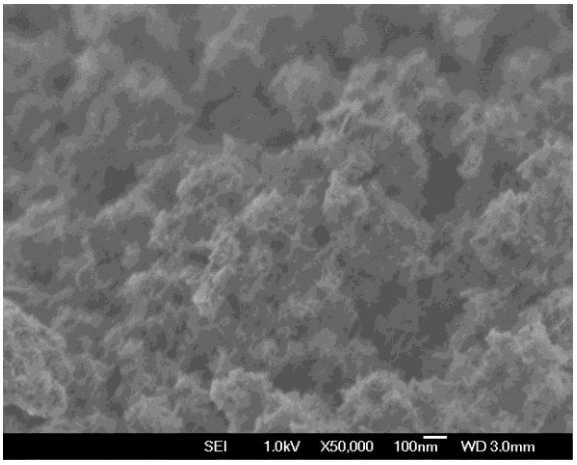

Fig. 4.57 Ex-HT R055MAs.

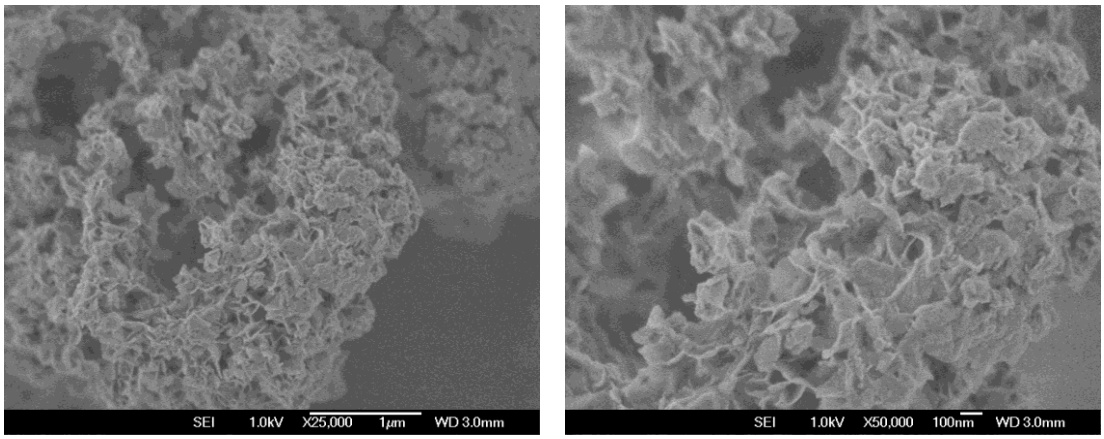

Fig. 4.58 HT R05M80As.

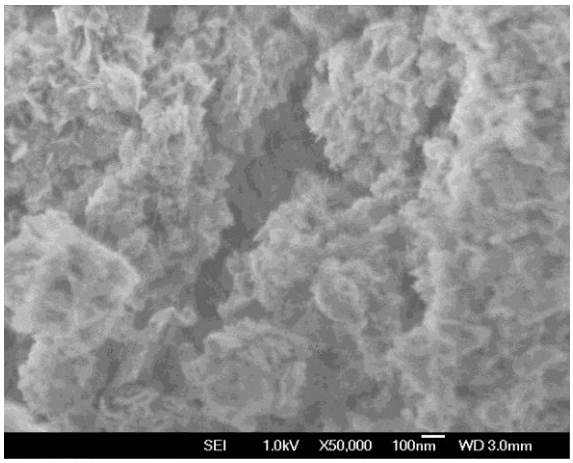

Fig. 4.59 Ex-HT R05M80As.

TEM analyses were carried on reduced samples. Two different temperature of reduction were chosen to compare the effect of reduction temperature on particle size and density. First temperature was 750 °C for two hours while the second one was 1000 °C for four hours, for both temperature the amount of H_2 was 3 % in Argon and the flow of mixture was 30 ml/min. In addition the catalyst R043MAc was reduced at 1000 °C for 30 minutes with the amount of H_2 at 3 % in Argon and the flow of mixture 50 ml/min.

All the fresh catalysts reduced at 750 °C show nanosize particles with low differences between the samples. Increasing temperature of reduction an increase of particle size is observed, both R043MAc and R05M80As show an increase of particle size which is about two times the value after reduction at 750 °C. In addition photos of samples reduced at 1000 °C show higher amount of particles than those one reduced at 750 °C. This is explained by TPR analyses: at higher temperature higher part of rhodium is reduced therefore the total amount of rhodium increases.

Dp (nm)	**Ro43MAc**	**Ro43M80Ac**	**Ro55MAs**	**Ro5M80As**
Fresh (750-2h)	1.4	1.1	1.0	1.1
Fresh (1000-4h)	2.6	/	/	2.0
Fresh (1000-30')	1.8	/	/	/

Tab. 4.14 Rhodium size of Ex-HT samples after different treatments.

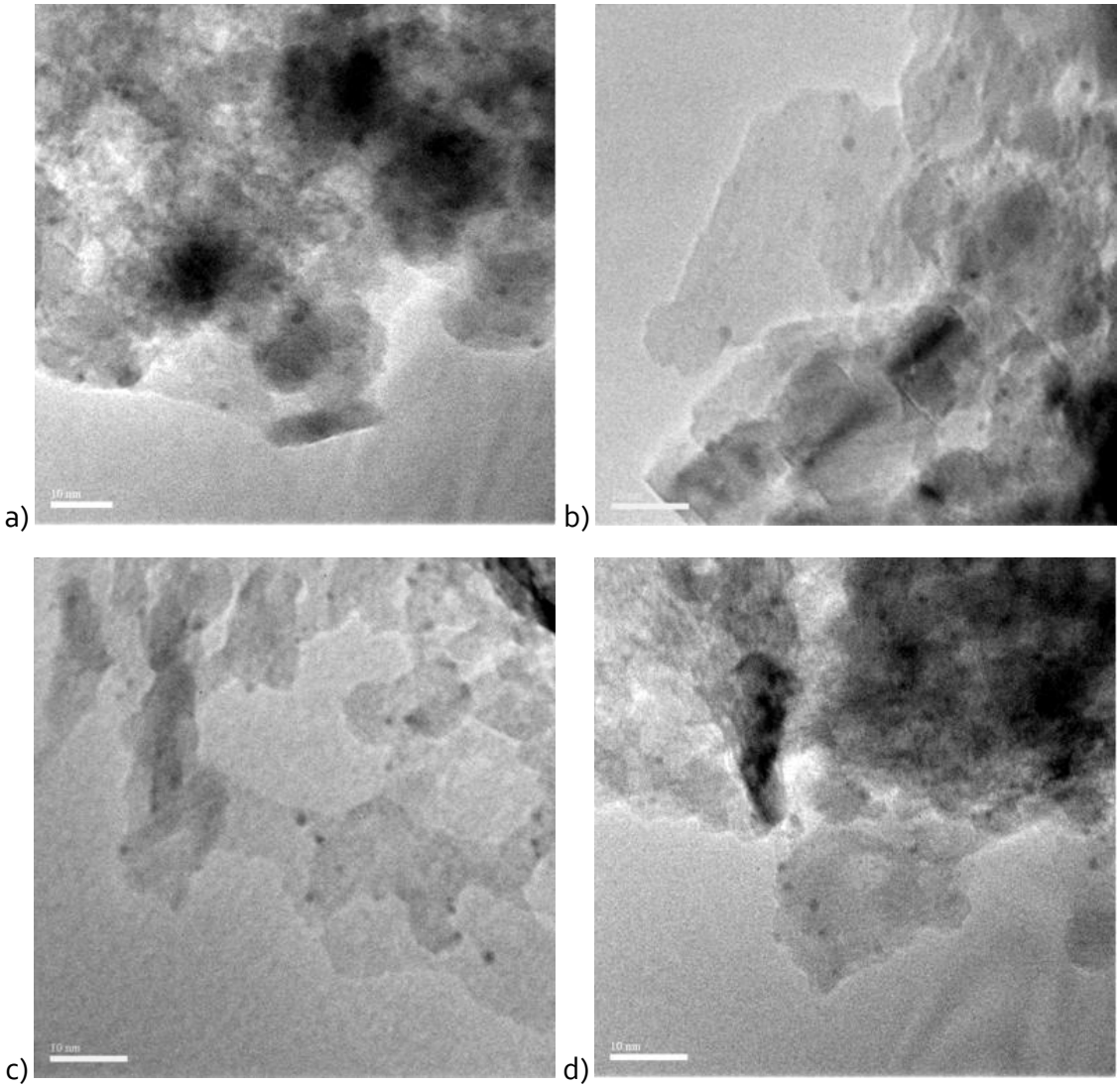

Fig. 4.60 TEM of samples reduced at 750 °C for two hours:
a) Ro43MAc, b) Ro43M80Ac, c) Ro55MAs and d) Ro5M80As.

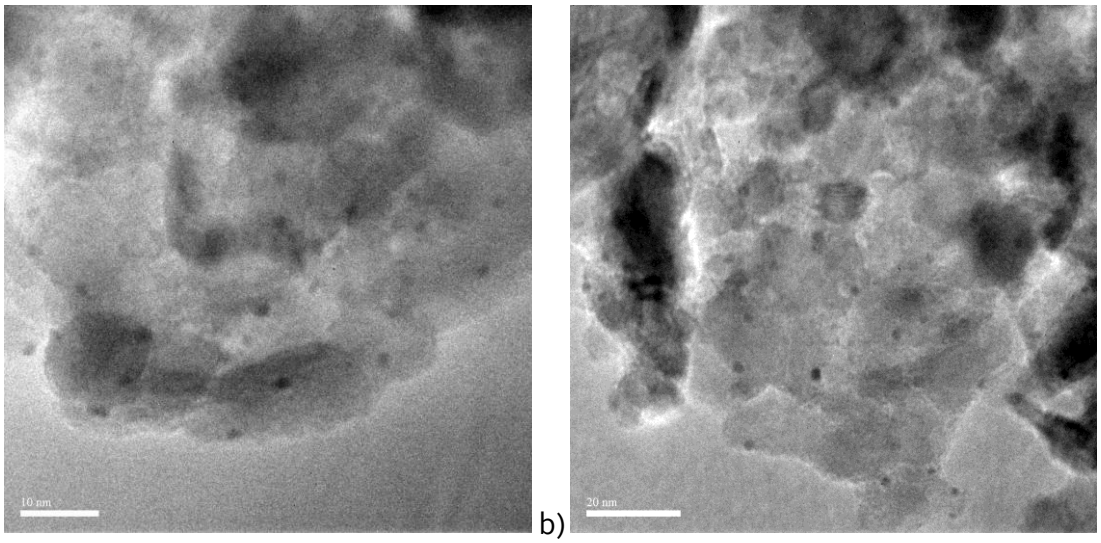

Fig. 4.61 TEM of samples reduced at 1000 °C for four hours:
a) R043MAc and b) R05M80As.

4.3.3.1.5 Infrared spectroscopy (IR) analysis

Probe molecules that were considered for IR analysis are CO and CO_2 at 77K and CO at room temperature (RT) to study the acid-base sites of samples which showed best catalytic performances. Some measurements of adsorption with CO at 77K were carried out on materials without rhodium to study the effect on rhodium on the matrix. Before every test a thermal pre-treatment in vacuum was realized at three different temperatures (100, 300 and 500 °C).

The Ex-HT carbonate $Mg_{68}Al_{32}$ (MAc) outgassed at 100 °C shows two bands in the region of the CO stretching mode, one at 2180-2160 cm^{-1} and the other at 2150 cm^{-1}, which are due to CO molecules interacting with two different sites. The former band, at higher frequencies, is due to CO interacting with coordinatively unsatured Al^{IV} sites (exposed octahedral Al ions) and with coordinatively unsatured Mg ions, which are Lewis sites of medium acidic strength.

The latter band, at lower frequencies, may be ascribed to both CO interacting with Al-OH species or to CO interacting with Mg ions which are less exposed (or less coordinatively unsatured), i.e. weaker acidic Lewis sites, with respect to the former Mg sites. Indeed this frequency is close to that observed for CO interacting with pentacoordinated Mg^{2+} ions at the surface of MgO.

Upon increasing outgassing temperature, the intensity of the latter band decreases, whereas that of the former band increases, revealing that dehydroxylation (and possibly elimination of carbonates) yields the exposure of medium-strength acidic Lewis sites. After outgassing at 500 °C only the band at 2180-2160 cm^{-1} is observed. This band shifts from 2178 cm^{-1} to 2164 cm^{-1} upon increasing CO coverage: this behaviour is ascribed to heterogeneity in CO adsorbing Lewis sites, where the stronger ones (Al ions) responsible of the IR absorption at higher frequencies, are

occupied at lower coverage. $Ce_{0.75}Z5_{0.25}O_2$ (CZO) shows only one band due to the CO stretching mode at 2164 cm^{-1}, shifting to 2155 cm^{-1} upon increasing coverage. Spectra do not change for sample outgassed at increasing temperature. In this case, the thermal treatment does not cause any significant surface modification. The band is assigned to CO interacting with coordinatively unsatured Ce ions and possibly to CO adsorbed through non-specific interactions.

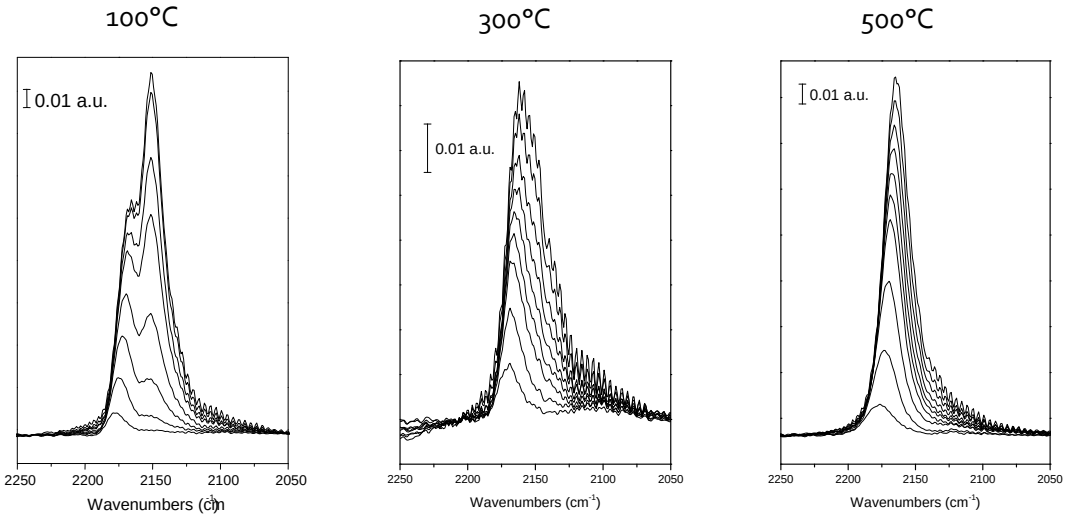

Fig. 4.62 CO 77K of MAc after different pre-treatment at 100, 300 and 550 °C.

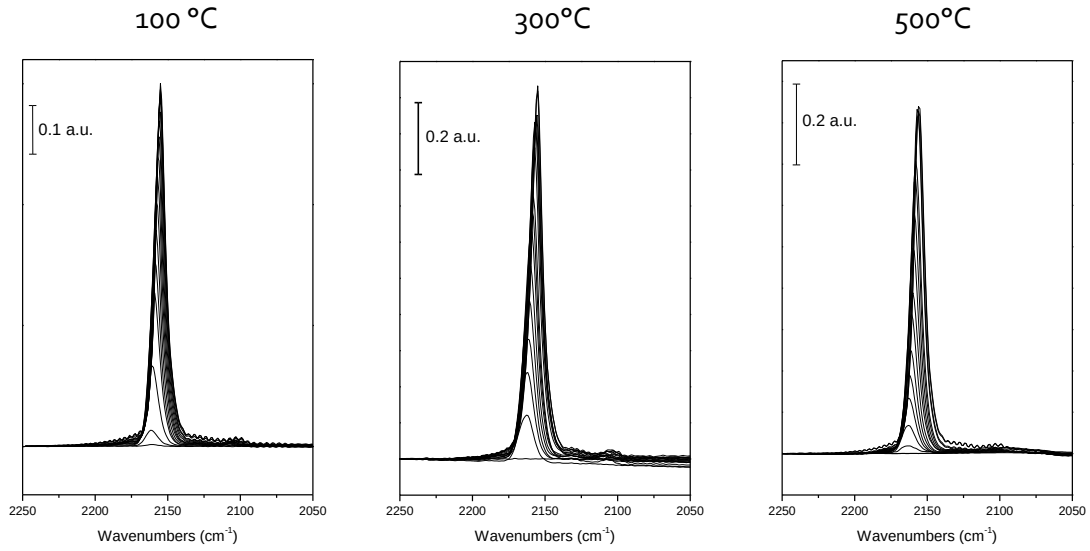

Fig. 4.63 CO 77K of CZO after different pre-treatment at 100, 300 and 550 °C.

For samples contain rhodium two reduction treatments are necessary to observe Rh^0 species: the former needs to reduce rhodium in the sample, instead the second one, since the sample was exposed to air before IR measurement, needs to reduce part of rhodium which could be reoxidize. The second reduction is the same for all sample and it was realized at 750 °C. IR spectra were recorded both in adsorption and in desorption, so that two sets of spectra were obtained.

When CO is adsorbed on metal particles, the electron back-donation from the metal to the chemisorbed molecule decreases its stretching frequency with respect to the unperturbed molecule. Thus, it can easily distinguish the bands of CO interacting with acidic Lewis sites of the support (Al and Mg ions) which are explained before from those of CO interacting with Rh^0 sites on the surface of Rh particles.

First reduction of the sample R043MAc was carried out at 750 °C.

Considering the measurement at 77K, at low CO coverage a band at 2050 cm^{-1} was observed, due to CO linearly chemisorbed on Rh^0 sites of metal particles (monocarbonyl species). At higher coverage the band shifts to 2060 cm^{-1} due to the dipole coupling between adjacent chemisorbed CO molecules (Fig. 4.64). In the same spectra, bands appear around 2200 cm^{-1}, which were not observed during MAc analysis (Fig. 4.62). These are ascribed to small amount of highly exposed Lewis sites formed during the reduction and activation treatment.

Increasing temperature (RT) two bands are detected close to CO monocarbonyl at ca. 2033 and 2096 cm^{-1} (Fig. 4.65) that can be attributed to dicarbonyl species, in these species rhodium is present as Rh^I. The presence of Rh^I is not common in literature where it is described an instable specie, therefore it could be produced by oxidative disruption of Rh-Rh bonds in small Rh^0 crystallites under CO atmosphere (strong Rh-CO bond) (*20*) (*21*). Furthermore analysis at RT shows some bands in the range of 1750-1200 that can be ascribed to carbonates formed by CO disproportion. The low amount of carbonates observed upon reaction with CO is not due to a lower ability of the surface for CO_2 chemisorption because during CO2 chemisorption the intensity of carbonates bands is higher Fig. 4.66.

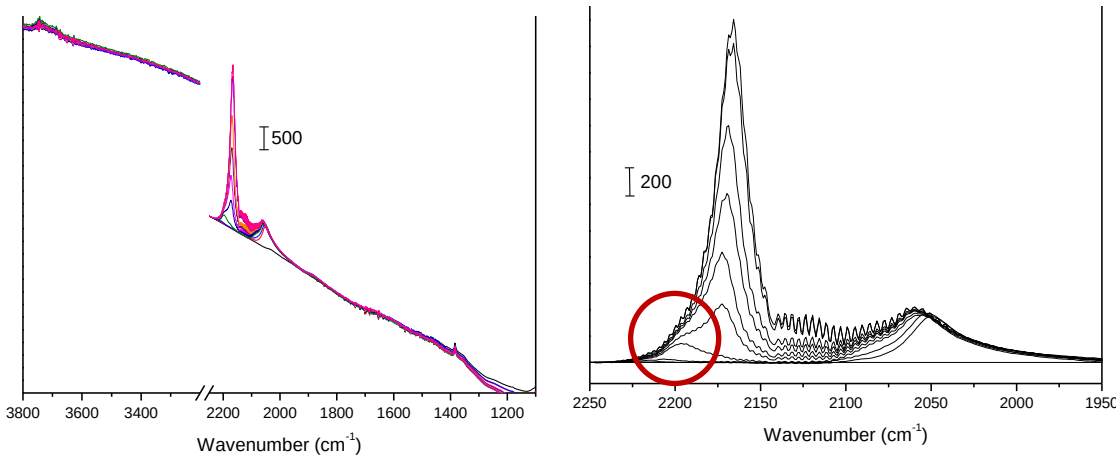

Fig. 4.64 CO 77K of R043MAc reduced at 750 °C.

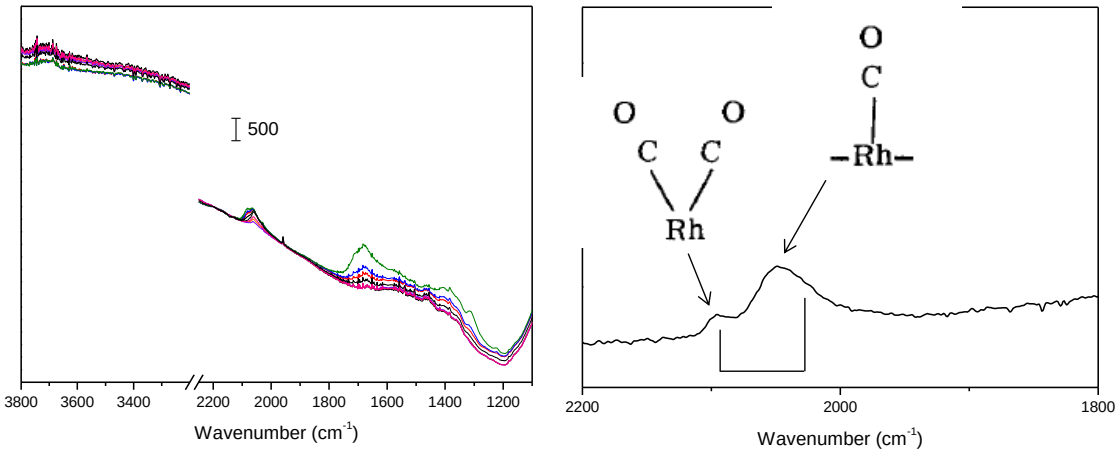

Fig. 4.65 CO RT of R043MAc reduced at 750 °C.

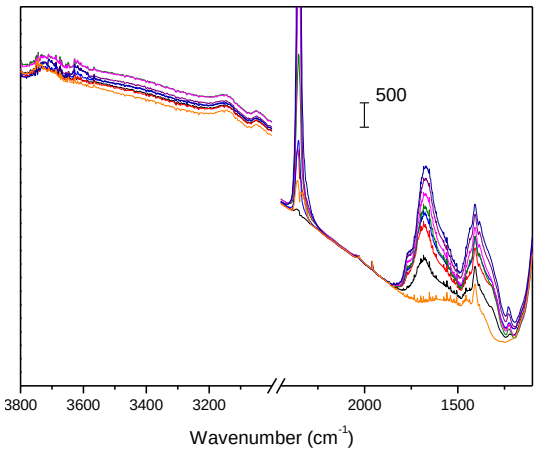

Fig. 4.66 CO_2 RT of R043MAc reduced at 750 °C.

The same measurements of adsorption and desorption are repeated for R043MAc with first reduction carried out at 950 °C to study if the slight increase of particle size could affect stretching of CO adsorption. At 77K only monocarbonyl is adsorbed at 2050 cm^{-1}, the same frequency of previous experiment, while at RM bands related to carbonates and dicarbonyl are detected although they show lower intensity (Fig. 4.67 and Fig. 4.68). Therefore the slight increase of particle size could affect mono-dicarbonyl ratio even if nanosize crystallites confirm that dicarbonyl could be due to break of Rh-Rh bond under CO atmosphere. As before, the presence of carbonates seems related to the presence of dicarbonyl species. In addition, a very broad and low in intensity band is observed at around 1900 cm^{-1} which could be attributed to bridged carbonyl (Fig. 4.68).

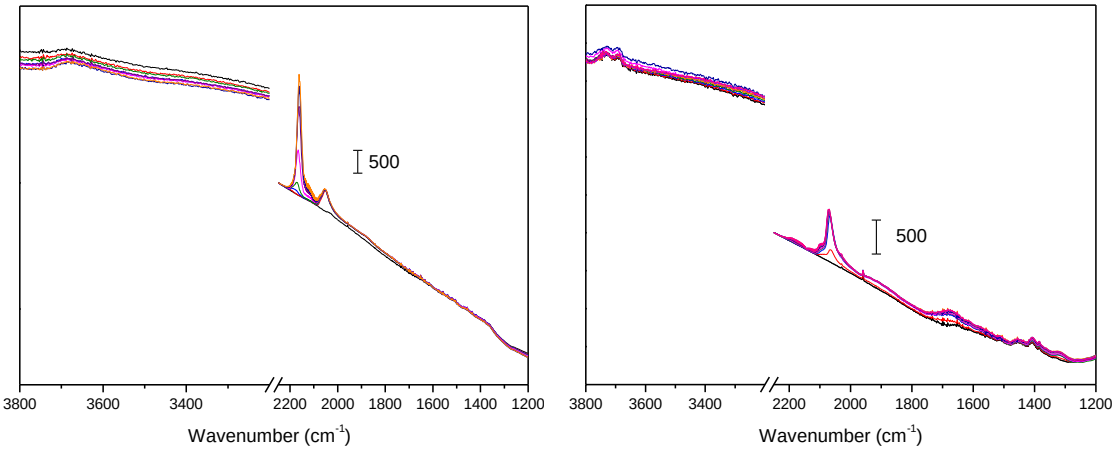

Fig. 4.67 CO 77K (left) and CO RT (right) of Ro43MAc reduced at 950 °C.

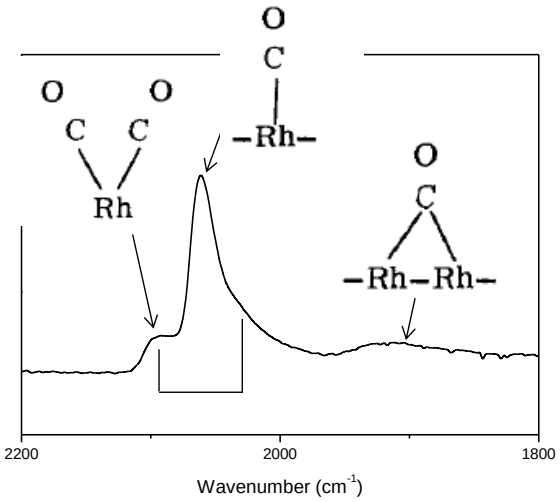

Fig. 4.68 CO RT of Ro43MAc reduced at 950 °C (detail).

Rh silicate reduced at 750 °C shows a main band at 2047 cm^{-1}, slightly lower than the band previously associated to monocarbonyl: it can be an effect of different matrix respect Ro43MAc. Furthermore a broad and low band at 1890 cm^{-1} is detected and ascribed to bridged carbonyl. No dicarbonyl or carbonates are observed confirming that the presence of the former specie affects the presence of the second one.

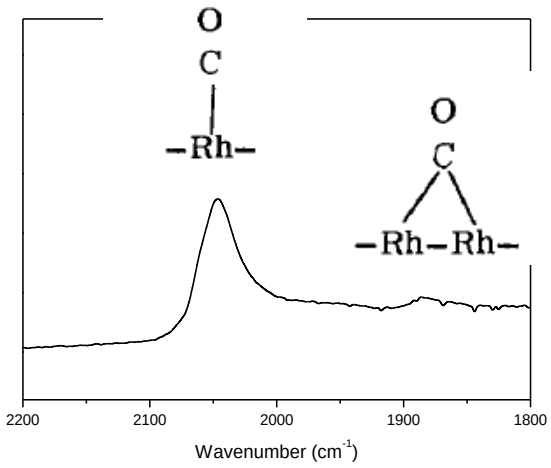

Fig. 4.69 CO RT of R5M80As reduced at 750 °C.

RCZO during adsorption at 77K shows typical band of linear CO chemisorbed at 2050 cm^{-1} as Ex-HTs. Despite of the low temperature two bands ascribed to CO dicarbonyl and some bands at 1650-1200 cm^{-1} attributed to carbonates are observed therefore this sample shows higher reactivity respect Ex-HTs. At RT bands related to dicarbonyl are higher than that one relative to monocarbonyl, differently from Ex-HT samples which show opposite trend. The comparison of CO_2 chemisorption of RCZO and R043MAc is reported in Fig. 4.72. Considering that higher is splitting Δν lower is the basicity, RCZO shows the highest basicity.

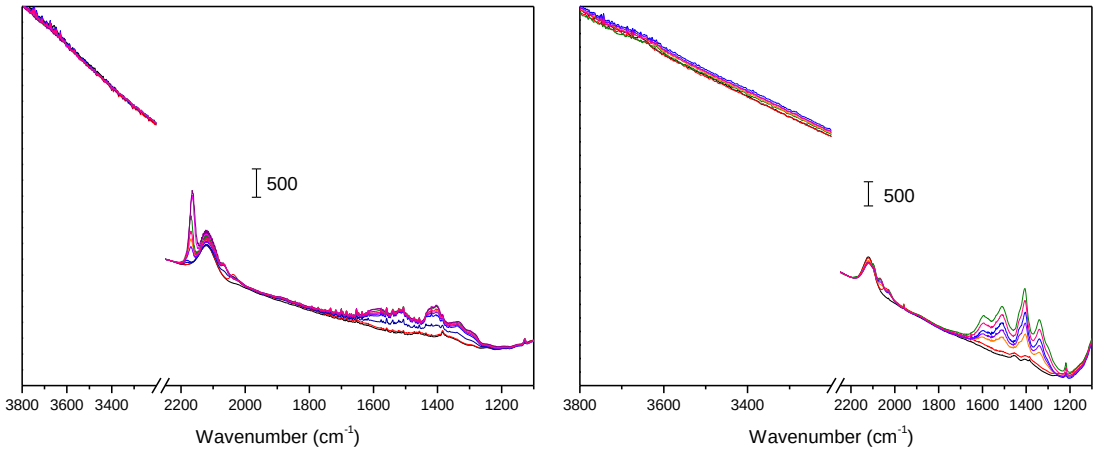

Fig. 4.70 CO 77K (left) and CO RT (right) of RCZO reduced at 500 °C.

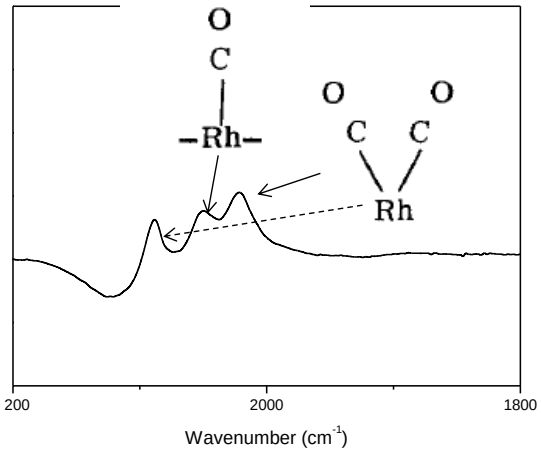

Fig. 4.71 CO RT of RCZO reduced at 500 °C (detail).

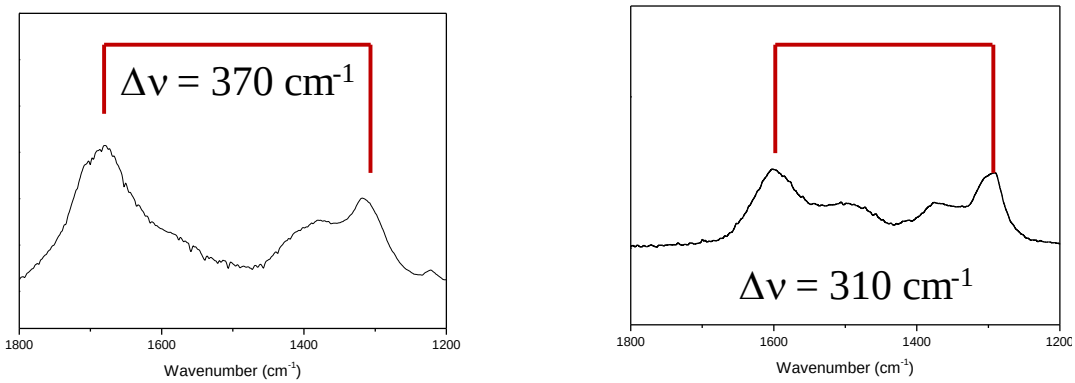

Fig. 4.72 CO_2 RT of Ro43MAc (left) and RCZO (right).

4.3.3.2 Activity

The new reaction conditions can be summarized in:

P = 1 bar;
Toven = 600 and 750 °C;
S/CH_3CH_2OH = 5 mol/mol;
fD = He/(H_2O+CH_3CH_2OH) = 4 mol/mol;
V = 1 mL;
Pellets size = 30-40 mesh

Conditions	x	6x	12x	18x	23x
CT (standard) (s)	0.333	0.056	0.028	0.018	0.014
CT (700°C) (s)	0.102	0.017	0.008	0.006	0.004
CT (550°C) (s)	0.121	0.020	0.001	0.007	0.005

Tab. 4.15 Contact time, calculated in standard conditions, at 750 and 600°C.

All catalysts were reduced at 750 °C for two hours. As in previous type of conditions tests were carried out at 700 °C for five different contact times, then the temperature was decreased at 550 °C and same type of tests were repeated. For these tests also the weight of catalysts was reported because all catalysts contain same % wt of rhodium and therefore it can be a further help to understand catalytic data.

Catalyst	R043MAc	R043M80Ac	R055MAs	R05M80As	RCZO
Weight (g)	0.545	0.815	0.638	0.668	1.412

Tab. 4.16 Amounts of samples weighted for catalytic tests.

At 700 °C, the high reduction of contact time doesn't affect significantly ethanol conversion of Rh carbonates samples which continue to show high values above 80 % although the temperature inside the bed is lower than first condition because higher amounts of reagents increase the heat consumed by the endothermic reactions.

When ethanol conversion is complete gas phase distribution is close to thermodynamic equilibrium for both catalysts, while when ethanol conversion is not complete, intermediates are observed in small amounts (CH_2CH_2+CH_3CHO < 6%) for R043MAc. Rh with less magnesium (R043MAc) shows only CH_2CH_2 and CH_3CHO which are intermediates of reaction while R043M80Ac shows also CH_3COCH_3 and some traces of CH_3CH_3 which are due respectively to aldolic condensation of CH_3CHO and hydrogenation of CH_2CH_2. As a confirm of previous assertion when CH_3COCH_3 selectivity decreases higher amount of CH_3CHO is obtained.

The decrease of contact time and the temperature inside the bed determine, for R043MAc, increasing trend of CH_4 selectivity due to less reforming and a maximum in CO_2 selectivity trend due to water gas shift as confirmed by K of equilibrium calculated. With R043M80Ac it is not possible observe the maximum of CO2 but only a decreasing trend because the decrease of temperature inside the reactor is less marked and the amount of intermediates and byproducts is higher.

At 550 °C the effect of contact time on ethanol and water conversions and gas phase distributions is more evident. As for tests at higher temperature, the sample R043M80Ac shows higher amount of intermediates and CH_3COCH_3. At increasing amount of CH_3CHO corresponds decreasing selectivities of CO and CH_4 because CH_3CHO doesn't decompose as mechanism of reaction explains.

The presence of CH_3COCH_3 with R043M80Ac and not with R043MAc seems suggest that an high amount of MgO respect $MgAl_2O_4$ and therefore an high amount of strong basic sites determines side reaction as aldolic condensation.

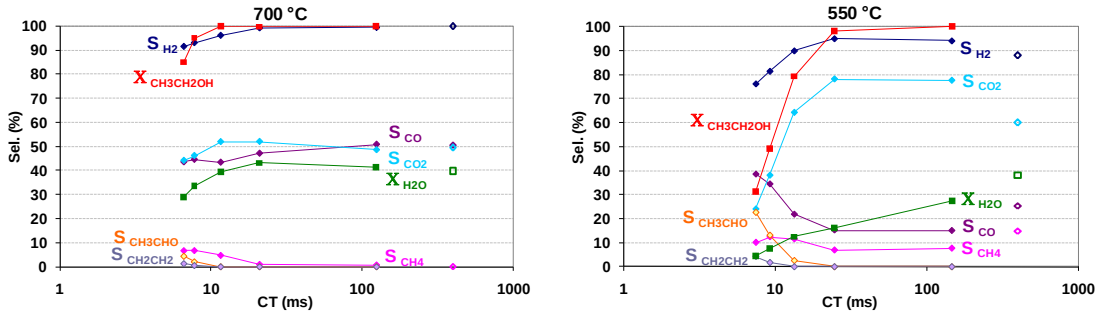

Fig. 4.73 Activity and selectivities of R043MAc.

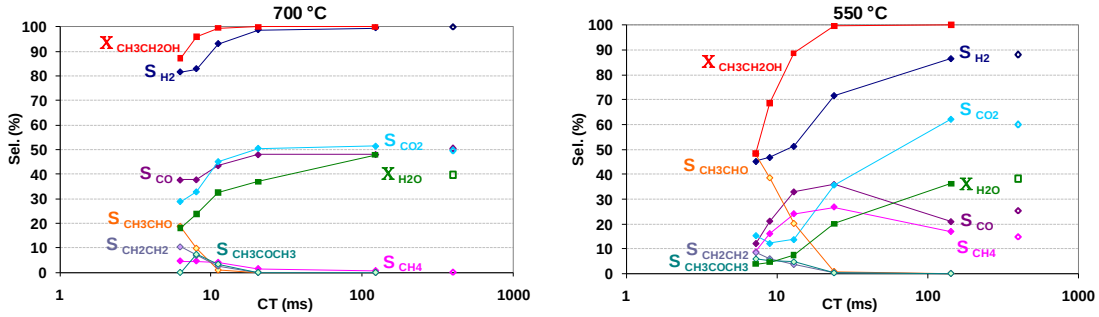

Fig. 4.74 Activity and selectivities of R043M80Ac.

Silicates samples show between them very different trends in activity and products distributions: at 700 °C R055MAs shows the most evident decreasing trend of ethanol conversion when R05M80As shows, also at very low contact time, total ethanol conversion. As observed before the low ethanol conversion affects gas phase distribution of R055MAs which presents not only intermediates but also CH_3COCH_3 and CH_3CH_3. In addition during initial tests CH_4 selectivity is close to zero for all catalysts except R055MAs which shows 5 %.

The insertion of higher amount of magnesium improves significantly catalytic performance: ethanol conversion reaches 100 % in all conditions and no intermediates or byproducts are observed. As for R043MAc the rapid decrease of catalytic bed temperature due to decrease of contact times affects CO / CO_2 and CO / CH_4 ratios.

At 550 °C R055MAs shows gas phase composition far from thermodynamic data even at high contact time. The high amount of CH4 decreases with decreasing contact time due to the higher presence of CH_3CHO , while CO has a maximum at intermediate residence time. These trends seem to suggest that this catalyst is not active in methane reforming differently from carbonates series and R05M80As sample.

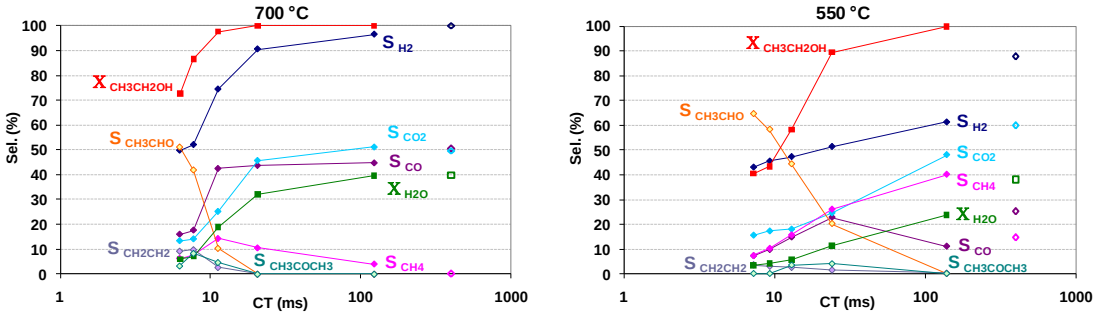

Fig. 4.75 Activity and selectivities of R055MAs.

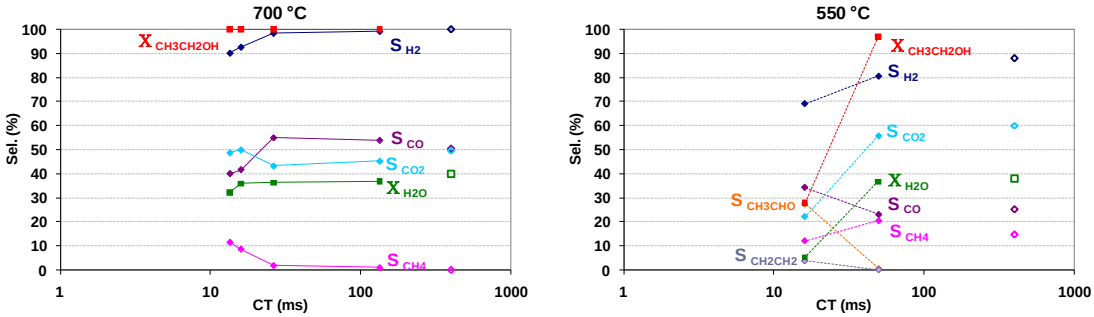

Fig. 4.76 Activity and selectivities of R05M80As.

At 700 °C ethanol conversion of RCZO is total and water conversion is kept rather constant and high for all conditions although the temperature inside the reactor decreases of about 25 °C or more as other catalysts. Despite of these data it has to be noted that the amount of total Rh loaded is higher (two times that of the R05M80Aa) due to high bulk density of the catalyst.

As in previous catalysts by decreasing contact time and temperature inside the bed, CO selectivity decreases while CO_2 and CH_4 selectivity increase. These trends are due to methane reforming reaction which occurs less at low contact time and temperature and water gas shift which is more favourite as it is confirmed by the increase of K of water gas shift consistent with the increase of the constant of equilibrium (22).

At 550 °C ethanol and water conversion decreases. In first condition, where CH_3COCH_3 is not detected the amount of CO_2 is very high, and only CH_4 and CO are observed. By decreasing contact time CH_3COCH_3 is detected and CH_4 decreased because part of CH_3CHO don't decompose to CH_4 and CO but give CH_3COCH_3. Only when CH_3COCH_3 doesn't appear at low contact time CH_4 increases again. CO trend is also affected by water gas shift reaction, as a consequence the CO selectivity increase more quickly only when CO_2 decreases significantly.

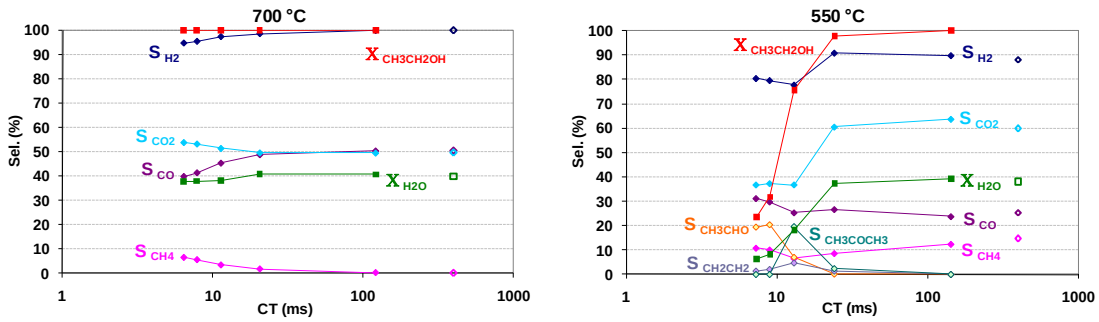

Fig. 4.77 Activity and selectivities of RCZO.

4.3.3.3 Characterization of spent catalysts

4.3.3.3.1 X-Ray diffraction (XRD) analysis

The calcined hydrotalcite samples shows the same phase distribution than the fresh one. In the carbonate samples beside the previous phases is present one peak at 10° 2θ which is characteristic of hydrotalcite phase that can be formed during storage or discharge. This behaviour is not observed in silicate sample, therefore the carbonate seem to have higher tendency to restore the hydrotalcite structure (i.e. the phenomena is known as memory effect) than silicate one.

No graphite or other amorphous coke were detected by XRD.

For what concern the XRD pattern of RCZO, spent sample is very similar to the XRD pattern of fresh sample.

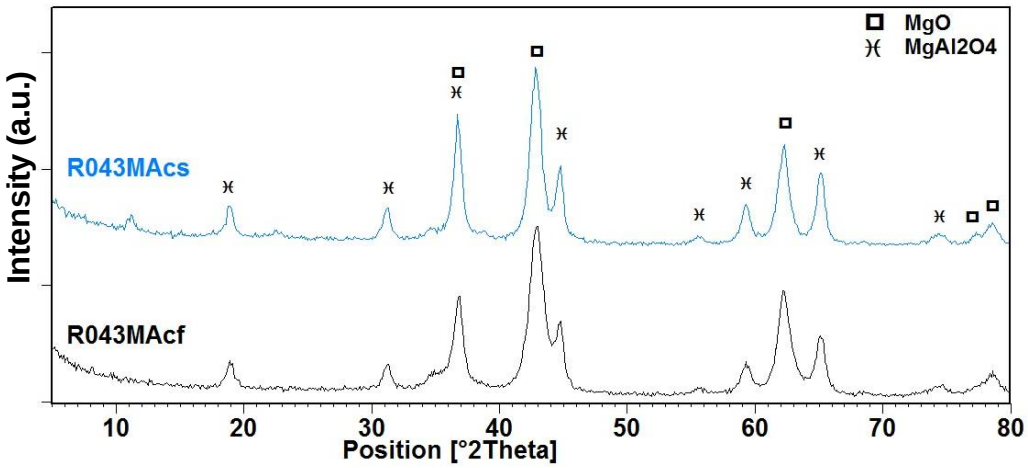

Fig. 4.78 XRD of fresh and spent R043MAc.

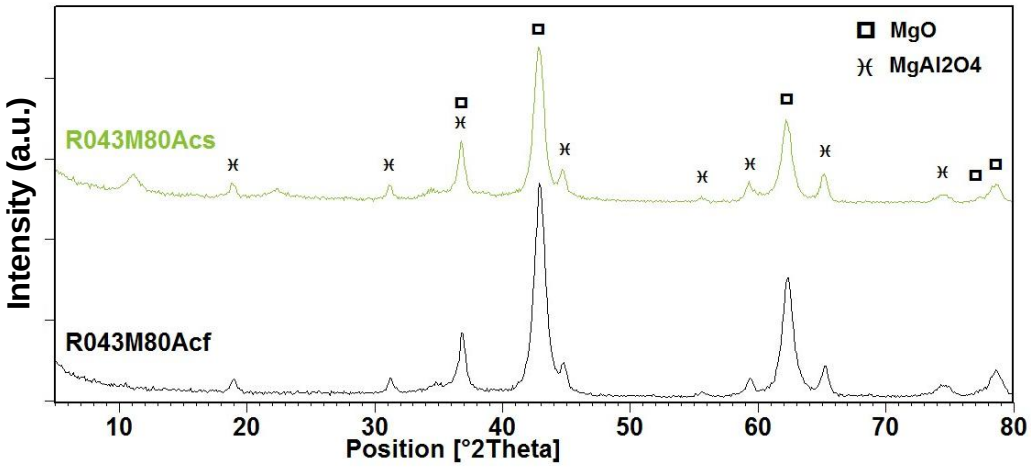

Fig. 4.79 XRD of fresh and spent R043M80Ac.

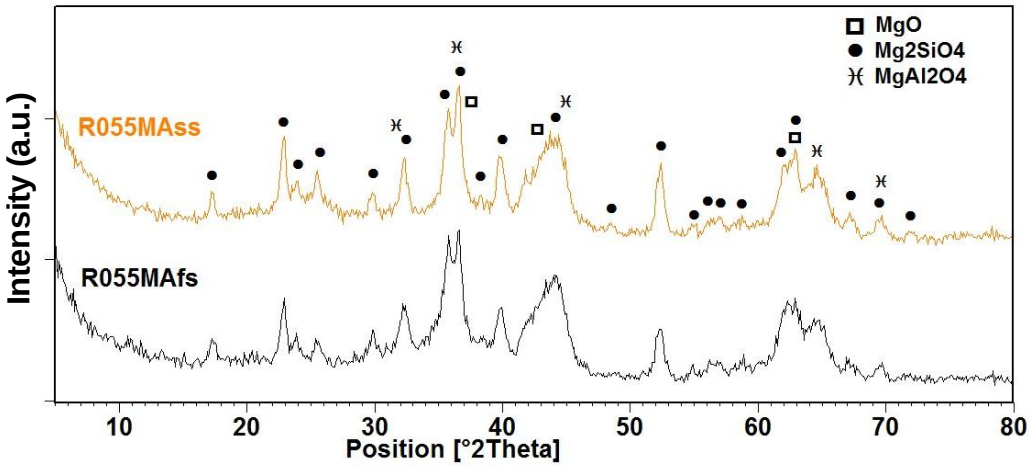

Fig. 4.80 XRD of fresh and spent R055MAs.

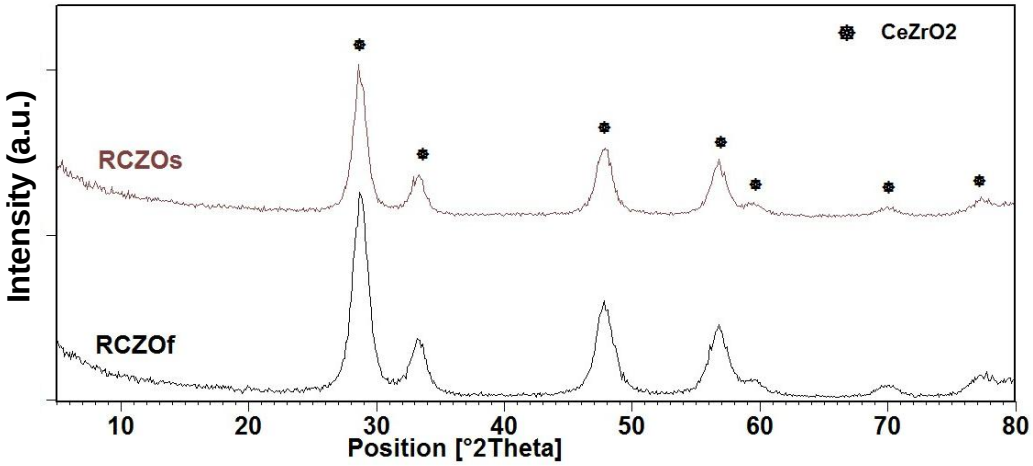

Fig. 4.81 XRD of fresh and spent RCZO.

4.3.3.3.2 Surface area and porosimetry analysis

After the catalytic tests the specific surface area and pore volume of spent samples based on carbonate are lower than those of fresh one, while in silicate sample the value of surface area is similar to fresh one; but the volume of the pore of spent samples is lower than fresh one. Carbonate samples show higher loss of surface area than silicate confirming the higher instability of these samples than silicates.

The pore size distribution plot of spent samples show for the sample R043M80Ac, R055MAs and RCZO an increase of volume for pore with lower width.

	BET surface area (m^2g^{-1})	t-plot micropore area (m^2g^{-1})	BJH desorption cumulative volume of pores (cm^3g^{-1})	BJH desorption maximums pore widths (Å)
R043MAcf	121.16	17.47	0.631	122
R043MAcs	77.12	2.12	0.428	73 , 172
R043M80Acf	105.16	19.97	0.250	37 , 60 , 125
R043M80Acs	71.01	8.05	0.160	35 , 45
R055MAsf	113.20	10.08	1.129	34 , 235
R055MAs	108.81	2.74	0.369	36 , 123
RCZOf	53.08	3.19	0.122	43
RCZOs	11.31	2.06	0.149	28

Tab. 4.17 Surface area, pores volume and width of spent catalysts.

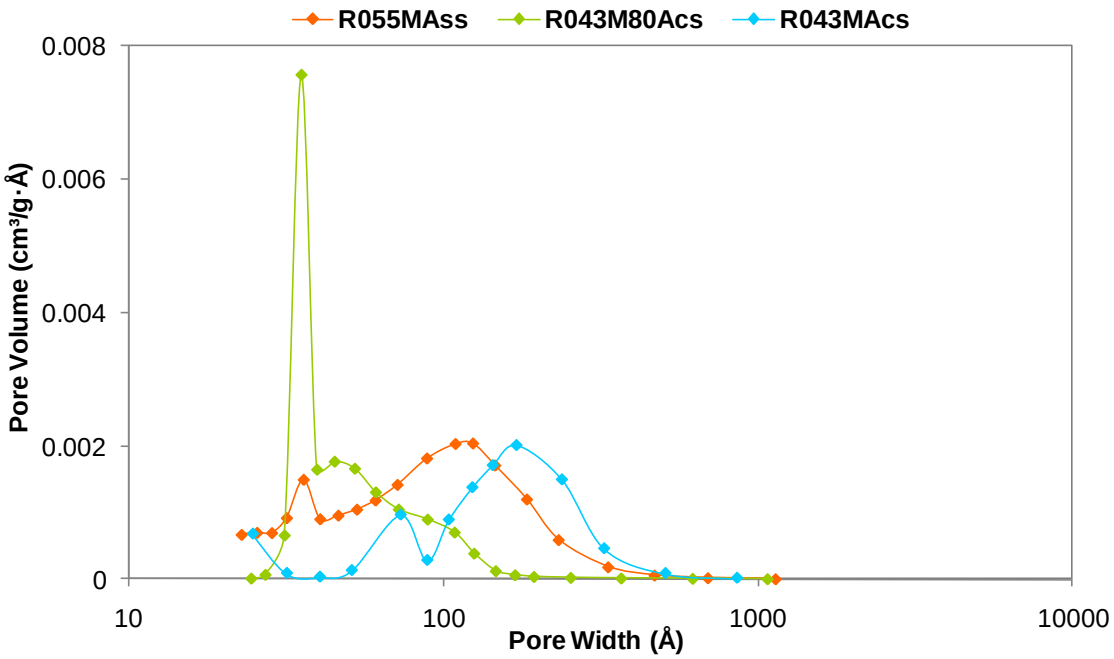

Fig. 4.82 BJH pore size distribution of spent Ex-HT.

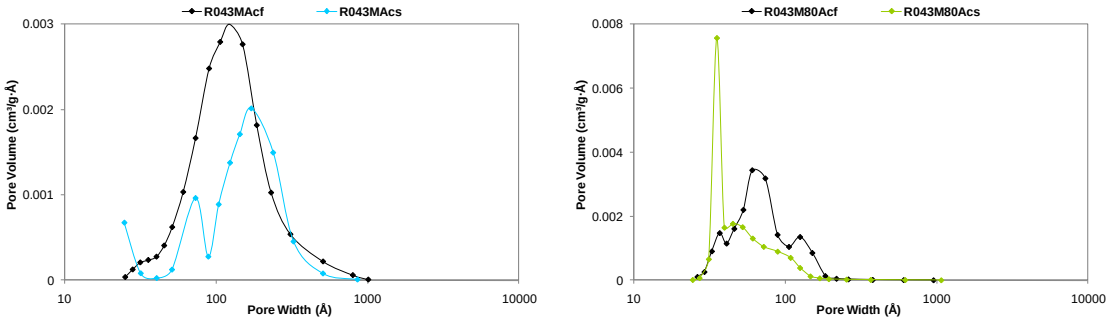

Fig. 4.83 BJH pore size distribution of spent Ex-HTs carbonates.

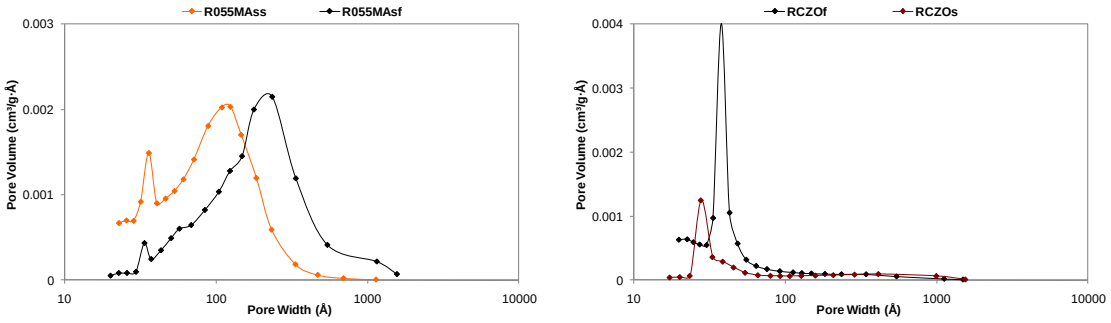

Fig. 4.84 BJH pore size distribution of spent R055MAs and RCZO.

4.3.3.3.3 Transmission Electron Microscopy analysis

The final calculated size of the particles was calculated considering about 20 particles. In Tab. 4.18 was summarized all the values, while in Tab. 4.19 was calculated the percentage of increase of particle size respect the fresh one.

Spent samples show different trend: rhodium carbonate (R043MAc), which shows best performance, shows lower increase of particle size, while the other two R043M80Ac and R055MAs show an increase of particle size two-three times respect the sample reduced at 750 °C. These last two sample show an higher instability of rhodium particle then R043MAc.

Dp (nm)	**R043MAc**	**R043M80Ac**	**R055MAs**	**R05M80As**
Fresh (750-2h)	1.4	1.1	1.0	1.1
Fresh (1000-4h)	2.6	/	/	2.0
Fresh (1000-30')	1.8	/	/	/
Spent (750)	1.9	3.3	2.6	/

Tab. 4.18 Rhodium size of Ex-HT samples after different treatments.

Dp (nm)	**% R043MAc**	**% R043M80Ac**	**% R055MAs**	**% R05M80As**
Fresh (750-2h)	100	100	100	100
Fresh (1000-4h)	185	/	/	181
Fresh (1000-30')	128	/	/	/
Spent (750)	136	300	260	/

Tab. 4.19 Percentage of increase of rhodium size for Ex-HT samples after different treatments.

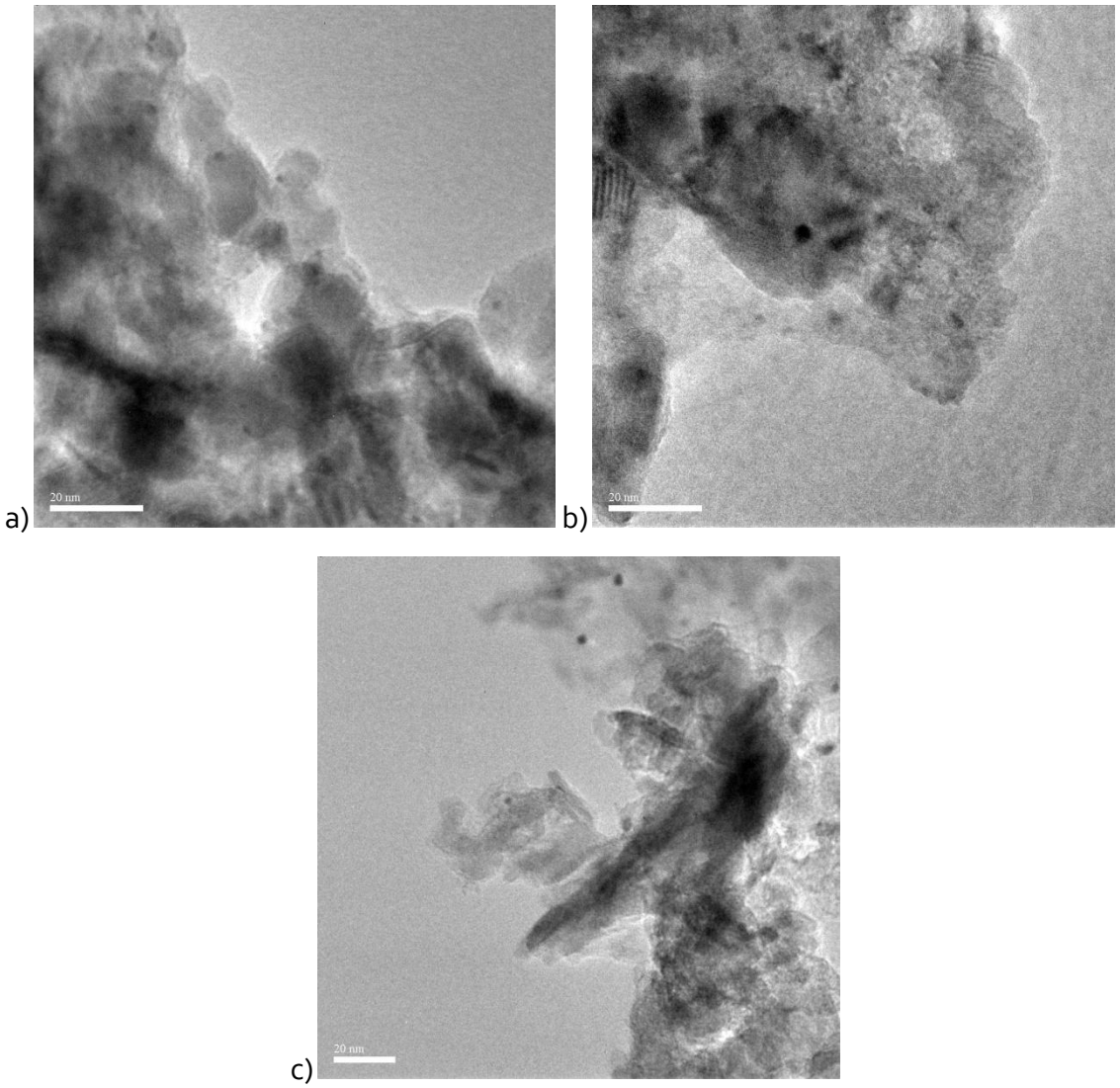

Fig. 4.85 TEM of spent samples tested at 700 and 550 °C for one week: a) R043Mac, b) R043M80Ac and c)R055MAs.

4.3.3.4 Comparisons and conclusions

At 700°C and high contact time all catalysts show complete ethanol conversion, gas phase distribution at thermodynamic equilibrium and H_2 selectivity close to 99%, except the sample R055MAs which is the catalyst less selective and it show H_2 selectivity close to 90% due to high amount of CH_4 (Fig. 4.86).

By decreasing contact time it is possible observing differences between catalysts: RCZO and R05M80As are the most active and they don't show intermediates or by-products. RCZO shows higher CO_2 selectivity than R05M80As which shows higher CH_4 selectivity (Fig. 4.87). Carbonate samples show similar activity, but different selectivities. The one with higher amount of Mg (R043M80Ac) and therefore higher basicity shows higher amount of intermediates and as consequence lower H_2 selectivity. R055MAs shows worse results in term of activity and selectivity: the lowest ethanol conversion with the highest intermediates selectivities.

At 550°C and high contact time all catalysts, except R055MAs, show ethanol conversion close to 97%, while the value of R055MAs is 90%. Differently from tests at 700°C, RCZO and R043M80Ac, despite the high ethanol conversion, show traces of intermediates and CH_3COCH_3, which is higher for RCZO. R043MAc and R05M80As show very high H_2 and CO_2 selectivities and only traces of intermediates under 1 %. No CH_3COCH_3 or CH_3CH_3 are observed.

By decreasing contact time R05M80As and R043MAc keep showing high CO and CO_2 selectivities even ethanol conversion is low, on the contrary R043M80Ac and R055MAs show higher ethanol conversion but also higher amount of CH_3CHO. Catalyst performances seem suggest that first group of catalysts favours more the break of C-C bond and reforming reaction while second group favours mainly the dehydrogenation of ethanol. RCZO shows a different and more complex trend. At very high ethanol when the amount of intermediates is negligible, H_2 selectivity, considered as the sum of CO and CO_2 selectivity to avoid H_2 obtained by decomposition, is high and similar to that one of first group of catalysts R043MAc and R05M80As. By decreasing contact time the amount of CH_3CHO follows same trend of first group of catalyst (Fig. 4.90) but the presence of CH_3COCH_3 changes the profile

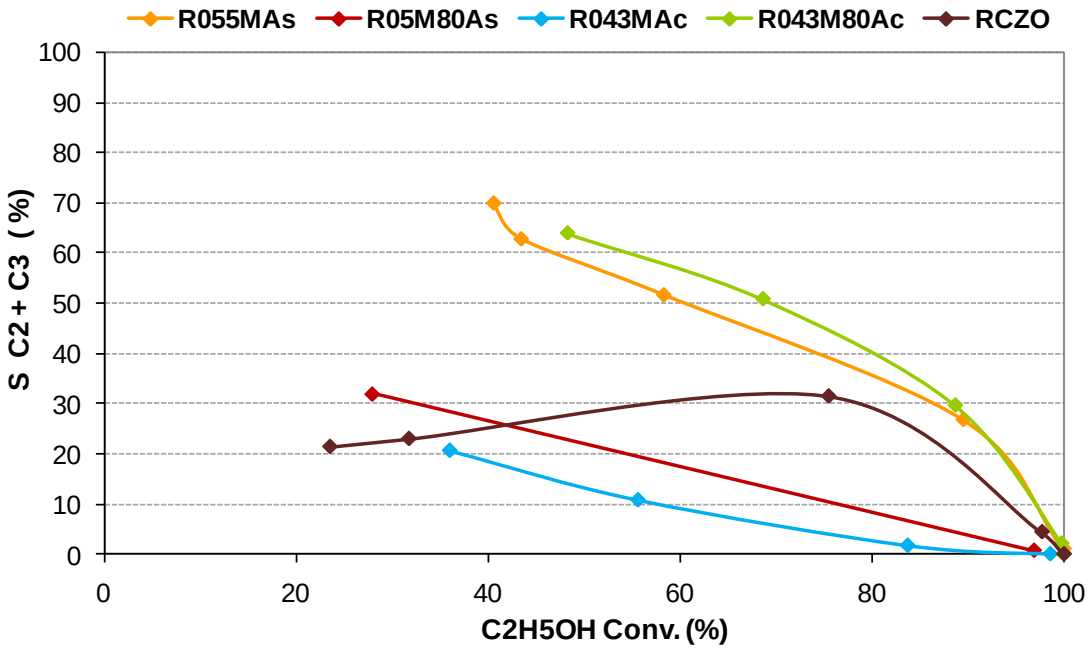

Fig. 4.91). Therefore this catalyst shows high ability to break C-C bond and favours CH_4 reforming but at the mean time is active versus aldolic condensation. IR measurements allows to show that RCZO exhibits higher basicity then R043MAc and highest reactivity to form carbonates species between R043MAc and R05M80As. This strong basic sites and the high reactivity could explain the high amount of acetone due to aldolic condensation.

Catalytic results show similar trends for samples with close $MgO/MgAl_2O_4$ ratio creating a relationship between high C1 selectivities and the ratio $MgO/MgAl_2O_4$. In particular the right ratio should be included in 1.1-1.5 (Fig. 4.42).

Regarding catalytic performances both R043MAc and R05M80As can be consider promising catalysts to study under pressure. Since hydrotalcite prepared with silicates have shown more stable catalysts, i.e. no reconstruction and no high decrease of surface area, R05M80As was chosen to continue the work under pressure.

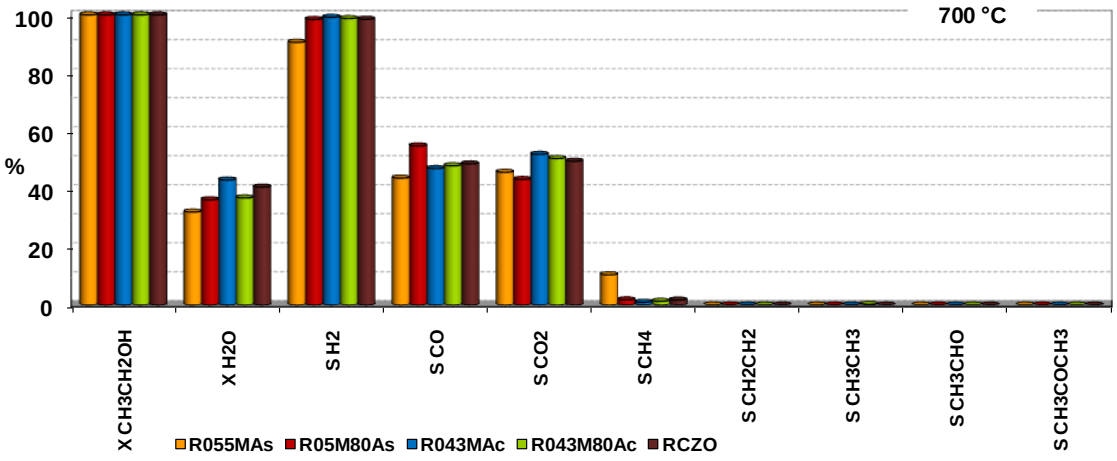

Fig. 4.86 Comparisons of gas phase distribution at 700 °C during 6x condition.

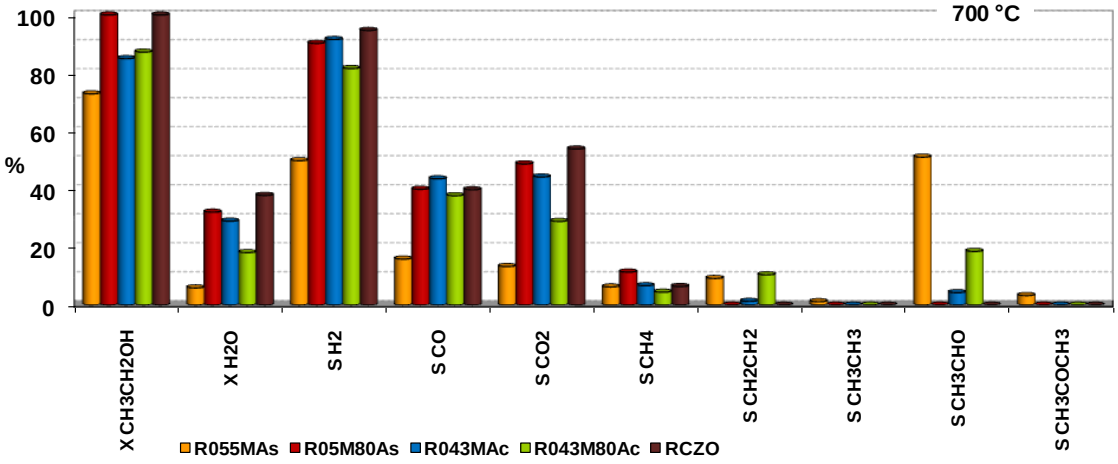

Fig. 4.87 Comparisons of gas phase distribution at 700 °C during 23x condition.

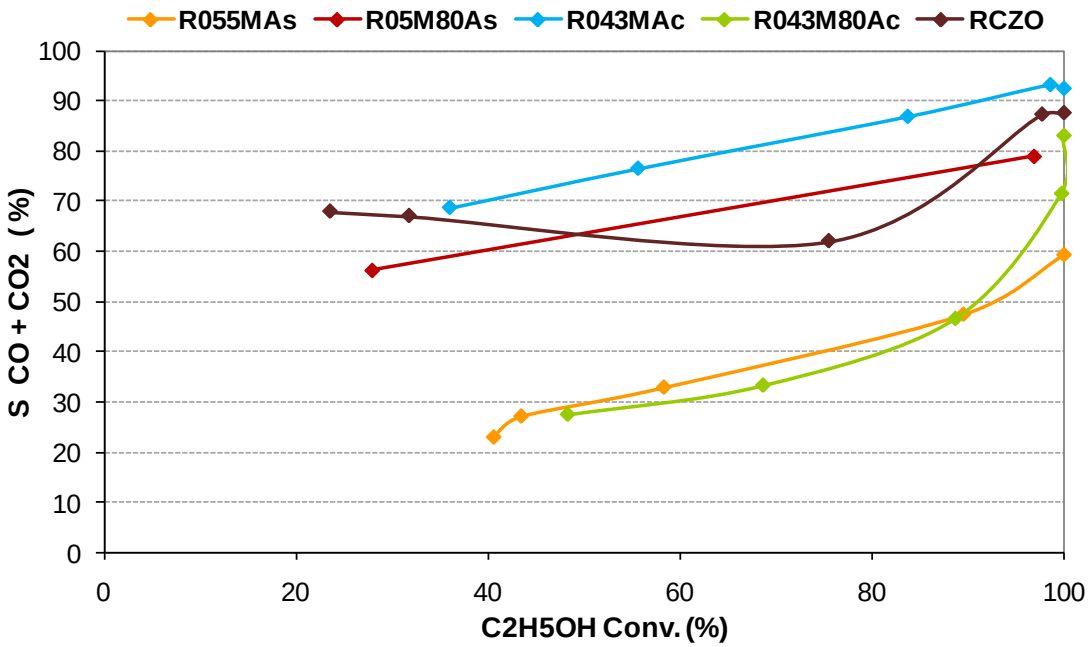

Fig. 4.88 Comparison of $CO+CO_2$ selectivities at 550 °C.

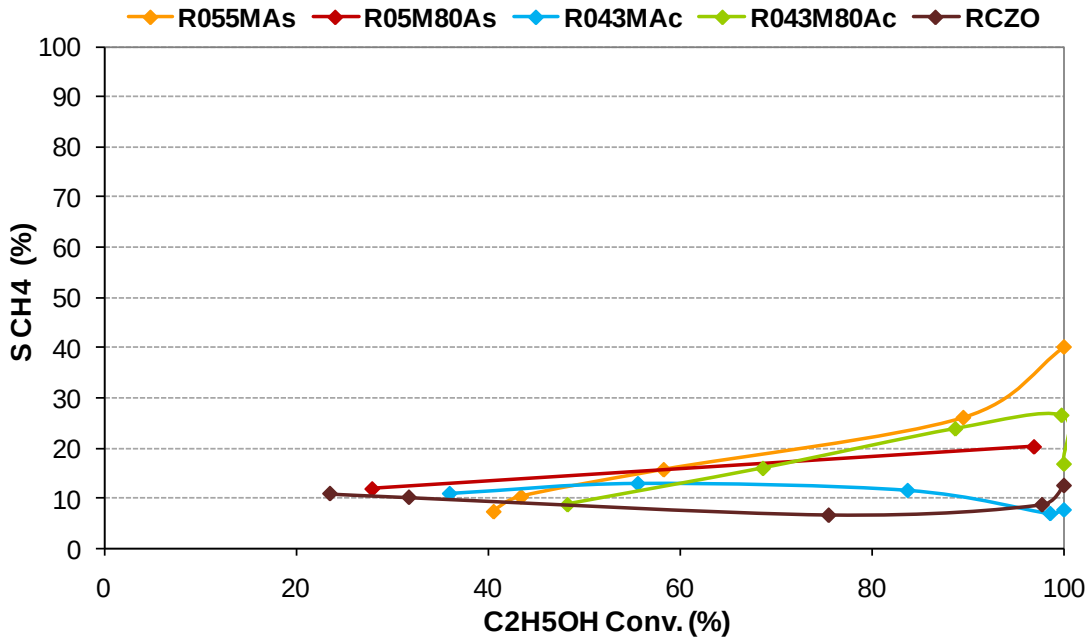

Fig. 4.89 Comparison of CH_4 selectivities at 550 °C.

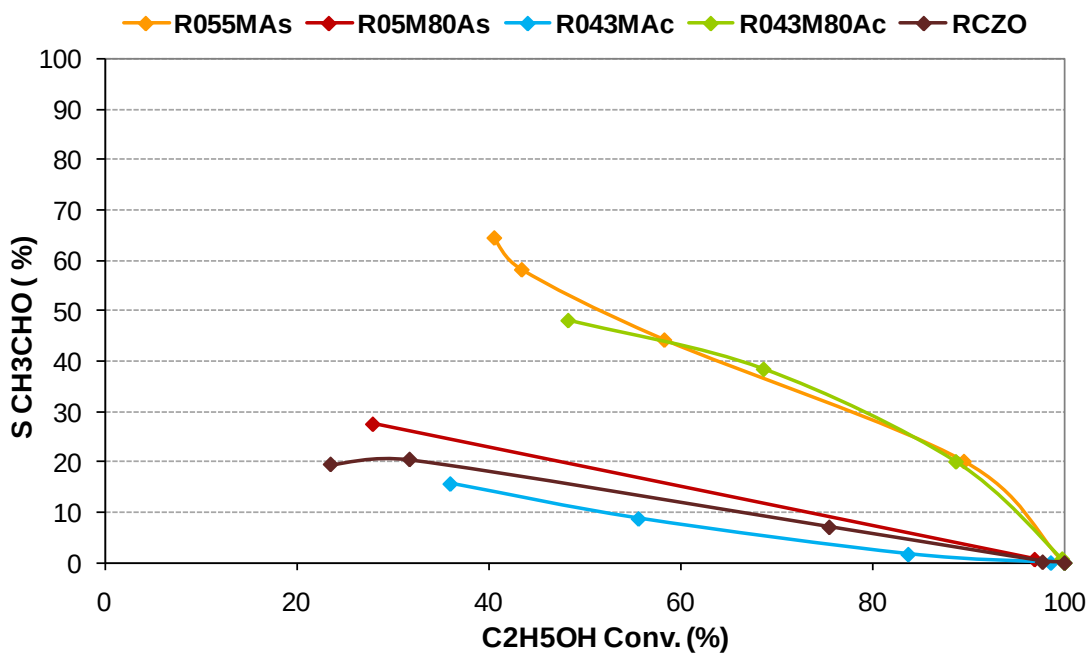

Fig. 4.90 Comparison of CH_3CHO selectivities at 550 °C.

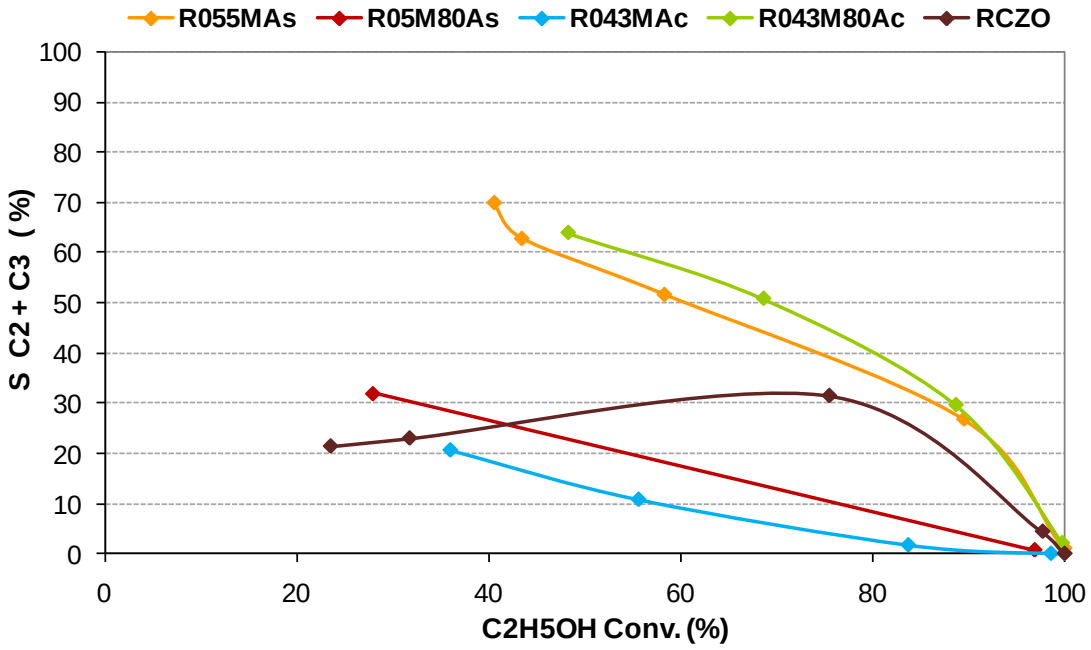

Fig. 4.91 Comparison of C2+C3 selectivities at 550 °C.

4.4 Preparation of foams with hydrotalcite

This part of the study was focus on the preparation of stable slurries to coat on ceramic (Al_2O_3) foams. Particular attention was dedicated to optimized the thickness of active phase on foams to avoid cracks or inhomogeneous coatings.

The work could be divided in two parts:

1. preparation of stable slurries in organic solvent and
2. preparation and characterization of foams.

To prepare a stable slurry, it is necessary to adapt the surface chemistry of the powder and the rheology of the slurry.

It requires the knowledge of basic data, such as:

- Granulometry
- Density — for powder
- Conductibility
- Sedimentation ability — for slurry
- Viscosity

4.4.1 Preparation of stable slurries in organic solvent

4.4.1.1 Preparation of slurries for planetary milling and attrition milling

Different slurries were prepared to observe the change of particles dimensions after each treatment. Treatments of planetary milling was named P while attrition milling treatments were named A. In planetary milling treatments the amount of catalyst depends on catalyst property and it usually is close to 5-10 % vol. Differently in attrition treatment there is 1/3 vol. of catalyst, 1/3 vol. of zirconia balls (Diam.) and 1/3 vol. of solvent. For all slurry the used solvent was a mix of MEK/EtOH = 3/2. After attrition the slurries were heated at 450 °C for 12 hours at 1°C/min to evaporate solvent and dispersing agent.

P1 : first planetary with 5 % vol of catalyst for 3 hours

A1 : first attrition for 4 hours

A1P1 : planetary with 5 % vol of catalyst after attrition

A2 : attrition with 6 % wt of dispersing agent respect to the weight of catalyst

A2P2 : planetary with 5 % vol of catalyst after attrition with dispersing agent and binding agent

4.4.2 Characterization of powder

4.4.2.1 Laser diffraction granulometric analyses

The granulometry analyses were carried out on slurry prepared with raw powder without treatments as attrition milling which decrease particles dimensions. The effects of times of ultrasound (US) and times of planetary milling were studied.

4.4.2.1.1 Effect of different times US (HT and Ex-HT)

Before US the size distribution of the powder is very large and three different granulometries are observed.

After US the size distribution is more homogeneous even if it is still quite large.

After 2 minutes of US the granulometry is quite stable. It appears to bimodal with two populations in the ranges [0.3 – 1] µm and [1 – 16] µm.

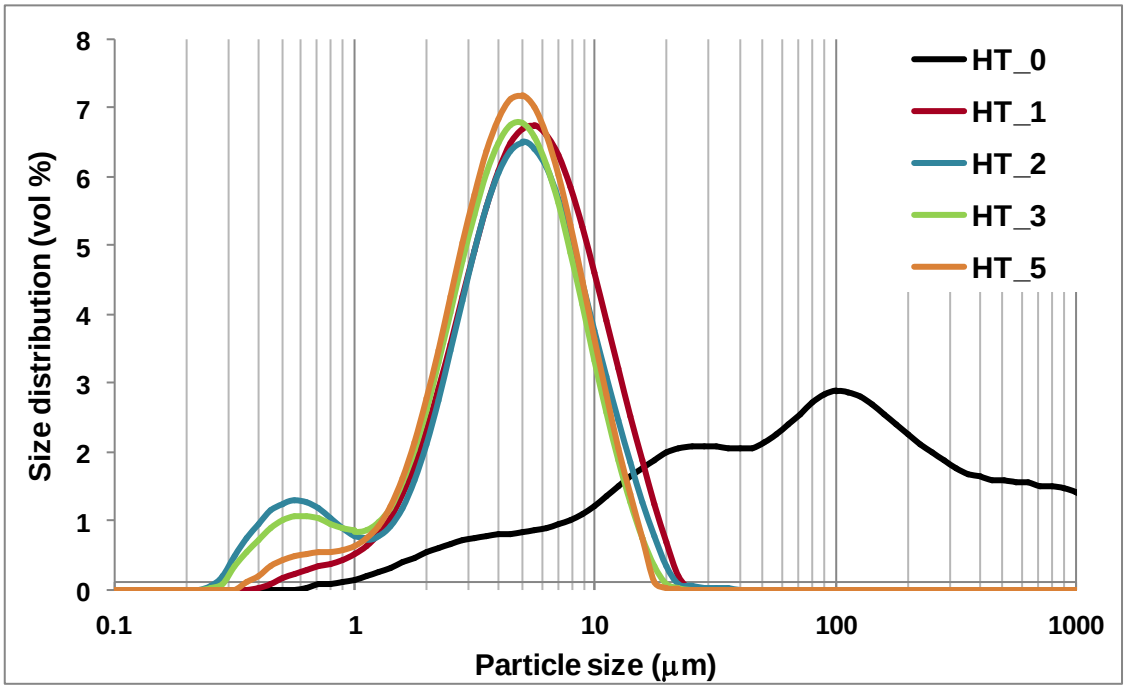

Fig. 4.92 Effect of time of US on granulometric analyse of HT.

Before US the size distribution of the powder is very large and three different granulometries are observed as for HT.

After US the size distribution is more homogeneous even if it is still quite large. Two regions of particle size are observed : the first between 0.4 and 31.7 µm and the second between 50 and 159 µm.

Only after 3 minutes of US the granulometry is quite stable and only one population is observed : [0.4 – 18] µm.

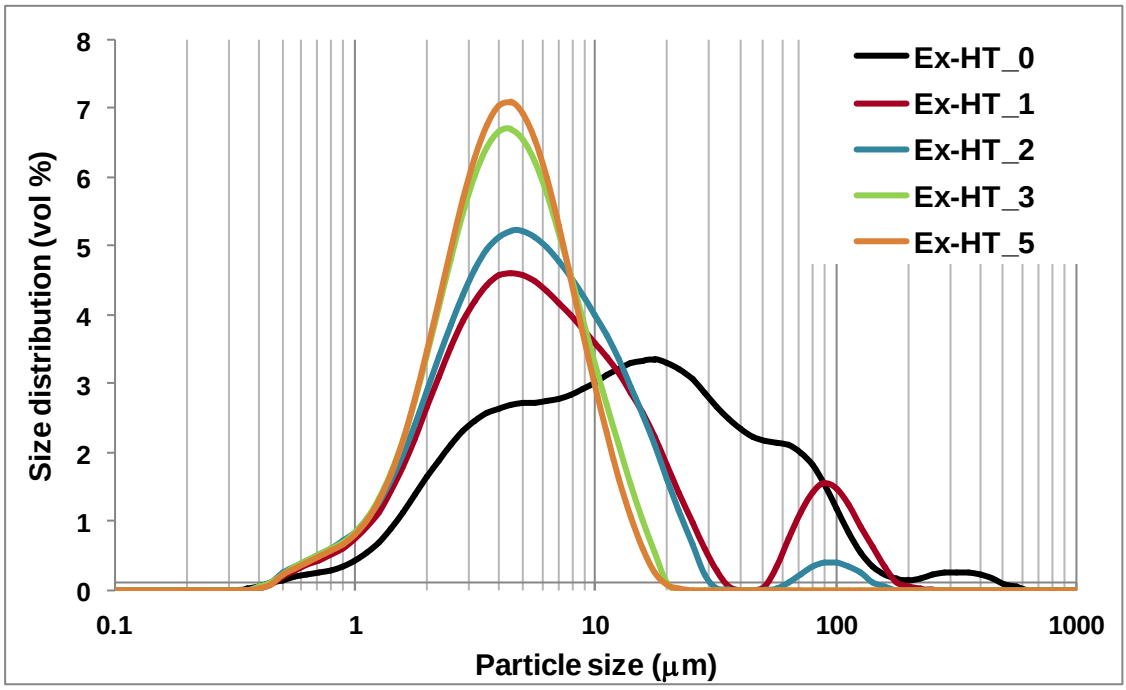

Fig. 4.93 Effect of time of US on granulometric analyse of Ex-HT.

4.4.2.1.2 Effect of different times planetary milling (HT and Ex-HT)

After 2 hours of planetary milling, large agglomerates are removed and two regions are observed: [0.35 – 1] µm and [1 -31] µm.

The effect of planetary milling is almost similar to that of US in its ability to deagglomerate the powder.

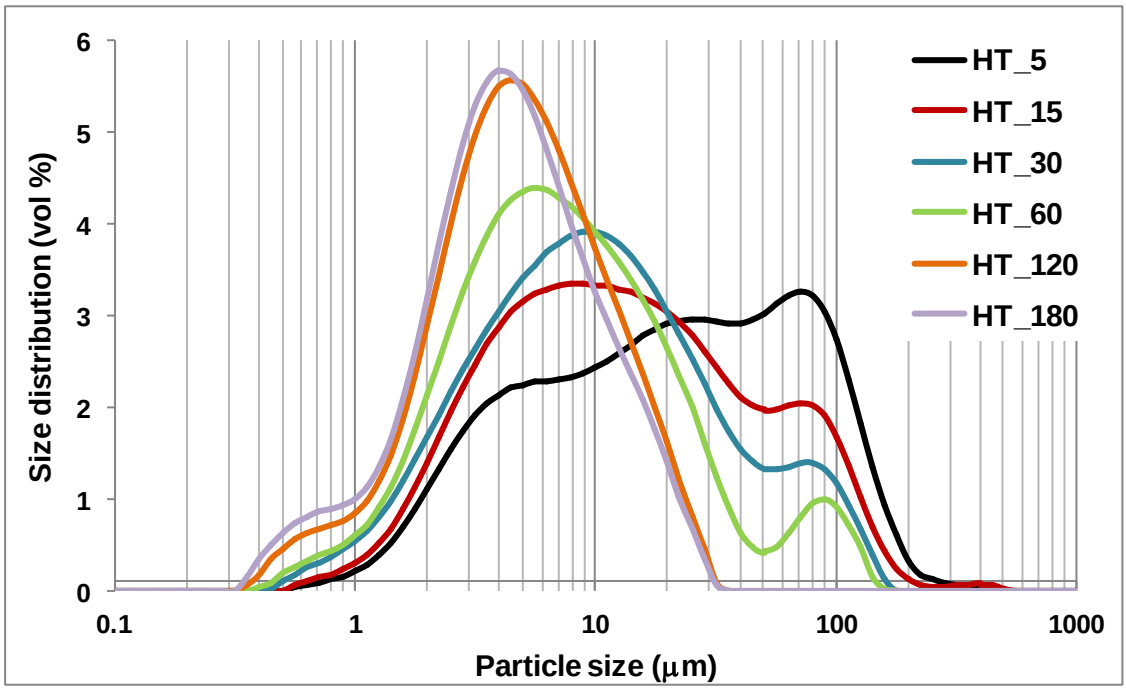

Fig. 4.94 Effect of time of planetary milling on granulometric analyse of HT (P1).

3 hours of planetary milling (P1) are not enough to break all the largest agglomerates. In this case, without a dispersing agent, it is very difficult to get rid of agglomerates.

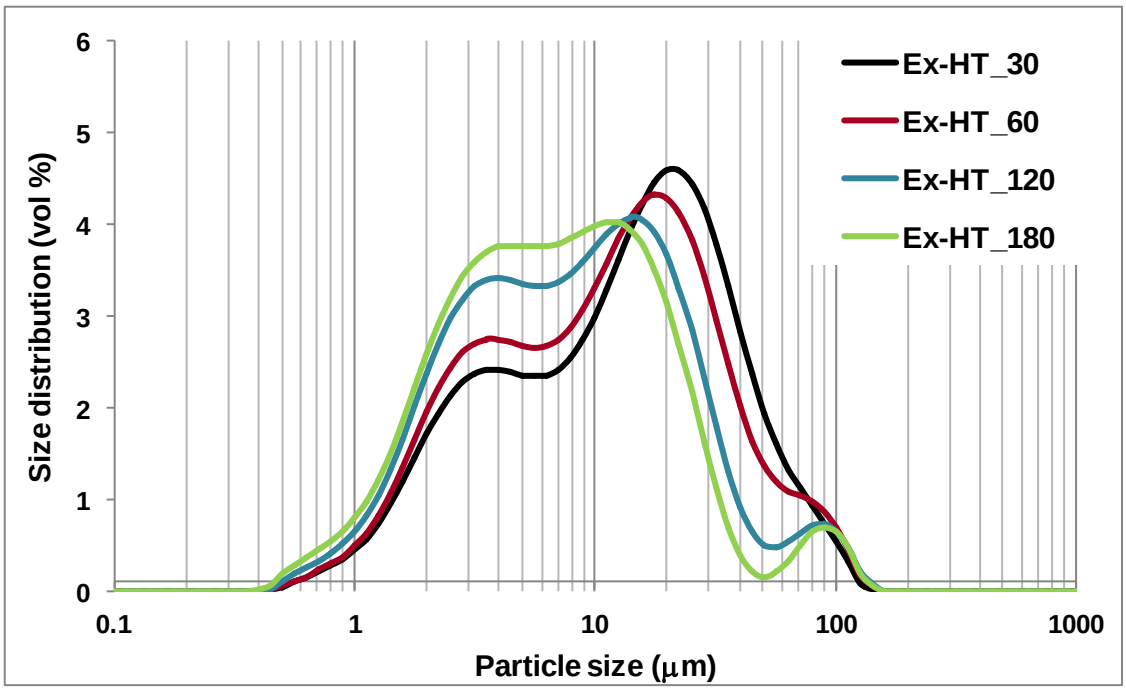

Fig. 4.95 Effect of time of planetary milling on granulometric analyse of Ex-HT (P1).

4.4.2.2 Density

Density of both hydrotalcites and ex-hydrotalcites was measured by mean of He-pycnometer at 20°C. The reported value is close to 2.00 g/mL for hydrotalcite and close to 3.00 g/mL for samples calcined at 900°C for 12h.

	HT density (g/mL)	Ex-HT density (g/mL)
R043MAc	1.84	2.90
R043M80Ac	1.96	3.01
R055MAs	2.08	3.03
R05M80As	1.89	2.97

Tab. 4.20 Density of HT and Ex-HT.

4.4.2.3 Conductibility

Two slurries with 2% wt of samples were prepared to measure the conductibility of both hydrotalcites and ex-hydrotalcites. The measure was carried out at 20 °C. The conductibility of distilled water is very low (4-5 μS) and it is necessary working with as low as possible conductibility to know the real amount of powder in the slurry. Both

before and after US, the ex-hydrotalcite shows lower value of conductibility then hydrotalcite, therefore it was chosen to work on ex-hydrotalcite to have more stable and reproducible slurries.

	Conductibility (μS)	pH
HT R043MAc	143	8.2
Ex-HT R043MAc	82	9.3
HT R043MAc after US	194	8.8
Ex-HT R043MAc after US	115	9.9

Tab. 4.21 Conductibility and pH of HT and Ex-HT.

4.4.3 Characterization of slurries

The granulometric analyses confirm that it is necessary a dispersing agent during planetary milling trying to destroy bigger agglomerates. A sedimentation test was carried out to know the better amount of dispersing agent to add to the slurry (P1).

In addition an attrition milling was carried out on the powder to decrease as big as possible particles dimensions (A1).

4.4.3.1 Sedimentation ability after planetary milling (P1)

The obtained slurry after planetary milling was divided in five test tubes and in each tube different amount of dispersing agent was added. In Tab. 4.22 the amount of dispersing agent for each tube was summarized. The percentage is referred to the weight of catalyst.

The Fig. 4.96 shows that the most compact sample is the fifth sample with 5% of dispersing agent. Therefore during planetary milling 5% wt of dispersing agent was added to the slurry.

Nr samples	Amount of dispersing agent
0	/
1	1 % wt of catalyst
2	2 % wt of catalyst
3	3 % wt of catalyst
4	4 % wt of catalyst
5	5 % wt of catalyst

Tab. 4.22 Amount of dispersing agent for sedimentation ability (P1).

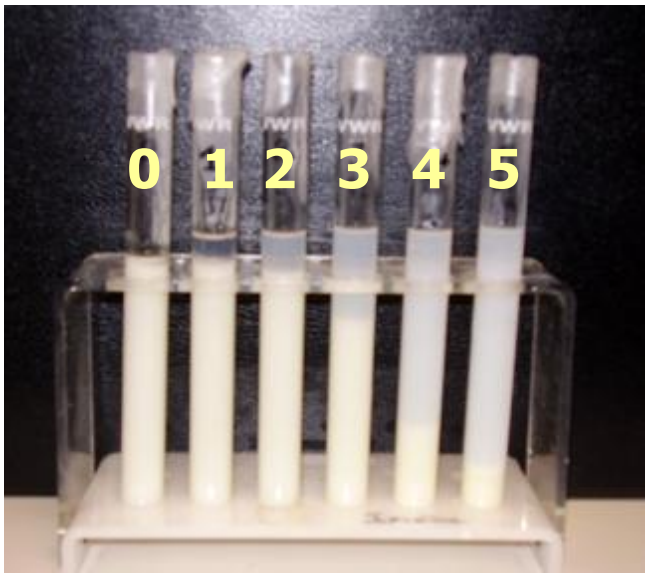

Fig. 4.96 Sedimentation ability (P1).

4.4.3.2 Laser diffraction granulometric analyses after attrition milling (A1)

After attrition milling three regions of particle size are observed: the first over 10 μm, the second at 4 μm and the third lower than 1 μm [0.3-1] μm.

A different trend of size distribution is observed only after four hours of attrition milling: this last condition doesn't show the particles bigger than 10 μm and it shows a decrease of particles from 4 to 3 μm.

After US the size distribution changes again: it observes a decrease of region with particle size close to 4 μm and an increase of region lower than 1 μm because there is a re-agglomeration of particles during the time between the end of attrition and the granulometric analyse.

Therefore during attrition milling it is necessary the addition of dispersing agent to avoid the re-agglomeration of particles. Also for this case the amount of dispersing agent is determinate by the sedimentation test.

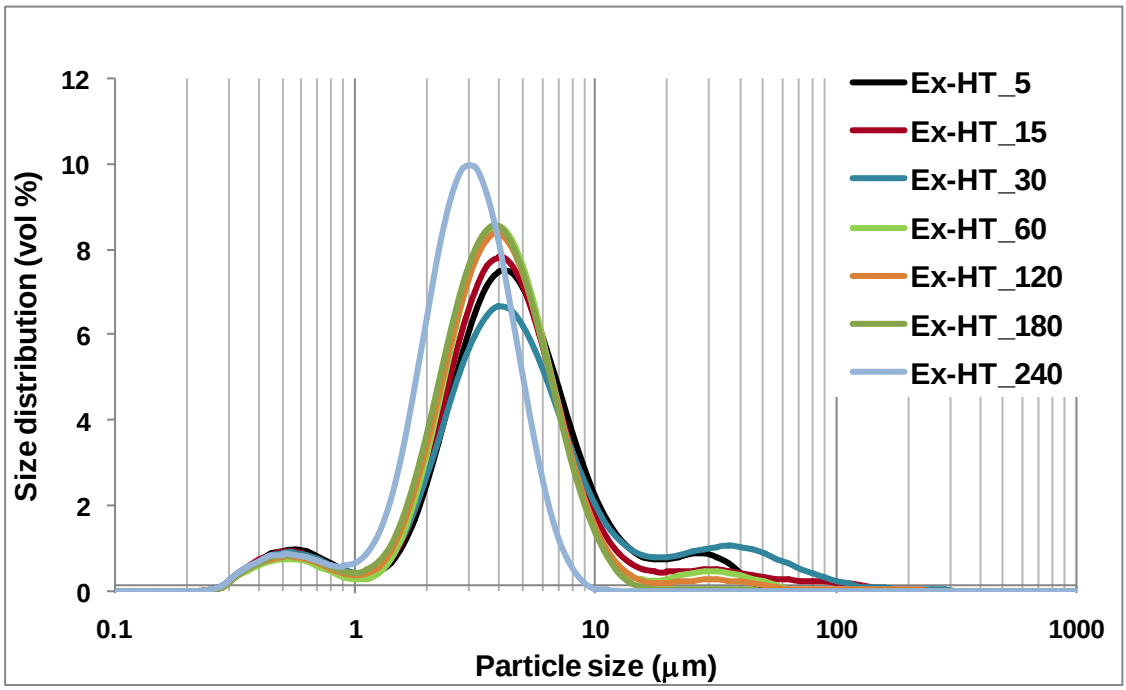

Fig. 4.97 Effect of time of attrition milling on granulometric analyse of Ex-HT (A1).

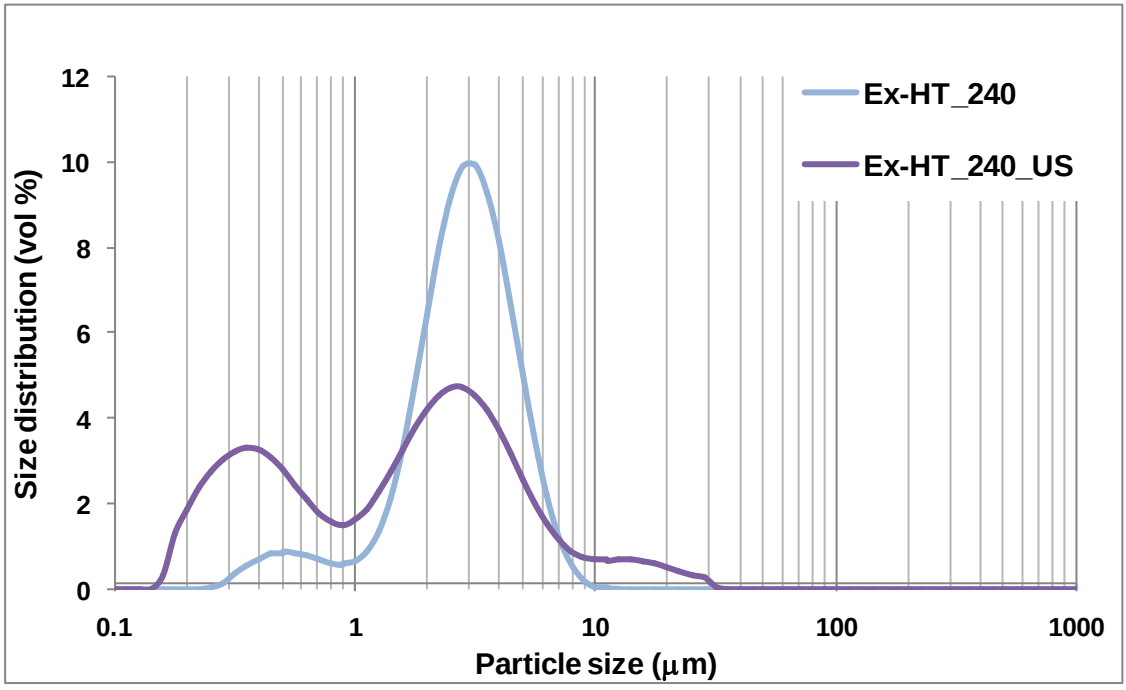

Fig. 4.98 Effect of US after attrition milling on granulometric analyse of Ex-HT (A1).

4.4.3.3 Sedimentation ability after attrition milling and planetary milling (A1P1)

After thermal treatment at 450 °C the attrited powder was used for planetary milling (A1P1).

As before the obtained slurry after planetary milling was divided in five test tubes and in each tube different amount of dispersing agent was added. In Tab. 4.23 the amount of dispersing agent for each tube was summarized. The percentage is referred to the weight of catalyst.

The Fig. 4.99 shows that the most compact sample with best separation between powder and solvent is the third sample with 6% of dispersing agent. Therefore during attrition milling 6% wt of dispersing agent was added to the slurry.

Nr samples	Amount of dispersing agent
0	/
1	4 % wt of catalyst
2	5 % wt of catalyst
3	6 % wt of catalyst
4	7.5 % wt of catalyst
5	10 % wt of catalyst

Tab. 4.23 Amount of dispersing agent for sedimentation ability (A1P1).

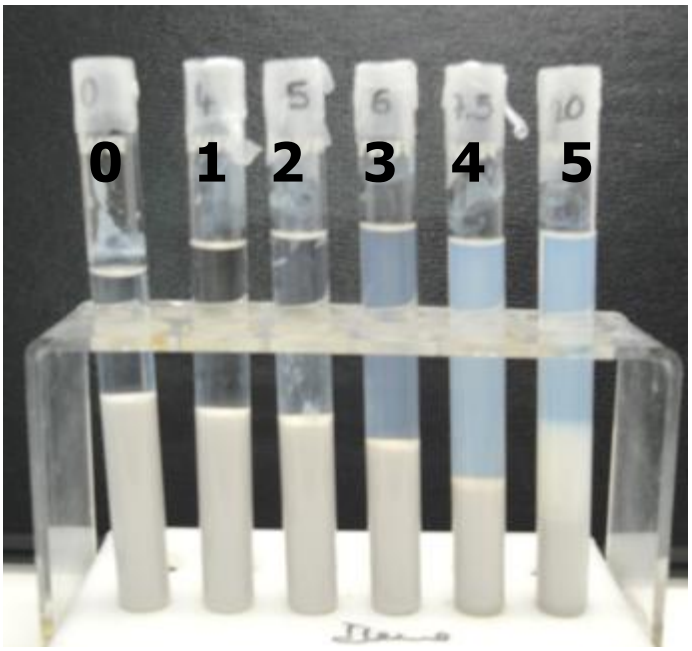

Fig. 4.99 Sedimentation ability (A1P1).

4.4.3.4 Laser diffraction granulometric analyses after attrition milling with dispersing agent (A2)

After attrition milling with 6% wt of dispersing agent two regions of particle size are observed: the first shows the maximum at 1.1 μm and it is between [1-7] μm, while the second is less defined and it is between [0.3-1] μm. No different trend is observed after three or four hours, therefore after three hours the distribution is stable.

The effect of dispersing agent is positive and a decrease of size distribution is observed in Fig. 4.100.

After US the size distribution changes again: it observes a decrease of region with the maximum of particle size close to 1.1 μm and an increase of region lower than 1 μm because there is a re-agglomeration of particles during the time between the end of attrition and the granulometric analyse.

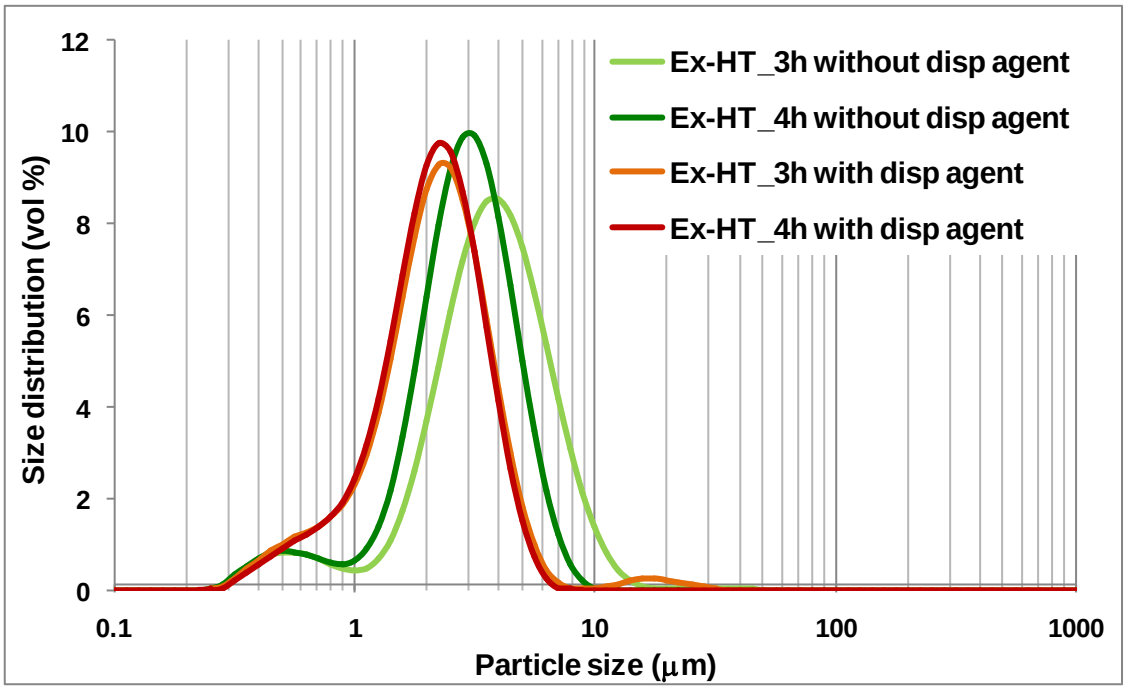

Fig. 4.100 Effect of dispersing agent after attrition milling on granulometric analyse of Ex-HT (A1 and A2).

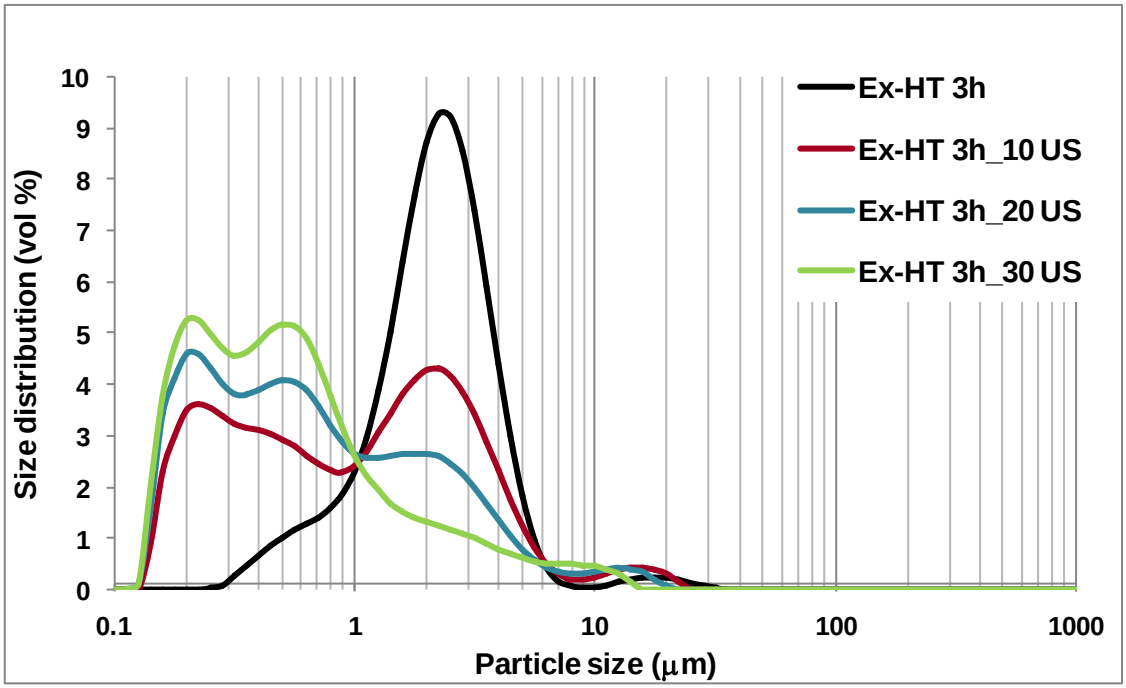

Fig. 4.101 Effect of US after attrition milling on granulometric analyse of Ex-HT (A2).

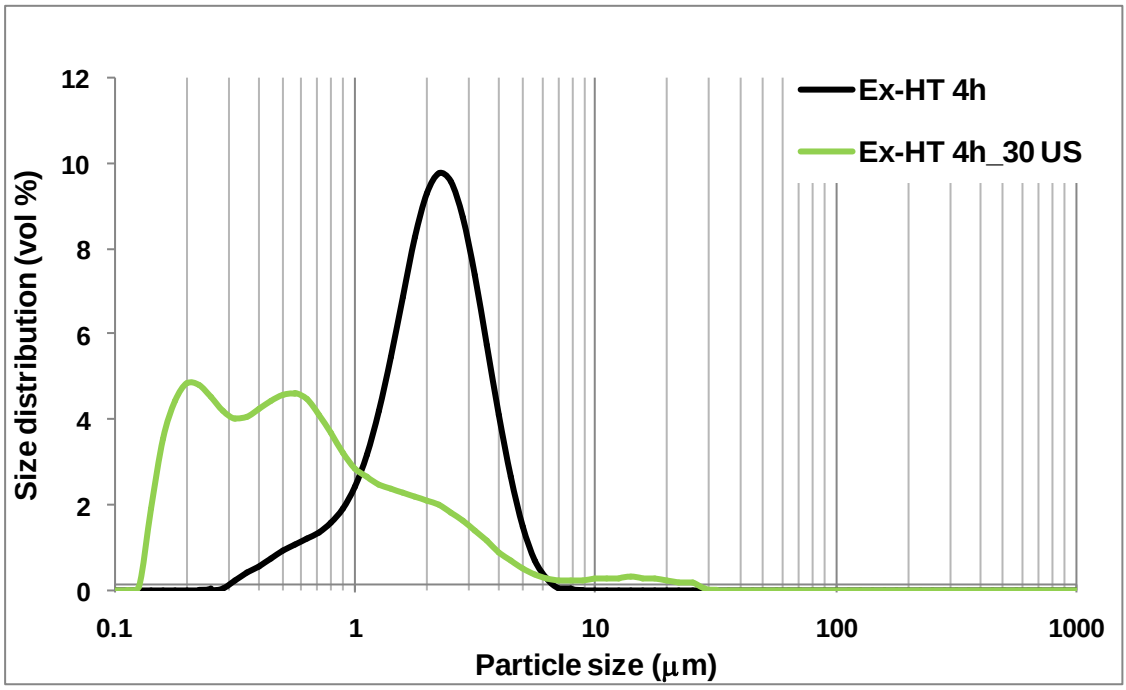

Fig. 4.102 Effect of US after attrition milling on granulometric analyse of Ex-HT (A2).

4.4.4 Viscosity (A2P2)

The measure of viscosity is very essential to determine the thickness of the coating on foams. It was measured with a starting strength of 2 N/m^2 for both slurries with 5 % wt and 7.5 % wt of catalyst. The two curves show a very similar trend because the amount of dispersing agent is so high that the weight of catalyst doesn't influence the viscosity.

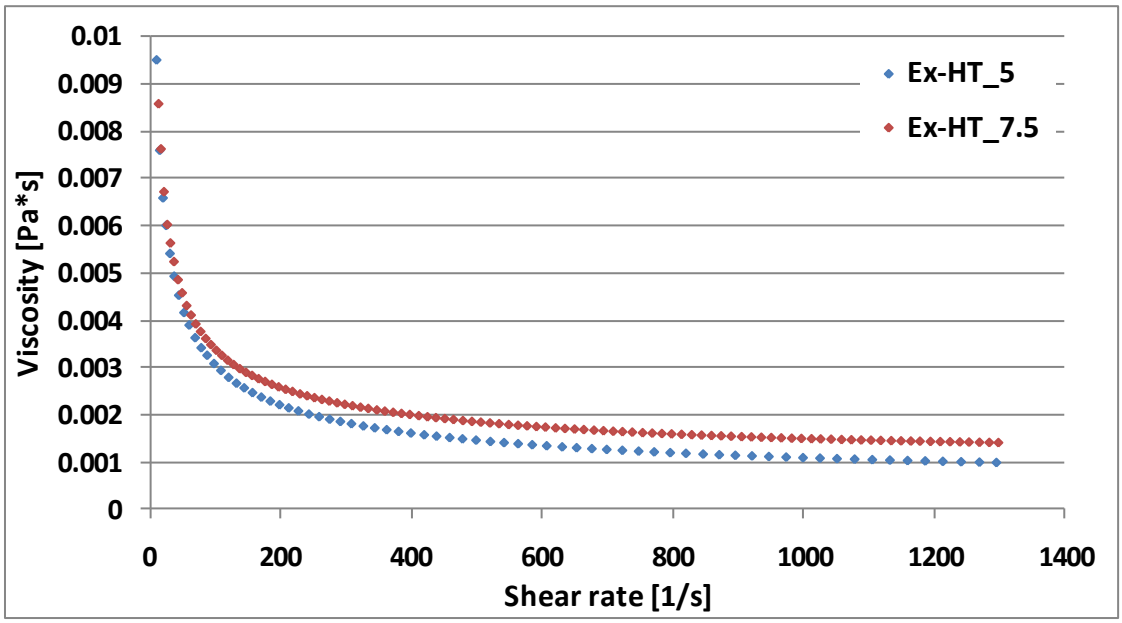

Fig. 4.103 Viscosity of the slurry versus shear rate.

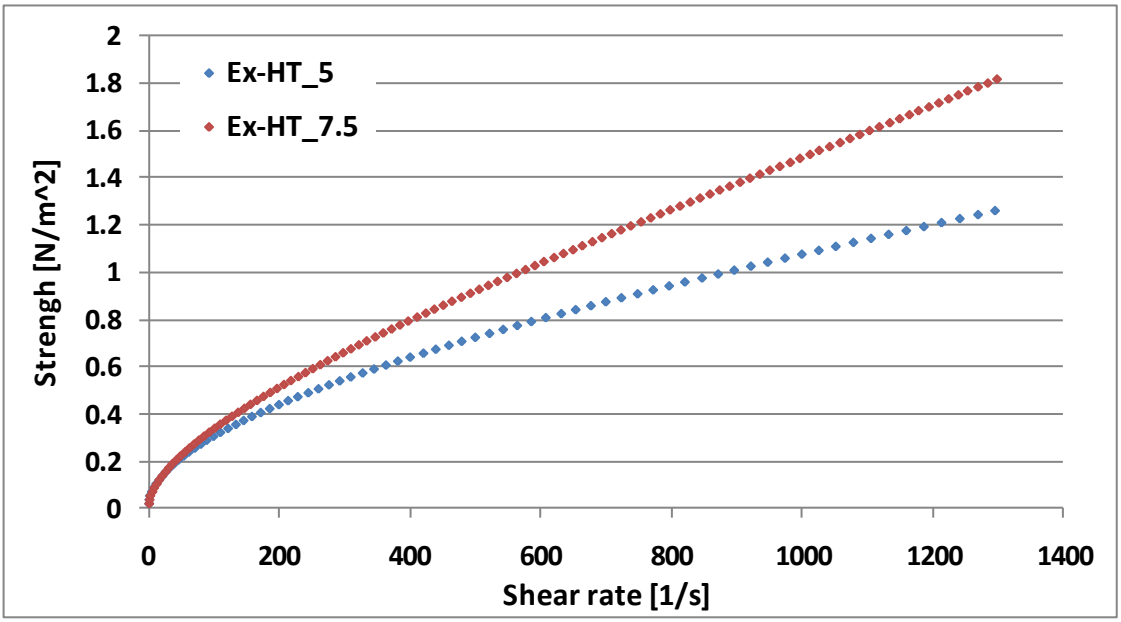

Fig. 4.104 Strength of the slurry versus shear rate.

4.4.5 Preparation and characterization of foams

4.4.5.1 Final receipt of preparation of slurry

After all analyses, hereafter it is written the receipt of preparation of slurry based on ex-hydrotalcite to coat foams.

a. Attrition milling with Ex-HT and 5 %wt of dispersing agent
b. Thermal treatment at 450 °C to evaporate dispersing agent
c. Planetary milling on the attrited powder (5 or 7.5 %wt of catalyst in MEK/EtOH 3/2) and 6 %wt of dispersing agent
d. Coatings of foams with 5 or 7.5 %wt of catalyst
e. Thermal treatment at 450 °C to evaporate dispersing agent

4.4.5.2 SEM analyses

The catalysts surface is observed by FEG-SEM (JEOL-6700F), equipped with an EDS detector (PGT Spirit, Si(Li) diode detector) to analyse chemical compositions.

FEG-SEM photos were taken both for 5 and 7.5 % wt of catalyst considering different zones to see the homogeneity and different samples to see the reproducibility. For both percentages of catalyst the coating is homogeneous and similar for different samples of same percentage; the thickness is close to 2-4 μm. The coating is well adherent and no zones with big cracks are evident. The similar coating both for 5 and 7.5 % wt of catalyst confirm the previous data regarding the viscosity.

4.4.5.2.1 SEM photos of foams with 5 % wt of catalyst

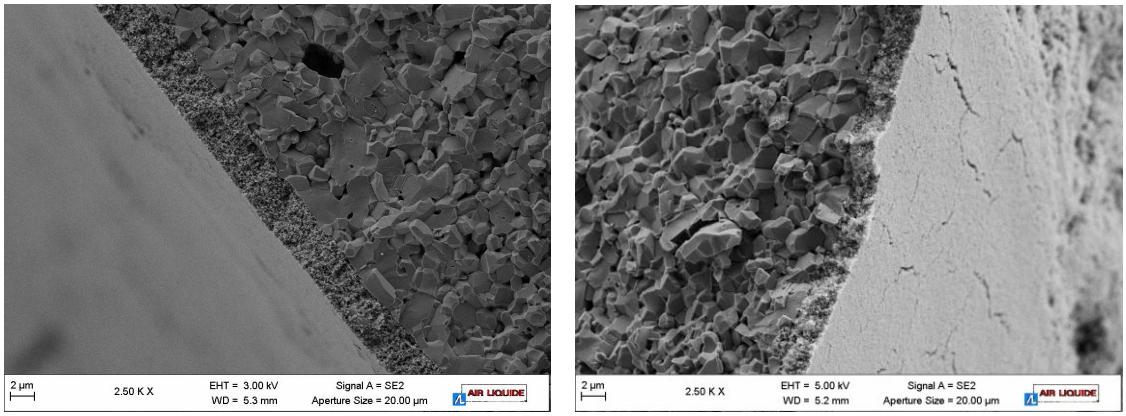

Fig. 4.105 SEM photos of Ex-HT coating (5 % wt) on alumina foam.

4.4.5.2.2 SEM photos of foams with 7.5 % wt of catalyst

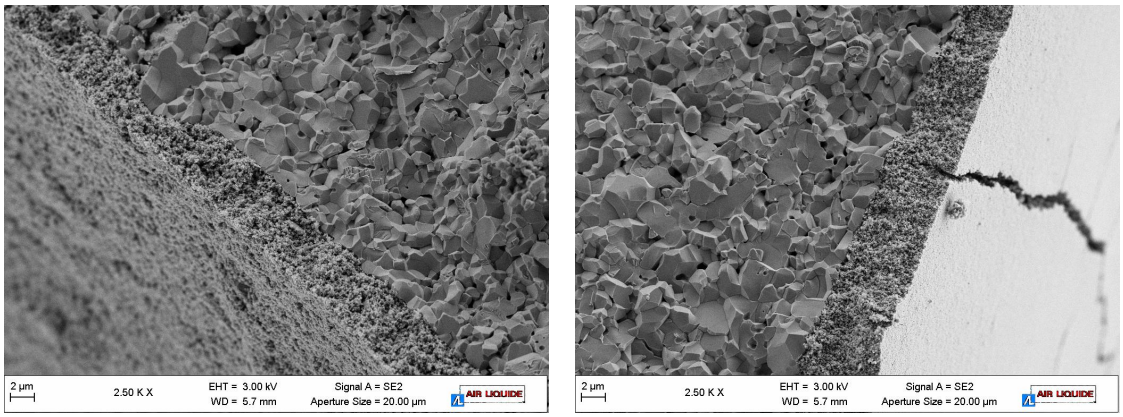

Fig. 4.106 SEM photos of Ex-HT coating (7.5 % wt) on alumina foam.

4.5 Under pressure conditions

The study to select best under pressure conditions was carried out with the Ex-HT $Rh_{0.5}Mg_{80}Al_{19.5}$ with silicate (R05M80As) which showed best performances at atmospheric pressure. First tests were carried out at 20 bar and 780 °C (real temperature inside the bed) but very high amount of coke was observed before catalytic bed, in the part with quartz due to cracking reaction and to the polymerization of CH_2CH_2 present in a significant amount. Therefore under pressure tests were carried out only with quartz to verify the optimal temperature in which coke will not be formed. During the former part of work pure ethanol was used to study the effect of contact time and temperature on catalytic performances, then, after the optimization of reaction condition, surfin ethanol was used to study its effect on activity and selectivities. Last part was dedicated to test foams coated of calcined hydrotalcite under pressure of 20 bar with surfin ethanol.

4.5.1 Under P tests with pure EtOH

4.5.1.1 Under P tests at 570°C

Reaction conditions are summarized in the following table. Respect previous conditions temperature at the end of catalytic bed was kept costant by changing the temperature of the oven. In addition contact time related to the weight of catalyst (CTw) is added in the table to compare the activity of pellets with foams because the different geometry doesn't permit an easy comparison if it considers the contact time related to volume of the catalysts.

	570,0,x	570,0,1.4x	570,0,2.3x
P (bar)	20	20	20
Toven (°C)	600	590	570
Tout (°C)	570	570	570
real CT (s)	1.4	1.0	0.60
real CTw* (s)	0.90	0.65	0.39
S/CH_3CH_2OH (mol/mol)	5	5	5
fD (mol/mol)	0	0	0
V cat (mL)	2	2	2
Pellets size (mesh)	14-20	14-20	14-20

Tab. 4.24 Under pressure conditions.

During first condition ethanol conversion is total and the catalyst activity and selectivities appear stable for 12 hours. It decides to decrease contact time to study the effect of contact time on byproducts in under pressure conditions. Ethanol conversion is total for first two conditions, while it decreases during last condition at 0.6 s. Even if the contact time is decreased of two times the C1 selectivities are very similar because the system is close to thermodynamic equilibrium (Fig. 4.109).

All reactions which entail a decrease of number of mole are more favourite during under pressure conditions respect at atmosphere pressure therefore methanation of CO and hydrogenation of CH_2CH_2 are more favourite

It is interesting to observe that CH_4 amount is slightly lower than equilibrium value while H_2 and CO_2 are slightly higher. By decreasing contact time CH_4 amount continues to decrease both for less decomposition of CH_3CHO but also for less methanation of CO which, at 570 °C and 20 bar, is more favourite than reforming.

During last condition some traces of CH_2CH_2, CH_3CH_3 and CH_3CHO were detected and they are due, as for previous tests at atmospheric pressure, to a not complete ethanol conversion.

The spent catalyst showed part of the sample black(R05M80AsB570) and part grey (R05M80AsG570).

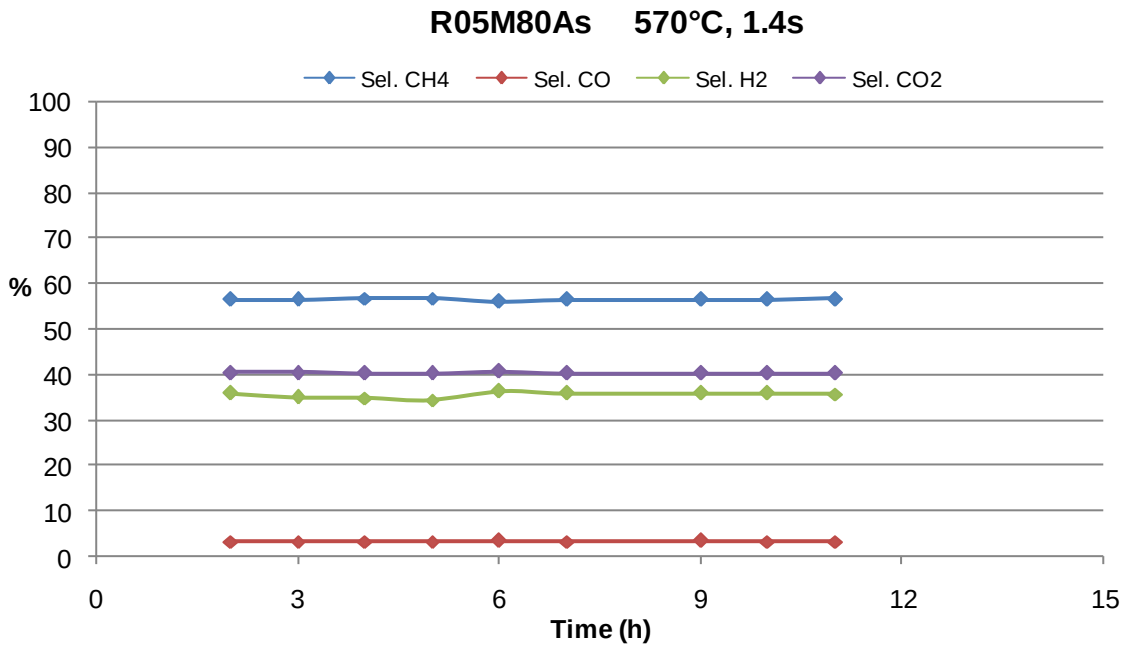

Fig. 4.107 Catalytic results (effect of time of stream).

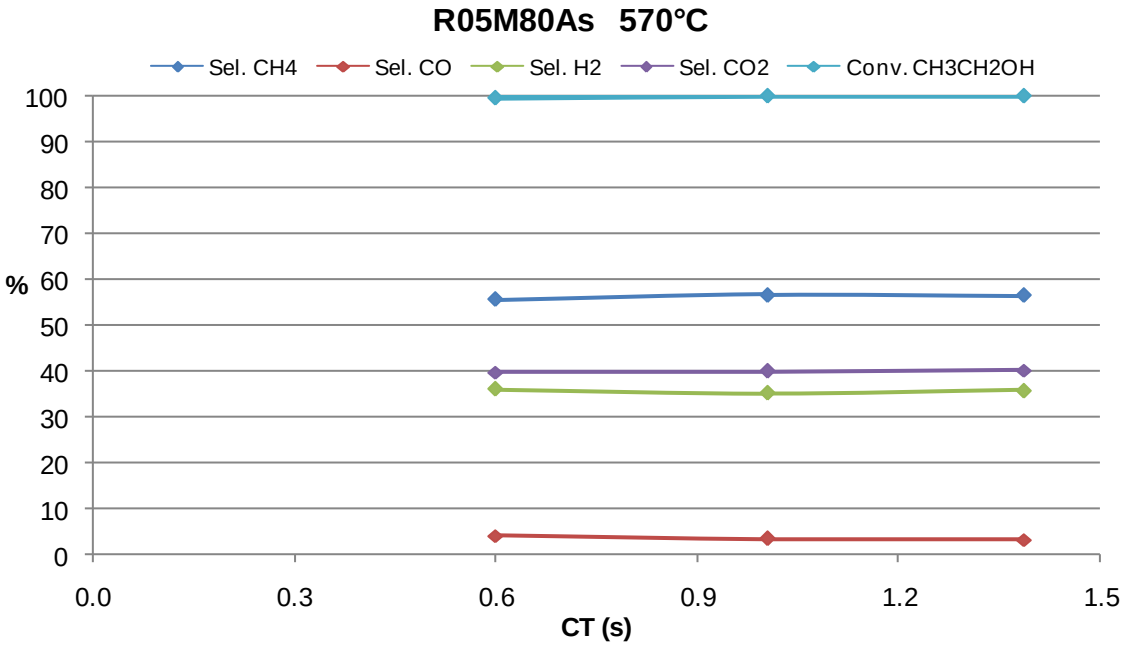

Fig. 4.108 Catalytic results (effect of CT).

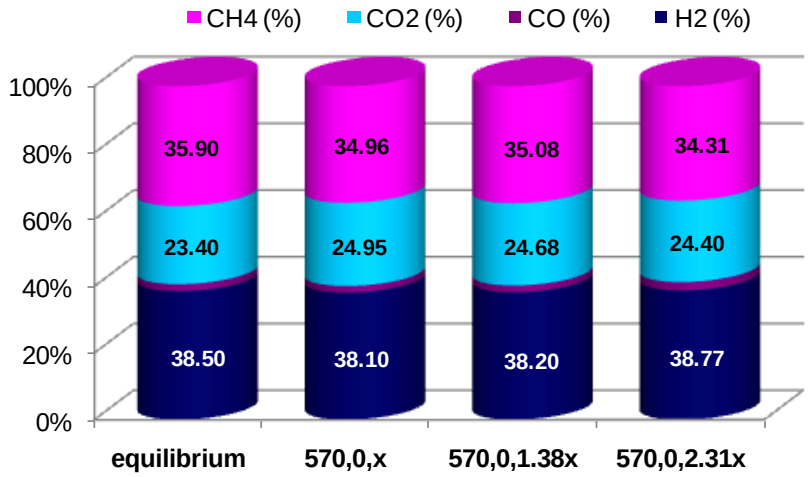

Fig. 4.109 Comparison of gas phase distribution considering dry gas.

4.5.1.2 Under P tests at 550 and 520°C

Part of the used catalyst of previous tests showed black deposits probably due to coke formation. A new load of catalyst with increased amount (4mL) was loaded, the amount was increased to discriminate a trend of deactivation along the catalyst bed. At the same time the temperature was decreased to study if it is possible to obtain only C1 products at lower temperature due to the higher residence time and to avoid coke formation by lowering the temperature.

	550,0,2.3X	520,0,2.3X
P (bar)	20	20
Toven (°C)	600	590
Tout (°C)	550	520
real CT (s)	1.2	1.3
real CTw (s)	0.40	0.41
S/CH_3CH_2OH (mol/mol)	5	5
fD (mol/mol)	0	0
V cat (mL)	4	4
Pellets size (mesh)	14-20	14-20

Tab. 4.25 Under pressure conditions.

Both at 550 and 520 °C catalytic activity and selectivities are very stable for a global time of 30 hours. No intermediates or by-product as CH_3CH_3 are observed for both conditions. The slight differences in selectivities of C1 products are due to difference of temperature. Decreasing temperature shifts equilibrium towards higher amount of CH_4 and CO_2 due to methanation and water gas shift reactions.

Since catalytic data appear very stable, after two days of tests for each temperature it decided to change and use surfin ethanol.

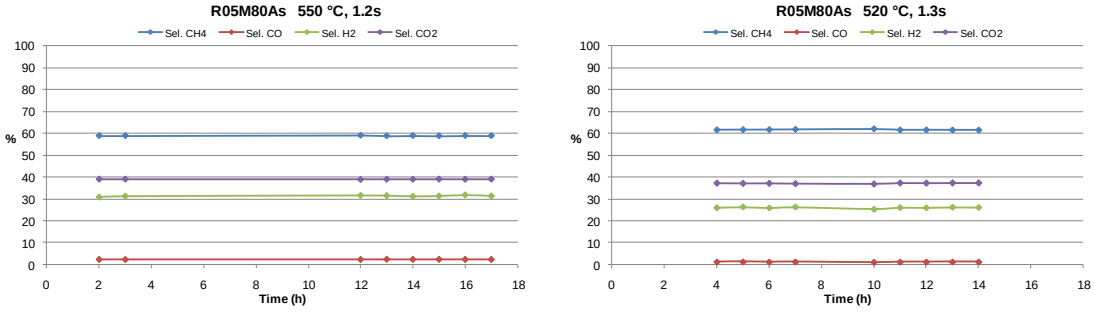

Fig. 4.110 Catalytic results (effect of time of stream).

4.5.2 Under P tests with surfin EtOH

The conditions are the same of previous paragraph. Tests with surfin ethanol at 520 °C were carried out after previous tests with pure ethanol. The Fig. 4.111 is related to first tests with pure ethanol then with surfin. The catalyst was tested for two days and then it was stopped and cooled down.

During all the tests the catalyst shows total ethanol conversion and no intermediates. Only after the break, the sample shows traces of CH_3CH_3 and it decided to stop and

download the reactor. Some coke is still present on the catalyst, but it is not possible to identify a particular zone of catalytic bed in which is preferentially formed.

The amount of CH_4 is lower than same condition with pure ethanol, confirming first under pressure tests at 780 °C which show that presence of surfin ethanol enhances reforming of CH_4, probably because the amount of water is higher in surfin ethanol than in pure ethanol.

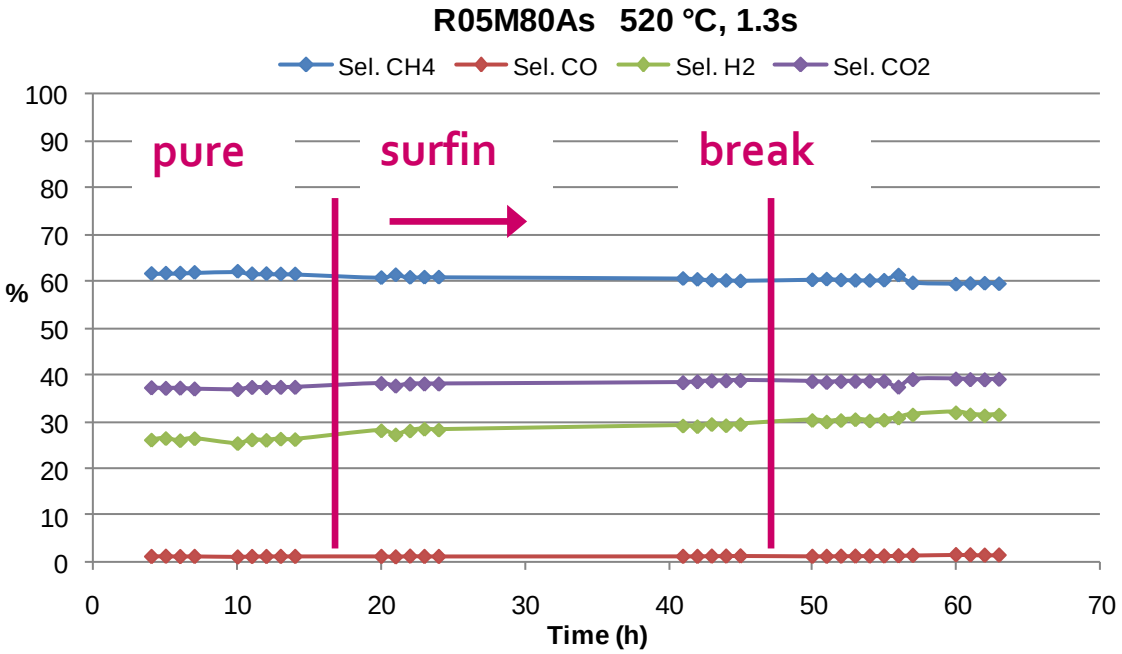

Fig. 4.111 Catalytic results (effect of time of stream).

4.5.3 Foams tests and comparisons

Foams loaded in the reactor were 6, for a total weight of active phase of ca. 0.06 g.

Catalyst	pellets	pellets	foam
Temperature (°C)	570	550 and 520	590
Volume of active phase (mL)	2	4	12
Weight of active phase (g)	1.30	2.65	0.06

Tab. 4.26 Summary of different conditions of pellets and foam catalysts.

Since the weight of rhodium is lower than that one presented in the pellets (Tab. 4.26) the amount of flows were decreased and temperature was increased to obtain high ethanol conversion and low amount of intermediates. Only the temperature at the beginning of the catalytic bed was possible measured therefore it was considered as temperature inside the reactor.

	590,1,0.1x	590,0,0.3x
P (bar)	20	20
Toven (°C)	640	640
Tin (°C)	590	590
real CT (s)	26.8	27.2
real CTw (s)	0.14	0.14
S/CH3CH2OH (mol/mol)	5	5
fD (mol/mol)	1	0
V cat (mL)	12	12

Tab. 4.27 Under pressure conditions.

Also foams show total ethanol conversion and no presence of intermediates: this is certainly due to very high contact time and temperature used. Foams show stable results for more than 30 hours with a costant inlet temperature (Fig. 4.112).

The helium presence improves H_2 selectivity because steam methane reforming is favoured as lower CH_4 selectivity confirms (Fig. 4.113). In diluted condition the partial pressure of reagents is lower than in non diluted and with lower partial pressures a reaction which involved an increase of number of mole, as methane reforming, is more favourite.

Foams catalysts show very interesting catalytic performances with very high ethanol and water conversions as pellets despite of the lower active phase. The high H_2 selectivity of foams is attributed to high temperature used for tests which favours CH_4 reforming. Foams catalysts can be consider as a promising alternative to pellets catalysts because they show comparable activity, selectivity and stability with pellets.

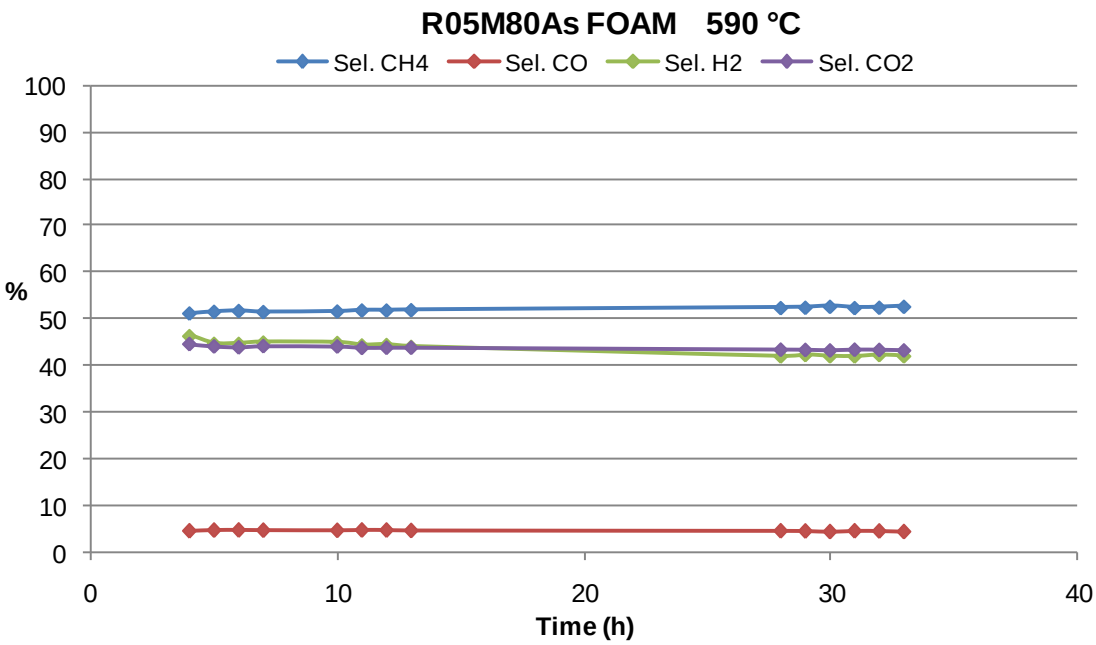

Fig. 4.112 Catalytic results (effect of time of stream) during 590,0,0.3x condition.

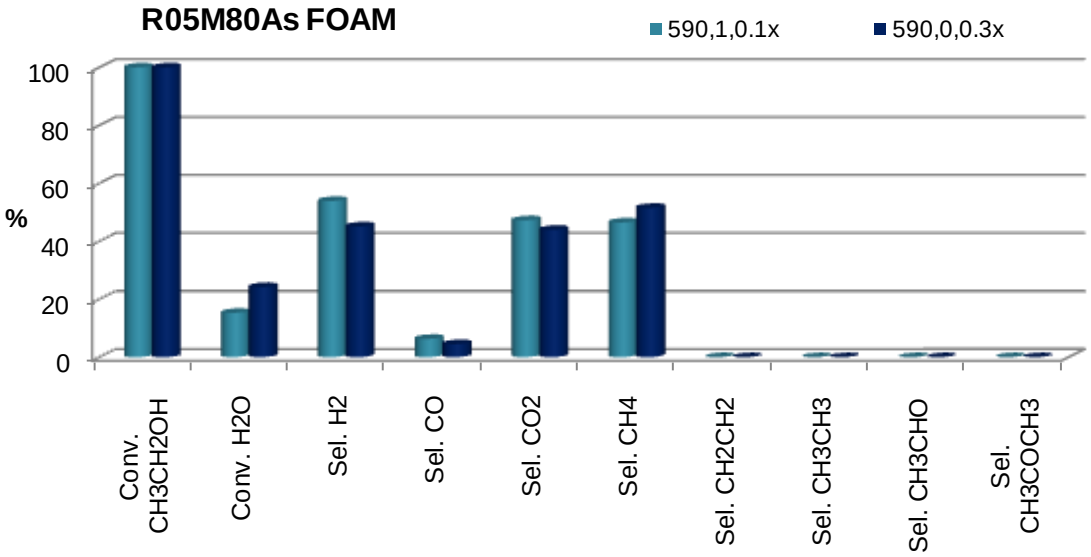

Fig. 4.113 Catalytic results (effect of dilution).

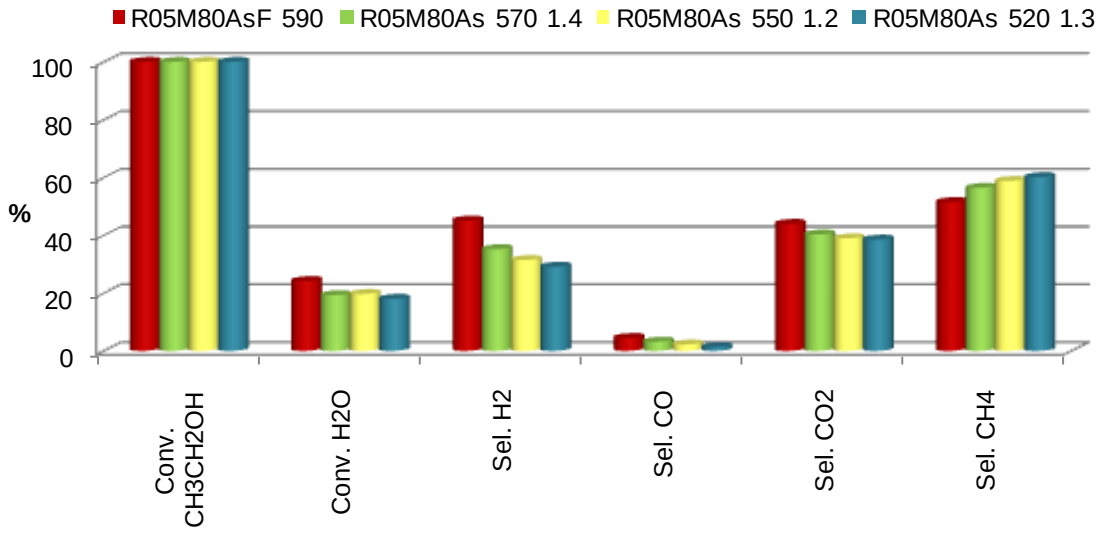

Fig. 4.114 Comparison of different conditions: effect of temperature and contact time.

4.5.4 Characterization of spent catalysts

Two spent catalysts are named as:

R05M80AsG570 for gray spent catalyst tested at 570 °C,
R05M80AsB570 for black spent catalyst tested at 570 °C,
R05M80AsG520 for gray spent catalyst tested at 520 °C and
R05M80AsB520 for black spent catalyst tested at 520 °C.

XRD diffraction of both black catalysts show same phases of fresh catalyst with more defined reflections, in particular those related to the spinel. No reflections attributed to amorphous or crystalline coke are observed.

After catalytic tests the specific surface area and pores volume of all samples are lower than fresh one. Pores distribution of gray samples show a shift of the maximum pore width that with previous observation seems suggest that sintering phenomena occur into the catalysts. Black samples show higher surface area than gray ones and common microporosity at around 35 Å which is absent in R05M80AsG570 and R05M80AsG520. Last points are related to the presence of microporous coke on the surface of catalysts.

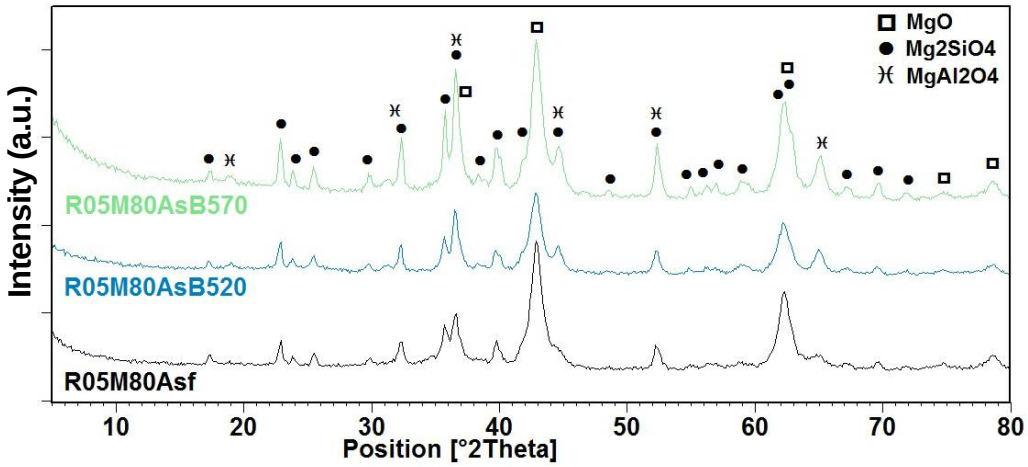

Fig. 4.115 XRD of fresh and spent R05M80As.

	BET surface area (m^2g^{-1})	t-plot micropore area (m^2g^{-1})	BJH desorption cumulative volume of pores (cm^3g^{-1})	BJH desorption maximums pore widths (Å)
R05M80Asf	107.13	16.52	0.452	34 , 127
R05M80AsG570	43.09	3.60	0.317	176
R05M80AsB570	63.37	1.63	0.279	37, 151
R05M80AsG520	64.67	0	0.402	176
R05M80AsB520	76.18	0	0.238	36 , 109

Tab. 4.28 Surface area and pores volume and width of fresh and spent R05M80As.

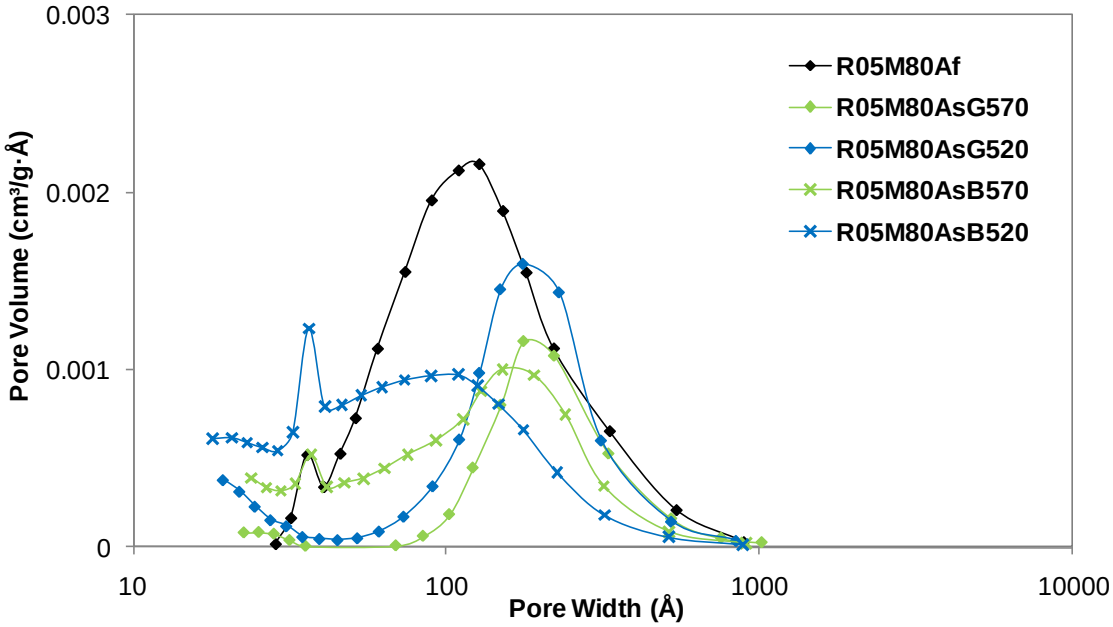

Fig. 4.116 BJH pore size distribution of fresh and spent R05M80As.

BIBLIOGRAFY

1. Rosetti, V. *Catalysts for H2 production;* Ph.D. thesis; University of Bologna: Italy, 2007.
2. Haga, F.; Nakajima, T.; Yamashita, K.; Mishima, S. Effect of crystallite size on the catalysis of alumina-supported cobalt catalyst for steam reforming of ethanol. *Reaction Kinetics and Catalysis Letters* **1998,** *63,* 253-259.
3. Cavallaro, S.; Mondello, N.; Freni, S. Hydrogen produced from ethanol for internal reforming molten carbonate fuel cell. *Journal of Power Sources* **2001,** *102,* 198-204.
4. Llorca, J.; Homs, N.; Sales, J.; Fierro, J.-L. G.; de la Piscina, P. R. Effect of sodium addition on the performance of Co-ZnO-based catalysts for hydrogen production from bioethanol. *Journal of Catalysis* **2004,** *222,* 470-480.
5. Llorca, J.; Homs, N.; Sales, J.; de la Piscina, P. R. Efficient production of hydrogen over supported cobalt catalysts from ethanol steam reforming. *Journal of Catalysis* **2002,** *209,* 306-317.
6. Kaddouri, A.; Mazzocchia, C. A study of the influence of the synthesis conditions upon the catalytic properties of Co/SiO2 or Co/Al2O3 catalysts used for ethanol steam reforming. *Catalysis Communications* **2004,** *5,* 339-345.
7. Aupretre, F.; Descorme, C.; Duprez, D.; Casanave, D.; Uzio, D. Ethanol steam reforming over MgxNi1-xAl 2O3 spinel oxide-supported Rh catalysts. *Journal of Catalysis* **2005,** *233,* 464–477.
8. Morgenstern, D. A.; Fornango, J. P. Low-temperature reforming of ethanol over copper-plated raney nickel: A new route to sustainable hydrogen for transportation. *Energy and Fuels* **2005,** *19,* 1708-1716.
9. Akande, A.; Aboudheir, A.; Idem, R.; Delai, A. Kinetic modeling of hydrogen production by the catalytic reforming of crude ethanol over a co-precipitated Ni - Al2 O3 catalyst in a packed bed tubular reactor. *International Journal of Hydrogen Energy* **2006,** *31,* 1707-1715.
10. Vaidya, P. D.; Rodrigues, A. E. Insight into steam reforming of ethanol to produce hydrogen for fuel cells. *Chemical Engineering Journal* **2006,** *117,* 39-49.
11. Mas, V.; Baronetti, G.; Amadeo, N.; Laborde, M. Ethanol steam reforming using Ni(II)-Al(III) layered double hydroxide as catalyst precursor Kinetic study. *Chemical Engineering Journal* **2008,** *138,* 602–607.
12. Fornasari, G.; Gazzano, M.; Matteuzzi, D.; Trifiro`, F.; Vaccari, A. Structure and reactivity of high-surface-area Ni/Mg/Al mixed oxides. *Applyed Clay Science* **1995,**

10, 69-82.

13. Basile, F.; Fornasari, G.; Gazzano, M.; Kiennemann, A.; Vaccari, A. Preparation and characterisation of a stable Rh catalyst for the partial oxidation of methane. *Journal of Catalysis* **2003,** *217*, 245–252.

14. Hardiman, K. M.; Cooper, C. G.; Adesina, A. A.; Lange, R. Post-mortem characterization of coke-induced deactivated alumina-supported Co–Ni catalysts. *Chemical Engineering Science* **2006,** *61*, 2565 – 2573.

15. Ge, X.; Li, M.; Shen, J. The Reduction of Mg`Fe`Oand Mg`Fe`Al`OComplex Oxides Studied by Temperature-Programmed Reduction Combined with in Situ Mossbauer Spectroscopy. *Journal of Solid State Chemistry* **2001,** *161*, 38-44.

16. Hadnadjev, M.; Vulic, T.; Marinkovic-Neducin, R.; Suchorski, Y.; Weiss, H. The iron oxidation state in Mg–Al–Fe mixed oxides derived from layered double hydroxides: An XPS study. *Applied Surface Science* **2008,** *254* , 4297–4302.

17. Cavani, F.; Trifiro, F.; Vaccari, A. Hydrotalcite-type anionic clays: Preparation, properties and applications. *Catalysis Today* **1991,** *11*, 173-301.

18. Albertazzi, S.; Basile, F.; Benito, P.; Del Gallo, P.; Fornasari, G.; Gary, D.; Rosetti, V.; Vaccari, A. Effect of silicates on the structure of Ni-containing catalysts obtained from hydrotalcite-type precursors. *Catalysis Today* **2007,** *128*, 258–263.

19. Reichle, W. T. Synthesis of anionic clay minerals (mixed metal hydroxides, hydrotalcite). *Solid State Ionics* **1986,** *22*, 135-141.

20. Yates, J. T. J.; Duncan, T. M.; Vaughan, R. W. Infrared spectroscopic study of activated surface processes: CO chemisorption on supported Rh. *Journal of Chemical Physics* **1979,** *71*, 3908-3915.

21. Bergeret, G.; Gallezot, P.; Gelin, P.; Taarit, Y. B.; Lefebvre, F.; Naccache, C.; Shannon, R. D. CO-Induced Disintegration of Rhodium aggregates supported in zeolites: in situ synthesis of rhodium carbonyl clusters. *Journal of Catalysis* **1987,** *104*, 279-287.

22. Twigg, M. V. *Catalyst Handbook,* 2nd ed.; Wolf Publishing Ltd, 1989.

5 Conclusions

Aim of this thesis was the study of new process for hydrogen production using bioethanol instead of methane in the steam reforming reaction.

First part of work was dedicated to the study of ethanol decomposition at 700 °C to understand the relevance of gas phase reactions and the reactivity of ethanol towards incoloy reactor and quartz which was used as inert to fill the reactor. Highest contribution to ethanol decomposition is mainly attributed to gas phase reaction with a order of reaction close to one. Considering the high reactivity of ethanol even at low temperature, quartz activity and selectivities at 700 °C can be considered negligible.

Operative conditions at atmospheric pressure were studied for a catalyst obtained after calcination of hydrotalcites like compounds and based on rhodium-nickel as active phase. This catalyst had shown very good performances in methane steam reforming. The range of temperature took in exam was very wide between 250 °C until 700 °C with two ratios of steam to ethanol (5 and 4). Rh-Ni catalyst shows high activity even at 250 °C and gas phase distribution close to thermodynamic equilibrium. Lower steam to ethanol affects negatively H_2, CO and CO_2 selectivities and it determines higher deactivation of the catalyst therefore the work was continued using water to ethanol equal to 5.

The study on catalysts was focus on mixed oxide obtained after calcination of hydrotalcites like compounds. This type of materials presents both redox and acid-basic properties which could play a determinant role in the selectivities of products. Moreover they show high surface area and very small crystal size of the mixed oxide structure produced after calcination, after reduction it is possible to obtain small and thermally stable metal crystallites.

First step was consisted in the study of the effect of a second metal as nickel or iron into a catalyst based on rhodium (ex-HT silicate $Rh_{0.15}Mg_{68}Al_{31.85}$). Five samples with different percentages of rhodium, nickel and iron was considered at two different temperatures (700 and 550°C). At 550 °C, when ethanol conversion is far from 100 %, is possible to observe some trends: Rh-Ni series show best results in H_2 selectivity and the lower amount of intermediates and by-products, whereas Rh shows the high amount of intermediates which are related with the low ethanol conversion of this sample. Rh-Fe exhibits low ability in reforming because of the high amount of CH_4 observed. Despite of the high activity and H_2 selectivity, Rh-Ni series shows the highest amount of coke respect other catalysts while Rh-Fe the highest instability of textural properties. Since Rh series show more stable samples it was decided to improve the catalyst performances of ex-HT silicate $Rh_{0.5}Mg_{68}Al_{31.5}$ by studying the effects of different matrix.

For this reason a deep characterization was carried out on five different samples with same amount of rhodium (1% wt). Two of these catalysts were constituted by silicates, as previous samples, but the ratio Mg/Al was changing (68/32 and 80/20), while other two were prepared with carbonates always with two ratio Mg/Al. A fifth catalyst was based on RhCeZrO2 (RCZO) with fixed ratio of Ce/Zr (75/25).

For catalysts obtained by calcination of hydrotalcite like phase the utilization of silicates instead of carbonates changes type of phases inside the samples because not only MgO and spinel are detected, as for carbonates, but also fosterite (Mg_2SiO_4) type phase. In addition different ratio Mg/Al affects the ratio of $MgO/MgAl_2O_4$.

All ex-HTs samples show rhodium nanosize with higher density of particles in the catalysts calcined at high temperature confirming TPR analyses that rhodium is well stabilized inside the structure and during reduction high dispersion is obtained without sintering of particles.

Most active catalysts are Rh silicate with higher amount of magnesium (R05M80As) and RCZO. At 700 °C these two catalysts and Rh carbonate with less magnesium (R043MAc) shows best H_2 selectivity, whereas Rh carbonate with higher magnesium (R043M80Ac) and Rh silicate with less magnesium (R055MAs) show high amount of intermediates and by-products as CH_3COCH_3. At 600 °C the decrease of contact time affects significantly ethanol conversion and therefore the amount of intermediates increases. R043MAc and R05M80As show only intermediates as CH_3CHO and CH_2CH_2, while RCZO shows high amount of CH_3COCH_3 due to high basicity of the $CeZeO_2$. Catalytic results show similar trends for samples R043MAc and R05M80As with close $MgO/MgAl_2O_4$ ratio creating a relationship between high C1 selectivities and the ratio $MgO/MgAl_2O_4$. In particular the right ratio should be included in 1.1-1.5. Since hydrotalcite prepared with silicates have shown more stable catalysts, i.e. no reconstruction and no high decrease of surface area, R05M80As was chosen to test under pressure.

Under pressure tests were carried out at 20 bar and temperature between 520-590 °C, firstly with pure ethanol then with ethanol after a purification denominated surfin. After optimization of contact time to avoid not complete ethanol conversion and/or intermediates, catalytic performances are very close to thermodynamic equilibrium with stable results for more than 60 hours.

Similar tests were carried out also on ceramic foams coated by R05M80As. Foams catalysts show very interesting catalytic performances with complete ethanol conversion and very high H_2 selectivity despite the low amount of active phase respect pellets. Foams catalysts can be consider as a promising alternative to pellets catalysts because they show comparable activity, selectivity and stability with pellets.

The high performances obtained with foams is due to the optimization of coating of ex-hydrotalcite on ceramics foams. Considering the high porosity of ex-hts samples it

was necessary high amount of dispersing agent to obtain homogeneous and thin coating without cracks.

This study touches different aspects of bioethanol reforming: thermodynamic trends; synthesis, characterization, tests of active phase; best under pressure conditions and preparation of foams with previously selected active phase trying to find best solutions through catalyst and operative conditions optimization.

Acknoledgments

First of all, I would like to thank my tutor Francesco Basile to help me and find creative solutions also during worse moments. I appreciated our discussions about data.

Special thanks go to Air Liquid, in particular to Daniel Gary and Pascal Del Gallo for the financial support.

I would like to thank Fabrice Rossignol of SPCTS of Limoges and Barbara Onida of Politecnico of Torino to give me the opportunity to delve to characterization study of my catalysts.

A huge thanks to Patricia, my desk colleague, for all scientific and friendly support.